Photodisintegration of ^{3}He with Double Polarizations

by

Georgios Laskaris

Department of Physics
Duke University

Date: _____

Approved:

_____
Haiyan Gao, Supervisor

_____
Calvin R. Howell

_____
Thomas C. Mehen

_____
Christopher W. Walter

_____
Ying K. Wu

Dissertation submitted in partial fulfillment of the requirements for the degree of
Doctor of Philosophy in the Department of Physics
in the Graduate School of Duke University
2015

Abstract

Photodisintegration of ^{3}He with Double Polarizations

by

Georgios Laskaris

Department of Physics
Duke University

Date: _____

Approved:

_____
Haiyan Gao, Supervisor

_____
Calvin R. Howell

_____
Thomas C. Mehen

_____
Christopher W. Walter

_____
Ying K. Wu

An abstract of a dissertation submitted in partial fulfillment of the requirements for the degree of Doctor of Philosophy in the Department of Physics in the Graduate School of Duke University
2015

Abstract

The first measurements of the two- and three-body phototdisintegration of ^{3}He polarized parallel and anti-parallel to a circularly polarized γ-ray beam were carried out at the High Intensity γ-ray Source (HIγS) facility located at Triangle Universities Nuclear Laboratory (TUNL). A high pressure ^{3}He target, polarized via spin-exchange optical pumping with alkali metals, was used in the experiments. The protons from the two-body photodisintegration experiment were detected using seventy two silicon surface barrier detectors of various thicknesses while the neutrons from the three-body photodisintegration were detected with sixteen 12.7 cm diameter liquid scintillator detectors. The spin-dependent cross sections and the contributions from the two- and three-body photodisintegration to the ^{3}He Gerasimov-Drell-Hearn sum rule integrand were extracted and compared with state-of-the-art three-body calculations at the incident photon energies of 29.0 MeV (two-body) and 12.8, 14.7, and 16.5 MeV (three-body).

These are the first measurements of the contributions of the two- and three-body photodisintegration of ^{3}He to the GDH integrand. These measurements were found to be in good agreement with the theoretical calculations which include the Coulomb interaction between protons in the final state. They also reveal–for the first time–the importance of the three-nucleon forces and the relativistic single-nucleon charge corrections which are responsible in the calculations for the observed difference between the spin-dependent cross sections.

Writing, Phaedrus, has this strange quality, and is very like painting; for the creatures of painting stand like living beings, but if one asks them a question, they preserve a solemn silence. And so it is with written words; you might think they spoke as if they had intelligence, but if you question them, wishing to know about their sayings, they always say only one and the same thing. And every word, when once it is written, is bandied about, alike among those who understand and those who have no interest in it, and it knows not to whom to speak or not to speak; when ill-treated or unjustly reviled it always needs its father to help it; for it has no power to protect or help itself.

Phaedrus, Plato, [275d-e]

Contents

List of Tables

List of Figures

List of Abbreviations and Symbols

Abbreviations

3N	Three-Nucleon
3NF	Three-Nucleon Force
ADC	Analog to Digital Converter
AFP	Adiabatic Fast Passage
AGS	Alt-Grassberger-Sandhas
AV18	Argonne V18
BC-501A	Bicron 501A
BGO	Bismuth Germanium Oxide
BPM	Beam Pick off Monitor
BTR	Booster To Ring
CD-Bonn	Charge Dependent-Bonn
CEBAF	Continuous Electron Beam Accelerator Facility
CERN	Conseil Européen pour la Recherche Nucléaire
CFD	Constant Fraction Discriminator
CIB	Charge Independence Breaking
CODA	CEBAF Online Data Acquisition
CSB	Charge Symmetry Breaking
CS	Charge Symmetry
DAPHNE	Detecteur à grande Acceptance pour la PHysique photoNucleaire Experimentale

DAQ	Data Acquisition
DRDY	Data Ready
χEFT	chiral Effective Field Theory
EB	Event Builder
ELSA	Eckert Life Science Accelerator
EPR	Electron Paramagnetic Resonance
FA	Fix-Arenhövel
FEL	Free Electron Laser
FID	Free Induction Decay
GDH	Gerasimov-Drell-Hearn
GEANT4	GEometry ANd Tracking, Version 4
GE180	General Electric 180
HIγS	High Intensity γ-ray Source
HP	High Precision
LEGS	Laser Electron Gamma Source
LEPS	Laser Electron Photon Source
LHEP	Low and High Energy Physics
LLNL	Lawrence Livermore National Laboratory
LTB	Linac To Booster
MAID2002	MAinz unitary Isobar Model 2002
MAMI	Mainz Microtron
MEC	Meson Exchange Current
MEOP	Metastability Exchange Optical Pumping
MPD-4	Multi-channel Pulse shape Discriminator 4
MSI-8	Multi-channel preamplifier and Shaper devices, Individual read-out 8

mSQL	mini Structured Query Language
NaI(Tl)	Natrium Iodide (Thallium)
NIM	Nuclear Instrument Module
NIST	National Institute of Standards and Technology
NMR	Nuclear Magnetic Resonance
NN	Nucleon-Nucleon
OBE	One Boson Exchange
OPE	One Pion Exchange
OK	Optical Klystron
PH	Pulse Height
PMT	Photo-Multiplier Tube
PRECO	Pre-Compound
PSD	Pulse Shape Discrimination
PTB	Physikalisch-Technische-Bundesanstalt
PWIA	Plane Wave Impulse Approximation
QCD	Quantum Chromo-Dynamics
RC	Relativistic Corrections
RF	Radio Frequency
ROKK	Backscattered Compton Photons
SBC	Single Board Computer
SEOP	Spin Exchange Optical Pumping
SLAC	Stanford Linear Accelerator Center
SSB	Silicon Surface Barrier
STAR	Solenoidal Tracker at RHIC
TAC	Time to Amplitude Converter
TCP/IP	Transmittion Control Protocol/Internet Protocol

TDC	Time to Digital Converter
TFA	Timing Filter Amplifier
TJNAF	Thomas Jefferson National Accelerator Facility
TOF	Time of Flight
TUNL	Triangle Universities Nuclear Laboratory
UIX	Urbana IX
VCO	Voltage Controlled Oscillator
VME	Versa Module Europa

Acknowledgements

Many throughout these years in the USA asked me the two following questions: why I decided to pursue a PhD in Physics and in particular why I decided to cross the Atlantic ocean and do that in the USA. All these years I did not give answers perhaps because these answers in my mind are obvious. I decided to study Physics because since I was a kid I could not dream to do anything else in my life. I decided to cross the ocean for the same reason that Hannibal crossed the Alps. As this great general knew that if he could occupy Rome then nobody would dare to stand in front of his army in a battle, I believed that if I can pursue a PhD in the USA, then I can succeed in any other place of the world since the standards and requirements for such a degree in this country are the highest.

The experience of the PhD in the USA changed my character and attitude towards life in ways that I could not imagine and it would not be wise to share with the reader. Many absolute beliefs of mine became relative and many ideas that I would condemn before, I see them now with sympathy. The one belief of mine that did not change is that nothing is impossible for a human given that the surrounding conditions are mature enough for its success. The conditions in modern science are the advisor, the collaborators and the funding agencies.

First, I would like to thank my advisor, Haiyan Gao, for supporting me all these years financially and for teaching me directly or indirectly through other students and postdoctoral associates in our group the art of doing physics. I have eternal gratitude

for her and I owe her a lot which I will never be able to pay back. Knowledge is one of those strange things that although are so valuable they do not have a price.

Next, I would like to thank all collaborators and their group members for their help in the experiments described in this thesis, namely: Professors M.W. Ahmed, H.R. Weller, H.J. Karwowski and the whole capture group including A. Kafkarkou, J.M. Mueller, L.S. Myers, B. A. Perdue, S. Stave, J.R. Tompkins, W.R. Zimmerman for their help with the detector setup in the experiments in FEL facility. I would also like to thank professor T. Averett for his help and advice concerning HIγS type ^{3}He cells, professor D. Dutta for participating in the first experiments in 2011 and for showing me the initial steps for a conclusive data analysis, professor C. R. Howell for approving beam time for the performance of a third experiment on the three-body photodisintegration of ^{3}He, professor B. Tsang for providing the SSB detectors for the performance of the two-body photodisintegration experiment and professor Y. K. Wu and the staff members of HIγS facility for doing their best to provide a high quality γ-beam with exceptionally high intensity. I would like to thank my thesis committee members, C. R. Howell, T. C. Mehen, C. W. Walter, Y. K. Wu for taking the time to read my thesis and providing useful comments and corrections. Last but not least, I would like to thank my instructors and professors at the National Technical University of Athens for helping me in my first steps in physics.

In these 7 years in the medium energy physics group, there were a lot of people that helped to different degrees the performance of our experiments. I would like to thank the postdoctoral associates P.-H.Chu, S. Jawalkar, B. Lalremruata, M. Meziane, Q. Ye and the graduate students W. Chen, M. Huang, C. Peng, X. Qian, W. Xiong, X. Yan, Q. J. Ye, Y. Zhang, W. Zheng, X. Zong for all their help with the experiments in many occasions. In particular, I would like to thank Q. Ye and X. Yan without whom the performance and success of the first polarized experiments in HIγS facility would be impossible. Both Qiang and Xuefei share my

attitude that it is impossible to succeed in science if you are not ready to sacrifice a part of yourself.

The USA offered me a shelter in the middle of the ongoing financial crisis in Europe. I would like to thank the American Physical Society, the Department of Energy and the School of Arts and Science of Duke University for providing me the means to pursue my PhD. I would like to assure the US taxpayers that their money was indeed used for discovering things that may be proven to be useful for the future of their nation.

An important part–not directly related with physics–but still important for me are the numerous friends that I was able to make in Durham. I would like to thank my roommates and friends H. Ashab, B. Cerio, C. LaGuardia M. Therezien, T. Wongjirad and his wife Anne for tolerating my impossible schedules, the habit to discuss about politics and physics even in the middle of the night and my tyrannic attitude to dominate the discussion and turn it always to things that are of my interest. Especially, I would like to thank W.R. Zimmerman, his wife Melanie and her friends from school for being close to me in very difficult moments. The late night gatherings in their apartment were perhaps the best times I had in the USA. Particularly, I would like to thank W.R. Zimmerman for taking the time to correct this thesis. I. Keramidas is the most long lasting loyal friend that I ever had located currently in Austin, Texas studying–what else–physics. Although, he is always far away, he has been a part of my everyday life. I would like also to thank the members of the Graduate Student Association of the Physics department and the Greek Scholars and Students Association for giving me the opportunity to serve both associations from various positions.

Except for the good moments, there were also some very unfortunate events during my presence at Duke. A. Kafkarkou loss was a great moment of sorrow for me. Adamos not only was a promising physicist and collaborator but he was also a

close friend. His loss a few months before the experiments in 2014 was a hit that I still can not accept and believe. If the human spirit continues after death, I am sure, we will meet again at the Elysian fields.

The loss of my father in 2012 was probably the worst moment of my life. He was the first teacher I ever had and one of the few that convinced me that his only motive for studying his subject–the history of East Roman empire–was to find the truth. He was a scientist that was working diligently day and night towards the completion of his works. The values that he taught me, loving Greece, respecting the Orthodox church and fighting for freedom and human decency will be always a chart for me in life.

I would like to thank my family and in particular my mother, brother and my fiancee. My mother is the first friend and supporter, I had. Without her sacrifices, I would not be able to study and reach here. My brother, who is currently pursuing his PhD in history, is the person I feel most proud of and I am sure that he feels the same for me. My fiancee, Aurelia Floratou, a vociferous woman with an adamant character is the person, I chose to live my life with. While we have spent 7 years apart with her being in Madison, Wisconsin and me in Durham, I would say that now I love her more than ever before.

Finally, every scientific criticism is welcomed. On the contrary, for any malicious criticism now as aforetime the Arabic proverb is mine: *the dogs bark but the caravan moves on!*

1

Introduction

Understanding the nature of strong interaction which is the mechanism responsible for nuclear force is one of the main objectives of nuclear physics. Since the discovery of the basic elements of visible matter, namely, the proton (Ernest Rutherford, 1920) and the neutron (James Chadwick, 1932), nuclear physicists have been trying to understand the force that holds together the nucleons. An important milestone of this quest was placed by the Japanese physicist Hideki Yukawa (Nobel Laureate 1949) who proposed the idea that the nuclear force is mediated by the exchange of a particle named meson from the Greek word for "middle", since this particle was predicted to have a mass between the light electron and the heavy proton and neutron. A few years after the discovery of the lightest meson, today known as the pion (1947 and 1950), two other physicists Murray Gell-Mann (Nobel Laureate 1969) and George Zweig proposed the existence of more elementary particles today known as quarks that are the constituents of all other particles, i.e., baryons and mesons. Their theory soon became the mainstream theory of particle physics and today contributes to the basis of the so-called Standard Model. A holistic fundamental theory that describes the strong interaction in terms of quarks and gluons, was developed as part of the

Standard Model at the last third of the 20^{th} century. This theory known as quantum chromodynamics (QCD) is today an object of rigorous theoretical development and experimental testing.

1.1 State-of-the-Art Three-body Calculations for ^{3}He

Few-body nucleon systems are an excellent testing ground for the study of nuclear interactions and consequently QCD. Three-body nuclei (e.g. ^{3}He and ^{3}H) are of fundamental importance since they are the simplest systems with more than two nucleons. Calculations based on phenomenological models can be applied and tested against the data from photodisintegration experiments on ^{3}He. Such state-of-the-art phenomenological calculations have been performed for the two- and three-photodisintegration of ^{3}He using the framework of Faddeev [Fad61] and the equivalent Alt, Grassberger, and Sandhas (AGS) [Alt67] equations. The main ingredients of these sets of equations can be a variety of nucleon-nucleon (NN) potentials and three-nucleon forces (3NFs).

Currently only two groups of theorists can perform calculations with meaningful uncertainties for the photodisintegration of ^{3}He using the aforementioned frameworks. The first group consists of the theorists A. Deltuva, A.C. Fonseca and P.U. Sauer while the second group is J. Golak, R. Skibiński and H. Witała. The calculations by Deltuva *et al.* [Del04, Del05b, Del05a, Del09] are based on the AGS equations and employ the coupled-channel extension of the charge dependent Bonn (CD Bonn) nucleon-nucleon (NN) potential [Sto94, Wir95, Mac96] including explicit excitation of a nucleon into a Δ-isobar, called CD Bonn + Δ-isobar [Del03]. In the three-nucleon (3N) system the Δ-isobar excitation yields effective 3NF and effective two-nucleon and three-nucleon currents that are mutually consistent [Del04, Del05b, Del05a, Del09]. In addition to single-baryon and meson exchange electromagnetic currents, the relativistic single-nucleon charge corrections

(RC) are taken into account [Del04, Del05b, Del05a, Del09]. The proton-proton Coulomb interaction is also included using the method of screening and renormalization [Del08]. The calculations by Skibiński *et al.* solve the Faddeev equations by using the Argonne V18 (AV18) NN potential [Gol05] and the Urbana IX (UIX) 3NF [Car83] taking into account the single-nucleon currents and the two most important meson exchange currents (MEC), namely the seagull and pion-in-flight terms [RS03, RS05]. Both sets of calculations were available to us at the time of the data analysis and all the data presented in this thesis are compared with these calculations.

In addition to the aformentioned calculations, Rozpędzik *et al.* [Roz11] carried out calculations of the photodisintegration of ^{3}He using chiral effective field theory [Wei92] (χEFT) in the Faddeev framework including the well-known one-pion exchange contributions and the long-range two-pion exchange parts of meson exchange currents at next-to-leading-order derived with the method of unitary transformation [K$\ddot{0}$9]. Their results are compared with the calculations obtained with the AV18 NN potential and the related exchange currents and good agreement is found between the two theories [Roz11]. However, the uncertainties of χEFT are much larger compared to the uncertainties of the calculations based on AV18 and neither approach includes the Coulomb force between the two-protons in 3N scattering states of ^{3}He. These uncertainties vote for inclusion of nuclear forces and currents in higher orders of chiral expansion to describe the ^{3}He photodisintegration. Unfortunately, such calculations are not available, thus in this thesis we compare the results of this work only with the calculations obtained based on the computational approaches of Deltuva *et al.* and Skibiński *et al.*

Polarized ^{3}He is also particularly important as an effective polarized neutron target because in its ground-state the two protons are predominantly in an S state in which their spins cancel and the effective nuclear spin is carried by the unpaired

neutron. Recent experimental advances such as the availability of polarized beams and hyper-polarized ^{3}He targets have allowed for the extraction of spin-dependent neutron structure properties such as the electromagnetic form factors [Gao94, Xu00, Mey94, Bec99, Roh99, Ber03, Rio10] and the spin structure functions [Ant96, Abe97, Ack97, Ama02, Qia11]. Hyper-polarized ^{3}He targets have also been used for the search for a new spin-dependent force between polarized neutrons and unpolarized nucleons [Chu13]. An important uncertainty in extracting the neutron information from ^{3}He is due to the nuclear corrections which can only be improved by testing theoretical calculations of three-body systems by experiments such as the polarized photodisintegration of ^{3}He.

1.2 Review of Photodisintegration Measurements on ^{3}He below pion production threshold

In this section, I will review all the two- and three-body photodisintegration experiments on ^{3}He that took place at photon energies below pion production threshold. The two-body photodisintegration experiments are divided into two main groups: the capture experiments where a proton is captured by a deuteron or vice versa and the resulting photon or ^{3}He nuclei is detected (d(p,γ)^{3}He,d(p,^{3}He)γ or p(d,γ)^{3}He, p(d,^{3}He)γ) and the actual photodisintegration experiments where an incident photon or electron (via a virtual photon) breaks the ^{3}He nuclei and the resulting proton is detected (^{3}He(γ,p)d).

The first result on the d(p,γ)^{3}He reaction was published more than half a century ago by Griffiths *et al.* [Gri62] at very low proton energies equivalent to a photon energy from 5 to 7 MeV. After this pioneering experiment, five more capture experiments using proton or deuteron beams took place during 60's and 70's detecting the produced γ or ^{3}He nuclei at the equivalent photon energies of 7 to 17 MeV [Wöl66] and 9 to 11 MeV [Sko79] for the reaction d(p,γ)^{3}He, at 13 and 15 MeV for the re-

action p(d,γ)^{3}He [Bel70], at 19.2 MeV and 20.6 MeV for p(d,^{3}He)γ [vdW71], and at 16.1 MeV for d(p,^{3}He)γ [Mat74].

Meanwhile, photodisintegration experiments for the reaction ^{3}He(γ,p)d were happened at various laboratories all over the world. The photodisintegration experiments can be divided into two main groups: those performed using a nearly mono-energetic γ-ray beam and those using bremsstrahlung photon beams. Various experiments belonging to the former group were performed at incident photon energies of 6.14 MeV, 6.97 MeV and 7.08 MeV [War63], 11-65 MeV [Tic73], 10.2 MeV and 16.0 MeV [Nai06] and more recently at HIγS at energies between 7 and 16 MeV [Tor11]. The latter group includes experiments that took data from two-body breakup threshold up to pion production threshold [Fet65] and from 13-45 MeV [Kun71].

In all aforementioned experiments quantities such as angular distributions, differential and total cross sections were extracted. The existing data for the total cross section of the two-body photodisintegration and its inverse equivalent proton-deuteron capture reactions are plotted in Fig. 1.1 and are compared with the state-of-the-art three-body calculations of Deltuva *et al.* and Skibiński *et al.*. The two calculations by Skibiński *et al.* include MEC explicitly and implicitly via the Siegert theorem [Sie37]. Obviously a discrepancy can be observed between the data acquired for energies above $\sim$8 MeV while theories favor the group of data indicating smaller cross sections. A reliable systematic study of this reaction is needed in order to resolve the observed discrepancy. Such a measurement was carried out at HIγS facility at 29 MeV and it is presented in this thesis.

Several measurements of the three-body photodisintegration of ^{3}He were performed below pion-production threshold by either measuring the neutron (^{3}He(γ,n)pp) or the produced protons (^{3}He(γ,pp)n) in coincidence. Prior to 1970, all measurements [Gor64, Gor74, Fet65, Fet65] were acquired by the use of bremsstrahlung photon beam which increased the difficulty of extracting precise information from

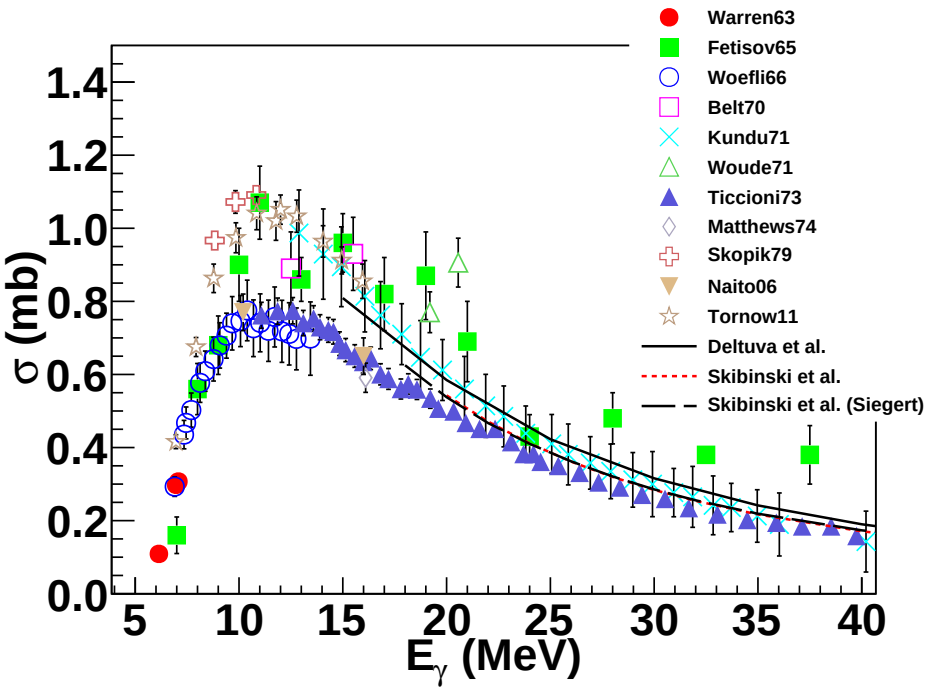

FIGURE 1.1: (Color online) All currently available total cross section data for the $^3He(\gamma, p)d$ reaction up to 40 MeV: Ref. [War63] (solid circles), Ref. [Fet65] (solid squares), Ref. [Wöl66] (open circles), Ref. [Bel70] (open squares), Ref. [Kun71] (crosses), Ref. [vdW71] (open upward triangles), Ref. [Tic73] (filled upward triangles), Ref. [Mat74] (open diamonds), Ref. [Sko79] (open crosses), Ref. [Nai06] (filled downward triangles), Ref. [Tor11] (open stars) in comparison to the calculations by Deltuva *et al.* (solid curve) and Skibiński *et al.* without (short-dashed curve) and with (long-dashed) explicit MEC included via Siegert theorem. We used filled markers for capture data, open markers for photodisintegration data and crosses for the data acquired with electron beam. The two calculations provided by Skibiński *et al.* almost coincide so different colors and line styles are used to distinguish them.

the data. After 1970, two measurements took place at LLNL using mono-energetic photon beam at incident photon energies from three-body breakup threshold (∼7.8 MeV) up to 30 MeV [Fau81, Ber74]. Two additional data points were taken by Naito *et al.* using a mono-energetic beam at 10.2 MeV and 16.0 MeV [Nai06] and by Zong *et al.* [Zon10] at the HIγS facility at 11.4 MeV. The first precise data that actually revealed the details of the neutron spectra at various scattering angles were also carried out at HIγS facility by Perdue *et al.* [Per11, Per10] at the incident photon

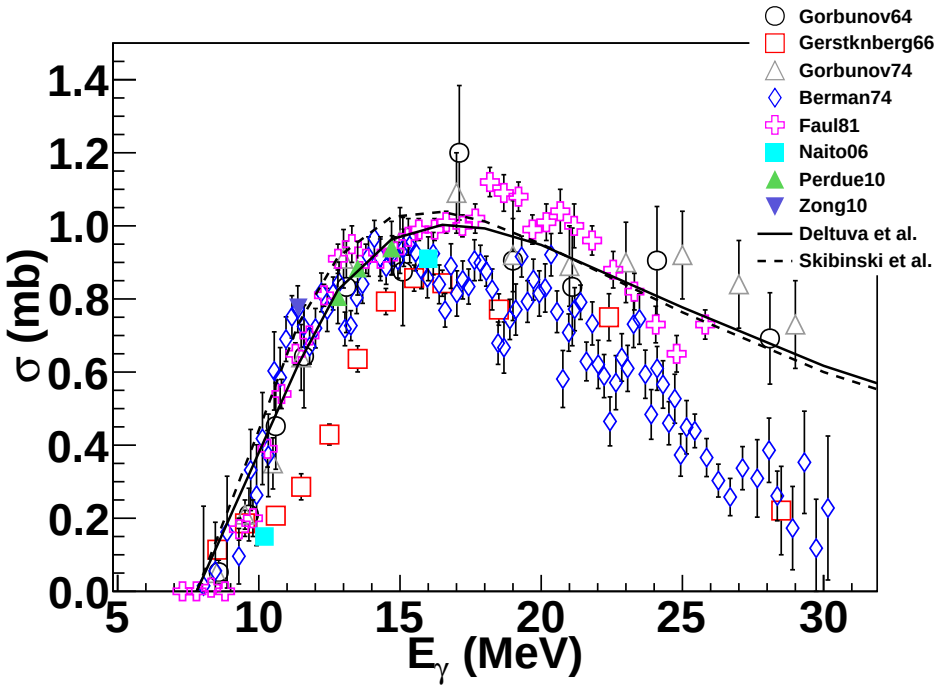

FIGURE 1.2: (Color online) All currently available total cross section data for the $^3He(\gamma, n)pp$ reaction up to 30 MeV: Refs. [Las13, Las14] (filled circles), Ref. [Gor64] (open circles), Ref. [Ger66b] (open squares), Ref. [Gor74] (open upward triangles), Ref. [Ber74] (diamonds), Ref. [Fau81] (open crosses), Ref. [Nai06] (filled squares), Ref. [Per10] (filled upward triangles), Ref. [Zon10] (filled donward triangle) in comparison to the calculations by Deltuva *et al.* (solid curve) and Skibiński *et al.* (dashed-curve). We used filled and open markers for the recent and old data, respectively.

energies of 12.8, 13.5 and 14.7 MeV.

Figure 1.2 shows all the total cross sections from the thee-body photodisintegration of ^{3}He up to 30 MeV prior to this work compared with the three-body calculations of Deltuva *et al.* and Skibiński *et al.* Although, a general agreement between the two models and most of the experimental data can be seen in Fig. 1.2 for incident photon energies below 15 MeV, a serious discrepancy can be observed above 15 MeV between the data of Refs. [Ger66b, Ber74, Nai06] and the theoretical predictions. This discrepancy leads to the need of more precise data at the energy region above 15 MeV using preferably monochromatic photon energy beams as the

one used at the HIγS facility.

The data taken and presented in this thesis [Las13, Las14] have better precision than any measurement before while they are the first measurements that used a mono-energetic circularly polarized photon beam and a polarized ^{3}He target. This allowed us to extract spin-dependent differential cross sections, and the Gerasimov-Drell-Hearn Sum Rule [Ger66a, Dre66] integrand of ^{3}He at the incident photon energies measured.

1.3 Investigation of the Gerasimov-Drell-Hearn Sum Rule

The experiment measuring the two- and three-body photodisintegration of ^{3}He is of further importance for the investigation of the Gerasimov-Drell-Hearn (GDH) sum rule [Ger66a, Dre66]. The GDH sum rule relates the energy-weighted difference of the spin-dependent total photoabsorption cross sections σ^P (for target spin and beam helicity parallel) and σ^A (for target spin and beam helicity anti-parallel) to the anomalous magnetic moment of the target (nuclei or nucleons) as follows:

$$I^{GDH} = \int_{\nu_{thr}}^{\infty} (\sigma^P - \sigma^A) \frac{d\nu}{\nu} = \frac{4\pi^2 e^2}{M^2} \kappa^2 I, \tag{1.1}$$

where ν is the photon energy, ν_{thr} is the pion production (two-body breakup) threshold on the nucleon (nucleus), κ is the anomalous magnetic moment, M is the mass and I is the spin of the nucleon or the nucleus. There have been significant efforts to test the GDH sum rule on the proton, neutron and deuteron.

For the case of proton, an experimental program started jointly by the GDH and A2 collaborations at the Mainz Microtron (MAMI) accelerator ($140 \leq \mathrm{E}_\gamma \leq 800$ MeV) in Mainz and ELSA in Bonn (600 MeV $\leq \mathrm{E}_\gamma \leq 3$ GeV). The first two experiments [Ahr00, Ahr01] took place at Mainz in the energy ranges of 200 to 450 MeV and 200 to 800 MeV, respectively, using a circularly polarized bremsstrahlung

photon beam and a butanol target that was ∼90% polarized. All final products of the reactions $\gamma p \rightarrow N\pi$ and $\gamma p \rightarrow N\pi\pi$ were detected by the multiwire proportional chamber DAPHNE [Aud91]. The measured value of the GDH integral between 200 and 800 MeV amounts to 226 ± 5(stat) ± 12(syst) μb (from 200 to 450 MeV was found to be 176 ± 8(stat) ±11(stat) μb). Two more experiments [Dut03, Dut04] took place in Bonn in the energy ranges from 700 to 1800 MeV and 1600 to 2900 MeV using the same frozen spin target polarized up to ∼80%. The reaction products were detected by a system of detectors including GDH detector [Hel02] and the silicon strip detector STAR [Sau96]. The GDH integral of proton in the energy range 800 to 2900 MeV was found to be 27.5 ± 2(stat) ± 1.2(syst) μb (with the measured values from 0.8 GeV to 1.82 GeV to be 29.1 ± 1.9 ± 1.3 μb and from 2.1 GeV to 2.9 GeV, -1.8 ± 0.6(stat) ± 0.1(syst)). Consequently, the combined results of all measurements is 254 ± 5(stat) ± 12(syst) μb which clearly overshoots the sum rule prediction for the proton of 205 μb. But if one includes the contribution from pion production threshold to 200 MeV which is -27.5 ± 3 μb based on Mainz Unitary Isobar Model (MAID2002) [Tia02] or -28 μb based on model SAID [Arn02] and the contribution above 2.9 GeV which vary from -13 μb [Sim02] to -14 μb [Bia99] then the estimate of the full integral becomes ∼212-214 μb which is clearly consistent within the statistical and systematic uncertainties with the sum rule prediction.

For the case of neutron, another experimental program started by the GDH collaboration at ELSA accelerator in Bonn. An experiment [Dut05] took place in the energy range of 815 to 1825 MeV using a deuterated butanol target and the GDH detector. The experimental contribution to the GDH integral in this energy range was found to be 33.9 ± 5.5(stat) ± 14.5(syst) μb. To allow for an estimation of the GDH integral on the neutron, the theoretical predictions for the missing parts below 815 MeV and above 1825 MeV have to be taken into account: below 815 MeV model MAID [MAI03, Chi02] gives an estimate for the single π and η-meson contributions

of 125 and -2.5 μb, respectively. The double π contribution on the neutron up to 815 MeV is equal to 40 μb based on the proton model of Ref. [Hol01]. Above 1.825 GeV the Regge approach from Ref. [Bia99] results in 30 μb. The total sum of all experimental and theoretical contributions is equal to 226 μb and in agreement within the uncertainties with the GDH sum rule value for neutron of 233 μb.

The same collaboration proceeded to the investigation of GDH sum rule on deuteron by performing two experiments in the energy region of 200 to 800 MeV using again a deuterated butanol target and the DAPHNE detector. In the first experiment, the polarization of target reached $\sim$35% and the integral value was found to be 407 $\pm$ 20(stat) $\pm$ 24(syst) μb. This measurement combined with results of [Dut03] for the proton and the neutron [Dut05] up to 1.8 GeV gives an integral value of 440 $\pm$ 20(stat) $\pm$24(syst) μb. The same measurement was repeated 3 years later using a deuterated butanol target $\sim$70% polarized and the integral value in the same energy region was found to be 388 $\pm$ 7(stat) $\pm$ 21(syst) μb while the value up to 1.8 GeV was 452 $\pm$ 9(stat) $\pm$ 24 (syst) μb [Ahr09]. Based on the last result, the known value for the GDH integral of proton in the energy region of 0.2 GeV to 1.82 GeV (255 $\pm$ 5(stat) $\pm$12(syst) μb) and assuming that the incoherent processes dominate in this energy region, one found the GDH integral value for neutron to be equal to 197 μb [Ahr09]. This prediction has to be compared to the GDH sun rule prediction for the neutron (233 μb). This is not a fair comparison since the contributions (i) below 200 MeV and above 1800 MeV and (ii) from coherent reactions (γd$\rightarrow\pi^0$d) are missing from this picture. Despite these complications, one can say that the GDH integral value of neutron should be of the same order of magnitude as the one for the proton.

An additional helicity dependent measurement was performed on the ^{3}He nuclei [Bar13] at MAMI (Mainz). This was the second measurement publishing resuts on ^{3}He nuclei after the first measurements presented in this thesis [Las13, Las14].

The experiment at MAMI took place in the photon energy range between 200 and 500 MeV using a detector system including: (i) the large acceptance highly segmented photon and hadron calorimeter, Crystal Ball [Sta01]; (ii) a particle identification detector [D.W05]; (iii) multiwire proportional chambers [Aud91]; and (iv) a theshold Cherenkov detector. The helicity dependent total inclusive photoabsoption cross sections together with the helicity dependent measurements for the reaction γ^3He$\rightarrow$ppn and the semi-inclusive γ^3He$\rightarrow\pi^0$X and γ^3He$\rightarrow\pi^{\pm}$X reactions were measured and the value of the GDH integral of the ^{3}He was found to be 135 $\pm$ 20(stat) $\pm$ 12(sys) μb.

While several helicity-spin dependent measurements took place in Germany above pion production threshold on various nucleons and nuclei, measurements below pion production threshold were performed at HIγS/FEL facility of TUNL, USA. M.W. Ahmed *et al.* [Ahm08] measured the GDH integral value of deuteron from the photodisintegration threshold up to 6 MeV as -603 $\pm$ 43 μb using a heavy water target. This value was found to be in good agreement with the theoretical value of -627 μb for the GDH sum rule integrated over the same energy range [Ahm08].

For the case of ^{3}He, the important energy range is from the two-body breakup threshold ($\sim$5.5 MeV) up to $\sim$40 MeV. According to the theoretical calculations by Deltuva *et al.* and Skibiński *et al.* this energy region dominates the integrand of ^{3}He below pion production threshold [Gao09]. The calculations also show that the contribution from the three-body photodisintegration channel to the GDH integral is larger than that from the two-body breakup. Therefore, the measurements of the spin-dependent cross sections of $^3\vec{H}e(\vec{\gamma},p)d$ and $^3\vec{H}e(\vec{\gamma},n)pp$ not only test the dynamics underlying the modern three-body calculations, but also are an important step towards the investigation of the GDH sum rule when one combines the measurements above pion production threshold from other laboratories [Bar13] with our reported measurements below it [Las13, Las14].

2

Physics Motivation

2.1 Introduction

The results from the spin-dependent two- and three-body photodisintegration experiments of ^{3}He are compared with the state-of-the-art three-body calculations. As discussed in Chapter 1 these calculations are performed mainly through the machinery of three-body Faddeev [Fad61] and AGS [Alt67] equations using a variety of (i) NN potentials like the CD-Bonn [Sto94, Wir95, Mac96] or the AV18 [Gol05] and (ii) 3NFs like UIX [Car83] or CD Bonn + Δ [Del03] with the latter yielding an effective 3NF through the Δ-isobar excitation. Additional theoretical ingredients such as the single-nucleon RC [Del04, Del05b, Del05a, Del09], the Coulomb interaction between the two protons of ^{3}He in the final state [Del08], the single-nucleon currents and the two most important MEC namely the seagull and pion-in-flight terms [RS03, RS05] are also included. The aspects of the theoretical models and the frameworks used to perform calculations for the two- and three-body photodisintegration of ^{3}He will be presented in the following sections.

2.2 Characteristics of Nuclear Force

All NN potentials that try to describe the nature of the strong force should take into account all the empirical features of the strong interaction that are considered fundamental. The fundamental characteristics of the strong force are the following: the **finite range**, the **tensor** component and the **spin-orbit** component.

- The empirical observation that the nucleons are bound together in a nuclei is evidence of the finite range and the attractive nature of the nuclear force. The strength of the force is dynamic and can change with respect to the energy or equivalently the distance between two nucleons. Typically, the range of the strong force can be divided into three sub-ranges [Tak56]:
  - long range (r$\geq$ 2 fm)
  - intermediate range (1 fm $\leq$ r $\leq$ 2 fm)
  - short range (1 fm $\geq$ r).

  A study of the S-wave phase shift based on the NN scattering data reveals that the nature of the strong force is attractive for energies below 250 MeV (or equivalently for the intermediate range) and repulsive for energies above 250 MeV (or equivalently for the short range) [Mac89].

- **Tensor Component**: An additional component to the spherically symmetric wave function of the lightest nuclei, deuteron was observed by Kellogg *et al.* [Kel40]. This electric quadrupole component indicates that the ground state of deuteron is not a pure $l = 0$ state. This discovery was the first indication that a non-central (tensor) component is necessary for the accurate description of any nuclear wave function and its symmetries.

- **spin-orbit**: The first evidence of a strong spin-orbit component of the strong interaction was found from the study of the NN scattering data at high energies [Sta57]. The addition of a spin-orbit term to the strong force was found to be necessary for the correct calculation of the P-wave phase shift.

All theoretical NN potentials have to comply with these observations related to the nature of the strong force in order to provide an accurate description of the strong interaction between nucleons. In the next section, we will present all NN potential models used to describe the photodisintegration of ^{3}He and their main characteristics.

2.3 Potential Models for Nucleon-Nucleon Interaction

Advancement in several NN potential models have been made in recent years. These phenomenological models are based on single- and multiple-pion exchange, they are fitted with high precision to the NN scattering data up to 350 MeV and reproduce the properties of deuteron. State-of-the-art examples of these potentials are the Nijmegen [Sto94], the CD-Bonn [Mac87, Mac01] and the AV18 [Wir95, Pud97] models. Before we continue with the description of the CD-Bonn potential, a necessary introduction to the meson exchange theory will be given in the next section.

2.3.1 Single- and Multiple- Meson Exchange Theory

As we saw in Chapter 1, the strong force in low-energies is mediated by massive particles known as mesons. There are several mesons in nature with masses varying from $\sim$140 MeV to $\sim$800 MeV. Different mesons are responsible for the mediation of nuclear force between nucleons depending on the distance or energy scale in meson-exchange models. In the long range region, one-meson exchange is dominant whereas the multi-meson exchanges are important in the intermediate energy region. The meson exchange model collapses in the short range region and a different phenomenological treatment as we will see in the next sections is needed.

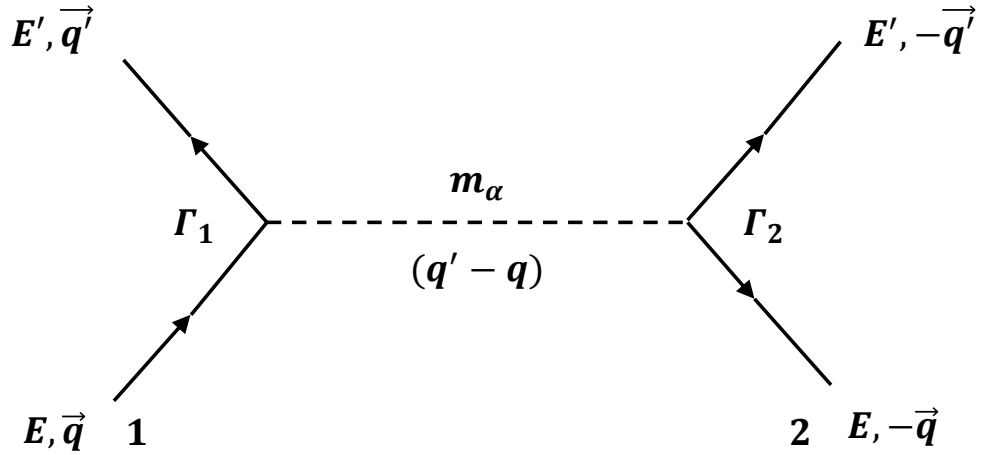

FIGURE 2.1: A NN Feynman diagram for the OBE following the notation of Ref. [Mac89]. The solid lines represent the nucleons while the dashed line represent a boson with mass m_α. The nucleon-meson vertices are labeled as Γ_1 and Γ_2.

The one-boson exchange is the lowest order contribution to the scattering between two nucleons. The bosons used to build the nuclear potential are the triplet of pions ($\pi^{\pm}$,π^0, $\sim$ 140 MeV), ρ (770 MeV), ω (782 MeV), and the σ (500-700 MeV). The σ is a boson used to mimic the multi-meson contribution to the potential.

Figure 2.1 shows the Feynman diagram of one boson exchange (OBE) with $\overline{V}_\alpha$ being the OBE Feynman amplitude. The full expressions of the $\overline{V}_\alpha$ amplitudes for each meson can be found in Ref. [Mac89]. The sum over all interactions mediated by any boson is given by Ref. [Mac01]:

$$V(q',q) = \sqrt{\frac{M}{E'}}\sqrt{\frac{M}{E}} \sum_{\alpha=\pi,\omega,\rho,\sigma} \overline{V}_\alpha(q',q) F_\alpha^2(q',q;\Lambda_\alpha) \tag{2.1}$$

where according to the notation of Ref. [Mac01], M is the nucleon mass, $E = \sqrt{M^2+q^2}$ and $E' = \sqrt{M^2+q'^2}$ and $\overline{V}_\alpha$ is the OBE amplitude for a meson with mass m_α. $F_\alpha^2(q',q;\Lambda_\alpha)$ are the form factor of the vertices between the mesons and

the nucleons given by [Mac87]

$$F_\alpha^2(q', q; \Lambda_\alpha) = (\frac{\Lambda_a^2 - m_a^2}{\Lambda_a^2 + (q' - q)^2})^{n_a}. \tag{2.2}$$

Λ_α is the mass of the heaviest meson used in the model in order to suppress exchanges in the short range region and $n_a = 1$ or 2 depending on the specific coupling. π mesons put a limit to the range of the strong force and mediate the attraction at the long range while ω is responsible for the short range repulsion. The mass of ω is used as the "cut off" mass of the form factor. The intermediate range is mediated by the meson σ. All mesons can contribute to the central portion of the nuclear potential. The tensor component is related to the exchange of π and ρ mesons while the spin-orbit term is associated with the exchange of ρ, ω, and σ.

2.3.2 The Bonn Model

The charge-dependent Bonn Model was introduced in 2001 by Machleidt [Mac01] and it is an extension of the full Bonn model developed at the University of Bonn [Mac87]. In this section we will first give an introduction to the full Bonn model describing its main features and assumptions and then we will proceed to the presentation of the charge-dependent Bonn model.

The full Bonn model is a comprehensive meson-exchange model for the NN interaction and today represents a benchmark for any other model that is used to describe the strong interaction at energies up to 350 MeV. The full Bonn model is based on the meson exchange concept described above and it is in excellent agreement with the measured properties of the relatively low energy NN scattering data and deuteron observables.

The description of the strong force provided by the full Bonn model is based solely on nucleons and isobars that are treated on equal footing. The model is considered

complete by the authors in the sense that it includes all processes which contribute to the NN interaction for the energy region below pion production threshold. Bonn model has been built by its authors gradually starting from the long-range components or equivalently from the lightest mesons and increasing gradually to heavier mesons with masses up to the cutoff mass used in the meson-nucleon vertex functions. The use of the cutoff masses is natural since it is related to the finite size of the hadrons. Finally, the nonrelativistic approximations are strictly avoided and the meson recoil effects are taken into account.

The underlying formalism of full Bonn model allows for a consistent extension of meson exchanges above pion production threshold. The same formalism allows for the consistent generalization to three-body forces and MEC contributions to the electromagnetic properties of nuclei such as deuteron and ^{3}He. Another important essential feature of the model as we will see later is the consideration of charge independence and charge-symmetry breaking of the nuclear force due to the mass differences between the charged states of mesons, nucleons and isobars.

One Meson Exchange Contribution

There are three mesons that are used for the one meson exchange contributions in the full Bonn Model: the pion which provides the long-range (tensor) force, the omega (a 3π resonance) which is responsible for the short-range repulsion and the spin-orbit interaction and the isovector a_0 or f_0-meson (4π resonance, mass $\sim$980 MeV) which are needed for a consistent description of both S-wave phase shifts and it has a very small contribution. The pseudoscalar mesons η (549 MeV), η' (958 MeV) which have a rather weak pseudoscalar coupling and the mesons with masses slightly below and above 1 GeV are not taken into account. These mesons provide rather short range exchanges which are either suppressed due to the $s\overline{s}$-content of the mesons or their contribution is masked to a considerable extent by the strong short-range repulsion

originating from ω-exchange. Although the OBE can explain important features of the two-nucleon force, it can not generate the intermediate-range attraction which is provided by 2π-exchange contributions.

Two Meson Exchange Contribution

The two meson exchange contributions contain both the contributions from nucleon resonances (isobars) as well as direct $\pi\pi$ interactions. Although other higher-mass πN resonances like the P_{11} (1470 MeV) and the F_{15} (1688 MeV) do exist, their contributions are rather small and they are not taken into account in the full Bonn Model. As expected, the one pion exchange (OPE) is dominant in almost all partial waves apart from the case of $^3F_4$, $^3H_6$ where the 2π-exchange contribution is quite appreciable. The 2π-exchange appears in general too attractive and a consistent description can never be reached for any possible choice of the cutoff parameters Λ_α. Based on the OBE calculations, the tensor forces of π and ρ have opposite signs. The inclusion of $\pi\rho$ two-boson-exchange diagrams counterbalances the corresponding 2π contributions.

3- and 4-π Exchange Contribution

Since the $\pi\rho$ contributions are found to be important, the resonant 3π-exchange (ω) and other 3π contributions are also considered. A pion can be combined with other 2π-exchange. The counter structure between π- and ρ-exchange and between 2π S-wave contributions (providing attraction) and (repulsive) ω-exchange lead to strong cancellations which remain in higher orders. However, the 3π and 4π exchange processes are added to the model in order to account for a noticeable piece of the intermediate-range tensor force and other higher-order contributions which lead to more consistent values of the cutoff masses and to an improvement in the quantitative description of the NN scattering data.

2.3.3 The Charge-Dependent Bonn Model

Although Bonn model reproduces with great precision many important features of NN scattering data, it presents some practical difficulties which for a large class of nuclear structure problems are without merit. The multi-meson exchange calculations which are one of the main features of the Bonn model are very involved and energy dependent. The energy dependence creates conceptual and practical problems when applied to nuclear many-body systems [Mac01]. An extension of the full Bonn model was developed. This extension reproduces important predictions by the Bonn Full Model while avoids the problems that the Bonn Full Model creates in applications. The charge-dependence (CD) predicted by the Bonn Full Model is reproduced accurately by the new potential. This is the reason why the new model is called CD-Bonn potential [Mac01]. In the next section we will give a brief description of charge symmetry breaking (CSB) and charge independence breaking (CIB).

Charge Dependence

By using the term charge symmetry in nuclear physics we mean the equality of the proton-proton (pp) and neutron-neutron (nn) forces after the removal of electromagnetic effects. The equality of the pp or nn with the neutron-proton (np) forces is called charge independence. It is obvious that the charge symmetry is a special case of charge independence. The breaking of the charge symmetry can be observed as the difference between the scattering length a and the effective range r for the interaction between the pp and nn nucleons. The scattering length a in a two-body scattering is defined as being equal to the intercept of the wave function at the maximum range of the scattering potential. For repulsive potentials and for potentials that support bound states the scattering length is positive while for attractive potentials it is negative. The value of the effective range parameter r expresses the range of the force. The most up to date values for a and r can be seen in Table 2.1.

Table 2.1: Summary of the latest empirical values for the singlet scattering length a and effective range r.

Nucleons	a (fm)	r (fm)
pp	-17.3±0.4 [Mil90]	2.85±0.04 [Mil90]
nn	-18.9±0.4 [How98, Tro99]	2.75±0.11 [Mil90]
np	-23.740±0.020	2.77±0.05

The charge symmetry is broken by an amount equal to the differences: $a_{pp} - a_{nn}$=1.6±0.6 fm and $r_{pp} - r_{nn}$=0.10±0.12 fm. Based on these results one concludes that the nn strong interaction is slightly more attractive than the pp strong interaction. The experimental CSB difference in the ground state is found to be explained in the Bonn meson-exchange model entirely by the mass differences of the proton and neutron.

The strength of the CIB can be identified by the difference between the averages $\overline{a} = \frac{a_{pp}+a_{nn}}{2}$=18.10 ± 0.6 fm, $\overline{r} = \frac{r_{pp}+r_{nn}}{2}$=2.80 ± 0.17 fm, and the a_{np}, r_{np} [Hou71, Koe75, Kla84, Dum83]. The values of the differences are equal to $\overline{a} - a_{np}$=5.6±0.6 fm and $\overline{r} - r_{np}$=0.03±0.13 fm, respectively. The negative value indicates that the np strong interaction is more attractive than the pp or nn strong interaction. One can calculate the CIB effect using the OBE theory. The leading order contribution of CIB is the difference between the up and down quark mass difference while the next to leading order contribution is due to the pion mass splitting between π_0 and $\pi^{\pm}$ [Mac01].

The charge dependence predicted by the Bonn full model is reproduced by the CD-Bonn model. The CD-Bonn model includes no local approximations through the use of relativistic Feynman OBE amplitudes. The CD-Bonn model uses the non-central Feynman amplitudes in each original form. The predictions made by the CD-Bonn potential differ in a characteristic way from the ones obtained with central NN potentials. The constructed CD-Bonn NN potential reproduces the world

NN scattering data below 350 MeV and the measured deuteron properties more accurately than any other known NN potential.

2.3.4 CD-Bonn + Δ-isobar Potential

Although the CD-Bonn NN potential can reproduce phase shifts of NN scattering data and properties of deuteron, it fails to reproduce properties like the binding energy of ^{3}He and ^{3}H. Due to this inaccuracies the idea of a 3NF is adopted in the CD-Bonn model. A 3NF is a force that depends on the coordinates, spins, momenta and internal quantum numbers of all three interacting particles simultaneously [Gib88]. The 3NF force can not be reduced to a sum of pairwise interactions. Since the one π exchange describes the long range part of NN interaction, by analogy the 2π exchange between three nucleons plays the role of the long range part of the 3NF.

An extension of the purely nucleonic CD-Bonn potential was developed in Ref. [Del03]. This extension is a couple-channel potential of two baryons. The coupling is mediated by a single Δ-isobar. The Δ-isobar is the lowest energy excitation of the nucleon with mass of 1232 MeV, spin and isospin $\frac{3}{2}$. The CD-Bonn + Δ-isobar model couples states comprised of two nucleons where one of the nucleons turns into a Δ-isobar. The excitation of one of the nucleons to a virtual Δ-isobar provides an additional attraction between two nucleons and results to an effective 3NF. A basic diagram presenting the 2π exchange can be seen in Figure 2.2. The cross-hatched region represents all the contributions to the 3NF.

The quality of the fitting of the CD-Bonn Δ-isobar model to the world NN scattering data below 350 MeV is the same as the one of CD-Bonn model alone [Del03]. The coupled-channel CD-Bonn + Δ-isobar potential is as good as any of the modern purely nucleonic potentials. The CD-Bonn + Δ-isobar model is used by Deltuva *et al.* [Del03, Del04] to perform calculations on the photodisintegration of ^{3}He.

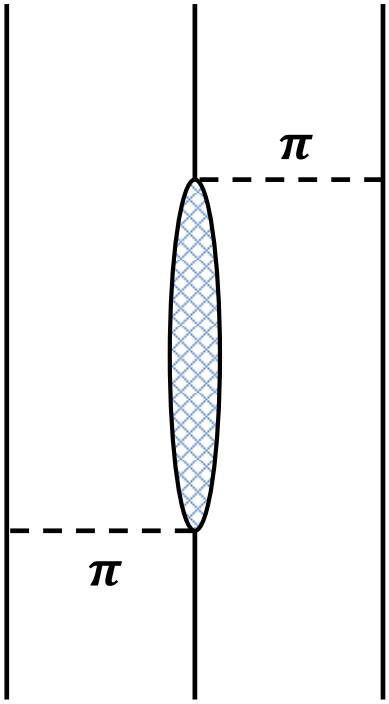

FIGURE 2.2: The 2π exchange which comprises the 3NF. The cross-hatched region represents all contributions to 3NF.

2.3.5 Argonne V18 + Urbana IX

The phenomenological model Argonne V18 [Wir95, Pud97] combined with the 3NF Urbana IX [Pud97] is employed by Skibiński *et al.* to predict the spin-dependent cross sections from the photodisintegration of polarized ^{3}He. In this section we will give a brief description of Argonne V18 NN potential and the accompanying 3NF force.

As we will see in the section, one should start with the Hamiltonian in order to determine the scattering amplitudes and consequently the cross sections of any reaction. For any given nuclei with N>3 the Hamiltonian can take the general form

$$H = \sum_{i=1}^{N} K_i + \sum_{i<j} V_{ij} + \sum_{i<j<k} V_{ijk} \tag{2.3}$$

where $H_0 = \sum_{i=1}^{N} K_i$ is the kinetic term of the Hamiltonian, V_{ij} is the potential term between two nucleons and V_{ijk} is the potential term between the three nucleons or in other words the term that gives rise to the 3NF.

In the case of ^{3}He, the kinetic operator can be written as the sum of charge-independent (CI) and charge-symmetry-breaking (CSB) components, the latter due to the difference between proton and neutron masses. The functional form of these components can be found in Refs. [Wir95, Pud97]. The NN potential AV18 can be generally expressed as a sum of electromagnetic, OPE terms and short range phenomenological terms and it can be written as [Wir95, Pud97]

$$V_{ij} = V_{ij}^{EM} + V_{ij}^{\pi} + V_{ij}^{R}. \tag{2.4}$$

The full form of the electromagnetic term, V_{ij}^{EM} is given by [Wir95, Pud97]

$$V_{ij}^{EM} = V_{C1} + V_{C2} + V_{VP} + V_{DF} + V_{MM} \tag{2.5}$$

where V_{C1}/V_{C2} are terms related to one- and two-pion exchange Coulomb interaction, V_{VP} is the vacuum polarization, V_{DF} is the Darwin-Foldy term and V_{MM} is a term related to magnetic moments that contains the tensor (noncentral) and spin-orbit components. In the case of pp interaction all terms are in principle non-zero and need to be calculated. In np scattering case, the only two terms that can survive are V_{C1} and V_{MM} while only V_{MM} survives in nn interaction case. The detailed mathematical expressions of these components can be seen in seen in Refs. [Wir95, Pud97].

The second part of the AV18 potential is the OPE term, V_{ij}^{π}. This term includes the charge-dependent (CD) terms due to the difference in neutral and charged pion masses as it was discussed in the previous section and its functional form can be seen in Refs. [Wir95, Pud97].

The remaining intermediate- and short-range phenomenological part of the po-

tential, V_{ij}^R, is expressed as a sum of central, angular momentum, tensor, spin-orbit and quadratic spin-orbit terms is

$$V_{ij}^R = V_c + V_L + V_t + V_{ls} + V_{ls2}. \tag{2.6}$$

The range of the V_{ij}^R potential is constrained with the use of Woods-Saxon function [Wir95, Pud97]. The OPE and the remaining short range phenomenological part, $V_{ij}^\pi + V_{ij}^R$, can be expressed collectively as a sum of 18 operators [Wir95, Pud97]. The first 14 of these operators are charge-independent while of the rest, three are charge-dependent and the remaining one is a charge-asymmetric operator. The model AV18 is named after the total number of eighteen operator components.

The Urbana series of three-nucleon potentials is used to express the last term V_{ijk} of the Hamiltonian. The UIX model can be written as a sum of two pion exchange and shorter range phenomenological terms

$$V_{ij}^R = V_{ijk}^{2\pi} + V_{ijk}^R. \tag{2.7}$$

The functional form of the two terms are given in Ref. [Pud97]. The terms are adjusted in conjunction with the AV18 interaction in order to reproduce the density of nuclear matter and the binding energy of ^{3}H and ^{3}He.

The construction of a Hamiltonian based on a realistic potential model is an essential but first step towards the extraction of the cross sections. A mathematical framework that will solve the kinematics of a three-body nuclei is also necessary. This framework will be described in the following section.

2.4 Theoretical Framework for Three-body Calculations

The photodisintegration of ^{3}He has been calculated in the whole phase space using consistent Faddeev-like [Fad61] equations. In this section, we will give an introduction to these calculations starting from the approach followed by Skibiński *et*

al. [RS03, San03] which does not include the Coulomb potential between the two protons in the final state and we will proceed then with the calculations of Deltuva *et al.* in which the Coulomb interaction is included using the method of screening and renormalization.

2.4.1 Calculations on ^{3}He photodisintegration using Faddeev Equations

Finding the analytical expression of the nuclear matrix elements is the first step towards the numerical calculation of the cross sections of any given reaction. The nuclear matrix elements for the two- and three-body photodisintegration of a ^{3}He bound state have the following form [RS03, San03]

$$N^{2b} = \frac{1}{2} \langle \phi_{\vec{q}} | P | \overline{U} \rangle \,, \;\; N^{3b} = \frac{1}{2} \langle \phi_0 | (tG_0 + 1) P | \overline{U} \rangle \tag{2.8}$$

where $\overline{U}$ obeys the Faddeev-type integral equation taking into account the NN potential and 3NF

$$|\overline{U}\rangle = (1+P) j_\tau(\overline{Q}) \, |\Psi_{^3He}\rangle + (tG_0 P + \frac{1}{2}(1+P) V^{3NF} G_0 (tG_0 + 1) P) \, |\overline{U}\rangle \,. \tag{2.9}$$

The $j_\tau(Q_W)$ is the electromagnetic current operator [Gol05], $|\Psi_{^3He}\rangle$ is the wave function of the bound state, $|\phi_0\rangle$ is a free 3N state, $|\phi_{\vec{q}}\rangle$ is a product of a deuteron wave function and a momentum eigenstate of the proton (with $\vec{q}$ being the asymptotic relative momentum between pd), t is the NN operator given by the Lippmann-Schwinger equation $t = V + VG_0 t$, V is the NN potential (in this case the AV18), $G_0 = \frac{1}{z - H_0}$ is the free resolvent [Glo83] and P the sum of a cyclical and anticyclical permutation of three particles [Gol05]. Finally, V^{3NF} (in this case UIX) is that part of a 3NF which is symmetrical like the NN t operator under exchange of particles 2 and 3. Faddeev equation can be solved rigorously in momentum space using a partial wave decomposition. Any NN force for the calculation of t and V^{3NF} can be used.

Based on the nuclear matrix elements, one can calculate the differential cross sections for the ^{3}He(γ,p)d and the semiexclusive differential cross sections ^{3}He(γ,n)pp. The analytical calculation and the functional form of the cross sections for the unpolarized case for both reactions can be found in Ref. [Gol05]. These calculations can become sufficiently more complicated once the helicity of the incident beam and the spin of the target are introduced. The analytical form of the polarization observables in the semiexclusive two- and three-body photodisintegration of ^{3}He can be seen in Ref. [RS05].

2.4.2 Calculations on ^{3}He using AGS Equations with Coulomb Potential

Deltuva *et al.* performed calculations for the two- and three-body photodisintegration of ^{3}He taking into account the Coulomb interaction [Del05b, Del05a, Del08]. The treatment of the Coulomb interaction is based on momentum-space integral equations together with the method of screening and renormalization. The screened Coulomb potential w_R in configuration space has the form [Del05b, Del05a, Del08]

$$w_R(r) = w(r)e^{(-r/R)^n} \tag{2.10}$$

where $w(r) = \frac{\alpha Z_1 Z_2}{r}$ is the true Coulomb potential, α=1/137 the fine structure constant, Z_i is the charge of each particle in units of the proton charge, R the screening radius and n controls the strength of the screening. Values of n between 3 and 8 provide a sufficiently smooth and rapid screening around $r = R$. The screening functions for different n values are compared in Figure 2.3.

The comparison shows that the choice $n = 4$ is much closer to Coulomb potential at short distances than the Yukawa screening. The screening radius R is chosen to be much larger than the range of the strong interaction which is on the order of the pion wavelength $\hbar/m_\pi c$=1.4 fm but still short enough so scattering theory is still applicable. A diverging phase factor is used to renormalize the screened Coulomb

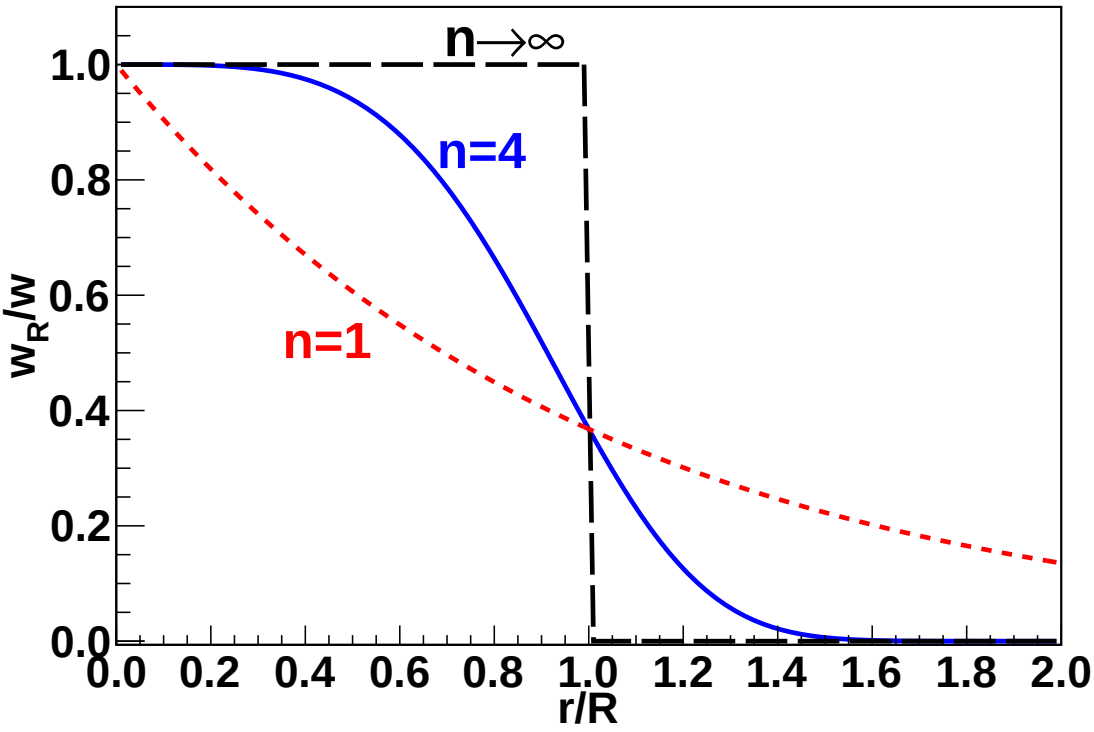

FIGURE 2.3: (Color online) The ratio of the screened ($w_R(r)$) to the real Coulomb potential ($w(r)$) as a function of the distance (r) between two charged particles for different parameters n.

amplitude in order to force it converge to the proper amplitudes for $R \to \infty$. Using this renormalization technique the screened potential converges to the pure Coulomb amplitude. More details about this technique can be found in Ref. [Del08].

The transition matrix elements in this case are given by

$$N = \langle \phi_\beta | U_{\beta\alpha} | \phi_\alpha \rangle \, . \tag{2.11}$$

where the letters α and β denote the initial and final configurations, respectively. A three-body initial and final state is denoted by $\alpha = 0$ and $\beta = 0$, respectively. The two-body states can be symbolized by α =1,2,3 and β =1,2,3 with the channel number referring to the particle which is not bound. The multichannel three-particle

transition matrix elements $U_{\beta\alpha}$ are given by the AGS [Alt67] equation:

$$U_{\beta\alpha} = \overline{\delta}_{\beta\alpha} G_0^{-1} + \sum_{\sigma} \overline{\delta}_{\beta\alpha} T_\sigma G_0 U_{\sigma\alpha} \tag{2.12}$$

where $\overline{\delta}_{\beta\alpha} = \delta_{\beta\alpha} - 1$ and T_σ is the transition matrix between two particles given as before by the Lippmann-Schwinger equation $T_\sigma = (V_\sigma + w_R) + (V_\sigma + w_R) G_0 T_\sigma$ [Del05b, Del05a, Del08]. V_σ is the nuclear potential (in this case the CD-Bonn + Δ-isobar Potential) and w_R is the Coulomb potential. One can see that Equation 2.12 is a Faddeev-like equation as the one shown above. This equation can be solved iteratively for any given potential and the differential cross sections can be calculated based on the functional form provided in Ref. [Del04].

Additionally to the study of the Coulomb force, Deltuva *et al.* also proceeded to an extensive study of the RC effects to the one-nucleon electromagnetic current operator. In particular, the relativistic spin-orbit charge effects are found to play a significant role in the calculations of the vector analyzing powers for the two-body photodisintegration of ^{3}He and–as we will see in the next section–in the difference between the spin-dependent cross sections of the three-body photodisintegration of ^{3}He. An extensive presentation of these results can be found in Ref. [Del09].

2.5 Predictions

In this section, we present the results of the calculations for the two- and three-body photodisintegration of ^{3}He performed at the incident photon energies of 29 MeV (two-body), 12.8, 14.7 and 16.5 MeV (three-body) provided by two different groups, namely Deltuva *et al.* and Skibiński *et al.* The calculations are compared and useful information concerning the contribution of each theoretical ingredient into the calculations is extracted.

2.5.1 Calculations for the Two-body Photodisintegration of ^{3}He with Double Polarizations

In the case of the spin-dependent photodisintegration of ^{3}He into proton and deuteron, the quantities that attract the theoretical and experimental interest are the spin-dependent single differential cross sections. These cross sections are calculated for both cases, namely for photon beam helicity parallel and antiparallel to the spin of the ^{3}He target and the results are presented in Figure 2.4. Deltuva's *et al.* calculations include CD Bonn + Δ-isobar taking into account the RC and the Coulomb force between the protons in the final state while Skibiński *et al.* calculations are performed using the AV18 NN potential and the UIX 3NF using the implicit MEC via the Siegert theorem [Sie37]. The solid curves show the spin-helicity parallel state while the long-dashed curves depict the spin-helicity antiparallel state.

As seen in the figure, the spin-dependent total cross sections are found to be larger in the antiparallel state compared to the parallel state and for this reason the contribution of the two-body photodisintegration of ^{3}He to the GDH sum rule at 29 MeV is expected to be negative.

2.5.2 Calculations for the Three-body Photodisintegration of ^{3}He with Double Polarizations

Extensive calculations are performed for the three-body photodisintegration of ^{3}He by both groups. Here, more attention is given to the calculations provided by Deltuva *et al.* (which include the Coulomb force) since as we will see in Chapter 6, these calculations are found to be in better agreement with the data.

Figure 2.5 shows a comparison between calculations with various combinations of ingredients for the unpolarized case at the incident photon energy of 14.7 MeV and neutron scattering angle of 90 °. The results of Refs. [RS03, RS05] (short-dashed curve) are very similar to the dotted curve which includes only the CD Bonn NN

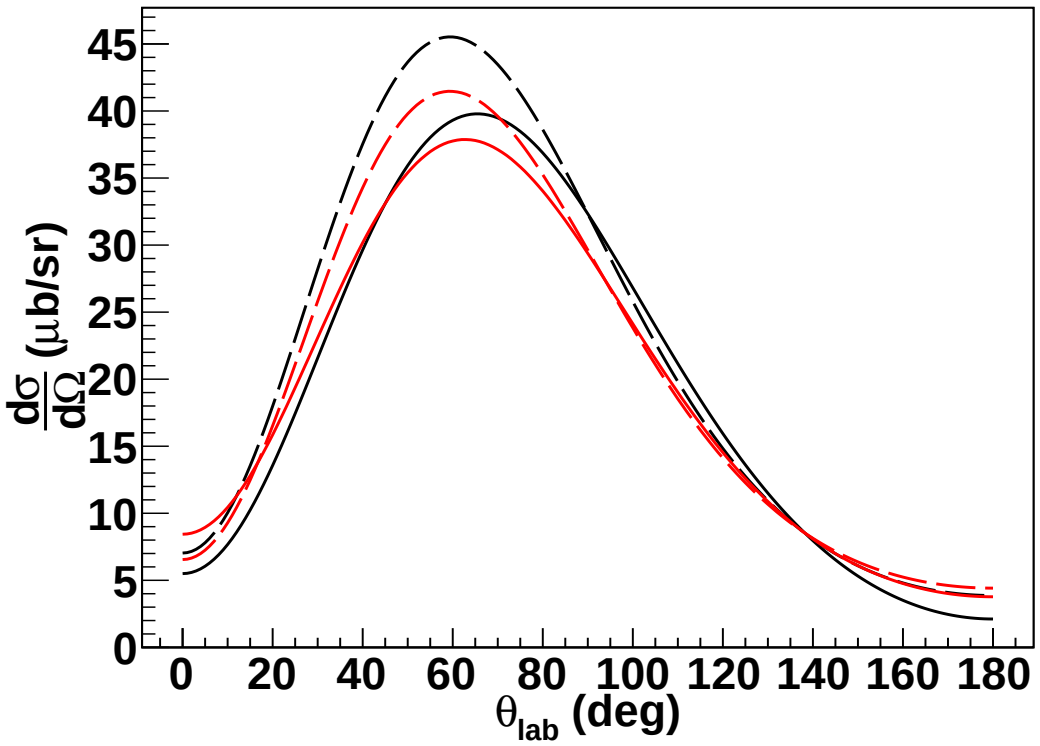

FIGURE 2.4: (Color online) The single-differential cross sections of the two-body photodisintegration of ^{3}He as a function of the proton scattering angle for both parallel (solid curves) and antiparallel (long-dashed curves) spin-helicity states at the incident photon energy of E_γ=29.0 MeV. The red curves are the calculation from Refs. [RS03, RS05] including AV18 + UIX + Siegert theorem. The black curves are from Refs. [Del04, Del05b, Del05a, Del09] including CD Bonn + Δ-isobar + RC + Coulomb force.

potential and the relativistic single-nucleon charge corrections. The magnitude of the distribution changes significantly once the Coulomb force between the protons is taken into account (long-dashed dotted curve). A shift of the high energy peak towards the lower outgoing neutron energies is also observed. The inclusion of Δ-isobar (solid curve) only slightly reduces the magnitude of the cross sections. An extensive comparison of the unpolarized double-differential cross sections at all incident photon energies and all neutron scattering angles measured at the experiment can be seen in Appendix A.

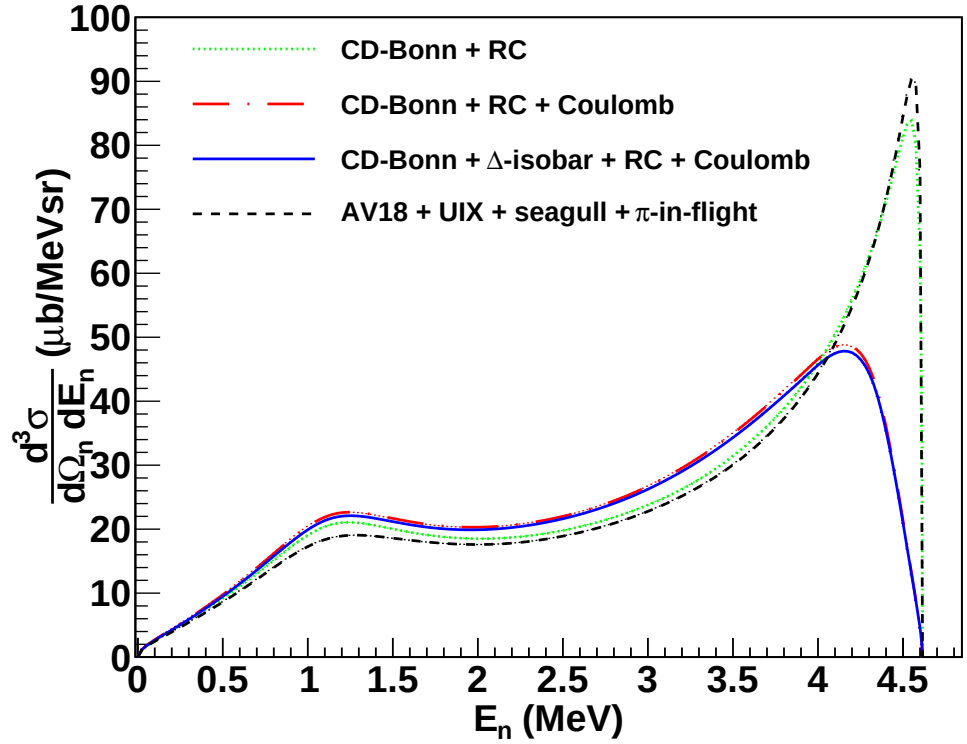

FIGURE 2.5: (Color online) The double-differential cross section as a function of the outgoing neutron energy for the unpolarized three-body photodisintegration of ^{3}He at E_γ=14.7 MeV and neutron scattering angle of 90 °. The short-dashed (black) curve is the calculation from Refs. [RS03, RS05] including AV18 + UIX + seagull + pion-in-flight-terms. The second group of calculations from Ref. [Del04, Del05b, Del05a, Del09] are (from top to bottom): dotted (green) curve: CD Bonn + RC; long-dashed dotted (red) curve (nearly invisible behind the solid curve): CD Bonn + RC + Coulomb force; solid (blue) curve: CD Bonn + Δ-isobar + RC + Coulomb force.

Although the Coulomb force plays a major role in determining the magnitude of the cross sections, it does not explain the difference observed between the spin-helicity states. This effect is due to the relativistic single-nucleon charge corrections and the inclusion of Δ-isobar as already found in Refs. [Del04, Del05b, Del05a, Del09]. Figure 2.6 shows the double-differential cross section distributions with (solid curve) and without (dashed-curve) relativistic single-nucleon charge corrections for

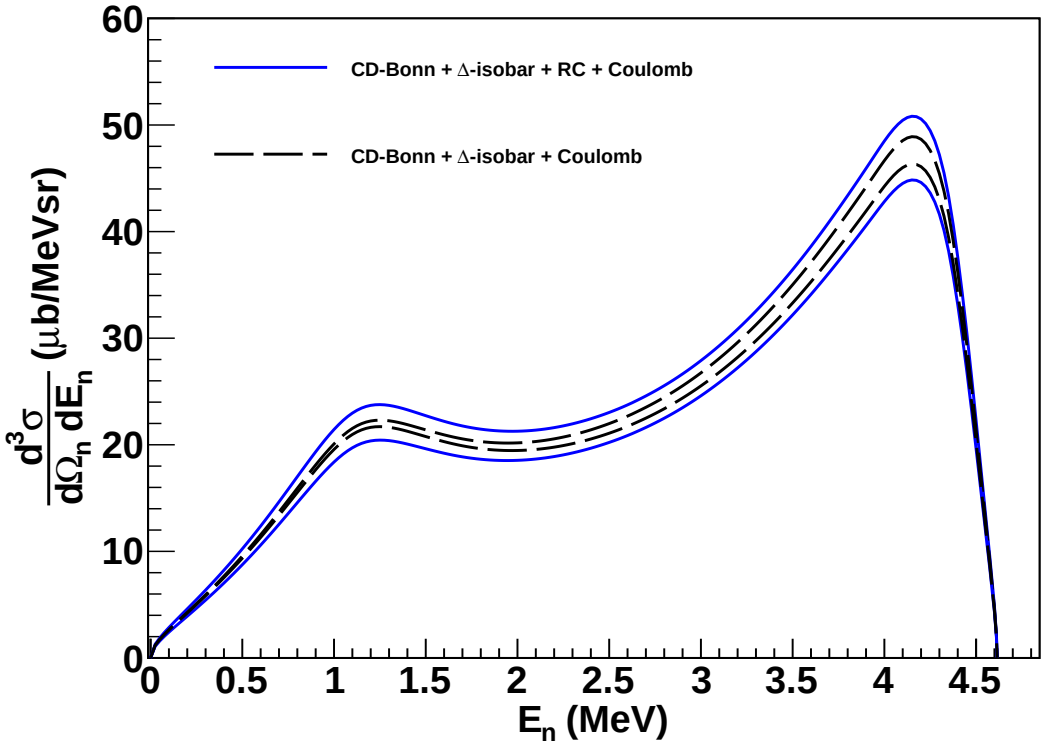

FIGURE 2.6: (Color online) The double-differential cross sections of the three-body photodisintegration of ^{3}He as a function of the outgoing neutron energy for both parallel (two top curves) and antiparallel (two bottom curves) spin-helicity states at E_γ=14.7 MeV and neutron scattering angle of 90°. The calculations from Refs. [Del04, Del05b, Del05a, Del09] are: solid (blue) curves: CD Bonn + Δ-isobar + RC + Coulomb; long-dashed (black) curves: CD Bonn + Δ-isobar + Coulomb force. The CD Bonn + Coulomb force alone do not have any significant contribution to the difference of the cross sections between the spin-helicity states and the corresponding curves—if plotted—would be in the middle of the long-dashed curves.

each spin-helicity state with all other ingredients being the same. About 2/3 of the overall difference between the spin-helicity states is from the relativistic single-nucleon charge corrections and 1/3 is from the inclusion of the Δ-isobar excitation.

In Appendix A, the spin-dependent double-differential cross section distributions with and without relativistic single-nucleon charge corrections (for 12.8 and 14.7 MeV) and with and without Δ-isobar (16.5 MeV) are presented for all experimentally

measured neutron scattering angles.

2.6 GDH Sum Rule

Sum rules involving the spin structure of the nucleon and nuclei offer an important opportunity to study QCD. Among spin sum rules, the Gerasimov-Drell-Hearn (GDH) sum rule [Ger66a, Dre66] is particularly interesting. It connects long distance behavior of the nucleon (nucleus), i.e. static property, to the entire excitation spectrum.

The GDH sum rule relates the energy-weighted difference of the spin-dependent total photo-absorption cross sections σ^P (for target spin and beam helicity parallel) and σ^A (for target spin and beam helicity anti-parallel) to the anomalous magnetic moment of the target nucleus/nucleon as follows:

$$I^{GDH} = \int_{\nu_{thr}}^{\infty} (\sigma^P - \sigma^A) \frac{d\nu}{\nu} = \frac{4\pi^2 e^2}{M^2} \kappa^2 I, \tag{2.13}$$

where ν is the photon energy, ν_{thr} is the pion production/photodisintegration threshold on the nucleon/nucleus, κ is the anomalous magnetic moment, M is the mass and I is the spin of the nucleon or the nucleus. A summary of the GDH integral values for nucleons and the lightest nuclei is given in Table 6.6 for reference.

This sum rule is based on fundamental principles such as Lorentz and Gauge invariance, crossing symmetry, causality and unitarity, and an assumption of unsubtracted dispersion relation. A detailed derivation of the GDH sum rule based on the aforementioned principles can be found in Ref. [Hel06].

2.7 Estimation of the GDH Sum Rule of ^{3}He below pion production threshold

In this section, we will estimate the GDH integral on ^{3}He below pion production threshold based on two-different approaches. The GDH sum rule for ^{3}He can be

Table 2.2: The anomalous magnetic moments in terms of nuclear magneton μ_N=e$\hbar$/M$_p$ and the GDH integral values for nucleons and light nuclei.

Nucleon/Nuclei	κ (μ_N)	I^{GDH} (μb)
Proton	1.79	205
Neutron	-1.91	233
Deuteron	-0.143	0.652
^{3}He	-8.37	496

written as the sum of two terms:

$$\int_{\nu_{thr}}^{\infty} GDH_{^3He} = \int_{\nu_{thr}}^{\nu_\pi} GDH_{^3He} + \int_{\nu_\pi}^{\infty} GDH_{^3He} \tag{2.14}$$

where the first term is from the two-body breakup threshold of ^{3}He ($\sim$ 5.5 MeV) to the pion production threshold ($\sim$ 140 MeV), which can be measured by carrying out double polarized two-body and three-body photodisintegration experiments in this energy region.

The second part in Eq. 2.14 can be written into neutron and proton integrals in the plane wave impulse approximation (PWIA) as:

$$\int_{\nu_{thr}}^{\infty} GDH_{^3He} = P_n \times \int_{\nu_{thr}}^{\infty} GDH_n + 2P_p \times \int_{\nu_{thr}}^{\infty} GDH_p \tag{2.15}$$

where P_n is the effective polarization of the neutron in ^{3}He (87%), and P_p is the effective polarization of proton in ^{3}He (-2.7%) [Fri90]. The factor of two in front of the proton term is to account for the two protons in ^{3}He nucleus. The GDH sum rule prediction for ^{3}He, proton and neutron are 496 μb, 204 μb and 233.5 μb, respectively from Eq. 2.13. A value of 191 μb is obtained for ^{3}He for the second part of the integral within PWIA, and the first part of the integral in Eq. 2.14 is therefore estimated to be 305 μb.

Although this approach is justified by the comparison between the experimental determination of the running ^{3}He GDH integral value above 250 MeV and the PWIA

prediction based on MAID [Bar13], it does not take into account the coherent reactions such as γ^3He$\rightarrow\pi^0+^3$He and γ^3He$\rightarrow\pi^{\pm}$+X which are expected to play a role in the energy range from pion threshold to 250 MeV. An indication of the size of nuclear effects in the energy range of 200 to 450 MeV is given in Ref. [Cos14] where the results of Ref. [Bar13] are compared with (i) the full Fix-Arenhövel (FA) model, which represents the first trial to include all possible photodisintegration channels for both coherent and incoherent reactions and (ii) the predictions of a simplified version of FA model based on PWIA in which the cross sections are evaluated as an incoherent sum of quasi-free single nucleon contributions. The comparison shows that the FA model describes the data better at lower energies $\sim$250 MeV although both models fail to describe the data $\sim$200 MeV where the nuclear effects and consequently the coherent reactions are dominant. This implies that a lot more experimental and theoretical work is needed in order to fully understand the photodisintegration of ^{3}He near the pion threshold.

Another way to estimate the first part of the integral in Eq. 2.14 is based on the state-of-the-art three–body calculations. Deltuva *et al.* and Skibiński *et al.* estimated the contibutions from the two- and three-body photodisintegration to the GDH integral based on the calculations described in detail in the previous section. Figure 2.7 shows the GDH integral for the two- and three-body photodisintegration of ^{3}He below pion production threshold. The short-dashed double dotted (green) and the long-dashed (black) curves are the estimations of the GDH integral for the two- and three-body photodisintegration from Deltuva *et al.* Their sum amounts to 142 μb. The short-dashed (purple) and short-dashed dotted (blue) curves are two different estimations by Skibiński *et al.* of the two-body channel contribution to the GDH integral taking into account explicitly or implicitly the MEC via the Siegert theorem. The long-dashed dotted curve is the estimation of the three-body contribution to the GDH integral coming from the same group. The maximum

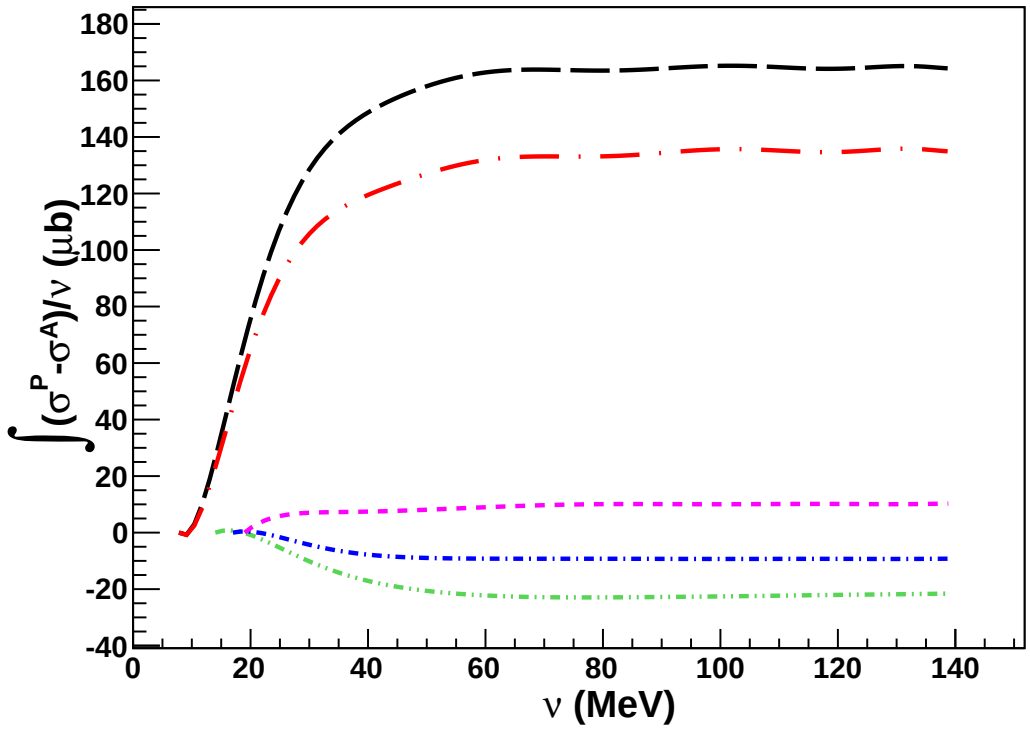

FIGURE 2.7: (Color online) Theoretical predictions of two- and three-body channel contributions to the ^{3}He GDH Integral below pion production threshold. The curves from top to bottom are: (i) long-dashed (black) curve: three-body channel contribution by Deltuva *et al.* (ii) long-dashed dotted (red) curve: three-body channel contribution by Skibiński *et al.* (iii) short-dashed (purple) curve: two-body channel contribution by Skibiński *et al.* (explicit MEC) (iv) short-dashed dotted (blue) curve: two-body channel contribution by Skibiński *et al.* (implicit MEC via Siegert theorem) (v) short-dashed double dotted (green) curve: two-body channel contribution by Deltuva *et al.*

estimation of the GDH integral below pion threshold according to Skibiński *et al.* is $\sim$145 μb. In both cases, the GDH integral value is more than a factor of $\sim$2 smaller than 305 μb based on PWIA.

In the next chapters, we will present the first measurements on the two- and three-body photodisintegration of ^{3}He below pion threshold and we will shed light into this discrepancy.

3

Experimental Apparatuses

3.1 Overview of the experiment

In this chapter, we describe the apparatuses for the first measurements of the two- and three-body photodisintegration of ^{3}He using a longitudinally polarized ^{3}He target and the circularly polarized γ-ray beam of HIγS facility produced by an Free Electron laser (FEL) at TUNL. The facility provided nearly monoenergetic, $\sim$100% circularly polarized γ-ray beam [Wel09] at the incident photon energies of 29 MeV (two-body); 12.8, 14.7 MeV and 16.5 MeV (three-body). The beam was collimated by a 12 mm collimator and was incident on a high-pressure ^{3}He cell polarized via spin exchange optical pumping (SEOP) technique [Hap72]. The protons and neutrons from the two- and three-body photodisintegration of ^{3}He were detected by an array of seventy two silicon surface barrier detectors (SSB) and sixteen liquid scintillator detectors, respectively. A simultaneous measurement of the d(γ,n)p reaction was carried out to monitor the γ-ray beam intensity.

3.2 The High Intensity γ-ray Source

After the discovery of Compton effect—the scattering of x-rays from electrons in metals [Com23]—several facilities worldwide [Mil63, Aru63, Kul64, Bem65] utilized the technique of Compton backscattering of photons by high-energy electrons to produce high energy γ-rays. While these efforts were successful, they were limited by the low photon yield. The first successful attempt to produce usable photon flux via Compton scattering was achieved by the Stanford Linear Accelerator Center (SLAC) [Bal69]. Since 1970s, several facilities were operated, including LEGS [San83], ROKK-1/ROKK-2/ROKK-1M [Kaz84, Kez93, Kez95, Kez98], Graal [Bab90], HIγS [Lit97] and LEPS [Nak98, Nak01] using the same principle. Unlike others, HIγS is the first facility that uses the electron beam in the storage ring of an FEL to produce intense beams of γ-rays inside the FEL optical cavity via Compton backscattering [Wel09]. Currently, HIγS has demonstrated the ability to produce a nearly monochromatic and highly polarized γ-ray beam in the energy range of 1–100 MeV with a maximum on-target total intensity of 3×10^9 γ/s at 15 MeV which is the highest in the world [Wel09]. In the following section, we give a description of the FEL operation.

3.2.1 Free Electron laser

A powerful electron source is necessary for the operation of any FEL. In the case of the FEL at TUNL, the electron source is a GaAs crystal which is pumped by a high power nitrogen laser [Wel09] in order to extract low energy electrons. The extracted electrons are gathered together into bunches and shot by a photo-cathode microwave electron gun into a linear accelerator (Linac) which can accelerate electrons from 0.18 to 0.28 GeV. After exiting the Linac, the electron bunches enter the Linac-to-Booster (LTB) injector and then to a booster ring. The booster ring is a very

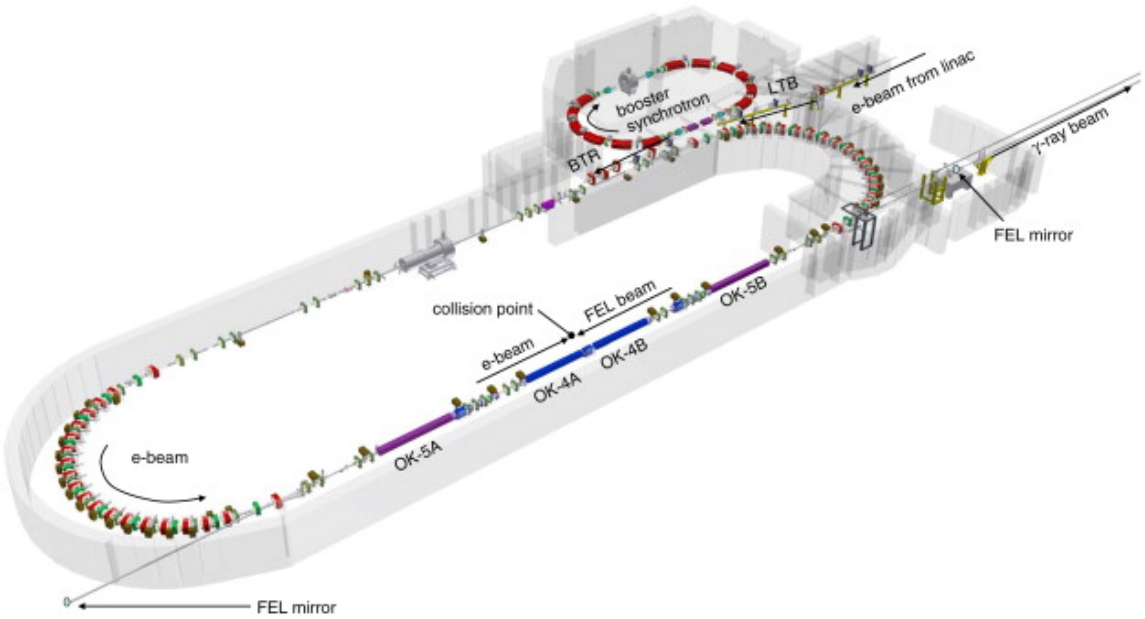

FIGURE 3.1: (Color online) Schematic of the storage ring and FEL [Wel09].

compact synchrotron with a circumference of 31.9 m that boosts electrons with an extraction energy between 0.24-1.2 GeV. An RF cavity operating at 178.55 MHz ramps up the energy of the electron bunches. The electrons, now boosted to higher energies, are injected into the FEL storage ring through the Booster to Ring (BTR) injection channel.

The total circumference of the storage ring is 107.46 m. The storage ring consists of two straight sections and two arcs. An RF cavity operating at the orbital revolution frequency of 178.55 MHz is responsible for restoring the energy of the electrons which is lost to synchrotron radiation due to the circulation of electrons into the storage ring. The lower section of the storage ring contains all the major components of the FEL namely the OK-4 [Wu96, Lit96], OK-5 [Wu06, Lit01b, Lit01a], the electron buncher and the FEL mirrors.

The OK-4 is an optical klystron (OK) consisting of two planar wiggler magnets which can produce a photon beam, linearly polarized in the horizontal plane. The

OK-5 helical wigglers which are constructed with two sets of magnet arrays, one placed horizontally and the other one vertically, are responsible for producing circularly polarized photon beams. The geometry of the magnetic field of the helical wigglers causes the electrons to travel in a helical trajectory. The acceleration caused by magnetic field forces the electrons to radiate energy in the form of photons. These photons are circularly polarized due to the cyclic motion of electrons.

After the exit of the electrons from the first OK wiggler magnet, they enter into the buncher. The electron buncher is located between the two OK-4 wigglers and it is responsible for making the electrons to cluster longitudinally. In the buncher magnet the high energy electrons travel a shorter distance than the lower energy electrons. Consequently, electrons are bunched longitudinally with spacing being the FEL wavelength. This process is called micro-bunching.

The most important part of the FEL is the set of two mirrors defining the laser cavity located at east and west side of the OK-5 wigglers. Different mirrors can be used to reflect photons at wavelengths between 190–1064 nm depending on the energy of the electrons. Every time that an electron bunch passes through the wiggler magnet photons are produced in the forward direction going towards the downstream mirror. The reflected photons from the downstream mirror travel upstream inside the cavity and are reflected back by the upstream mirror. The length of the cavity is one half the length of the circumference of the storage ring. This allows the photons to be reflected by the upstream mirror and the circulating electrons to re-enter at the same time into the wiggler magnet. The electromagnetic field of the FEL beam inside the wiggler magnet exerts a force—called the pondermotive force [Mar85]—onto the electrons. The micro-bunched electrons radiate coherently with the FEL beam inside the FEL wiggler to enhance the FEL beam intensity. This procedure is repeated many times per second (2.8 MHz) in order to enhance the laser gain. The most important components of the FEL can be seen in Figure 3.1.

3.2.2 γ-ray Production

Once the lasing is established a second bunch of electrons comes into play. The second bunch is injected into the ring one half circumference behind the first electron bunch. The trajectory of the second electron bunch is tuned so it collides head-on with the photons produced by the first bunch. The head-on collision of relativistic electrons and photons pushes the energy of the back-scattered photons into the γ-ray energy range. The energy of the γ-rays after the collision is given by (in the geometry of head-on collision):

$$E_\gamma = E_{FEL}\frac{1+\beta}{1+\frac{E_{FEL}}{E_e}-(\beta-\frac{E_{FEL}}{E_e})cos\theta}, \tag{3.1}$$

where E_{FEL} is the energy of the FEL photon, E_e is the energy of the incoming electron bunch, β is the ratio of the speed of the incoming electron to the speed of light, and θ is the scattering angle of the outgoing γ-ray. For the case where $\gamma = E_e/m_ec^2 \gg 1$ and consequently θ is small equation 3.1 becomes [Lit97]

$$E_\gamma = E_{FEL}\frac{4\gamma^2}{1+(\gamma\theta)^2+\frac{4\gamma E_{FEL}}{m_e}} \tag{3.2}$$

where clearly E_γ is at maximum when $\theta = 0$. The collimation of the γ beam is of utmost importance in order to select only the high energy γ-rays. Figure 3.2 illustrates a photon back-scattered by a high energy electron producing a γ-ray (courtesy of W.R. Zimmerman [Zim13]).

3.3 Beam Diagnostics

The quality of the beam is one of the most important preconditions in order to acquire meaningful data. In this section, we give an overview of the four most important qualities of the beam namely: the energy resolution, the polarization, the

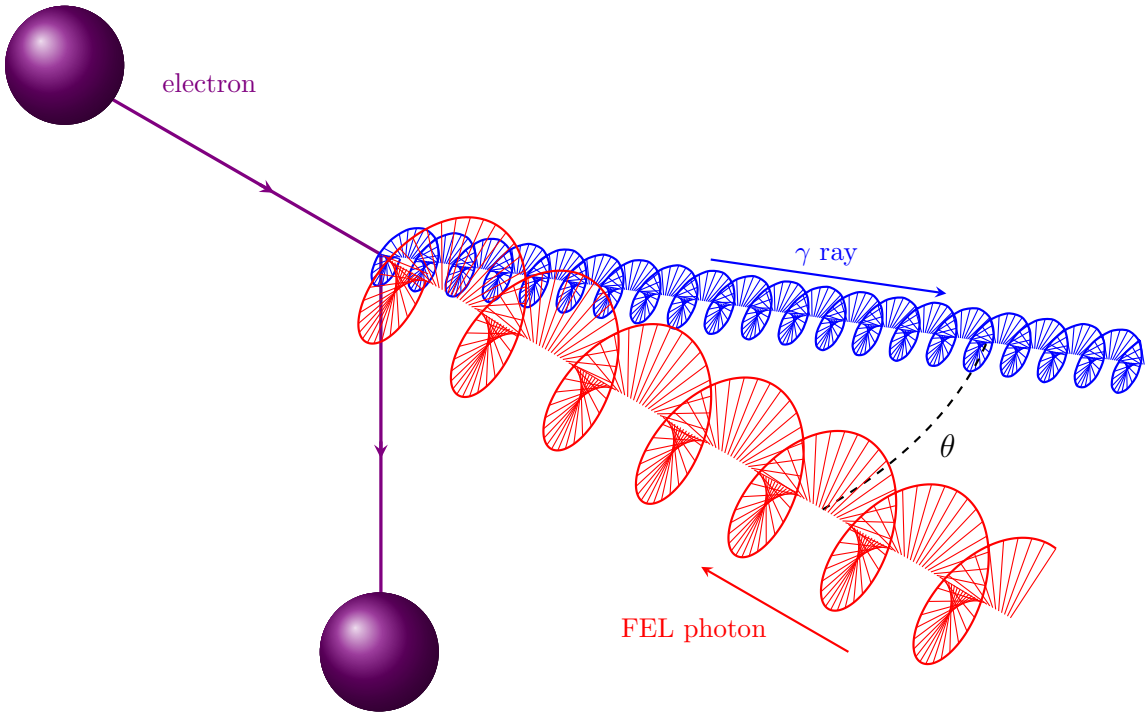

FIGURE 3.2: (Color online) An illustration of a produced γ-ray through Compton backscattering. A low energy photon (1–10 eV) collides with a high electron (0.2–1.2 GeV) resulting in a γ-ray (1–100 MeV) [Zim13]. The electron scattering angle is exaggerated in the figure for illustration purposes.

time structure and the alignment. A separate section is dedicated to the instruments that we used to measure the intensity of the beam later in this Chapter.

3.3.1 Energy Resolution

The energy spread of the beam is mainly defined by the collimator aperture. A 12 mm lead collimator was used in all measurements for both two- and three-body photodisintegration experiments. In order to measure the spread of the γ beam a NaI (Tl) detector was employed. Figure 3.3 shows the result of a γ-ray beam energy measurement at 12.8 MeV.

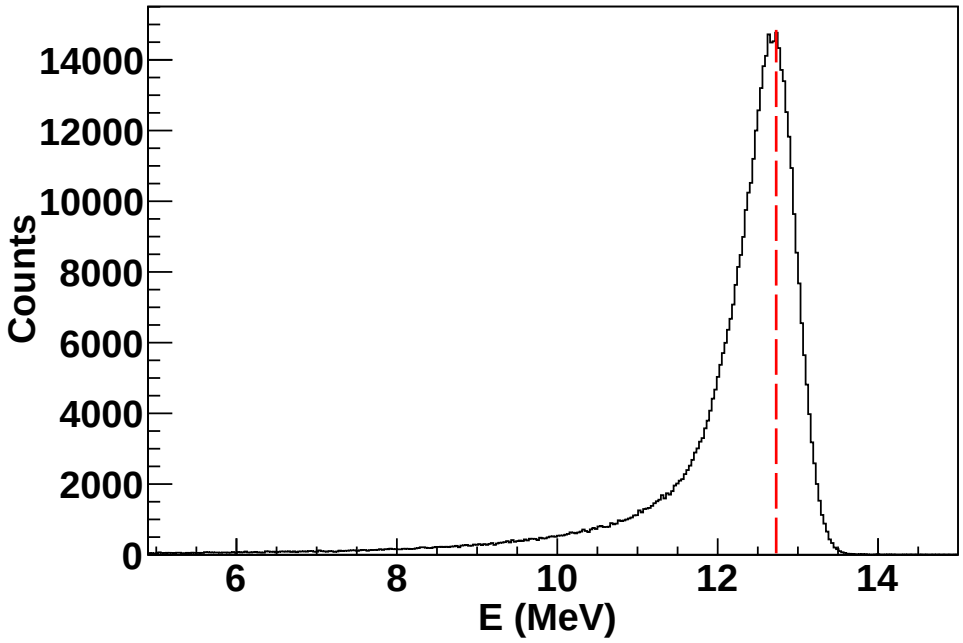

FIGURE 3.3: (Color online) The calibrated gamma spectrum measured with the NaI(Tl) detector named Molly. The dashed (red) line is located at 12.8 MeV. The energy spread of the beam is ∼2%.

3.3.2 Polarization

The HIγS facility can produce both linearly and circularly polarized γ-rays depending on whether the facility is operating using the OK-4 (linear) or OK-5 (circular) wiggler magnets, respectively. In both cases, the degree of polarization is assumed to be ∼100%. Many indirect measurements based on nuclear reactions have been tried [Rus] but no reliable method that can measure the polarization of the beam concurrently during experiment up to now. For the purpose of this analysis the beam polarization is considered to be ∼100% for both normal and reversed beam helicity states.

3.3.3 Time Structure

During normal operation, two electron bunches are circulating in the storage ring. These bunches are traveling one half the ring circumference apart and both of them produce γ-rays upon their collision with the FEL photons. The frequency of the electron bunch circulation in the storage ring is 2.79 MHz, but since two electron bunches are circulating in the ring, the collisions happen twice as frequent at the rate of 5.58 MHz. This rate defines the time between two consecutive γ-ray pulses, which is 179 ns. This time interval is particularly important for the data acquisition of any experiment performed at HIγS that depends on the timing information. It sets an upper limit to the time that it should take for a particle to travel from the point of production to the detectors in order to be associated uniquely with one γ-ray pulse.

3.3.4 Alignment

In the case of the two- and three-body photodisintegration experiments, a lead collimator of 15.24 cm long and 12 mm in diameter was chosen. Although the optical laser system in HIγS target room was sufficient to align all targets with dimensions much greater than the dimension of the beam, it did not allow us to proceed to a precise alignment of the $\sim$30 mm (diameter) ^{3}He and N_2 reference cell with respect to the γ beam. These targets were instead aligned using the FEL γ-ray beam and a BGO (bismuth germanium oxide, $Bi_4Ge_3O_{12}$) based γ-ray imaging system [Sun09] placed downstream of the targets. Two 4 mm thick cylindrical lead plugs with diameters of 2 and 4 mm, respectively, were placed co-axially at the front and back of the cylindrical target chamber of the ^{3}He and N_2 reference cell. An iterative procedure was followed until both cylindrical plugs become also co-centric with the beam. Figure 3.4 shows the shadows of the two lead plugs located at the center of the beam.

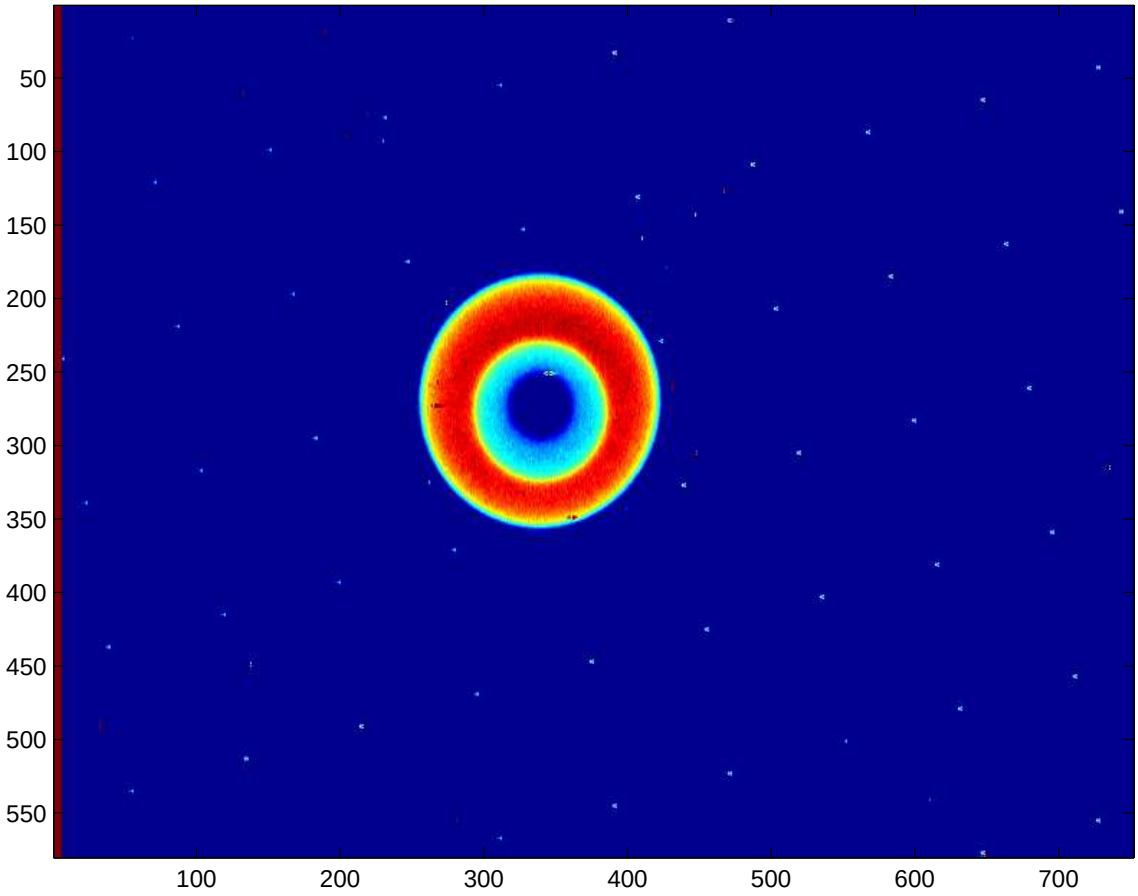

FIGURE 3.4: (Color online) Images of the BGO γ-ray imager. The shadows of two the lead plugs mounted at the center of the front and back windows of the ^{3}He cell are visible with the smaller and larger plug being on the front and back window, respectively.

3.4 Targets

Several different targets were used for the two- and three-body photodisintegration experiments. Apart from the ^{3}He and the N_2 reference cell other targets including an aluminum target and several deuterium targets were used. These targets are described in the following sections.

Table 3.1: Summary of the dimensions of deuterium targets. Error of cell dimensions is 0.01 cm

Target	Length (cm)	Diameter (cm)
D_2O (1)	4.74	4.08
D_2O (2)	5.03	3.18
C_6D_6	10.56	3.24

3.4.1 Aluminum Target

An aluminum rod, 12 mm in diameter and 5 cm long was used during data acquisition for the three-body photodisintegration experiments. This aluminum rod was placed at the center of the detector array and photons undergoing Compton scattering were collected by the detectors. These Compton events were used to define time zero for the calibration of the time of flight. More details about this technique will be given in the data analysis chapter.

3.4.2 Deuterium Targets

Several deuterium targets were used in both two- and three-body photodisintegration experiments. A deuterated benzene (C_6D_6) target was used during the two-body photodisintegration experiment at 29 MeV and the three-body experiment at 16.5 MeV to monitor the γ-ray intensity. A D_2O target was used to test the performance of the liquid scintillator detectors located at the main apparatus by reproducing the angular distribution of the d(γ,n)p reaction for all three-body photodisintegration experiments. The second heavy water target served as the γ-ray intensity monitor for the three-body experiments at 12.8 and 14.7 MeV. Table 3.1 is a summary of the dimensions of the various targets.

3.4.3 ^{3}He Target

The ^{3}He target cell was a one-piece glassware made of Pyrex glass consisting of two chambers: a spherical pumping chamber 8.1 cm in diameter, and a 39.3 cm long

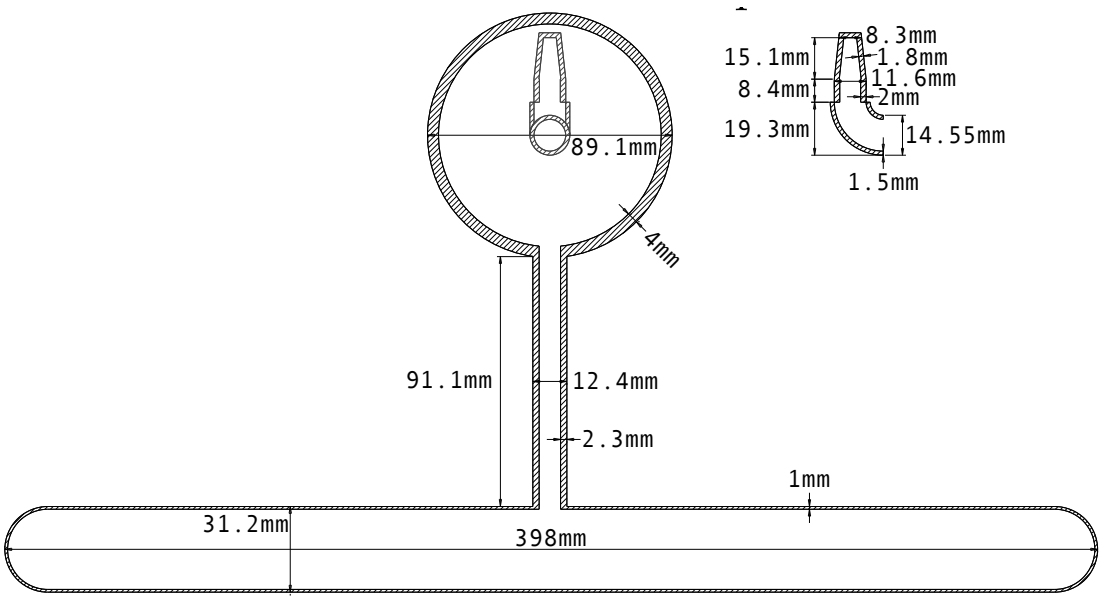

FIGURE 3.5: The dimensions of the ^{3}He Pyrex cell named SPOT measured by Professor's Averett group at the College of William and Mary.

cylindrical target chamber 2.9 cm in diameter having entrance and exit windows of 250 μm thickness. The two chambers were connected through a 9.1 cm long transfer tube which was 7.8 mm in diameter. All length measurements refer to the inner dimensions of the target cell. A schematic with the dimensions of the ^{3}He cell can be seen in Figure 3.5. The filling density of ^{3}He was 6.48$\pm$0.1 amg[1]. Two beams were incident on the cell at the time of the experiment: the HIγS beam on the target chamber and a near infrared laser beam in order to polarize ^{3}He on the pumping chamber. Chapter 4 is dedicated to the operational principles of the ^{3}He target and no more details will be given here.

3.4.4 N_2 reference cell

A reference cell almost identical to the target chamber of the ^{3}He cell and filled with only 0.110 amg ($\sim$90 torr) of N_2 gas was employed for measuring the backgrounds.

[1] An amagat is the number density of an ideal gas at 0°C and 1 atmosphere: 1 amg=2.6894$\times 10^{19}$ atoms/cm^3.

The dimensions of the N_2 reference cell can be seen in Figure 3.6. The thicknesses of front and rear windows were measured at Princeton University and found to be 250 μm. Figure 3.6 shows the dimensions of N_2 reference cell.

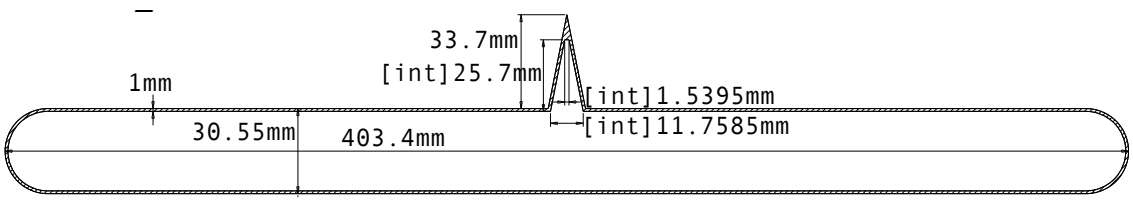

FIGURE 3.6: The dimensions of the N_2 reference cell Kielbasa measured by Professor's Averett group at the College of William and Mary.

3.5 Neutron Detectors

Eighteen liquid scintillator neutron detectors were used to perform the measurement of the three-body photodisintegration of ^{3}He. Sixteen of those detectors were used as the primary detector array to detect the neutrons from the $^3\vec{H}e(\vec{\gamma},n)pp$ reaction and two to measure the γ-ray intensity based on the reaction $d(\gamma,n)p$.

3.5.1 Physical construction

There are two main components of any liquid scintillator: the active material and the photo-multiplier tube (PMT). The active material of neutron detectors is the liquid scintillator BC-501A. BC-501A is an organic compound consisting of xylene (C_8H_{10}) and naphthalene ($C_{10}H_8$). The scintillating compound is sealed inside a cylindrical cell with dimensions that can be seen in Figure 3.7. The front side of the cell is made of aluminum while the rear side is made of glass. All surfaces of the cell are coated with the reflective paint BC-622 apart from the side made of glass. The glass surface is directly coupled to a Hamamatsu PMT R1250 with optical grease. The PMT is enclosed in μ-metal which shields it from magnetic fields. This μ-metal shield was not enough to protect the PMT from the holding field we used to keep ^{3}He polarized.

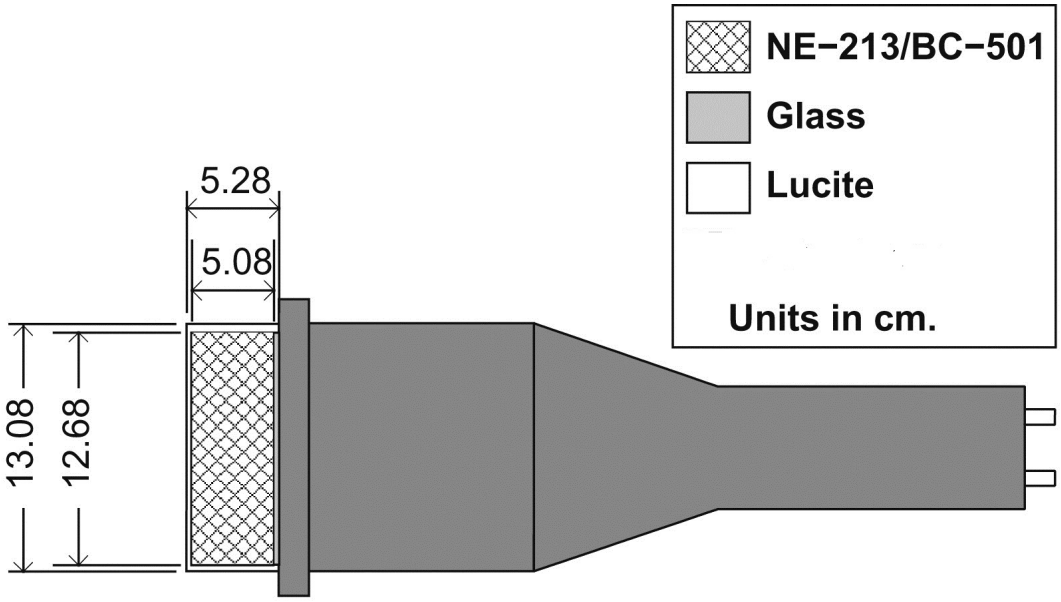

FIGURE 3.7: The BC–501A liquid scintillator neutron detector [Tro09].

For this reason, all detectors were placed inside additional μ-metal tubes. The base of the PMT has two connectors: one to supply high voltage for the operation of the PMT and the other a connection to the anode of the PMT to read the electrical signal.

3.5.2 Operational Principles

One of the oldest techniques for the detection of ionizing radiation is the production of scintillation light inside certain materials. There are three ways that ionizing radiation can produce light in a material: (i) Fluorescence is the prompt emission of visible light following its excitation by some means; (ii) Phosphorescence is the delayed emission of light with much longer wavelength; and (iii) Delayed fluorescence is the delayed emission of light with visible wavelength [Kno10]. A large portion of organic scintillators is based on molecules with a certain π-electron symmetry. The electron levels of such molecule are characterized by the co-existence of a series of

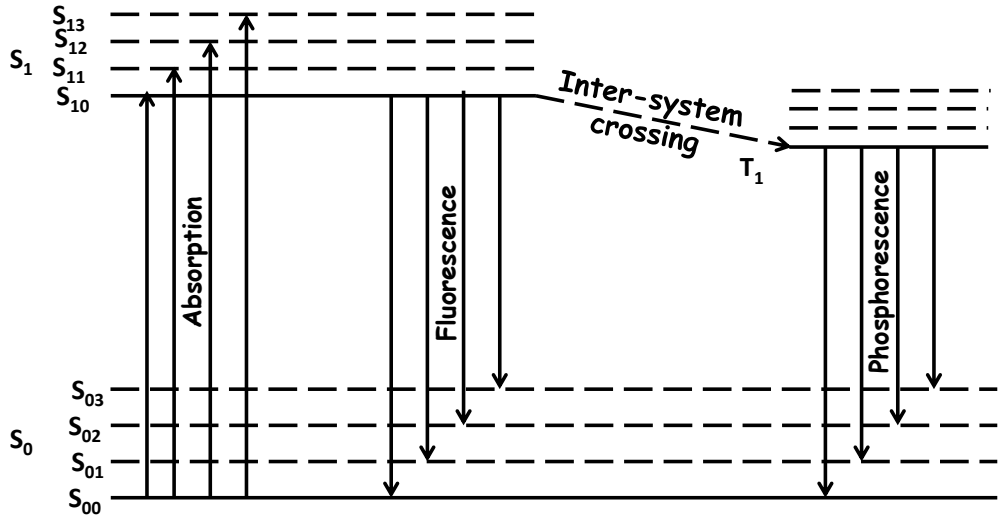

FIGURE 3.8: Energy levels of an atomic molecule with π-electron structure [Bir64].

single energy levels with spin 0 labeled S_i and triple energy levels labeled as T_i as can be seen in Figure 3.8. Each of the levels can be further divided into a series of vibrational states symbolized as S_{ij}.

When a particle pass through the scintillating material, its energy can be absorbed by exciting the electron into any one of many excited states. Although transitions happen between the ground state S_0 and the S_{1x} vibrational states, the vibrational states quickly lose their energy and return to the S_{10} state. A few nanoseconds after that, the prompt fluorescence light is emitted by the transitions from S_{10} state to the lower energy ground state S_{0x}.

The fluorescence intensity at a time t is given by

$$I = I_0 * e^{-t/\tau} \tag{3.3}$$

where τ is the decay time of S_{10} level and for BC-501A is 3.2 ns [Kno10]. A transition called an inter-system crossing can also happen between the S_{10} and the triplet state T_1. The lifetime of the triplet state can be up to 1 ms and the emitted radiation can

be characterized as phosphorescence. While in T_1 state some molecules can go back to S_1 and eventually decay to S_{0x} states. This delayed decay producing light in the visible wavelength, is the cause for the delayed fluorescence.

The organic scintillators can be transparent to their own emissions. While the absorption of the ionizing radiation can happen between the ground state S_0 and any S_{1x} level, the fluorescence can only happen between S_{10} and S_{0x}. This results in photons having a lower energy than the minimum required for re-excitation.

An additional substance is usually added into the main liquid scintillator that can serve as a wave-shifter. The wave-shifter absorbs the primary fluorescence light and re-radiates it at a longer wavelength. This shift is usually useful for better matching to the spectral sensitivity of the PMT. The maximum emission wavelength of the BC-501A is 425 nm and its refractive index 1.51.

Since the neutrons are charge-less, they do not interact with the organic scintillator via Coulomb force. Instead they interact within the medium usually through elastic scattering. The energy of a nucleus with mass number A after the collision with a neutron is given by the equation [Kno10]

$$E_R = \frac{4A}{(1+A)^2} * cos^2\theta E_n, \tag{3.4}$$

where E_R is the kinetic energy of the recoiling nucleus, θ is the recoil angle of the nucleus, and E_n is the kinetic energy of the incoming neutron. In a collision with a hydrogen nucleus a neutron can give up all of its energy to the proton. A collision with a heavier nucleus only transfers a small portion of the kinetic energy of the neutron. This is the reason behind the fact that proton rich organic liquid scintillators are preferred. The ratio of H/C nuclei for BC-501A is 1.212 while its density is 0.874 g/cm^3.

The probability for an elastically scattered neutron to deposit a given amount of

energy E_R in the detector is given by [Kno10]

$$P(E_R) = \frac{(1-A)^2}{A}\frac{\sigma(\Theta)}{\sigma_s}\frac{\pi}{E_n}, \tag{3.5}$$

where Θ is the center-of-mass scattering angle, σ_s is the total elastic scattering cross section, and $\sigma(\Theta)$ is the differential elastic scattering cross section. If $\sigma(\Theta)$ is isotropic and the scintillator light output depends linearly with energy deposited in the detector, then the ideal light output response is given by:

$$\frac{dN}{dH} = \frac{(1-A)^2}{A}\frac{1}{4E_n}, \tag{3.6}$$

where N is the number of counts observed with a pulse height H.

Based on the previous discussion one would expect that the light generated by the scintillator depends linearly on the energy deposited by the particle which mathematically can be expressed as [Kno10]

$$\frac{dL}{dx} = S\frac{dE}{dx}, \tag{3.7}$$

where S is the normal scintillation efficiency. Assuming that the density of damaged molecules along the path of the particle is directly proportional to the ionization density, we can represent their density by $B\frac{dE}{dx}$ where B is a proportionality constant. Birks also assumed that a fraction k will lead to quenching. This is true for the ^{12}C nuclei in the case of which the quenching effects are expected to be significant since much less light is generated from elastic scattering off of ^{12}C nuclei. By taking both effects into account we can write Birks' formula [Bir64]

$$\frac{dL}{dx} = S\frac{\frac{dE}{dx}}{1+\kappa B\frac{dE}{dx}}. \tag{3.8}$$

To match the experimental data, other empirical formulas were developed [Cra70]

$$\frac{dL}{dx} = S\frac{\frac{dE}{dx}}{1 + \kappa B\frac{dE}{dx} + C(\frac{dE}{dx})^2}. \tag{3.9}$$

The parameters κB and C can be adjusted to fit the data. The total light output, L(E), is given by

$$L(E) = \int_0^R \frac{dL}{dx}dx. \tag{3.10}$$

Other effects that can change the light output response are the finite size of the scintillating cell which makes it possible for particles to escape without fully depositing their energy into the active volume; and the multiple scattering of neutrons off protons which can lead to an increase of the observed pulse height. Due to all these effects the reconstruction of the neutron energy based on the pulse height is impossible. Instead we can take advantage of the fast response of the detector, which makes it possible to reconstruct the neutron energy based on the time-of-flight.

Pulse Shape Discrimination

Due to the co-existence of fast and slow fluorescence, the composite light yield curve can be represented by the sum of two exponential decays. Compared to the fast fluorescence of few nanoseconds, the slow fluorescence has a decay time of several hundred nanoseconds. The majority of the light yield occurs in the prompt component and does not depend on the kind of the incident ionizing radiation but the fraction of the light that appears in the slow component depends on the nature of the incident radiation [Kno10]. This can be used to discriminate between the fast neutrons which leave a long lasting signal and the γ-rays which have a short fast decaying signal.

The discrimination based on the pulse height of neutrons and γ-rays can happen with the use of commercially available units such as the MPD-4 [mes08b]. The method of pulse shape discrimination employed in this unit is a zero-crossing method [Rub07]. After the amplification of the pulse, two copies are generated. One goes to a constant fraction discriminator (CFD) to start the internal time to analog converter (TAC) while the other goes through a 6^{th} order trapezoidal filter which shapes the input pulse and preserves its rise and decay times. The time at which this pulse crosses zero provides the stop time for the TAC. The first 20 ns of the pulse are integrated and subtracted by the overall integrated pulse. The difference between these two pulses is converted to TAC amplitude. Since neutrons have longer signals than γ-rays, the output TAC amplitude is greater for a neutron than for a γ-ray.

Intrinsic Efficiency

The intrinsic efficiency is defined as the amount of neutrons recorded to the amount of neutrons that were incident on a detector. This number is always $\leq$1 and for the case of the BC-501A detector depends on the pulse height (PH) threshold. The increase of the threshold leads to a reduction of efficiency. The precise knowledge and consequently the calibration of the PH signal is required to determine the efficiency. Details about the method followed for the calibration of the detectors will be given in the next chapter. Figure 3.9 shows the dependence of the neutron detection efficiency on pulse height threshold.

3.6 Proton Detectors

Seventy two silicon surface barrier (SSB) detectors were used to perform the measurement on the two-body photodisintegration of ^{3}He. In the next sections, we give an overview of the physical and operational principles and characteristics of the SSB

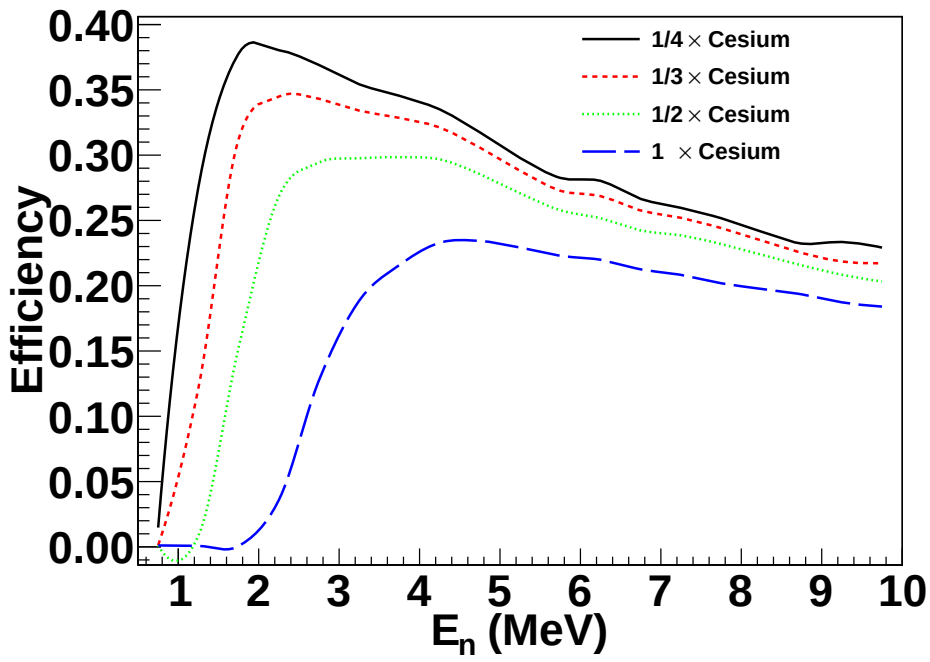

FIGURE 3.9: (Color online) The simulated efficiency of a BC-501A neutron detector as a function of neutron energy. A 1×Cesium is considered to be equal to 0.517 MeV_{ee}. More details about the calibration of the detectors can be found in the data analysis chapter.

detectors.

3.6.1 Physical Characteristics

In this section, we present the important steps for manufacturing silicon surface barrier detectors. The n-type silicon, in others words a piece of silicon with atomic impurities that can donate electrons, is cut, polished and etched until a thin wafer with a high-grade surface is obtained. The silicon is left in the air or other oxidizing agent for several days, which leads to a formation of a p-type layer. The p-type is a silicon layer where there is a good population population of holes—atoms with fewer valence electrons. After the formation of this thin p-type layer, the initial pure n-type silicon wafer is converted into an n-p junction. Very thin layers of gold and aluminum on the order of ∼200 nm evaporated on the front and rear surfaces

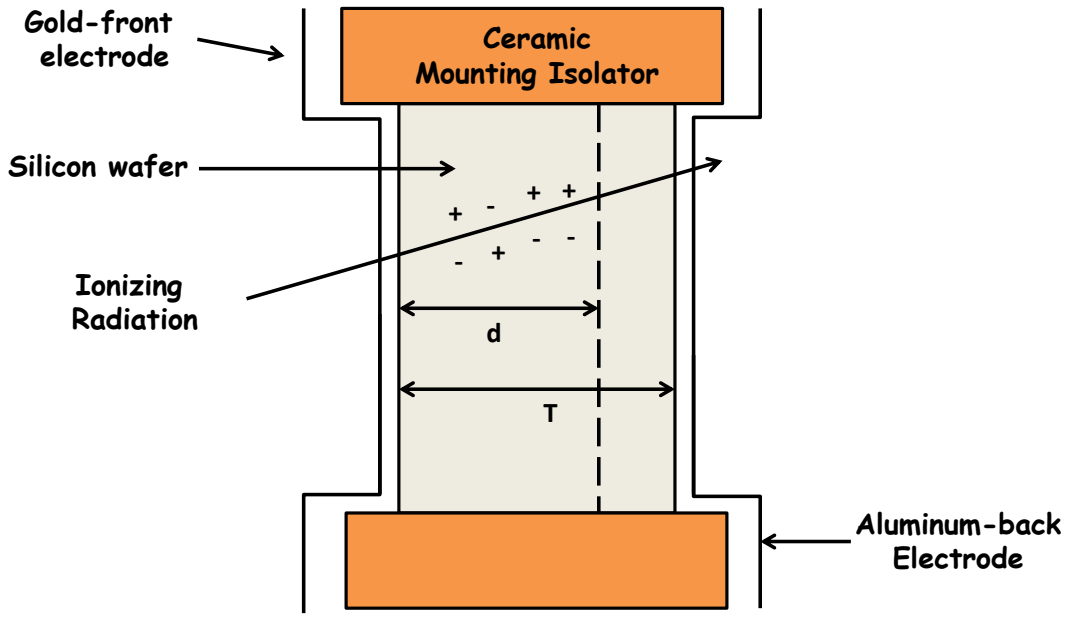

FIGURE 3.10: (Color online) A schematic representation of a SSB detector [Tso11].

of the silicon wafer serve as the electrical contacts through which the reversed bias is applied and the signal is led to the preamplifier. A schematic representation of an SSB detector can be seen in Figure 3.10. The thickness of the wafer of the SSB detectors used in the two-body photodisintegration experiment were 300 – 500 μm and their area 450 mm^2. One of the detectors used in the experiment can be seen in Figure 3.11.

3.6.2 Operational Principles

The formation of a np-junction creates a special zone at the interface of the two materials. Because of the difference in the concentration of the electrons and holes between the two materials, there is an initial diffusion of holes towards the n-region

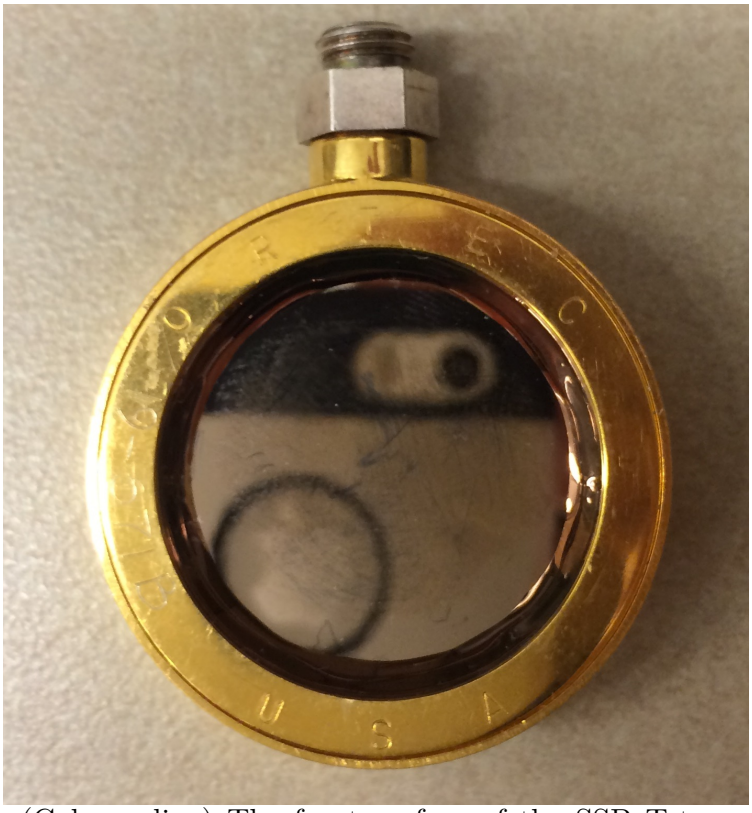

FIGURE 3.11: (Color online) The front surface of the SSB T-type detector. The reflective surface is the silicon wafer coated with a very thin layer of gold. The wafer in encased into a cylindrical Faraday cage and connected to a microdot connector.

and a similar diffusion of electrons towards the p-region. The diffused electrons fill up holes in the p-side while the diffused holes capture electrons on the n-side [Leo94]. Since the n and p structures are initially neutral the recombination of electrons and holes causes a charge build-up to occur on either side of the junction. The p-region which was injected with extra electrons becomes negative while the n-region becomes positive. The contact potential is about 1 V. The region for changing potential is known as the depletion zone. Figure 3.12 presents a schematic diagram of an np-junction.

When a charged particle passes through the depletion zone the overall effect is the production of many electron-hole pairs along the track of the particle which are then

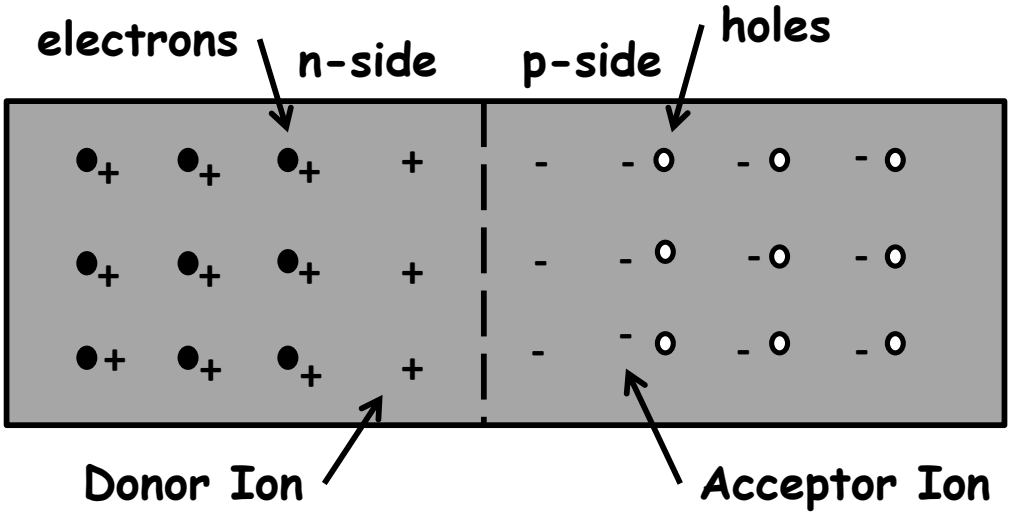

FIGURE 3.12: (Color online) A schematic diagram of an np-junction [Leo94]. The recombination of electrons and holes causes a charge build-up to occur on either side of the junction. The injected with extra electrons p-region becomes negative while the n-region becomes positive.

swept out by the electric field. The production of the pairs may be direct or indirect. Direct is called the production where the incident particles produce high-energy electrons through elastic scattering with the electrons of the semiconductor while indirect is the production of γ-rays due to the straggling of the incident particles in the semiconductor. These γ-rays subsequently lose their energy by producing more electron-hole pairs. The width of the depletion zone is generally small. The energy needed for the production of an electron-hole pair in an SSB detector is 1.1 eV.

In order to increase the depletion zone, an additional reversed bias, V_d, needs to be applied which accentuates the potential difference across the junction. The value of the potential ϕ at any point can be found by the solution of Poisson's equation

$$\frac{d^2\phi}{dx^2} = -\frac{\rho(x)}{\epsilon}, \tag{3.11}$$

where $\rho(x)$ is the charge density.

$$\rho(x) = \begin{cases} -eN_A & (-\alpha < x \leq 0) \\ eN_D & (0 < x \leq b), \end{cases}$$

where N_D and N_A are the concentrations of donors and acceptors. α and b are the lengths of p and n-sides, respectively. By substituting charge density into Equation 3.11 we take

$$\frac{d^2\phi}{dx^2} = \begin{cases} \frac{eN_A}{\epsilon} & (-\alpha < x \leq 0) \\ -\frac{eN_D}{\epsilon} & (0 < x \leq b), \end{cases}$$

where ϵ is the dielectric constant. By carrying out an integration and applying the boundary conditions of

$$\frac{d\phi}{dx}(-\alpha) = 0 \; and \; \frac{d\phi}{dx}(b) = 0,$$

we can get the electric field $\varepsilon = -d\phi/dx$ where

$$\frac{d\phi}{dx} = \begin{cases} \frac{eN_A}{\epsilon}(x+\alpha) & (-\alpha < x \leq 0) \\ -\frac{eN_D}{\epsilon}(x-b) & (0 < x \leq b). \end{cases}$$

By integrating one more time using the boundary conditions

$$\phi(-a) = 0 \; and \; \phi(b) = V,$$

where V is the value of an applied reverse bias. We can get the electric potential $\phi(x)$

$$\phi(x) = \begin{cases} \frac{eN_A}{2\epsilon}(x+\alpha)^2 & (-\alpha < x \leq 0) \\ -\frac{eN_D}{2\epsilon}(x-b)^2 + V & (0 < x \leq b). \end{cases}$$

Since the solutions should be equal at x=0 we can write

$$V = \frac{eN_A\alpha^2}{2\epsilon} + \frac{eN_Db^2}{2\epsilon}$$

or

$$N_Db^2 + N_A\alpha^2 = \frac{2\epsilon V}{e}.$$

By taking into account that the net charge is zero, $N_A\alpha = N_Db$ then

$$(\alpha + b)b = \frac{2\epsilon V}{eN_D}$$

where the depletion depth is d=$\alpha + b$. If $N_A \gg N_D$ then follows that $b \gg \alpha$. So the length of the depletion zone is $d \cong b$ and we can write

$$d \cong (\frac{2\epsilon V}{eN_D})^{(1/2)}.$$

It follows that the voltage needed to fully deplete a detector is given by

$$V_d \cong \frac{eN_DT^2}{2\epsilon},$$

where T is the wafer thickness. Figure 3.13 presents a schematic of a reversed-bias junction before and after the application of the bias.

3.6.3 Operational Characteristics

Leakage Current

Although the np-junction is nonconducting, a small current usually called leakage current, I_L flows through the junction when voltage is applied. The leakage current has three sources as described here. The first source is the minority carriers, i.e. the holes, which move from the n-region to the p-side and the electrons from the

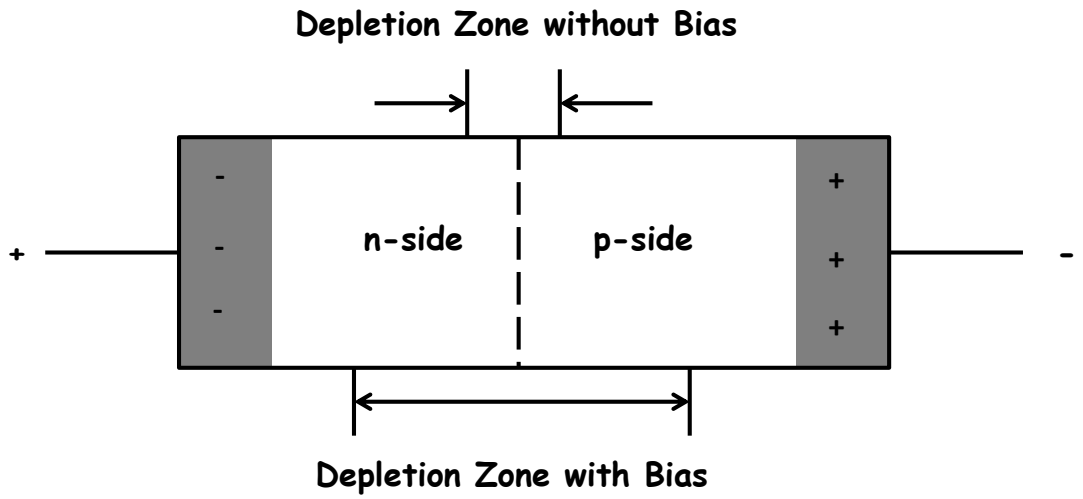

FIGURE 3.13: A reversed bias junction [Leo94]. The application of the reversed bias increases the depletion zone and accentuates the potential difference across the junction.

p-region to the n-side. This source is on the order of nA/cm^2. The second source is the thermally generated electron-hole pairs originating from recombination and trapping centers in the depletion zone. This depends on the absolute number of traps in the depletion region and the expected current densities should be on the order of μA/cm^2. The third source is the surface channels which depend on several factors like the surface chemistry, the existence of contaminants, the surrounding atmosphere, the type of mounting etc. [Leo94]

The bias voltage, V_d, is supplied to the detector through a large-value series resistor, R_L, in order to isolate the signal. The true bias voltage applied to the junction is reduced by the product of the leakage current and the series resistance. During our experiment, this resistance was 20 MΩ and the leakage currents were found to be on the order of $\sim$1 μA. The applied voltage was corrected for all detectors.

Linearity

Another important property of the semiconductor detector is its linear response to the incident radiation energy. If E is the energy of the radiation and w is the average energy needed to produce one electron-hole pair, then a charge of Q=nE/w can be collected by the electrodes of the detector, where n symbolizes the collection efficiency of the charge by the electrodes. The observed voltage on the electrodes has a linear dependence to the radiation energy:

$$V = \frac{Q}{C} = n\frac{E}{wC}. \tag{3.12}$$

Energy Calibration

The energy calibration obtained for one particle type is very close to that obtained from a different type. This allowed us to calibrate the detectors using the alpha emitter ^{241}Am. This isotope emits alpha particles of 5.486 (85%) and 5.443 MeV (13%). More details about the calibration of the SSB detectors using ^{241}Am will be given in the data analysis chapter.

3.7 Beam Monitoring

Two different beam intensity monitors were used during the measurements of $^3\vec{H}e(\vec{\gamma},p)d$ and $^3\vec{H}e(\vec{\gamma},n)pp$ reactions at HIγS. The first monitor is based on a NaI(Tl) detector while the second is based on the neutron detection from d(γ,n)p reaction using two BC-501A based detectors.

3.7.1 Beam Energy and Intensity Measurement using a NaI(Tl) Detector

In order to perform intensity and energy measurements using the NaI(Tl) detector, the attentuation of the γ beam is necessary. The beam is attenuated by a factor of 1000 – 40000 using 4, 5 or 6 copper attenuators and the NaI(Tl) detector is placed

directly into the beam exposed to the γ-rays for about a minute. The beam intensity is estimated by assuming that every non-background event corresponds to a γ-ray interacting with the detector. The result is corrected for dead time and extrapolated to the unattenuated case using the known copper attenuation factors from NIST database. Due to the number of attenuators and the large systematic errors of the attenuation factor, the error in the beam intensity determined using this method is found to be 10% – 15%.

Using the same acquired spectrum, the beam energy is extracted. The NaI detector is calibrated using an ^{241}Am/Be source. The ^{241}Am/Be source can emit both γ-rays and neutrons. The 4.4 MeV γ-rays emitted by the source and the γ-rays produced by the neutron capture into the Iodine nuclei inside the NaI crystal are used to perform a two-point calibration of the acquired spectra. The calibrated spectrum can be seen in Figure 3.3.

3.7.2 Absolute Beam Intensity Monitor based on d(γ,n)p Reaction

A deuteron target and two neutron detectors are used to monitor the γ-ray beam intensity via the d(γ,n)p reaction. The targets used for this purpose are described in a previous section of this chapter and the details will not be repeated here. Two neutron detectors are placed on either side of the deuteron target at 90° and shielding walls are built on the upstream side of the detector as can be seen in Figure 3.14. The integrated photon flux is calculated based on the well-known total cross sections [Ber86, Bir85] and angular distributions [Bla07] of the neutrons produced by deuteron photodisintegration. More details about the extraction of the absolute beam intensity will be given in data analysis chapter.

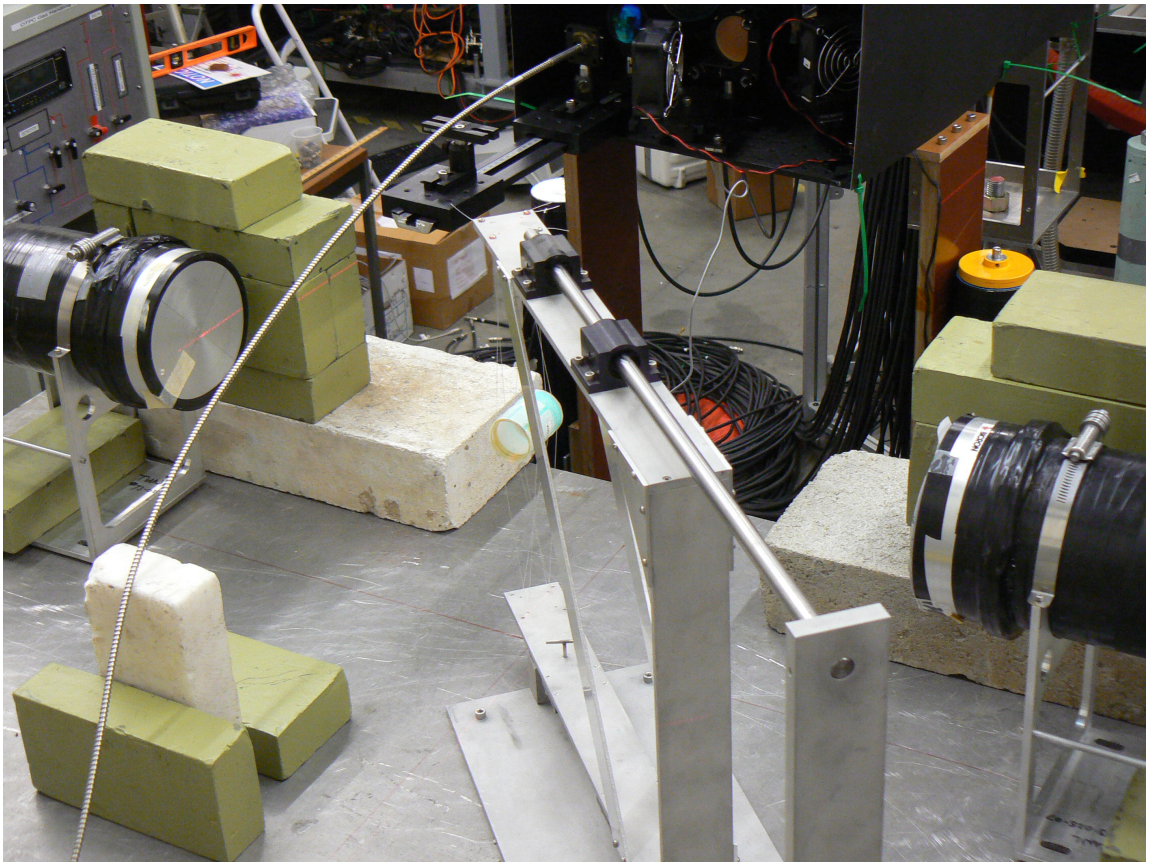

FIGURE 3.14: (Color online) A heavy water cell surrounded by two neutron detectors. Two lead walls are built to shield detectors from the γ-rays halo. Part of the optical apparatus used to polarize ^{3}He can be seen in the top right part of the figure.

3.8 Signal Processing and Storage

Several electronic circuits are used to process the signals received by the detectors. In these sections we describe the electronics circuits related to: the beam pick off (BPM) monitor, the Data Acquisition (DAQ) busy (Veto), the neutron detectors, the proton detectors and the NaI(Tl) detector.

3.8.1 Beam Pick Off Monitor Circuit

A beam monitor is required, in order to record the frequency of the γ-ray bursts on target and associate these bursts with the events recorded by the primary detector

arrays. This beam monitor is a capacitance pick-up detector located inside the storage ring. Each time an electron bunch passes through the detector a signal is induced with an amplitude proportional to the amount of electron current in the ring. This signal goes through a Timing Filter Amplifier (TFA) to shape the pulse for better timing information and subsequently through a constant fraction discriminator (CFD). The output of the CFD serves as the stop signal of the time-to-digital-converter (TDC) of the primary detectors array and it was used in the experiment for the time of flight measurements. The frequency of the signal (5.58 MHz) is twice the orbital frequency of the electron bunches, when running in a two-bunch mode.

3.8.2 DAQ busy/Veto Circuit

A circuit necessary to prevent the acquisition of additional events while previous events are being processed was used in both two- and three-body photodisintegration experiments. This circuit combines the busy signals from the trigger, ADC and TDC modules, and can be seen in Figure 3.15. If a pulse from a neutron or a proton detector is generated within the coincidence window of the system, this pulse triggers both the ADC and the TDC modules. While the ADC and TDC modules are processing the signal, they send out NIM pulses busy pulses which have the same durations as the processing time. Once the conversion is done a NIM pulse is sent by both the ADC and TDC module to the trigger module. This pulse is the "data are ready" (DRDY) pulse which tells the trigger module to read out the ADC and TDC modules. All TDC, ADC and trigger busy pulses are sent to a Linear Gate Fan In. This module combines all three pulses and gives the overlap of all busy signals. The overall busy vetoes the production of ADC gates and TDC stops.

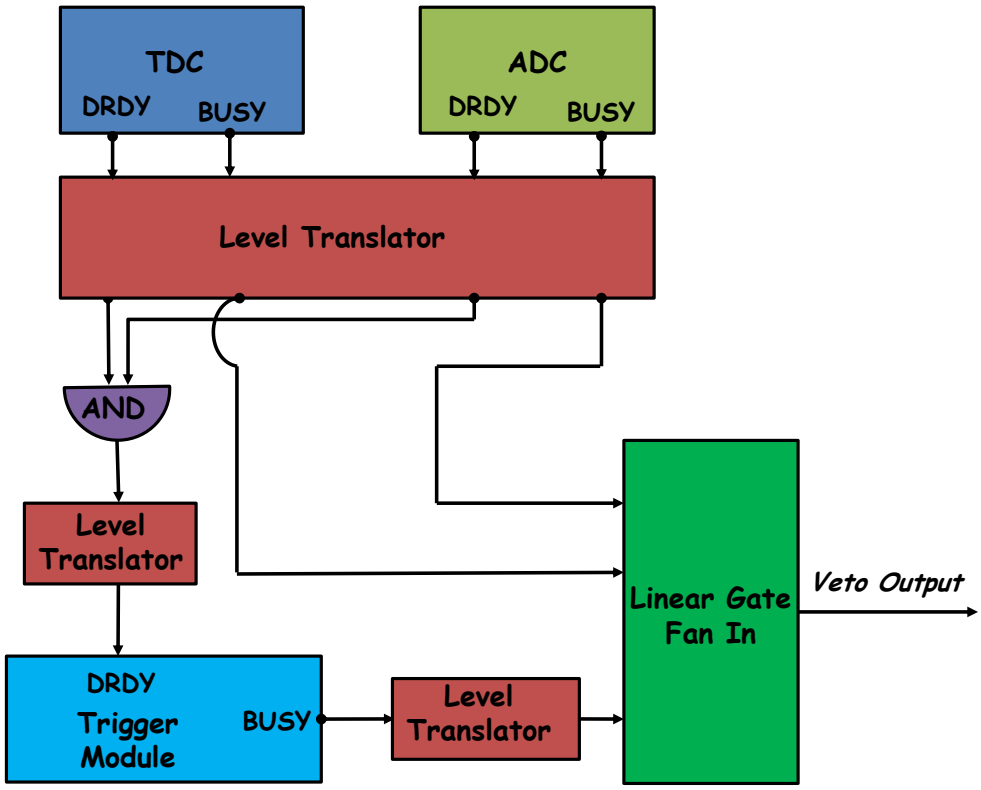

FIGURE 3.15: (Color online) The DAQ busy/Veto circuit. This circuit is used to prevent the acquisition of additional events while current events are being processed.

3.8.3 Neutron Detector Circuit

The incident neutrons and γ-rays produce signals in the neutron detectors which are processed through the electronic circuit of Figure 3.16. The produced signal first goes to the MPD-4 [mes08b]. The MPD-4 module contains: (i) a TAC to measure the time duration of the pulse for PSD, (ii) a CFD and (iii) a fast variable gain amplifier. The module is normally operated in the neutron detection mode so it can accept the neutrons with reduced triggers from the γ-rays. The MPD-4 module processes all the neutron-like events and produces five outputs:

1. **Ampl.** This is the integrated PMT charge output with a full range between 4 V and 8 V. The pulse height of the output is proportional to the deposited energy in the detector.

2. **TAC.** Corresponds to ratio of fast to slow component of scintillator light output with a full range of 4 V to 8 V. A large TAC amplitude corresponds to a neutron.

3. **n/γ-Trig.** This outputs a NIM logic pulse if the input signal passes both the pulse height and the TAC thresholds.

4. **Gate.** It generates a NIM pulse when signal exceeds CFD threshold. Its length is adapted to deliver ADC gate for **Ampl.** and **n/γ-Trig.** outputs.

5. **Comm. Trig.** Each MPD-4 module has four input channels and emits a NIM pulse if any of the four inputs receives a signal that is above the TAC threshold. This is the OR of all n/γ-Trig. outputs.

Four MPD-4 modules were used to process the data received by 16 sixteen neutron detectors. The output of the **Comm. Trig.** which produced a NIM pulse when any of the outputs of a module responded was an input to a global OR module. One output of the global OR was sent to a logic unit where the trigger was vetoed by the DAQ busy/Veto circuit of the previous section. The output of the logic unit was sent to form a gate for the ADC. The outputs of the **Ampl.** and **TAC** were sent as inputs to the ADC module.

Apart from the ADC and the TAC values, the time intervals between events and γ-ray bursts were also recorded using a TDC unit. The common start of the TDC was the vetoed output of the global OR. The stops of the TDC came either from the output of the BPM circuit or from the **Gate** of the MPD-4 module produced for each detector.

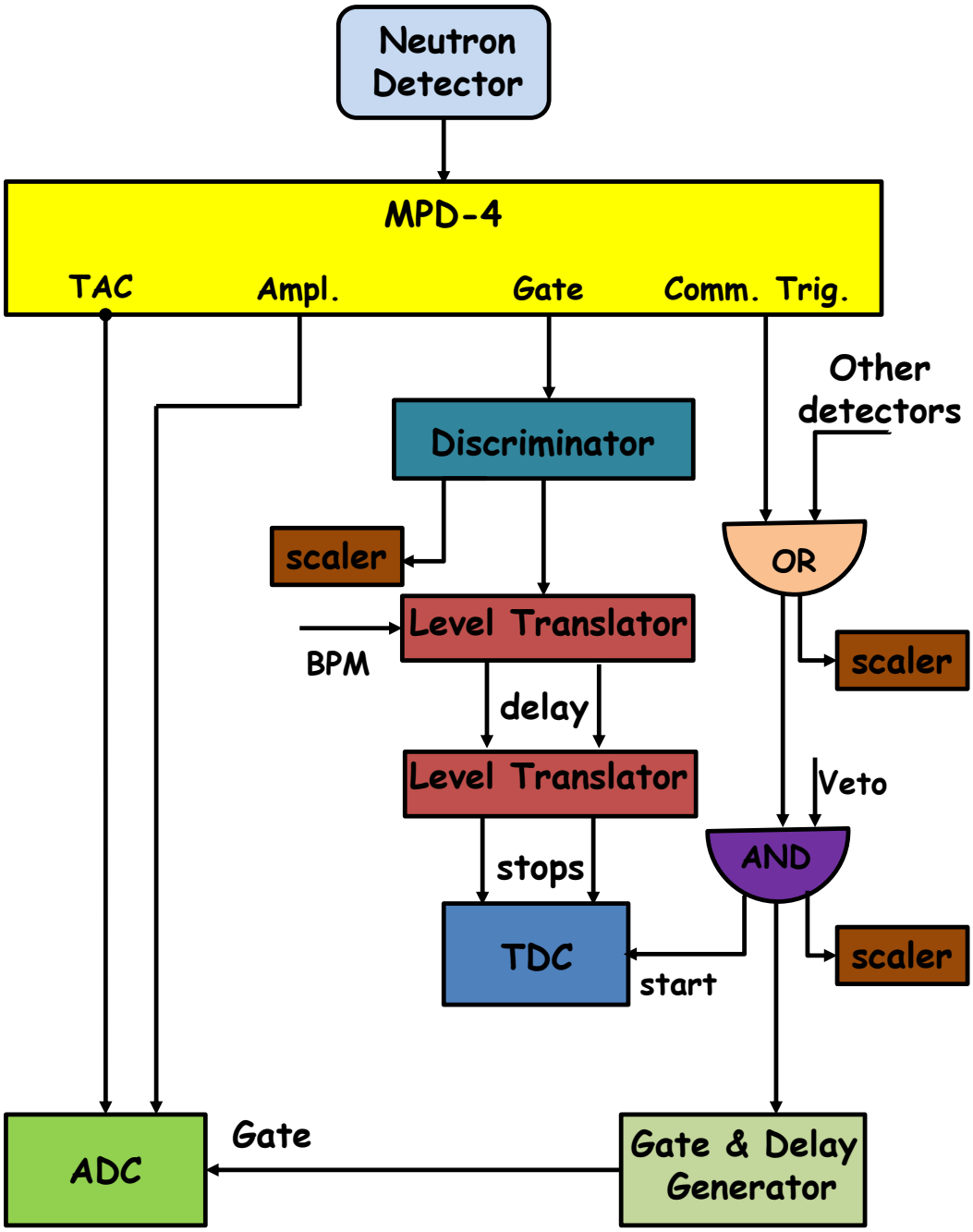

FIGURE 3.16: (Color online) The electronics circuit for the signal processing of the sixteen neutron detectors used to detect the neutrons from $^3\vec{H}e(\vec{\gamma},\mathrm{n})\mathrm{pp}$ reaction and the two used to monitor the γ-ray intensity based on the reaction $\mathrm{d}(\gamma,\mathrm{n})\mathrm{p}$.

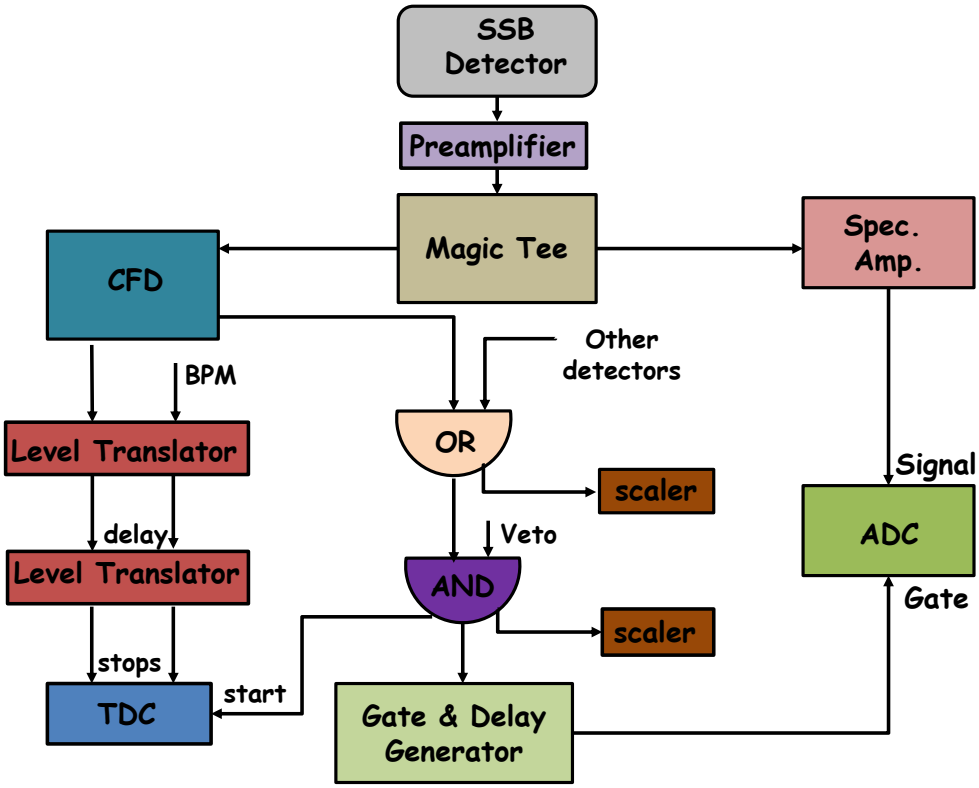

FIGURE 3.17: (Color online) Electronics diagram of the SSB circuit. The SSB detectors were used to detect protons from $^{3}\vec{H}e(\vec{\gamma}$,p)d reaction.

Each time that a neutron-like event passed the TAC threshold of any of the MPD-4 module, two different TDC values were recorded. The first value is the so-called self timing raw TDC value and it is the time interval between the start time of a signal and a delayed copy of the same signal. The second TDC value is the time interval between the start time of the detector signal and the stop time coming from the BPM. The difference between the two values is the time interval, usually called TDC value and it is directly proportional to the time of flight of the event.

3.8.4 Proton Detector Circuit

In this section, we describe the electronic circuit used for the study of $^3\vec{H}e(\vec{\gamma},p)d$ reaction. The incident charged particles produce usually weak pulses in the SSB detectors. An amplification of the pulses is required and takes place right after the detectors. In the case of two-body photodisintegration experiment, nine modules of the MSI-8 [mes08a] preamplifier were used to amplify the signals from the seventy two SSB detectors. This eight channel preamplifier had the ability to provide common bias to all the detectors connected to it while it amplified the signal of each detector separately. After the amplification, the pulse went through a Magic Tee and split into two branches. The one branch passed through a spectroscopy amplifier which shaped the signal into an appropriate form for the ADC. The second branch went to a VME [Leo87] CFD and then after a delay to the stop of the TDC. The CFD modules had the ability of producing a NIM pulse if any of their channels was triggered. The output of the global OR of all five CFD modules was sent to a logic unit where the trigger was vetoed by the DAQ busy/Veto circuit of the previous section. One output of the Logic Unit was sent to form a gate for the ADC while a second one was used to start the TDC. Figure 3.17 presents all the major components used for the signal processing in the two-body photodisintegration experiment.

3.8.5 NaI(Tl) Circuit

The circuit for the signal processing of the NaI(Tl) detector is simple and can be seen in Figure 3.18. The signal of the NaI(Tl) detector splits into two branches. The one branch passes through a TFA to shape the pulse for better timing information and then goes through a CFD. The discriminated signal is used as an input to a Gate & Delay Generator which in turn produces a gate on the order of a few μs for the ADC. The second branch passes through a spectroscopy amplifier which shapes the signal into an appropriate form for the ADC.

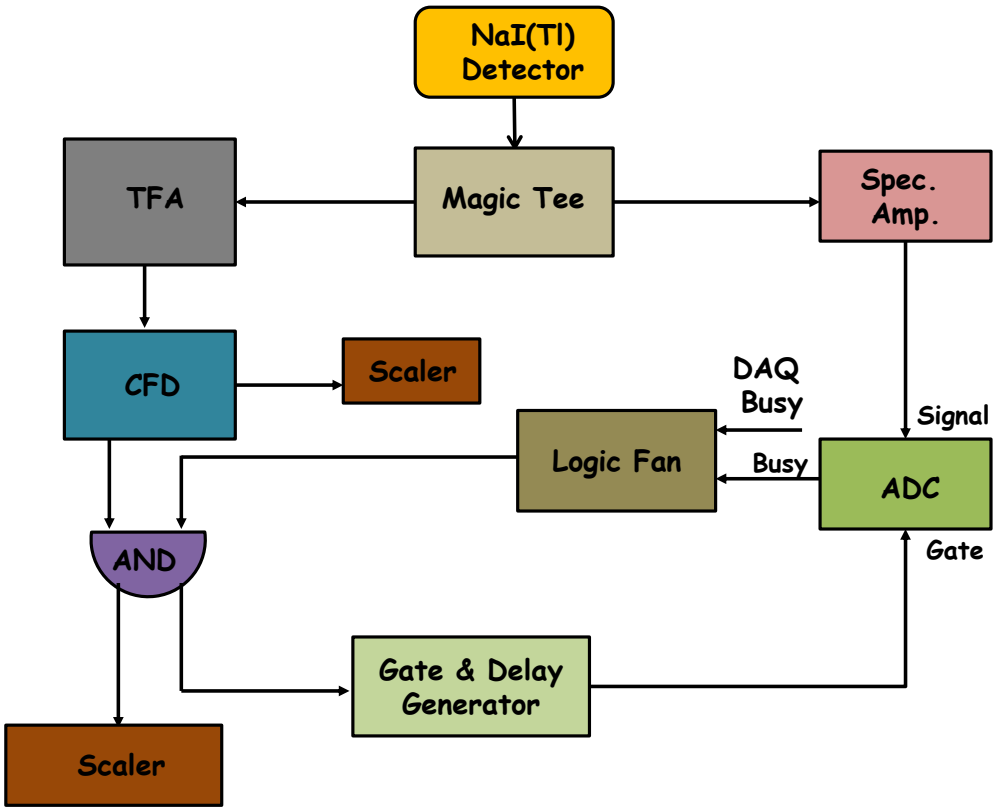

FIGURE 3.18: The electronic circuit for the signal processing of NaI(Tl). The NaI(Tl) detector was used to estimate the γ-ray beam intensity and energy.

3.8.6 Data Acquisition (DAQ) System

The DAQ system used at TUNL to manage and store the events received by the detectors is the software package CEBAF Online Data Acquisition (CODA). The CODA package was developed by TJNAF based on Unix using modern network infrastructure such as Ethernet and TCP/IP protocols [Abb99]. CODA at TUNL consists of four components: (i) the mSQL database which is responsible for maintaining the file paths for the data storage, (ii) the Single Board Computer (SBC) terminal which manages the communication between the VME crate where ADC/TDC lay and the host computer that is running CODA, (iii) the Event Builder (EB) which stores the

data into CODA format and (iv) the Run Control which manages the previous three components.

Several steps need to be taken in order to configure the Run Control. The first step is the "Configure", which reads the mSQL database and sets path variables. The second step is the "Download". In this step two tasks are performed: first, the DAQ computer sends the drivers to SBC for the coordination of the communication between the SBC and the ADC/TDC; second the DAQ computer sends the pre-compiled code called CRL to SBC in order to coordinate their communication. The next step is the "Prestart", which clears of the buffer of the ADC/TDC, sets the time range of the TDC, and enables the ADC/TDC. The final step is the "Go", which activates the ADC/TDC. One can "End the Run" once sufficient data are collected.

Apart from the TDC and ADC modules, three other modules are connected to the VME crate. The Scaler module, when receiving NIM logic pulses, increments a counter in order to keep track of scaler data i.e. clock, veto clock, etc. The Trigger module receives the trigger signals from the ADC/TDC and informs the SBC to read those modules. Finally, the SBC module transmits the data to the host computer.

CODA package does not provide an analysis component. Instead ROOT [Bru97], a software developed at the Conseil Européen pour la Recherche Nucléaire (CERN), was used for the data analysis.

4

The Polarized ^{3}He Target

4.1 Overview

Many different facilities developed polarized ^{3}He targets during the last decade of the 20^{th} century for nuclear experiments sensitive to spin dependent quantities. The initial objective of these efforts was to use a polarized ^{3}He nucleus as an effective polarized neutron target because, in its ground-state, the two protons are predominantly in an S state in which their spins cancel and the nuclear spin is carried by the unpaired neutron. The first experiments for the extraction of spin-dependent neutron structure properties such as the electromagnetic form factors [Gao94, Xu00, Mey94, Bec99, Roh99, Ber03, Rio10] and the spin structure functions [Ant96, Abe97, Ack97, Ama02, Qia11] took place at TJNAF using a polarized ^{3}He target and electron beam.

All previous efforts used the polarized ^{3}He target in order to extract information for the neutron. The doubly-polarized experiments at HIγS facility require a polarized ^{3}He target to acquire information not for the neutron but instead for the ^{3}He nucleus. The development of the polarized ^{3}He target at Duke University started in

2003. The first experiment using a polarized ^{3}He target at HIγS took place in 2008 by X. Zong *et al.* [Zon10] on the three-body photodisintegration of ^{3}He with double polarizations at the incident photon energy of 11.4 MeV. An overwhelming contamination to the signal was observed as the neutron background produced mainly by the barium content of GE180 glass container of the ^{3}He cell. A new target made by Pyrex glass was developed [Ye10] and several successful beam tests and experiments on the two- and three-body photodisintegration took place between 2010 and 2014. The next sections present the basic principles for characterizing, polarizing and measuring the polarization of a ^{3}He target.

4.2 Spin Exchange Optical Pumping (SEOP)

There are two commonly used optical pumping techniques to polarize ^{3}He nuclei. The first technique is the metastability exchange optical pumping (MEOP) [Col63]. MEOP is based on the direct pumping of the metastable 2^3S_1 state of ^{3}He. Initially, a weak RF discharge is used in a relatively low pressure ^{3}He gas cell to create a metastable 2^3S_1 state. Then, circularly polarized laser light with a wavelenght of 1.08 μm excites the ^{3}He atom from the 2^3S_1 to $^3P_0$ state. The excited atom decays back to the metastable state with probabilities determined by Clebsch-Gordan coefficients. The polarization is transferred to the ground state of ^{3}He nuclei by metastability exchange collisions in which the excitation of the electronic cloud is exchanged.

In order to polarize larger quantities of ^{3}He gas the spin exchange optical pumping (SEOP) [Hap72] technique is routinely employed. This technique was employed to polarize the ^{3}He target cell named "SPOT" used in both two- and three-body photodisintegration experiments. Following this technique, ^{3}He is polarized in two steps. The first step is to introduce a mixture of Rb and K alkali-metal into the ^{3}He cell. The cell is heated up to a temperature $\sim$200°C in order to vaporize Rb and K vapor atoms. The alkali-metal number densities with respect to temperature can be

calculated based on the vapor pressure curves given in Ref. [Lid04]. Rb atoms have one electron in the 5s shell which dominates the atomic magnetic moment. The Rb outer shell electrons are polarized by laser light tuned to the $5S_{1/2} \rightarrow 5P_{1/2}$ transition at 794.8 nm [dZ60, Ben65] known as the D_1 transition. Circularly polarized photons with positive helicity can excite electrons from $5S_{1/2}$ (m_J=-1/2) to $5P_{1/2}$ (m_J=1/2) state while photons with negative helicity can excite electrons from $5S_{1/2}$ (m_J=1/2) to $5P_{1/2}$ (m_J=-1/2). The electrons can decay back from $5P_{1/2}$ to $5S_{1/2}$. The decay probability between $5P_{1/2}$ (m_J=1/2) and $5S_{1/2}$ (m_J=-1/2) is 1/3 while it is 2/3 between the $5P_{1/2}$ (m_J=1/2) and $5S_{1/2}$ (m_J=1/2). If a laser light with positive helicity is used to pump the target all electrons will eventually populate the $5S_{1/2}$ (m_J=1/2) state. When electrons decay back to the ground state they emit photons at the same D_1 transition wavelength. These photons are not polarized and can depolarize the electrons. For this reason, a small quantity of N_2 ($\sim$100 torr) is introduced inside the ^{3}He cell. The number density of N_2 is orders of magnitude less than the ^{3}He density and orders of magnitude more than the Rb and K density. The collisions between the N_2 and Rb atoms allow Rb electrons to decay without emitting photons by absorbing energy into rotational and vibrational motion. This process is usually called non-radiative quenching [App98]. The collisions between the N_2 and Rb atoms randomize the P state decay rates which eventually become equal. A diagram of the optical pumping of Rb outer shell electrons can be seen in Figure 4.1.

Some of the polarized Rb atoms can transfer their polarization to K atoms. In turn the Rb and K can both transfer their polarization to ^{3}He nuclei through spin-exchange collisions between Rb-^{3}He and K-^{3}He. The spin exchange probability between Rb-^{3}He and K-^{3}He is κ_{se}^{Rb}=6.8$\times 10^{-20}$ cm^3/s [Cha02, Bar98, BAB98] and κ_{se}^{K}=5.5$\times 10^{-20}$ cm^3/s [Bab05], respectively.

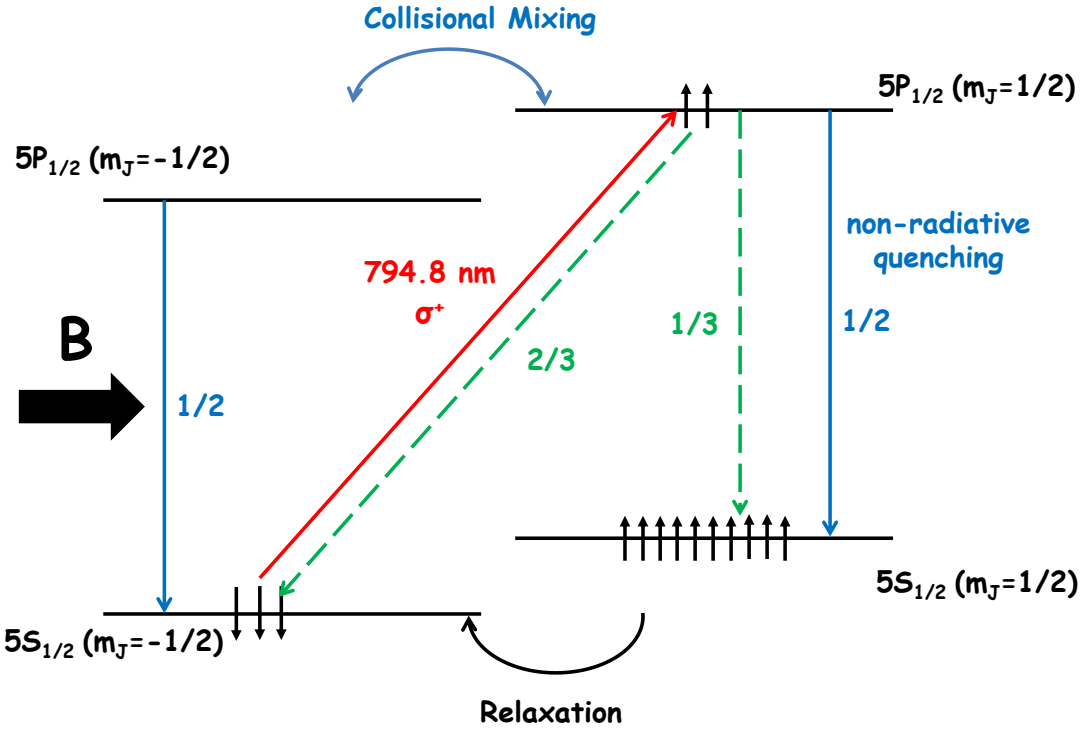

FIGURE 4.1: (Color online) Optical pumping of Rb outer shell electrons through right-handed circularly polarized photons.

The Rb polarization at any given location along the laser beam is given by [Che07]

$$P_{Rb}(z,P) = \frac{R(z,P)}{R(z,P)+\Gamma'_{Rb}} \tag{4.1}$$

where $R(z,P) = \int \phi(z,\nu,P)\sigma_{Rb}(\nu)d\nu$ is the optical pumping rate with a certain laser power P and Γ'_{Rb} is the total spin destruction rate on the order of 1kHz [Che07]. $\phi(z,\nu,P)$ is the number of photons per unit area A per unit time in the frequency interval $d\nu$ ($d\nu = \frac{c}{\lambda^2}\delta\lambda$) along the laser beam direction at a given z and ν. $\sigma_{Rb}(\nu) = \frac{\sigma_{Rb0}}{1+4\Delta^2/\gamma_{Rb}^2}$ [Che07] is the frequency interval absorption cross section, assuming a Lorentzian form, where the peak cross section is $\sigma_{Rb0} = 3.2\times10^{-13}$ cm^2. $\Delta = \nu - \nu_0$ is the frequency offset from the optical pumping resonant frequency ν_0 (λ_0=794.8

nm), and $\gamma_{Rb} = (18.7 \pm 0.3)$ GHz/amg [Rom97] is the pressure broadened width of the D_1 transition of Rb. $\phi(z, \nu, P)$ can be expressed with respect to the power P, the frequency of the laser and the location along the laser beam [Rom98, Che07] (see Appendix B.1) as:

$$\phi(z, \nu, P) \cong \frac{P}{Ah\nu_0 d\nu} e^{-[Rb]\sigma_{Rb}(\nu)\left(1-P_\infty P_{Rb}(z,P)\right)z} \tag{4.2}$$

where $[Rb]$ is the Rb number density and P_∞ is the mean photon spin of the pumping light. It follows that the pumping rate at a certain location z is given by (see Appendix B.1)

$$\begin{aligned} R(z, P) \quad &\cong \quad \frac{\pi\sigma_{Rb0}\gamma_{Rb}P}{2Ah\nu_0 d\nu} e^{-[Rb]\sigma_{Rb0}\left(1-P_\infty P_{Rb}(z,P)\right)z/2} \\ &\cdot I_0\Big(- [Rb]\sigma_{Rb0}\big(1 - P_\infty P_{Rb}(z, P)\big)z/2\Big) \end{aligned} \tag{4.3}$$

where I_0 is the zeroth order Bessel function of the first kind. Equation (4.3) gives a conservative estimate of the pumping rate and consequently of the P_{Rb}. It also suggests that Rb atoms are polarized to different degrees along the laser light direction. By substituting Equation (4.3) into Equation (4.1) and taking the volume average, the value of P_{Rb} can be estimated numerically in an iterative way by varying the laser power value P with a finitely small step each time as shown in Ref. [Ye10]. Given a laser power which usually exceeds ∼100 watts, the Rb vapor atoms are considered to be fully polarized when the laser light is incident on the target.

The polarized Rb atoms will collide with ^{3}He nuclei and exchange their spins through hyperfine interactions. In order to hold ^{3}He nuclei polarized a magnetic field, B_0 on the order of few Gauss is needed. The polarization of ^{3}He is given by Equation (A43) in [Chu92]. This equation needs to be modified according to Equation (2) in [Cha03] (or (1) in [Bab06]) in order to include the X parameter, which is a phenomenological parameter that reflects additional unknown spin decay

processes. The ^{3}He polarization for a double-chamber ^{3}He cell in equilibrium can be expressed as (see Appendix B.2) [Ye10]

$$P_{3He} = P_{Rb}(z=0,P)\frac{f_{opc}\cdot\gamma_{se}^{Rb/K}}{f_{opc}\cdot\gamma_{se}^{Rb/K}(1+X)+\Gamma} \tag{4.4}$$

where $\gamma_{se}^{Rb/K} = k_{se}^{Rb}[Rb] + k_{se}^{K}[K] \sim 10^{-4}$ Hz [Che07, Bab06] is the spin exchange rate of Rb and K with ^{3}He and f_{opc} is the fraction of ^{3}He nuclei in the pumping chamber of the double-chamber cell. Finally, Γ is the total destruction rate that includes the contributions of all relaxation mechanisms presented in the next section.

4.3 Spin Relaxation Mechanisms

Three are the main relaxation mechanisms that can depolarize the ^{3}He nuclei. The first mechanism is related to the dipole-dipole interaction between the ^{3}He atoms' magnetic moments. The leading order of the potential of the interaction between two ^{3}He atoms can be written as [New93]

$$V = (\frac{\mu_{^3He}}{I})^2\frac{1}{r^3}(\vec{I_1}\cdot\vec{I_2} - \frac{3(\vec{I_1}\cdot\vec{r})(\vec{I_2}\cdot\vec{r})}{r^2}) \tag{4.5}$$

where $\vec{I_1}$ and $\vec{I_2}$ are the nuclear spins of the two ^{3}He atoms separated by $\vec{r}$ and $I = |\vec{I_1}| = |\vec{I_2}|$. The dipole-dipole spin relaxation rate is equal to [Mul90]

$$\Gamma_{dipole} = \frac{\hbar^2\gamma^4}{\alpha^2}\frac{[^3He]\sqrt{m_{^3He}}}{(k_BT)^{1/2}} \tag{4.6}$$

where $\gamma = 2\pi\times3.24$ kHz/G is the gyromagnetic ratio of ^{3}He, α is the distance of closest approach between the two ^{3}He nuclei, $[^3He]$ is the ^{3}He number density and $m_{^3He}$ is its atomic mass. At room temperature Equation 4.7 becomes [New93]

$$\Gamma_{dipole} = \frac{[^3He]}{744}hrs^{-1} \tag{4.7}$$

The typical density of ^{3}He cell used in HIγS facility is 6–7 amg. The expected relaxation due to dipole-dipole interaction is on the order of few hundreds of hours.

A second relaxation mechanism is related to the existence of the magnetic field gradient over the volume of the ^{3}He cell. The ^{3}He nuclei relaxation rate due to the magnetic field gradient is given by [Gam65]

$$\Gamma_{\nabla B} = \frac{\bar{u}^2}{3} \frac{|\nabla B_x|^2 + |\nabla B_y|^2}{B_0^2} \frac{T_c}{1 + \omega_0^2 T_c^2} \tag{4.8}$$

where $\omega_0 = \gamma B_0$ is the Larmor precession frequency, $\bar{u}$ is the average speed of ^{3}He given by $\bar{u} = \sqrt{\frac{8k_B T}{\pi m}}$ and $|\nabla B_x|$, $|\nabla B_y|$ are the gradients of the two transverse field components B_x and B_y. The mean time between atomic collisions is given by $T_c = \frac{\lambda_{mfp}}{\bar{u}}$ where $\lambda_{mfp} = \frac{k_B T}{\sqrt{2}\pi P d^2}$ [Lid04] with P being the pressure and d the diameter of the ^{3}He atoms. If $\omega_0 T_c \ll 1$ then Equation 4.8 becomes [Cat88]

$$\Gamma_{\nabla B} = \frac{\bar{u}\lambda_{mfp}}{3} \frac{|\nabla B_x|^2 + |\nabla B_y|^2}{B_0^2} \tag{4.9}$$

Assuming a commonly used holding field of $\sim$20 G, a typical gradient of 5 mG/cm and a typical pressure of the target cell $\sim$11 atm when in operation, the depolarization of ^{3}He nuclei due to magnetic field gradient is on the order of hundreds of hours.

The major contribution to the ^{3}He longitudinal relaxation is the wall effect. The relaxation due to the quality of the ^{3}He cell wall can be a result of several factors such as: (i) the paramagnetic impurities like the alkali metal oxides formed on the walls of the ^{3}He cell; (ii) the out-gassing of paramagnetic compounds like molecular oxygen and nitrogen oxide from the cell walls when the cell is heated; (iii) the striking of the ^{3}He atoms on the surface and the consequent relaxation by a local magnetic field [Lus88] or exchanging with other nuclear spins [Dri96] and other unknown effects associated with the wall. The relaxation due to wall effect can not be predicted. Instead the attention is focused on the fabrication and filling of the ^{3}He cells. The

filling procedure needs to take place in good vacuum while several factors such as temperature, pressure and the quality of the alkali metals introduced in the ^{3}He are controlled. The wall relaxation time can vary from less than an hour to 100 hours. The expected overall relaxation time of a well-performing hybrid HIγS-type cell is typically more than 30 hrs.

4.4 Experimental Apparata

In this section we give an overview of the experimental apparatus of the ^{3}He target system used for both two- and three-body photodisintegration experiments that took place at the HIγS facility. The target system in both experiments is the same, while apart from the different detectors were used to detect the produced protons (two-body) and neutrons (three-body).

A schematic overview of the experimental apparatus for the three-body photodisintegration experiment including the ^{3}He target system, optics support, the detectors, and the deuteron flux monitor is shown in Figure 4.2.

The circularly polarized beam produced by the HIγS facility is incident on the ^{3}He target cell "SPOT". As described in the previous chapter, "SPOT" is a one-piece glassware made of Pyrex glass consisting of two chambers: the target chamber which is a $\sim$ 40cm long cylinder through which the γ-ray beam passes and the pumping chamber, a spherical volume where SEOP takes place. The two chambers are connected through a narrow transfer tube. A mixture of Rb and K alkali-metals is inside the pumping chamber of "SPOT". Circularly polarized light provided by one $\sim$60 W Coherent DUO-FAP broad-band and three VBG-locked Comet $\sim$30 W narrow-band diode lasers is incident on the pumping chamber. The pumping chamber is heated up to $\sim$473 K using hot air and an oven. To circularly polarize the laser light, a set of optics is used positioned downstream from the ^{3}He target. The Rb atoms are optically pumped and polarized, and they in turn transfer their

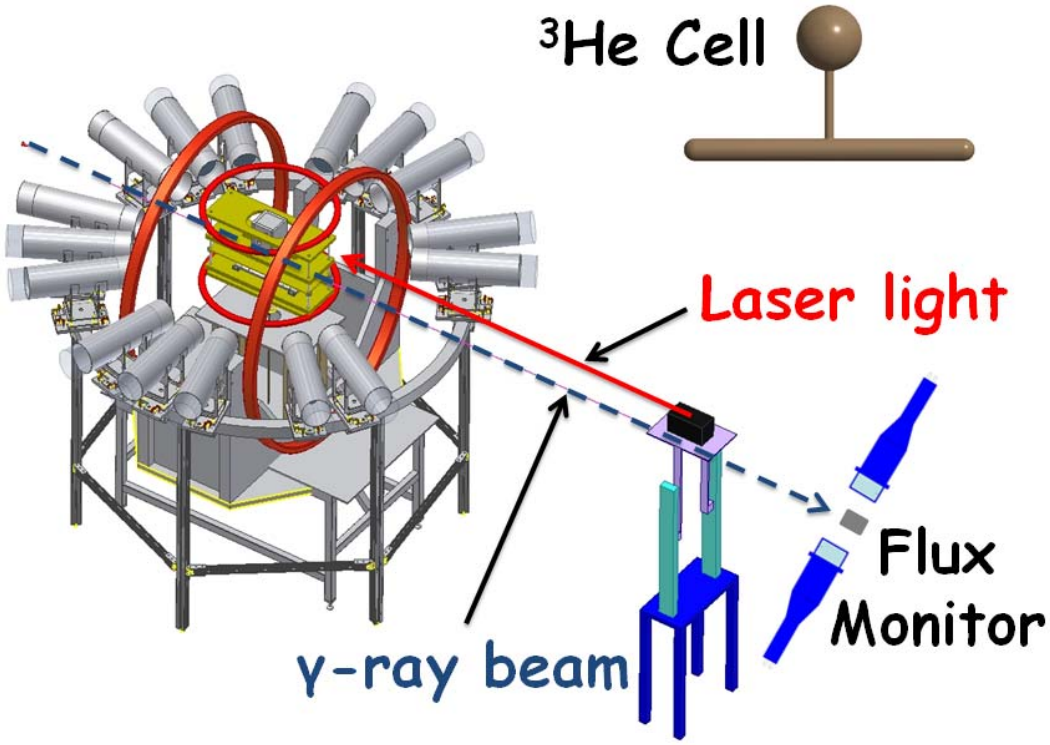

FIGURE 4.2: (Color online) Schematic of the experimental apparatus. The movable target system (yellow) that was used to cycle between the ^{3}He target and the N_2 reference cell is surrounded by 16 liquid scintillator detectors placed inside μ-metal tubes (gray). The Helmholtz coils (red) are providing the holding field. The movable support of the optics that is employed to polarize the ^{3}He target and the deuteron flux monitor can be seen in the bottom right corner of the figure, next to the flux monitor.

polarization to K atoms. Spin exchange collisions between Rb, K and ^{3}He atoms transferred the polarization to ^{3}He nuclei through hyperfine interactions [Hap72]. The filling density of ^{3}He is 6.48±0.1 amg. In addition to the ^{3}He gas, about 0.1 amg of N_2 gas is used in the target as a buffer gas. A 20.2 G magnetic holding field is provided to define the ^{3}He spin direction by a pair of Helmholtz coils ∼170 cm in diameter.

The layout of the optics used to circularly polarize the laser light can be seen

in Figure 4.3. A five to one combiner fiber delivers the laser light to the optical apparatus. A convex lens is placed to a distance equal to its focal length so that the diverging laser beam becomes parallel. The beam is reflected by a mirror and passes through a cube splitter. The cube splits the beam into s and p linearly polarized waves. The beam passing through the beam splitter is the p wave with its $\vec{E}$ component polarized in the horizontal plane. This wave is reflected by a mirror and passes through a $\lambda/4$ wave plate. The reflected beam from the beam splitter is the s wave with its $\vec{E}$ polarized in the vertical plane. The reflected beam passes through the $\lambda/4$ wave plate, reflected by a mirror and passes again through the $\lambda/4$ wave plate. By passing through the $\lambda/4$ wave plate two times the beam changes from an s wave to a p wave and now can pass through the beam splitter. After the beam passes through the beam splitter a $\lambda/4$ wave plate makes it circularly polarized.

The reference cell "Kielbasa" filled with only 0.1 amg of N_2 gas is employed for measuring the backgrounds. To reduce systematic uncertainties, the ^{3}He target and the N_2 reference cell were switched frequently with the help of an integrated stepper motor connected with a jack placed under the ^{3}He target apparatus. Another stepper motor is used to move the set of optics vertically following the ^{3}He target movement. In this way, the ^{3}He target was polarized continuously throughout the experiment.

The protons from the two-body photodisintegration of polarized ^{3}He were detected by 72 fully depleted SSB detectors positioned at 45°, 70°, 95° and 120° (eighteen detectors at each angle), ∼11 cm away from the center of the polarized ^{3}He target cell. Figure 4.4 shows the overview of the experimental apparatus used for the two-body photodisintegration experiment. The detector support is composed of six aluminum hemispheres, three on each side of the cell facing each other. Twelve SSB detectors are mounted on each aluminum hemispherical shell. Collimators with rectangular apertures of 2 cm × 0.4 cm, and a length of 3 cm, are positioned in front

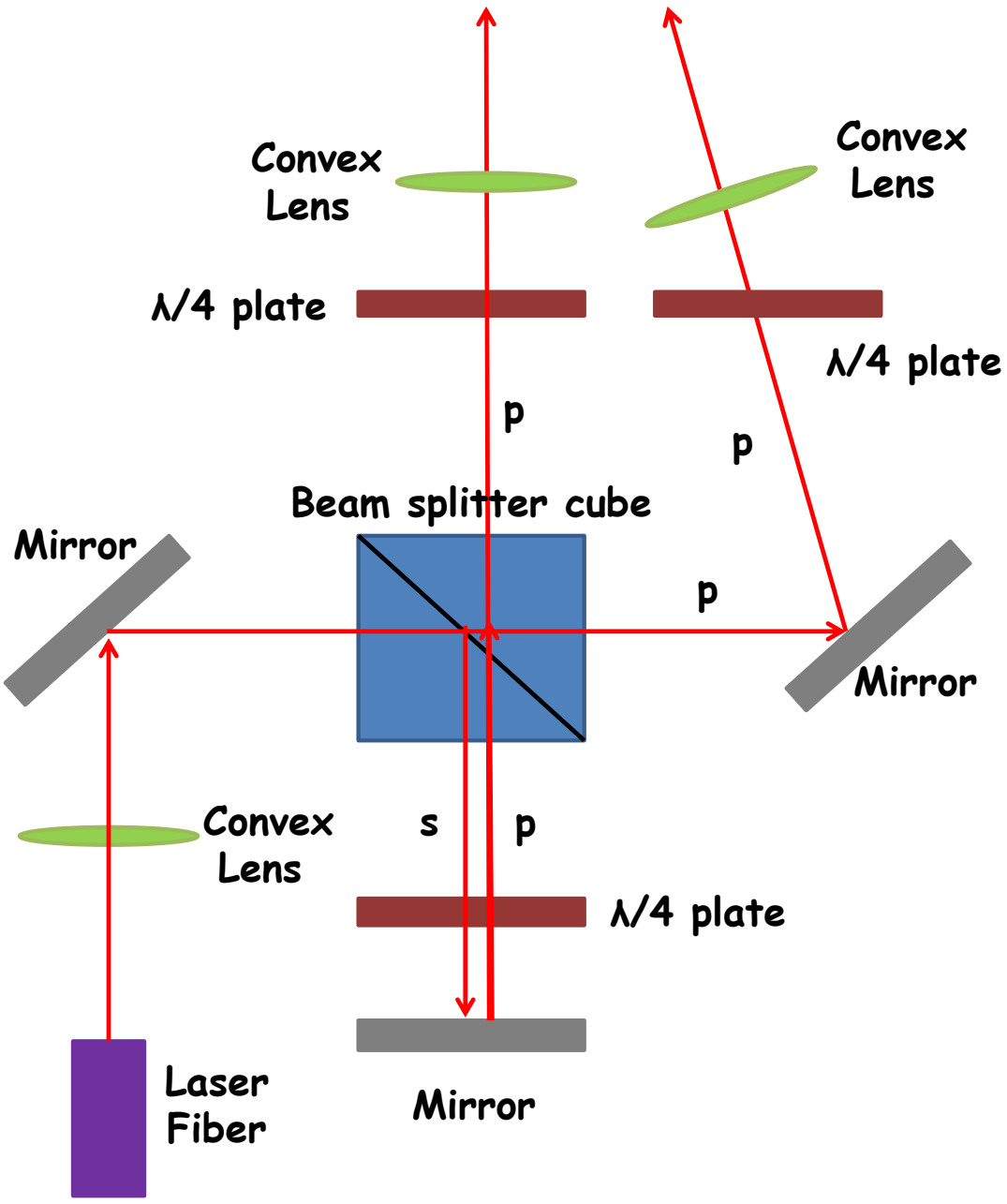

FIGURE 4.3: (Color online) The layout of the optics setup.

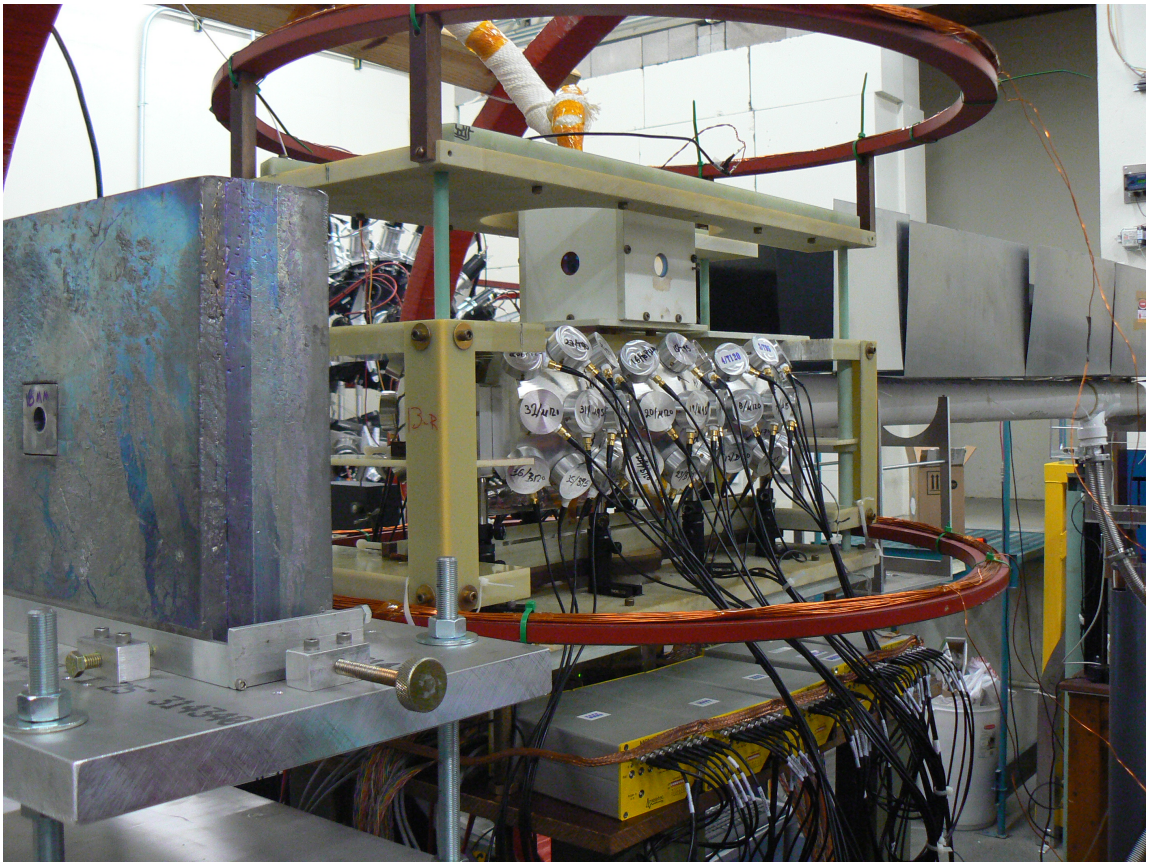

FIGURE 4.4: (Color online) Photograph of the two-body experimental setup in the target room. Three of the hemispheres surrounding the ^{3}He target and N_2 reference cell and the back part of the oven enclosing the pumping chamber of the ^{3}He cell can be seen in the photograph. A second collimator in front of the targets (left) is used to attenuate the beam halo.

of the detectors. The collimators define the solid angle and reduce the uncertainty in the angular acceptance. This apparatus allowed us to maximize the number of SSB detectors positioned around the target chamber of the ^{3}He cell.

The neutrons from the three-body photodisintegration of ^{3}He are detected using sixteen liquid scintillator detectors. The detectors are placed 1 m away from the center of the target at laboratory angles 30 °, 45 °, 75 °, 90 °, 105 °, 135 °, 150 ° and 165 °. The photomultiplier tubes are inside μ-metal shields to protect them from the magnetic field of the Helmholtz coils. Figure 4.5 shows an overview of the

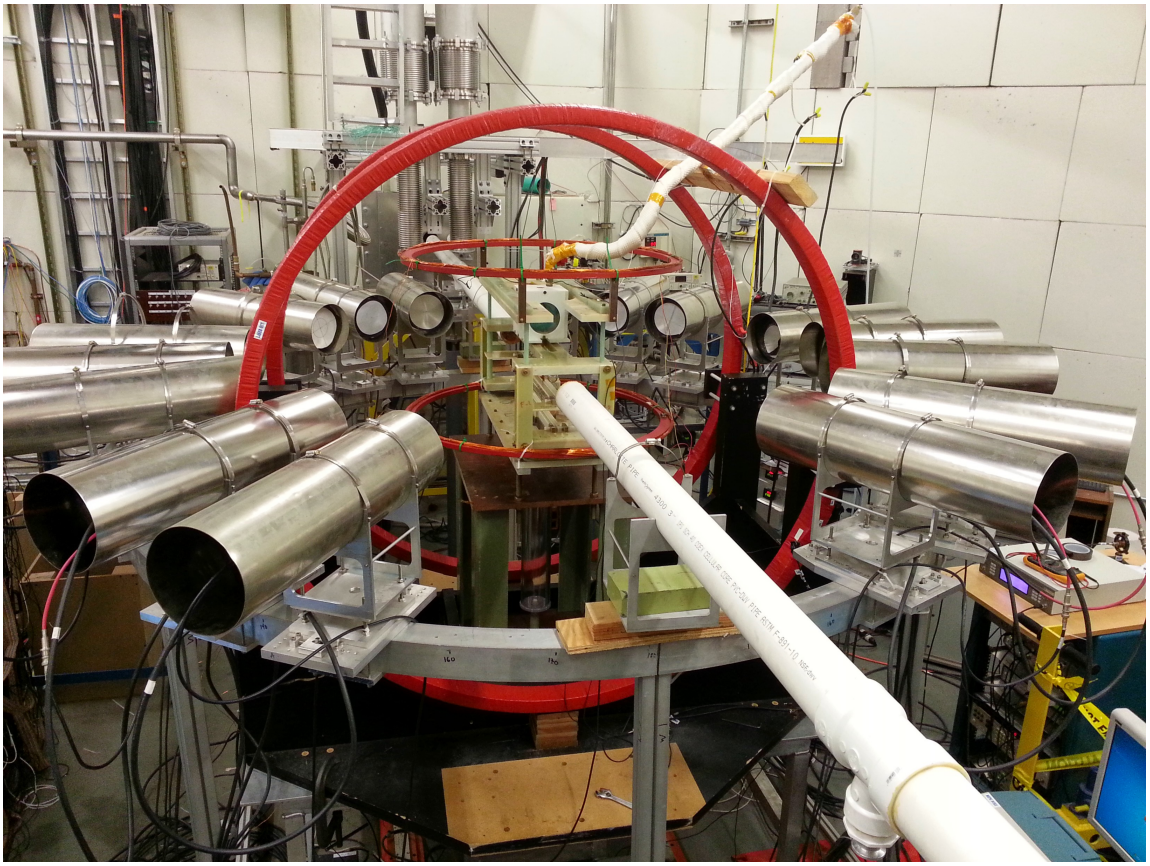

FIGURE 4.5: (Color online) Photograph of the three-body experimental setup in the target room. The pumping chamber of the ^{3}He cell is enclosed in the oven laying in the middle of the detector array. The beam is delivered to and from the target with the use of vacuum pipes to reduce the neutron background. The movable target is surrounded by sixteen neutron detectors encased in μ-metal tubes.

experimental apparatus located in the HIγS target room.

A deuteron target along with two neutron detectors are employed as a γ-ray flux monitor. The setup is positioned downstream of the target and the detectors are placed at 90° on either side of the deuteron target. The detectors count neutrons from the ^{2}H(γ,n)p reaction to determine the incident γ-ray intensity.

4.5 Polarimetry

Two techniques were employed to measure the polarization of a ^{3}He target cell: the nuclear magnetic resonance-adiabatic fast passage (NMR-AFP) technique [Lor93] and the electron paramagnetic resonance (EPR) [Rom98]. In the next sections, we will give an overview of these techniques.

4.5.1 Nuclear Magnetic Resonance-Adiabatic Fast Passage (NMR-AFP)

The NMR-AFP is employed to measure the polarization of ^{3}He target. This method can give only the relative polarization and a calibration using a cell filled with water is needed to extract the absolute polarization. In this section we will describe the basic principles of NMR-AFP technique and the calibration using a water cell.

When a particle with magnetic moment, $\vec{M}$, is placed in a constant external magnetic field, B_0, it experiences a torque [Abr61]:

$$\frac{d\vec{M}_{lab}}{dt} = \gamma\vec{M} \times \vec{B}_0 \tag{4.10}$$

In a rotational frame which rotates with a frequency ω around B_0, the precessing magnetic moment in the laboratory frame is related with the precessing magnetic moment in the rotational frame by

$$\frac{d\vec{M}_{lab}}{dt} = \frac{d\vec{M}_{rot}}{dt} + \vec{\omega} \times \vec{M} \tag{4.11}$$

By substituting Equation 4.10 into Equation 4.11 one can find the $\frac{d\vec{M_{rot}}}{dt}$. The effective holding field in the rotational frame is equal to $\vec{B}_0 + \frac{\vec{\omega}}{\gamma}$.

Assuming that an RF magnetic field $\vec{B} = 2B_1 cos(\omega t)\vec{x}$ with a magnitude $B_1 \ll B_0$ and a frequency equal to that of the rotational frame ω, is applied to the sample magnetized by the $B_0\vec{z}$ field and is perpendicular to it. The RF can be expressed as

$$\vec{B_1} = B_1(cos(\omega t)\vec{x} + sin(\omega t)\vec{y}) + B_1(cos(\omega t)\vec{x} - sin(\omega t)\vec{y}) \tag{4.12}$$

This magnetic field consists of two magnetic fields with frequencies $\vec{\omega} = \pm\omega\vec{z}$. In the reference frame rotating with frequency $-\omega\vec{z}$, the one component of the RF field is static while the other component is rotating with a 2ω frequency. The latter is far off the resonance and can be ignored. The effective field experienced by the sample is equal to

$$\vec{B_{eff}} = (B_0 - \frac{\omega}{\gamma})\vec{z} + B_1\vec{x}. \tag{4.13}$$

While the ^{3}He cell is being polarized, a holding field is present in order to define the polarization in a certain direction. During the AFP measurement another constant RF field is applied to the ^{3}He target. In order to perform the AFP measurement, the holding field is ramped towards the resonance field (ω/γ). While the holding field is changing, the effective field $\vec{B_{eff}}$ together with the magnetization of the ^{3}He nuclei are changing from the $\vec{z}$ axis towards the $\vec{x}$. The effective magnetic field can be seen in Figure 4.6.

When $B_0(t)$ becomes equal to $B_0(t) = \omega/\gamma$ the magnetic moments of ^{3}He nuclei induce a signal in a pick up coil which is proportional to the polarization of ^{3}He. As the magnitude of the holding field becomes larger than the resonance field $B_0(t) > \omega/\gamma$, the effective field and the magnetization of the ^{3}He nuclei start moving from $\vec{x}$ towards the $-\vec{z}$ axis. This procedure is called a spin-flip. The holding field is ramped up to a maximum value away from the resonance field to ensure a full spin-flip and then it is ramped down passing by the resonance a second time. This procedure results in two spin-flips which induce signal in the pick up coil. Figure 4.7 shows the change of the holding field with respect to time.

The functional form of the induced signal can be described by a Lorentzian Q-

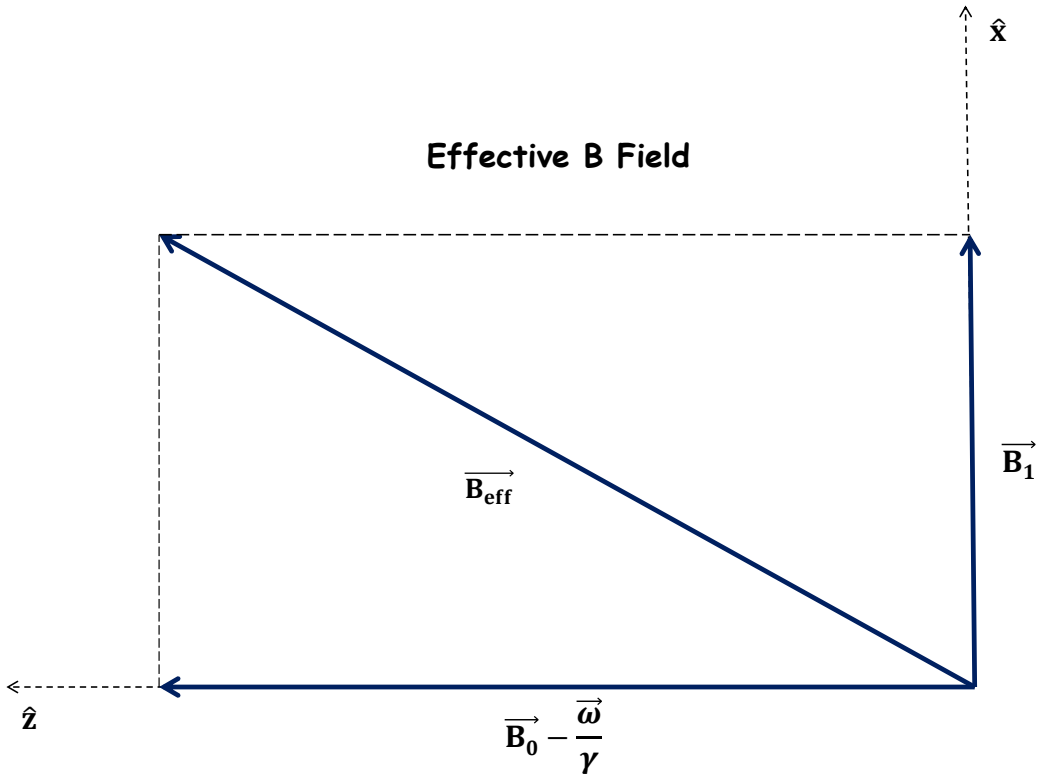

FIGURE 4.6: (Color online) The effective magnetic field in the rotational reference frame.

curve [Kra03]:

$$S_{^3He}^{NMR}(t) = \frac{< M > B_1}{\sqrt{(B_0(t) - \omega/\gamma)^2 + B_1^2}} + A \cdot B_0(t) + C \tag{4.14}$$

where $< M >$ is the amplitude of the signal, which is proportional to the polarization and $A \cdot B_0(t) + C$ is a term to fit the linear background. There are two necessary conditions for an AFP measurement [Lor93]: (i) the magnetic field should change adiabatically according to $\frac{1}{B_1}|\frac{dB_0}{dt}| \ll \gamma B_1$ so the magnetization of ^{3}He can follow the effective field and (ii) the rate of change should be fast enough $\frac{1}{B_1}|\frac{dB_0}{dt}| \gg \Gamma_1$ and Γ_2. Here Γ_2 is the transverse relaxation rate. A typical NMR-AFP measurement can be seen in Figure 4.9.

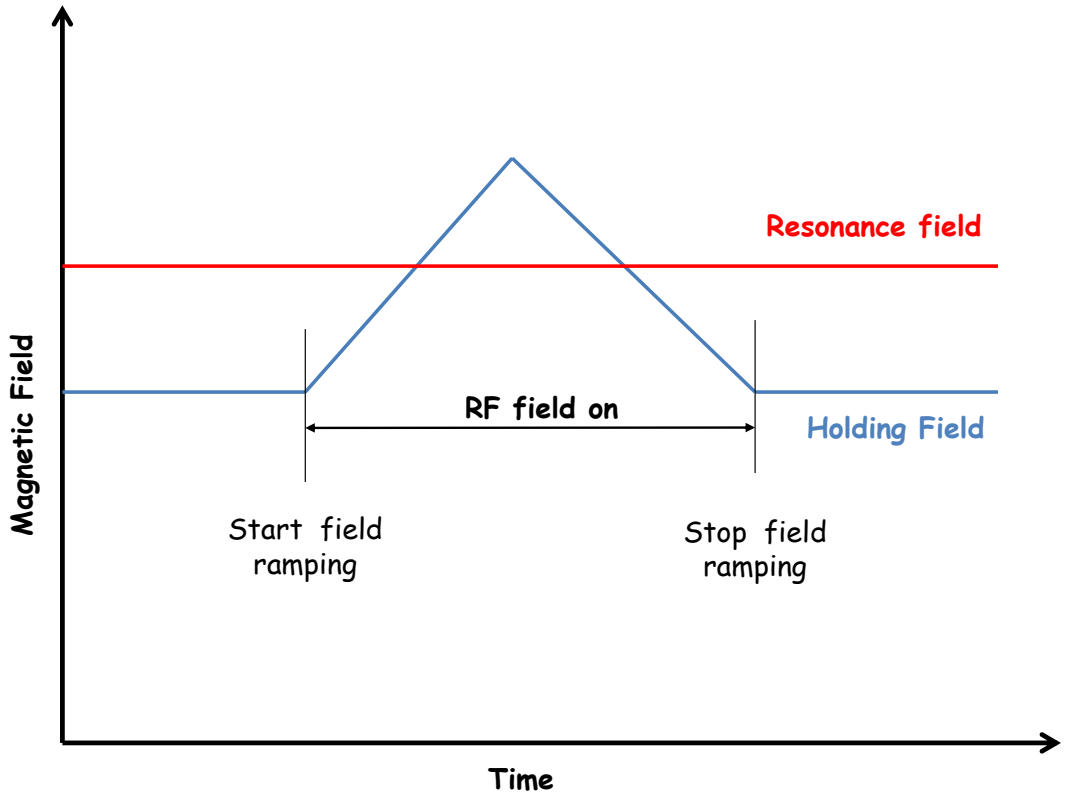

FIGURE 4.7: (Color online) The change of the holding field with respect to time. The holding field is ramped up and down passing through two times from the resonance field.

The accumulation of the ^{3}He signal with respect to time is studied extensively for every ^{3}He cell. The acquired curve, commonly known as pump-up curve, is an indicator of the quality of the ^{3}He cell and the efficiency of the optical pumping. A short pump-up time indicates the low quality and consequently the large relaxation rate of the ^{3}He while an unusually long one is an indication of the existence of an inefficiency in the system such as: (i) a reduction of laser power; (ii) a shift of the laser from the resonance wavelength; (iii) an improper optimization of the oven temperature and others. A typical pump-up curve for cell "SPOT" can be seen in Figure 4.9.

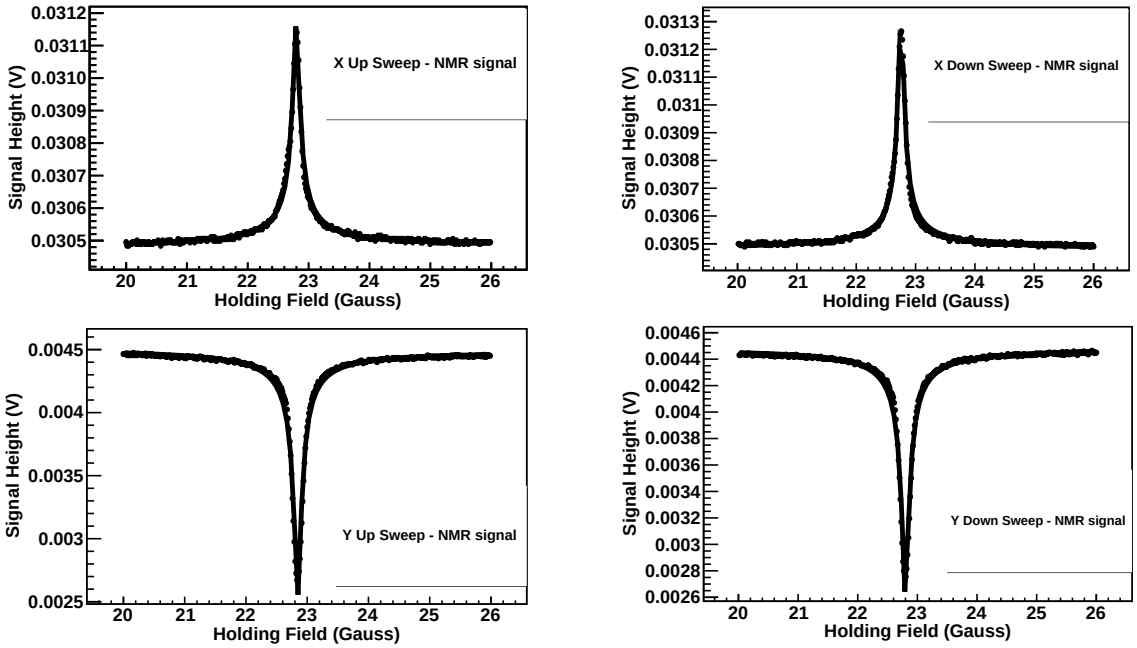

FIGURE 4.8: The NMR-AFP signal as recorded by the X and Y channel of lock-in amplifier. The AFP signal is the average of $\sqrt{x_{up}^2 + y_{up}^2}$ and $\sqrt{x_{down}^2 + y_{down}^2}$.

The signal is fitted to the following function:

$$P(t) = A_0 * (1 - (1 - L)^n * e^{-\frac{t}{T_p}}) \tag{4.15}$$

where A_0 is a constant, L is the loss of a small portion of the signal every time that a measurement is performed, n is the number of the consecutive measurement and T_p is the pump-up time. The pump-up times observed for well-performing HIγS-type ^{3}He cells are between 8 to 12 hrs depending on the cell.

Another important number which is directly related to the polarization gradient between the pumping and the target chamber is the relaxation time. The relaxation curve is measured with the laser beam off and the oven at room temperature. A typical relaxation curve for cell "SPOT" can be seen in Figure 4.10.

The relaxation curve is fitted using the following formula:

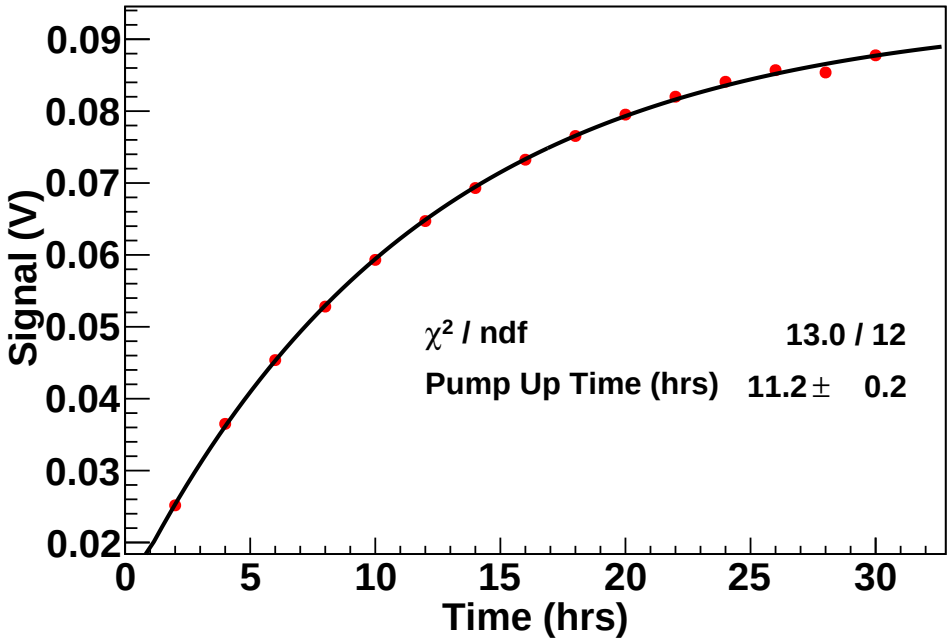

FIGURE 4.9: (Color online) A pump-up measurement for the ^{3}He cell "SPOT" fitted with Equation 4.15.

$$R(t) = A_0 * (1 - L)^n * e^{-\frac{t}{T_1}}. \tag{4.16}$$

The relaxation time is correlated with the quality of the wall surface of the cell. A longer relaxation time indicates a cell which can potentially reach a high polarization while a short relaxation time is correlated with a poor quality cell. The relaxation time at room temperature for all well performing HIγS-type ^{3}He cells is beyond 30 hrs.

Water Calibration

Water calibration can be used to calibrate the NMR-AFP signal. To perform a water calibration, a glass cell with the same geometry as the ^{3}He cell and filled with water is mounted at the same position as the ^{3}He cell. The thermal polarization of the protons in the water is given by [Lor93]

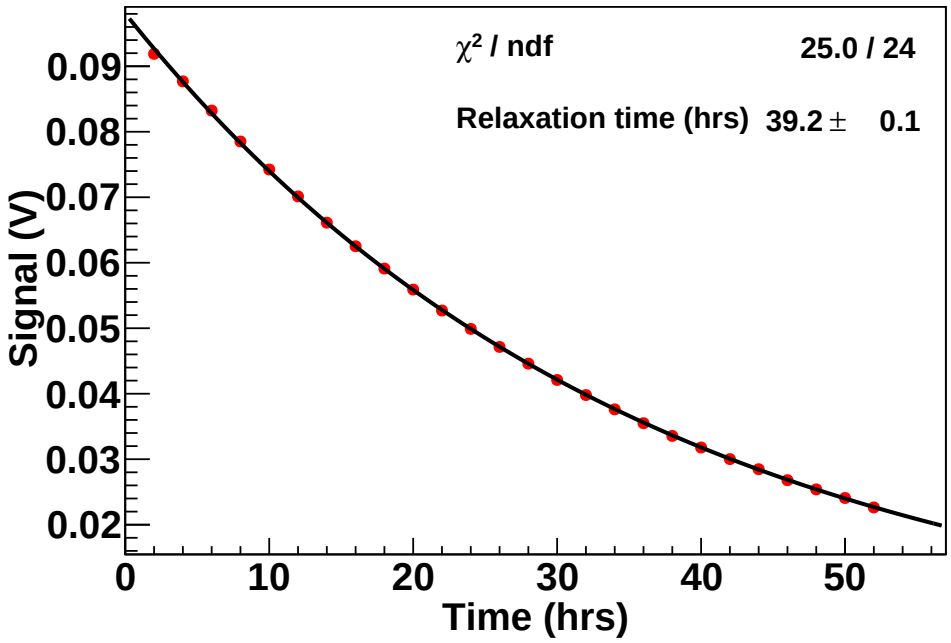

FIGURE 4.10: (Color online) A relaxation measurement for the ^{3}He cell "SPOT" fitted with Equation 4.16.

$$P_p = \tanh(\frac{\mu_p B}{k_B T}) = \tanh(\frac{\mu_p \omega}{k_B T \gamma_p}) \tag{4.17}$$

where the μ_p is the magnetic moment and γ_p is the gyromagnetic ratio of proton. If the magnetic field is $\sim$20 G, we have

$$P_p = \tanh(\frac{\mu_p \omega}{k_B T \gamma_p}) \approx \frac{\mu_p \omega}{k_B T \gamma_p} = 7 \times 10^{-9} \tag{4.18}$$

assuming that the measurement takes place at room temperature. The ratio of the proton to ^{3}He signal can be written as:

$$R = \frac{Q_{^3He} \omega_{^3He} P_{^3He} n_{^3He} V_{^3He} \mu_{^3He}}{Q_p \omega_p P_p n_p V_p \mu_p} \tag{4.19}$$

where Q is the response factor of the pick-up coils used for the measurements, ω the resonance frequency and V the volume of the target or pumping chamber depending on the location where the measurement takes place, the same for both cells. P, n and μ are the polarization, number density and the magnetic moment of ^{3}He and proton. By substituting Equation 4.18 into Equation 4.19 we have:

$$R = \frac{P_{^3He} n_{^3He} k_B T_p \mu_{^3He} \gamma_p}{\omega_p n_p \mu_p^2}. \tag{4.20}$$

where $n_p = 6.7 \times 10^{28}/cm^2$. By solving Equation 4.19 with respect to $P_{^3He}$ we can obtain the polarization of ^{3}He. The polarization of the water cell is small and an average of hundreds of runs are needed to observe it. The AFP measurement on the water cell takes place in a similar way as in the ^{3}He case. The relaxation time of protons in the water is $\sim$4 sec, and it is important to wait for water polarization to be re-established before ramping down. Figure 4.11 shows the holding field change with respect to time.

During the experiment at HIγS facility the calibration of the NMR-AFP signal using the water cell is not possible due to time limitations. Instead the NMR-AFP measurement is calibrated using the electron paramagnetic resonance technique which can give the absolute polarization of ^{3}He and it will be presented in the next section.

The DAQ system for the NMR-AFP measurement

In order to perform the NMR-AFP measurement, a function generator is needed to ramp the holding field of Helmholtz coils. While the holding field is ramped another function generator provides a sinusoidal RF field. When at resonance, the induced signal is picked up by a coil and fed to a lock-in amplifier locked at the frequency provided by the RF function generator. A PC dedicated for the DAQ and

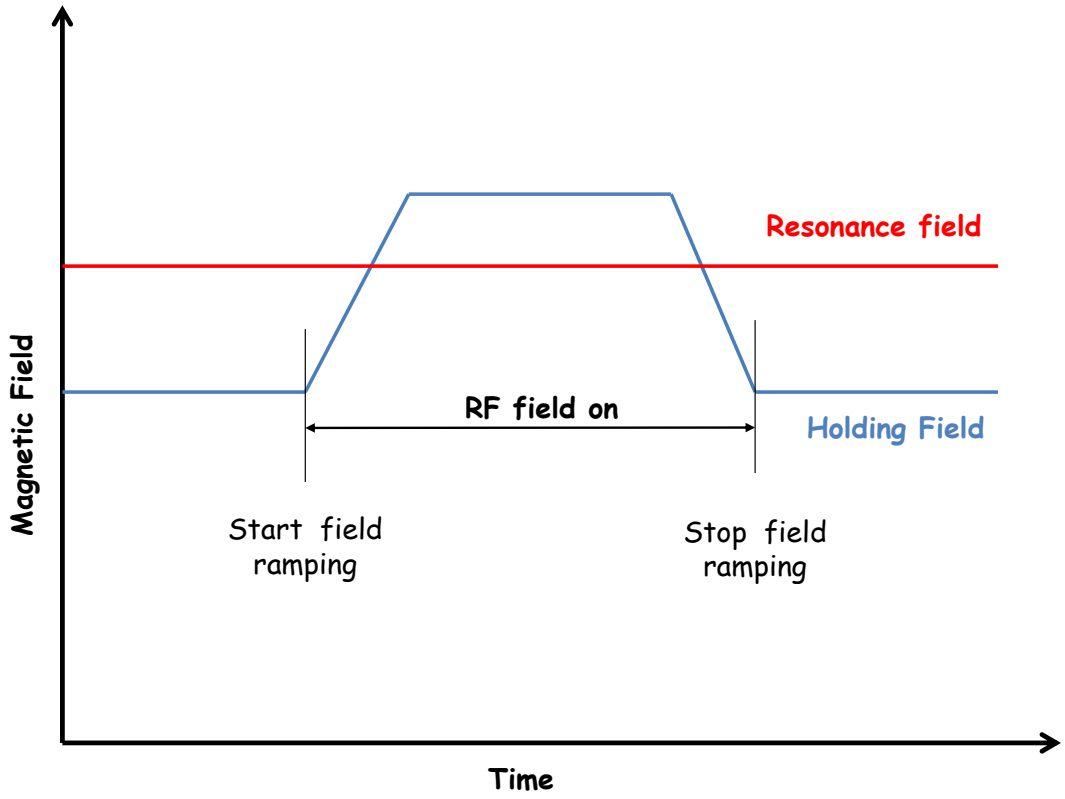

FIGURE 4.11: (Color online) The change of the holding field with respect to time. The holding field is ramped up and stays at a plateau before it is ramped down passing through two times from the resonance field.

the coordination of the measurement through GPIB is used to acquire the signal and display it through the commercial program Labview. Figure 4.12 shows a schematic of the electronics used for the NMR-AFP measurement.

4.5.2 Electron Paramagnetic Resonance (EPR)

The EPR technique is used to the calibrate the NMR-AFP measurement. This method is based on the frequency shift that the energy levels of alkali atoms experience due to the magnetic field of the polarized ^{3}He nuclei. During the SEOP the rubidium and potassium atoms experience a combination of magnetic fields. One is a strong holding field from the large set of Helmholtz coils, and the other is a smaller

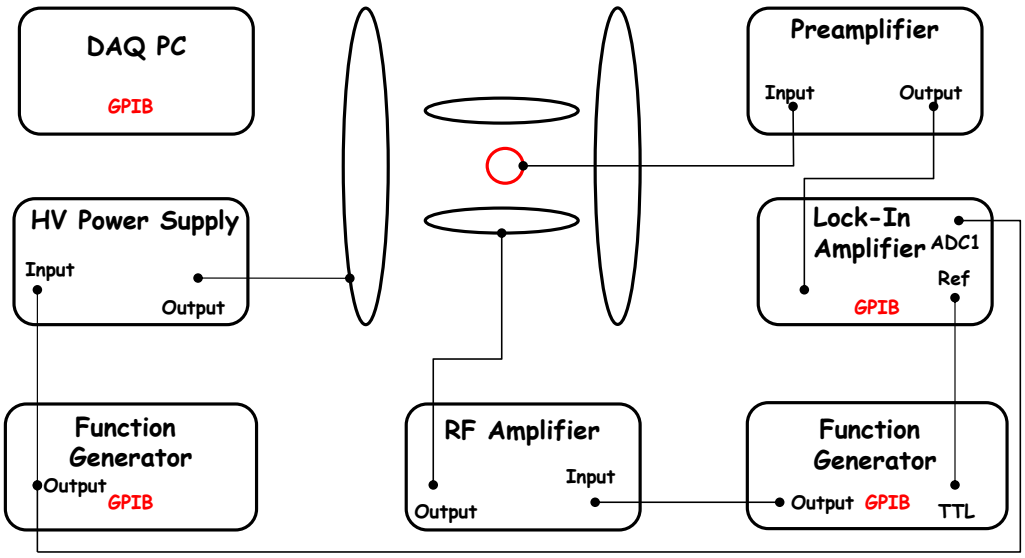

FIGURE 4.12: (Color online) The electronics circuit for the NMR-AFP signal processing.

magnetic field due to the polarized ^{3}He nuclei. The existence of the magnetic field lifts the hyperfine degeneracy of the energy levels and separates them into 2F+1 levels symbolized by m_F quantum numbers. Figure 4.13 shows the quantum levels of Rb atoms after removing the hyperfine degeneracy of rubidium levels. The measured shift caused by the polarized ^{3}He has two sources: a classical bulk magnetic field and a contact term due to the spin exchange interaction [Rom98]. The transitions between two Zeeman levels are used to determine the strength of the magnetic field and consequently the polarization of ^{3}He. The difference in the frequency of a Zeeman transition is measured between the polarization states in which the ^{3}He polarization is parallel and antiparallel to the magnetic holding field. The polarization of ^{3}He can

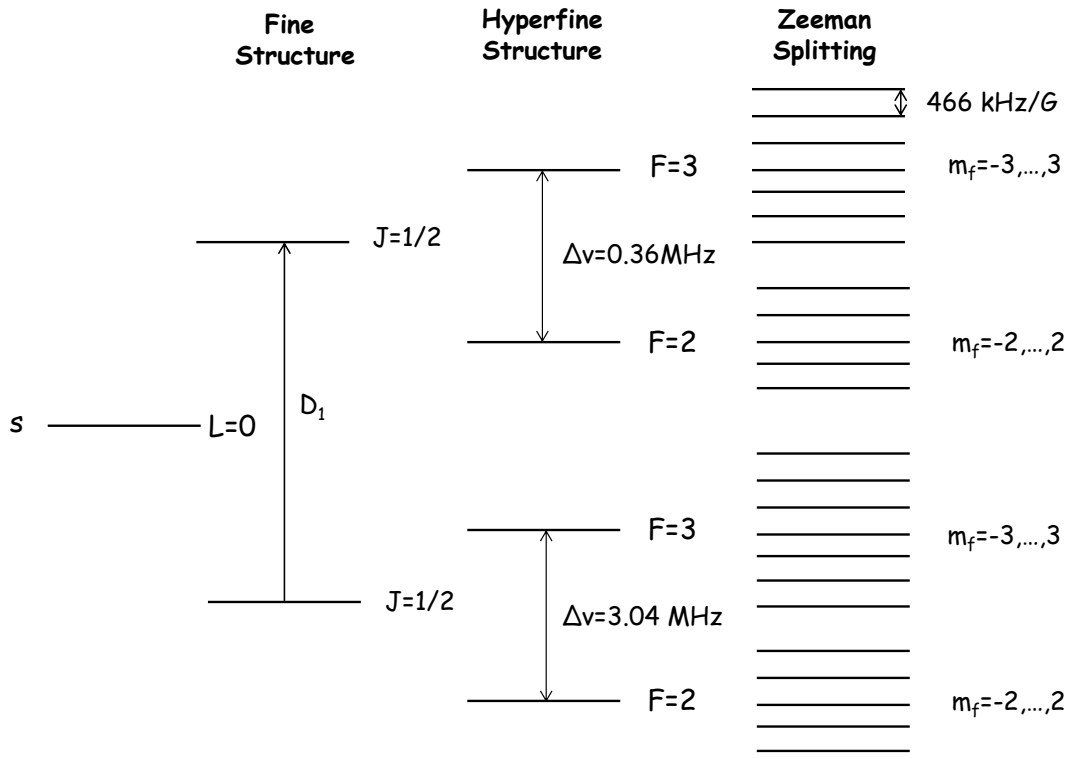

FIGURE 4.13: Fine structure, hyperfine structure and Zeeman splitting of atomic levels of Rb.

be determined by [Kra07, Rom98]

$$P_{pc} = \frac{2\Delta\nu_{EPR}}{2 \times \frac{2\mu_0}{3}\frac{d\nu_{EPR}}{dB}\kappa\mu_{^3He}n_{pc}} \tag{4.21}$$

where P_{pc} is the polarization of the pumping chamber, $\Delta\nu_{EPR}$ is the EPR frequency shift in kHz, $\frac{d\nu_{EPR}}{dB} = 0.47 + 7.38 \times 10^{-4}B$ (MHz) [Kor98] with B being the holding field magnitude, μ_0 is the permeability of vacuum, $\mu_{^3He}$ is the magnetic moment of ^{3}He, and n_{pc} is the number density of ^{3}He in the pumping chamber. The constant $\kappa = 4.52 + 0.00934T_{pc}$ [Rom98], where T_{pc} is the pumping chamber temperature. κ is related to the spin-exchange cross section and is independent of ^{3}He polarization.

Since all other parameters in Equation 4.21 are known, the only quantity be

determined experimentally is the EPR frequency shift, $\Delta\nu_{EPR}$. In order to determine this quantity, we need to find the frequency that the transitions between the Zeeman levels takes place. For the experiments performed in the laboratory both right and left handed circularly polarized laser light was to optically pump Rb. The right-handed polarized light causes transitions which occur from $F \rightarrow F+1$ and $m_F \rightarrow m_F+1$. This forces all polarized Rb atoms at equilibrium to be in the m_F=+3 state, from which they cannot absorb D_1 light. The left-handed polarized light causes transitions from $F \rightarrow F+1$ and $m_F \rightarrow m_F-1$, and at equilibrium all Rb atoms will end at m_F=-3 state. If an RF frequency provided by a coil close to the pumping chamber of the ^{3}He and resonant with these transitions is applied, the Rb atoms will decay. The Rb atoms are re-polarized and the intensity of the laser light passing through the pumping chamber is reduced. The frequency between m_F levels can be identified by a dip in D_1 intensity monitored by a photodiode positioned at the back of the oven behind the pumping chamber.

To identify the RF frequency, a sweep takes place over the possible frequencies of the transitions between the m_F levels. This sweep starts below the frequency determined by the product of the difference between the Zeeman levels (equal to 466kHz/G) with the magnetic field $\sim$20 G and extend beyond that. A typical frequency modulated (FM) sweep can be seen in Figure 4.14.

The observed lineshape of the FM-sweep is the derivative of the Lorentzian-like profile of the intensity of the laser light recorded by the photodiode plotted against the scanned frequencies as it is shown in Ref. [Sin10].

After the identification of the frequency at which the transitions between m_F levels take place commonly referred to as EPR frequency, the EPR measurement can be performed. The goal of the EPR measurement is to isolate the frequency shift at Zeeman levels due to the magnetic field produced by the polarized ^{3}He. To quantify this effect and in parallel remove all other effects due to other magnetic

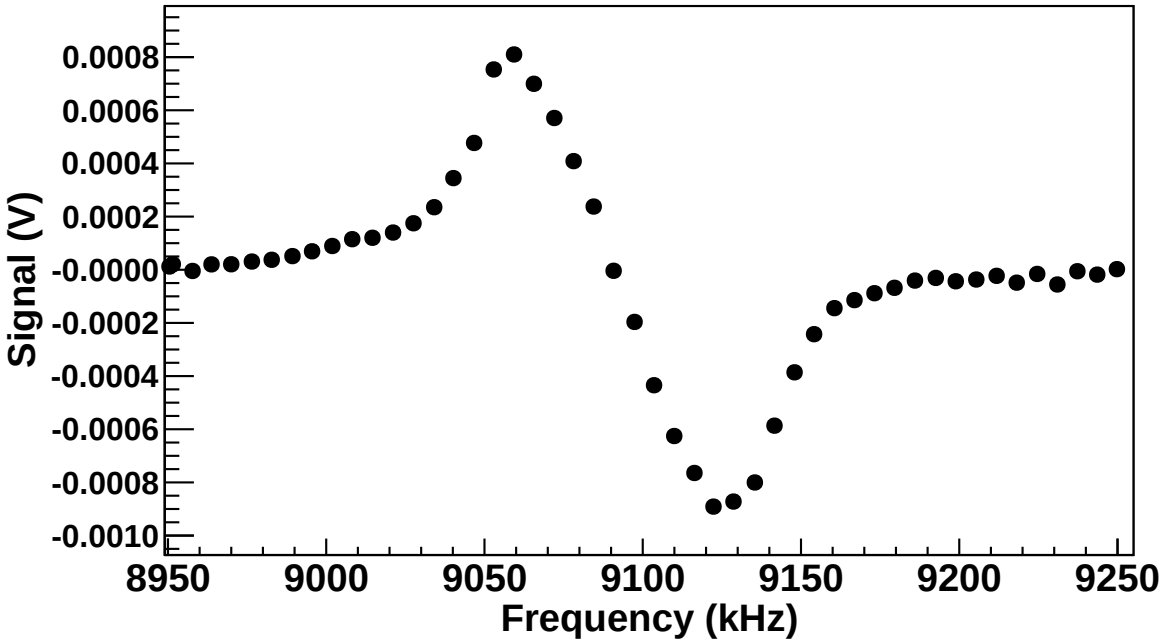

FIGURE 4.14: A typical FM sweep measurement.

fields, an AFP measurement is performed. In this AFP measurement instead of sweeping the holding field, we sweep the AFP-RF field up and down in frequency while the holding field remains constant. During the measurement, EPR frequency measurements are taken by forcing transitions between the Zeeman levels as described above. After that a sweep of the RF-AFP is performed automatically and the spin of the ^{3}He is flipped together with its magnetic field. A new EPR frequency shifted by an amount proportional to the polarization of ^{3}He is observed. A sweep down is performed again flipping the ^{3}He spin to its original direction. The average of the two differences between the EPR frequencies before and after the spin is equal to $\Delta\nu_{EPR}$. Figure 4.15 shows a typical EPR measurement.

Polarization gradient

The NMR-AFP and EPR measurements are performed at the pumping chamber while the HIγS beam is incident on the target chamber. The relation between the

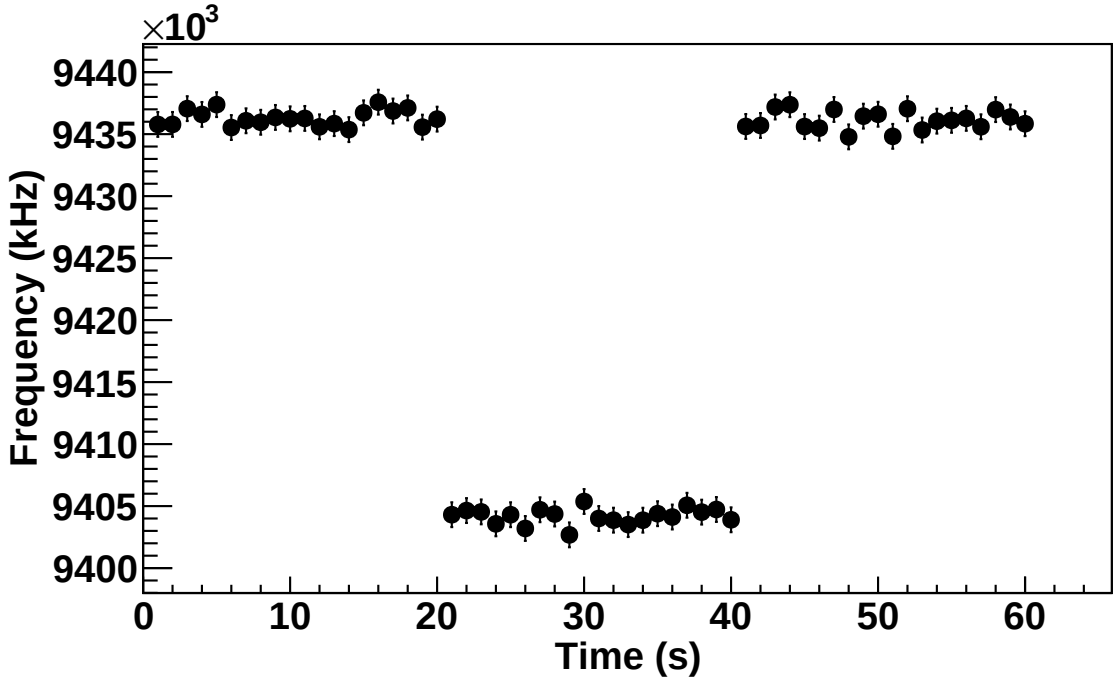

FIGURE 4.15: A typical EPR measurement performed at Rb D_1.

measured polarization of ^{3}He in the pumping chamber, P_{pc} and the polarization of the target chamber, P_{tc}, is given in Appendix B.2 as $P_{tc} = P_{pc} \times \frac{d_{tc}}{d_{tc}+\Gamma_{tc}}$ where d_{tc} is the diffusion rate from the target chamber to the pumping chamber and Γ_{tc} is the relaxation rate of ^{3}He in the target chamber. Both diffusion and relaxation rates are measured and typical values can be seen in Figures 4.16 and 4.10. P_{tc} is found to be $\sim$1.5% less than P_{pc}.

The DAQ system for the FM-sweep and EPR measurements

In this section, we describe the DAQ system used to perform the FM-sweep and EPR measurements. An RF field provided by a function generator is applied to the ^{3}He cell through an EPR coil forcing transitions between the Zeeman levels. The RF field is modulated by a function generator providing a frequency of 200 kHz. The same modulation frequency is used as a reference frequency to a lock-in amplifier. The input signal to the lock-in amplifier is the intensity of the laser light recorded by a

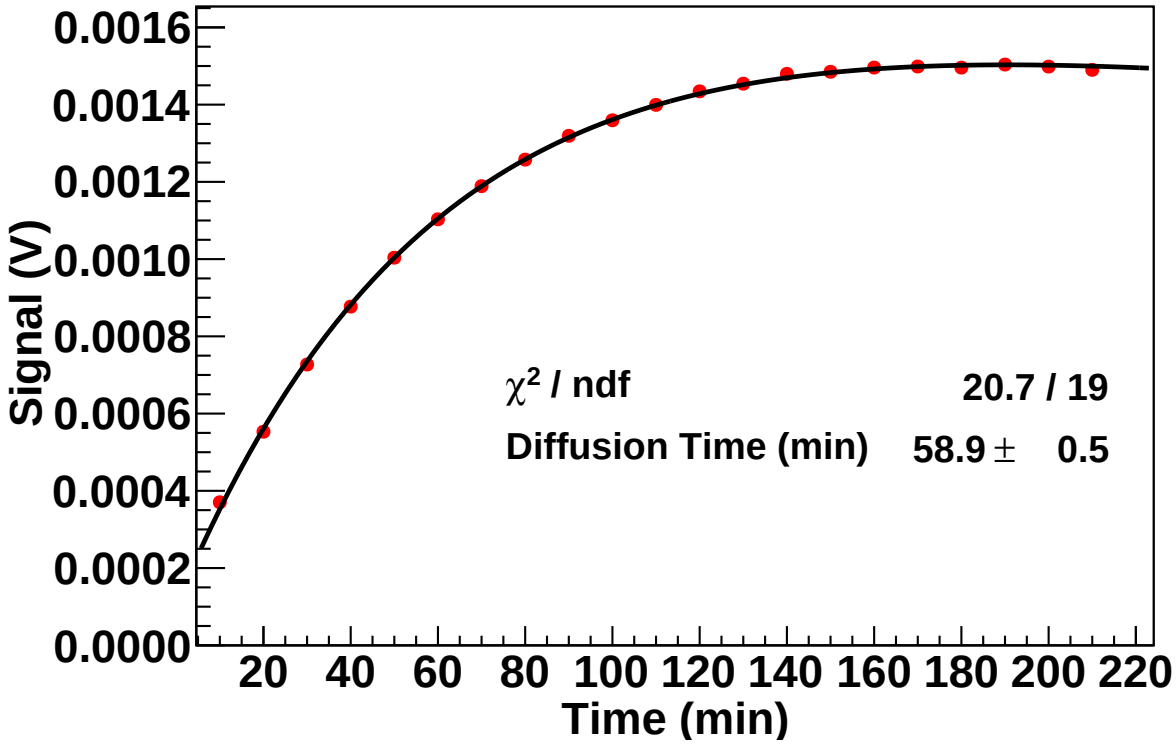

FIGURE 4.16: (Color online) The diffusion time as it is measured for ^{3}He cell "SPOT".

photodiode positioned at the back of the pumping chamber of the ^{3}He cell. The RF field is swept over a range of frequencies passing over the frequency that the Zeeman transitions take place. A PC dedicated for the DAQ with GPIB interface is used to acquire the signal from the lock-in amplifier using Labview. The electronics circuit for the FM-sweep measurement can be seen in Figure 4.17.

The DAQ system used for the EPR measurement is similar to the one used for the FM-sweep. Initially an RF field provided by a function generator and modulated at the frequency of 200 kHz forces transitions between the Zeeman levels. Another RF field is used to perform an AFP by sweeping up and down the frequency of the RF field instead of the holding field. The intensity of the light after the pumping chamber is recorded by a photodiode and its signal is the input to a lock-in amplifier locked

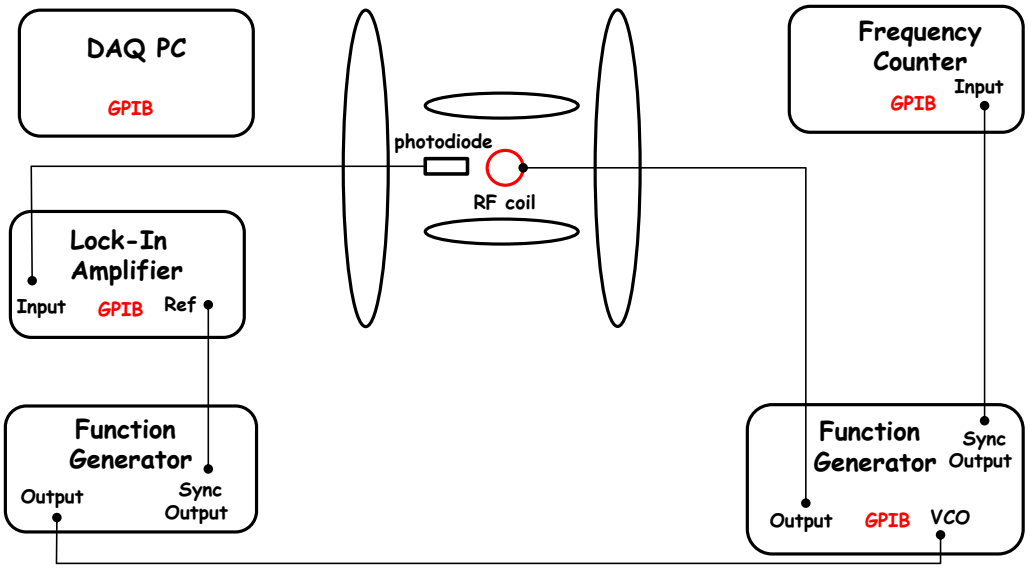

FIGURE 4.17: (Color online) The electronics circuit for the FM sweep measurement.

at the modulation frequency. A proportional integral (PI) feedback circuit is used to help the amplifier locking-in at the correct frequency. This PI circuit compares the input modulation frequency with the frequency recorded by the lock-in amplifier and adjusts the output frequency accordingly. The output of the PI box is the input to the voltage-controlled oscillator (VCO) of the function generator. The same PC dedicated for the DAQ of the FM-sweep measurement is used for the acquisition of the signal from the lock-in amplifier. Figure 4.18 gives an overview of the electronics circuit used for the EPR measurement.

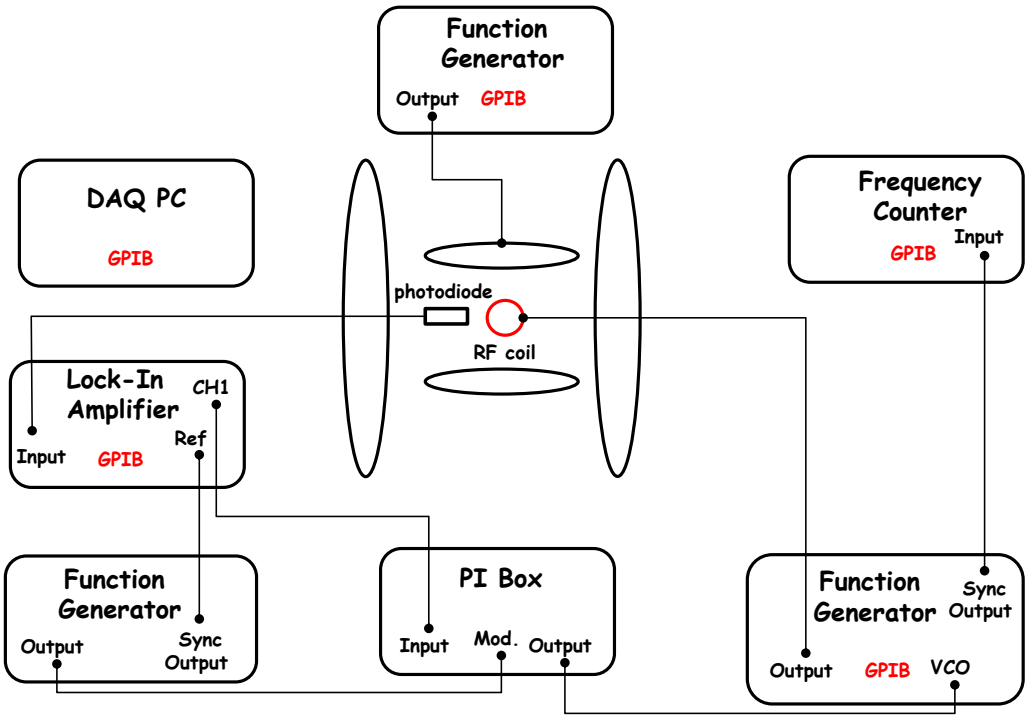

FIGURE 4.18: (Color online) The electronics circuit for the EPR measurement.

4.6 The Spin-Flipping System

In order to probe spin-dependent quantities such as cross sections and asymmetries, it is necessary to flip either the spin of the target or the helicity of the beam. The flip of the beam helicity is time consuming and it took place only one time during the three-body photodisintegration experiments at 12.8 and 14.7 MeV. Instead the spin of the target was flipped every 15 min and this time interval was found to be sufficient to reduce systematic uncertainties due to target polarization and detector drift to a negligible level.

A set of coils is used in combination with the Helmholtz coils to flip the spin of the ^{3}He target. The coil system used for the spin-flip is coaxial to the RF-coils

employed for the performance of the NMR-AFP and EPR polarimetry measurements and it shares the same support structure with them. These coils are able to provide a magnetic field on the order of few Gauss which is perpendicular to the holding field provided by the Helmholtz coils. In order to perform the spin-flip an automated system controlled by the DAQ PC reduces gradually the magnitude of the holding field while it increases the perpendicular field. The concurrent adiabatic change of both fields forces the spins of the polarized ^{3}He nuclei to follow the effective magnetic field. Once the effective field is perpendicular to the original direction of the holding field, an inversed current is provided to the Helmholtz coils which generates a holding field in the opposite direction. A slow increase of the magnitude of the holding field and a concurrent decrease of the perpendicular field forces the spin of the ^{3}He target to flip.

To identify the spin state of the ^{3}He target, a free induction decay (FID) measurement is performed. The FID measurement is using a small coil placed below the target chamber of the ^{3}He cell. An RF pulse tuned at the Larmor frequency of ^{3}He is used to force a small portion of the polarized ^{3}He nuclei inside the target chamber to precess. The decaying signal from the precession of the ^{3}He nuclei is acquired and delivered by the same coil to a commercial DAQ card. An automated Fourier transform of the signal with respect to time gives the actual Larmor frequency of the decay. This frequency is sensitive only to the effective local field at the position of the coil. The FID measurement took place right before and after the spin-flip and was able to provide an indication that a spin-flip was performed. The DAQ system used to perform the spin-flip and the FID measurements can be seen in Figure 4.19.

4.7 Target Thickness Measurement

The ^{3}He cell was filled in February of 2010 and the filling density was found to be 6.48$\pm$0.1 amg. The first three-body experiments on ^{3}He took place a few months

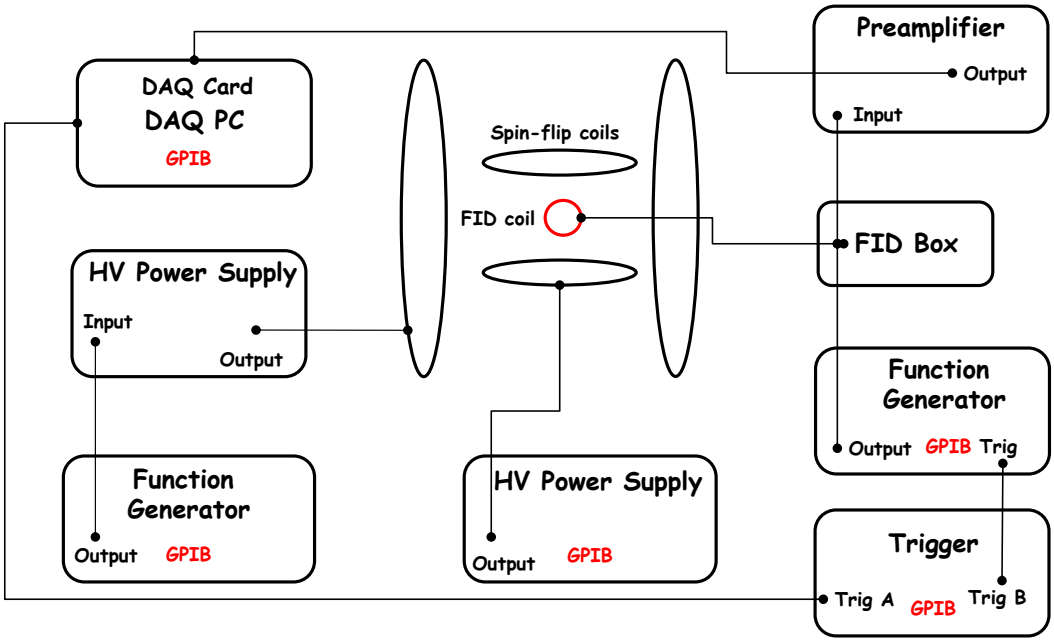

FIGURE 4.19: (Color online) The electronics circuit for the FID measurement.

after that in 2011 and the density at the time was considered to be equal to the filling density. A second set of measurements on the two- and three-body photodisintegration experiment took place in 2014 almost three-years after the construction of the ^{3}He cell and the density of the cell is measured anew. The density of the cell is measured using the technique described in Refs. [Klu12, Klu13, Rom97]. This technique is based on the broadening of the width of the D_1 and D_2 transitions of Rb and K due to ^{3}He and N_2 gas inside the cell. The apparatus located at the College of William and Mary and used for the performance of this measurement can be seen in Figure 4.20.

A Ti:sapphire laser with tunable wavelength is used to scan through the frequencies of e.g D_1 transition of K. The ^{3}He cell is heated to a temperature above $\sim$100°

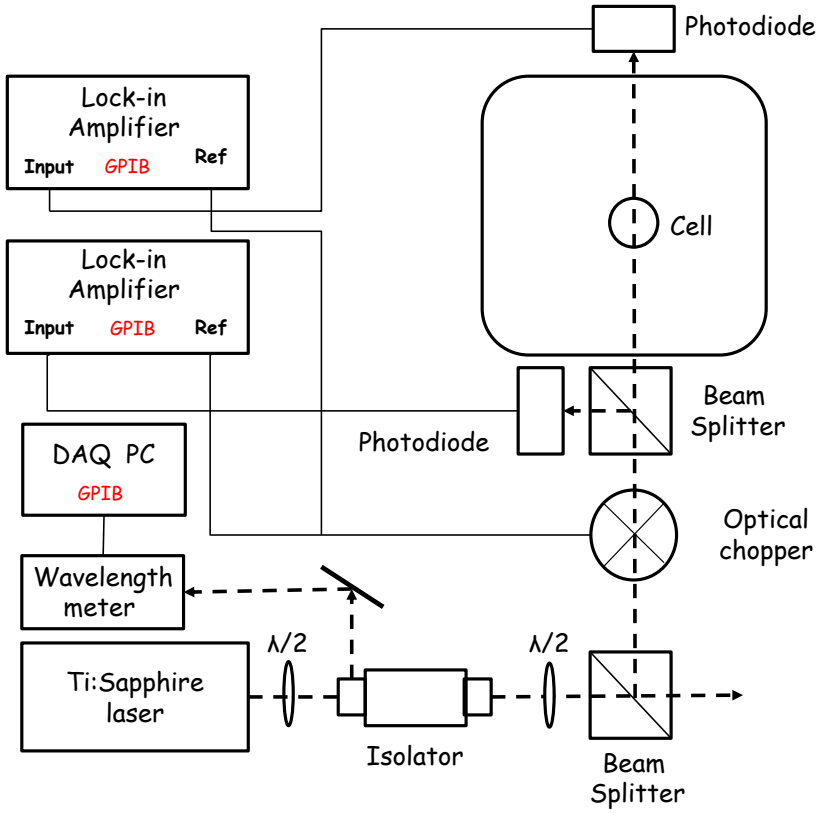

FIGURE 4.20: (Color online) Schematic of the electronics circuit used for pressure broadening measurement. Solid lines indicate the connections between electronics; dashed lines represent the laser path.

where enough alkali vapor is available to perform the measurement. The laser beam is incident on the ^{3}He cell and the laser light is partly absorbed by the alkali transitions. The intensity of the laser light is measured right before and after the cell and the ratio of the two intensities with respect to the laser frequency is used to extract the density of ^{3}He. Figure 4.21 shows a pressure broadening measurement taken at the D_1 transition of potassium.

The signal was fitted using the formula [Klu12, Klu13, Rom97]:

$$y(\nu) = \frac{A[1 + 0.6642 \times 2\pi(\nu - \nu_c)t_d]}{(\nu - \nu_c)^2 + (\frac{\gamma}{2})^2} + y_0 \tag{4.22}$$

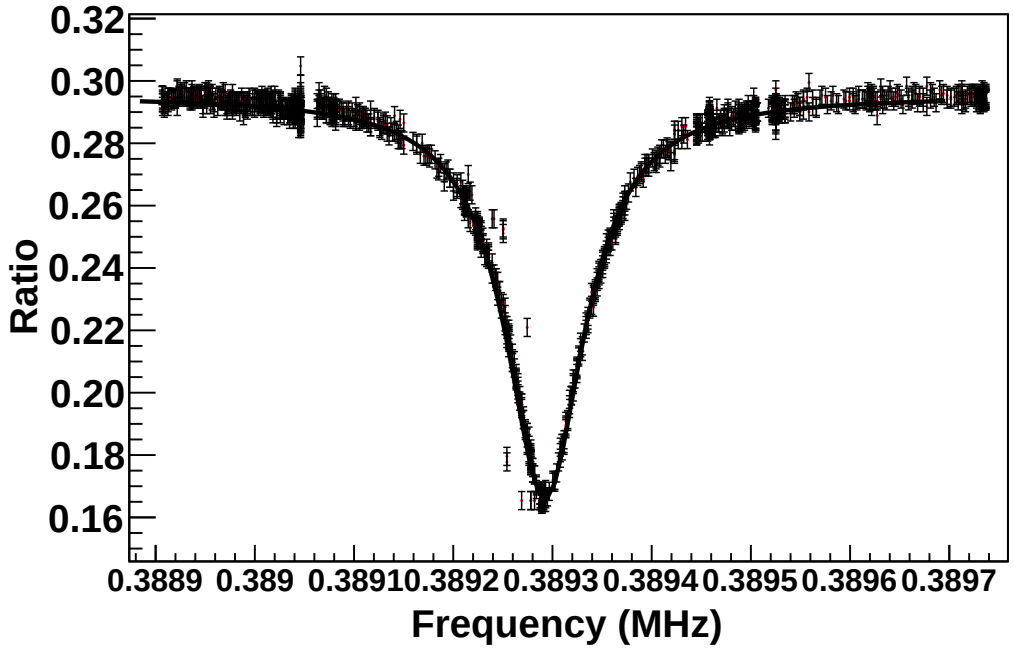

FIGURE 4.21: (Color online) The thickness measurement performed at the K D_1 transition fitted using the Equation 4.22.

where A is an overall normalization constant, t_d is the time between two collisions for an alkali atom, $\nu_c = \nu + \delta$ is the resonant frequency, y_0 is the transmitted to incident intensity ratio in the absence of absorption and γ is the width of the broadening. δ is the shift of any transition from the resonance. The goal of the fit is to extract the width γ. This width is related to the number densities of $[^3He]$ and $[N_2]$ gases in amagats by the equation:

$$\gamma([^3He],[N_2],T) = \alpha[^3He](\frac{T}{T_0})^n + \beta + \alpha^{'}[N_2](\frac{T}{T_0})^{n^{'}} + \beta^{'} \tag{4.23}$$

where T_0=353 K. α, β, n and $\alpha^{'}$, $\beta^{'}$, $n^{'}$ are constants for ^{3}He and N_2 gases measured in Refs. [Klu12, Klu13, Rom97]. The density of the ^{3}He cell "SPOT" is measured using all four D_1 and D_2 transitions of Rb and K and the weighted average was found to be 6.4±0.2 amg.

5

Data Reduction and Analysis

5.1 Introduction

The objective of the data analysis of the two- and three-body photodisintegration experiments is to extract the spin dependent differential and total cross sections. As described in chapter 3, the data were collected and stored using CODA and analyzed using the ROOT framework. In the three-body photodisintegration case, the ADC corresponding to pulse height (PH), the TDC corresponding to time of flight (TOF), and the TAC value corresponding to pulse-shape discrimination (PSD) were recorded for each event. The ADC value corresponding to proton energy (E_p) and the TDC to extract the TOF for protons were recorded during the two-body experiment. In the next sections, we will describe the techniques used to calibrate the electronic signals and convert them into meaningful physical quantities.

5.2 Calibrations of Neutron Detectors

5.2.1 ADC Calibration

The calibration of the ADC to PH in units of MeV_{ee} was carried out for each neutron detector. The reasons for PH calibration are the following: (i) the calibration places all detectors on the same absolute scale; (ii) it takes care of any gain differences between the detectors and allows a common PH threshold in the analysis; (iii) the common threshold ensures the same neutron detection efficiency as a function of the neutron energy.

A ^{137}Cs source emitting monoenergetic γ-rays of 662 keV was employed to calibrate the PH. The source was used for the calibration of the neutron detectors, both the primary detector array and the beam intensity monitor. The calibrations were performed at the beginning and the end of the working day and the interpolation between these runs is used for the PH calibration. A typical response of a neutron detector to ^{137}Cs source can be seen in Figure 5.1.

The γ-rays interact with the organic liquid scintillator primarily through the Compton scattering process producing recoiling electrons inside the scintillator volume. The majority of the events interact with the liquid scintillator through a single Compton scattering while the multiple Compton scattering is not negligible. The maximum energy, E_R, of an electron recoiled by a γ-ray of Eγ=662 keV is given by

$$E_R = \frac{2E_\gamma^2}{2E_\gamma + m_e} \tag{5.1}$$

Figure 5.2 shows the response (red curve) of a neutron detector based on GEANT4 simulation to a point-like γ-ray source. The location of the cesium edge depends on the scintillator volume and detector resolution. The neutron detector consist of a large volume scintillator cell that allows for multiple scattering events. These events

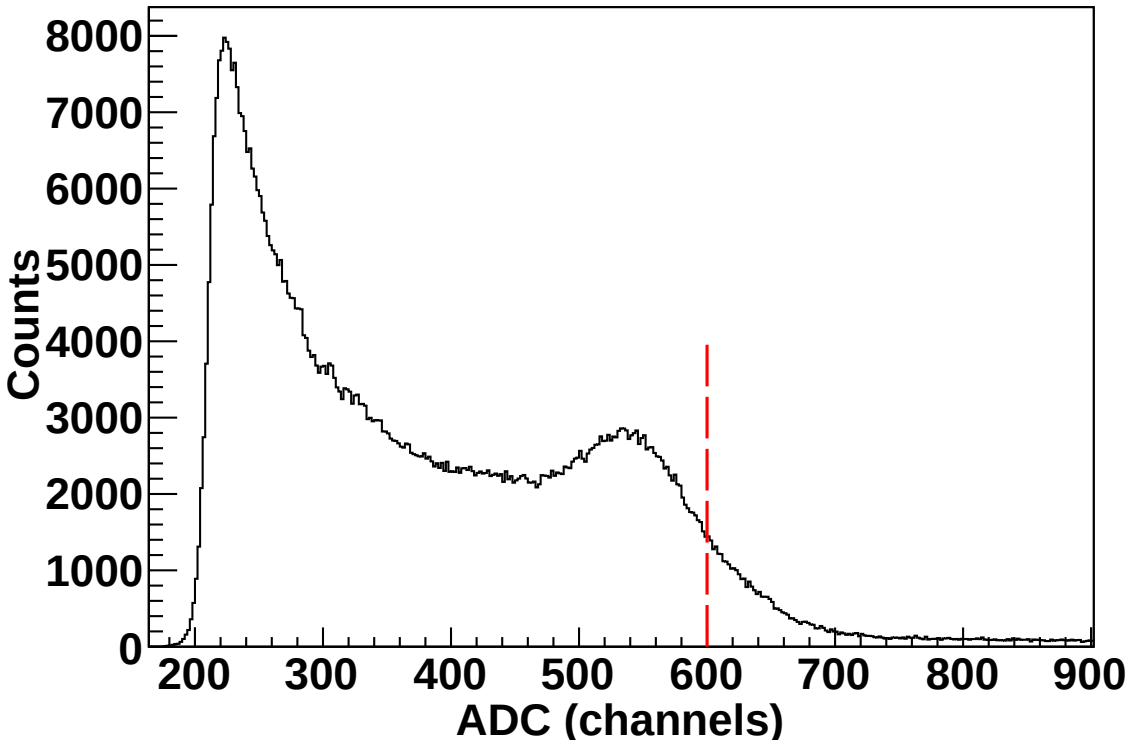

FIGURE 5.1: (Color online) The response of a neutron detector to a point-like ^{137}Cs source. The red dashed-line points to the cesium edge.

can produce pulses with greater heights than those expected by the kinematics as it can be seen in the figure (red curve). The light output is smeared based on the following formula:

$$\Delta L_s = \Delta L + G(\sigma_1)\sqrt{\Delta L} + G(\sigma_2) \tag{5.2}$$

where ΔL is the total light output and $G(\sigma)$ is a Gaussian distribution with centroid μ=0 and standard deviation σ. The term $G(\sigma_2)$ takes into account any potential noise in the detector and electronics whereas $G(\sigma_1)\sqrt{\Delta L}$ incorporates statistical fluctuations in light collection process. The σ_1 and σ_2 are determined for all detectors by matching the spectra taken with the ^{137}Cs source with the simulated response curve.

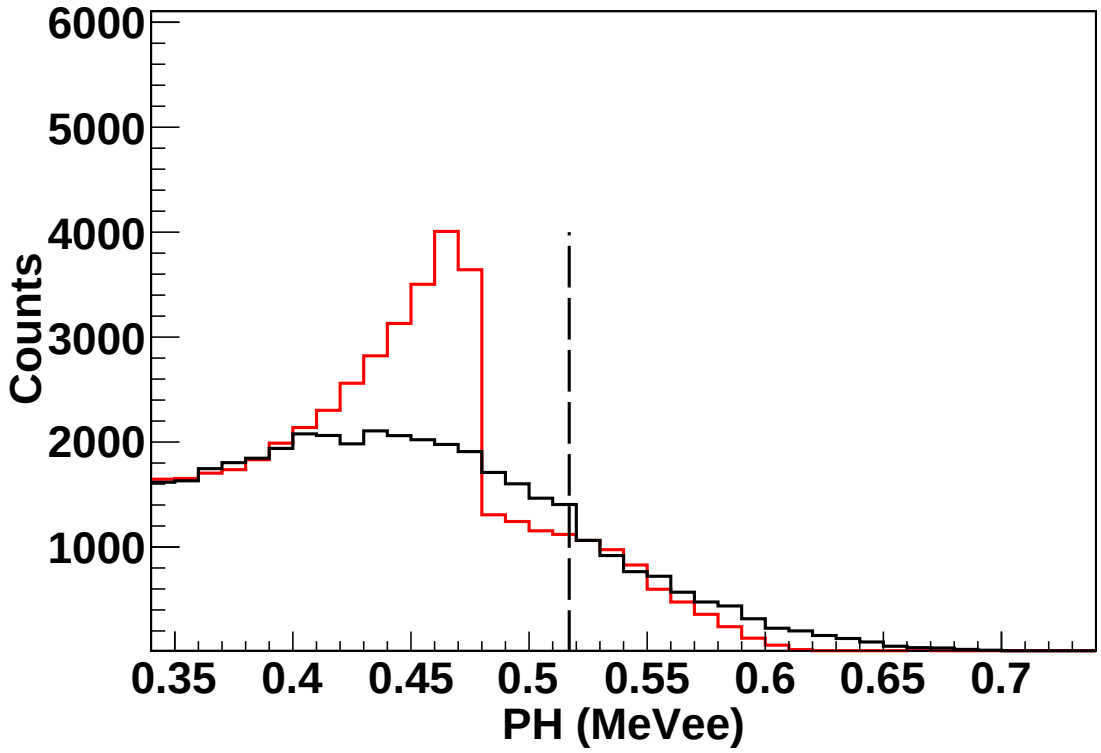

FIGURE 5.2: (Color online) The simulated response of the neutron detectors to a point-like ^{137}Cs source with (black curve) and without (red curve) smearing. The Compton and cesium edges are located at 0.478 MeV$_{ee}$ and 0.517 MeV$_{ee}$, respectively. The black-dashed line points to the cesium edge.

The black curve is the response of the detector smeared to match the experimental resolution.

The formula used for the conversion of ADC to PH is

$$PH = PH_{edge}\frac{ADC - PED}{ADC_{edge} - PED} \tag{5.3}$$

where PH_{edge}=0.517 MeV$_{ee}$ is the location of the cesium edge according to the simulation, ADC_{edge} is the ADC channel number of the cesium edge and PED is the channel location of the ADC pedastal. The pedastal is the ADC value when no input signal is present and does not correspond to the zero channel of the ADC. The

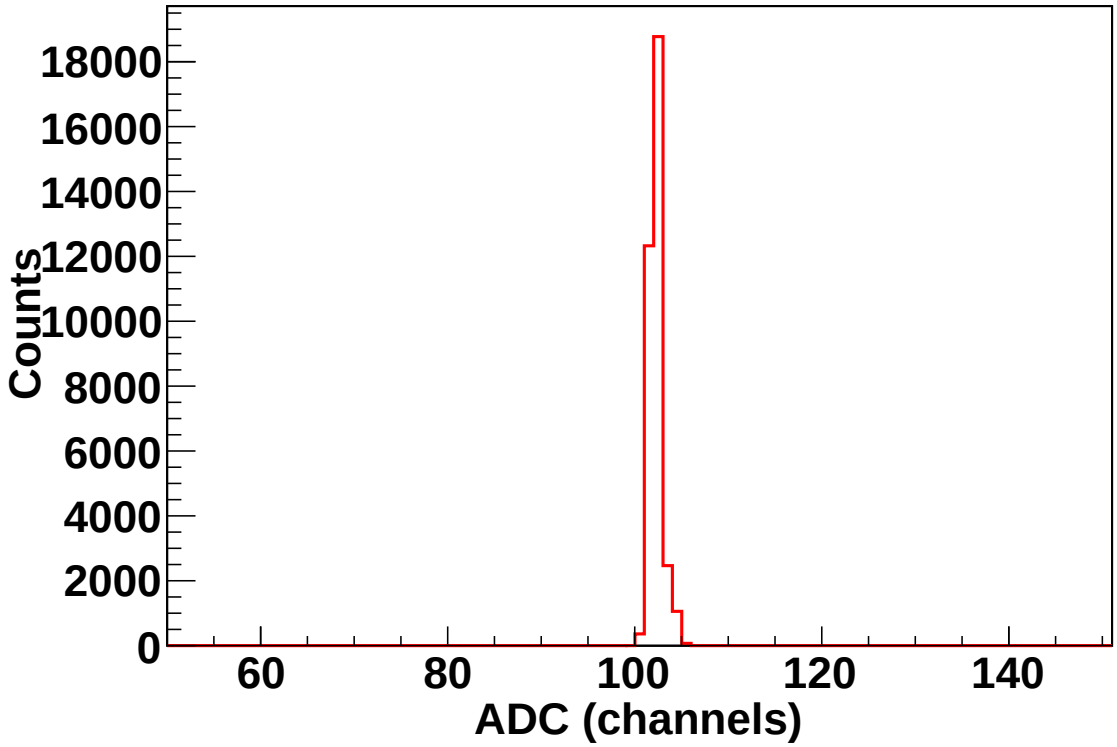

FIGURE 5.3: (Color online) A pedastal spectrum of a neutron detector.

pedastal value is determined for each and every neutron detector by taking designated pedastal runs. An example of a pedastal for one of the neutron detectors can be seen in Figure 5.3.

In order to determine the ADC_{edge}, the maximum of the sloping edge in Figure 5.1 is found and the cesium edge is defined to be the channel at which the half-maximum occurs. Figure 5.4 shows the calibrated spectra of a ^{137}Cs source in comparison to the simulated response of the detector after smearing.

Hardware thresholds were placed during the setup of the experiment. These thresholds were lower than the anticipated unique software threshold used in the offline analysis. The software threshold for the ^{3}He data is $\frac{5}{16}\times 0.517$ MeV$_{ee}$ while for the deuteron data is 1×0.517 MeV$_{ee}$.

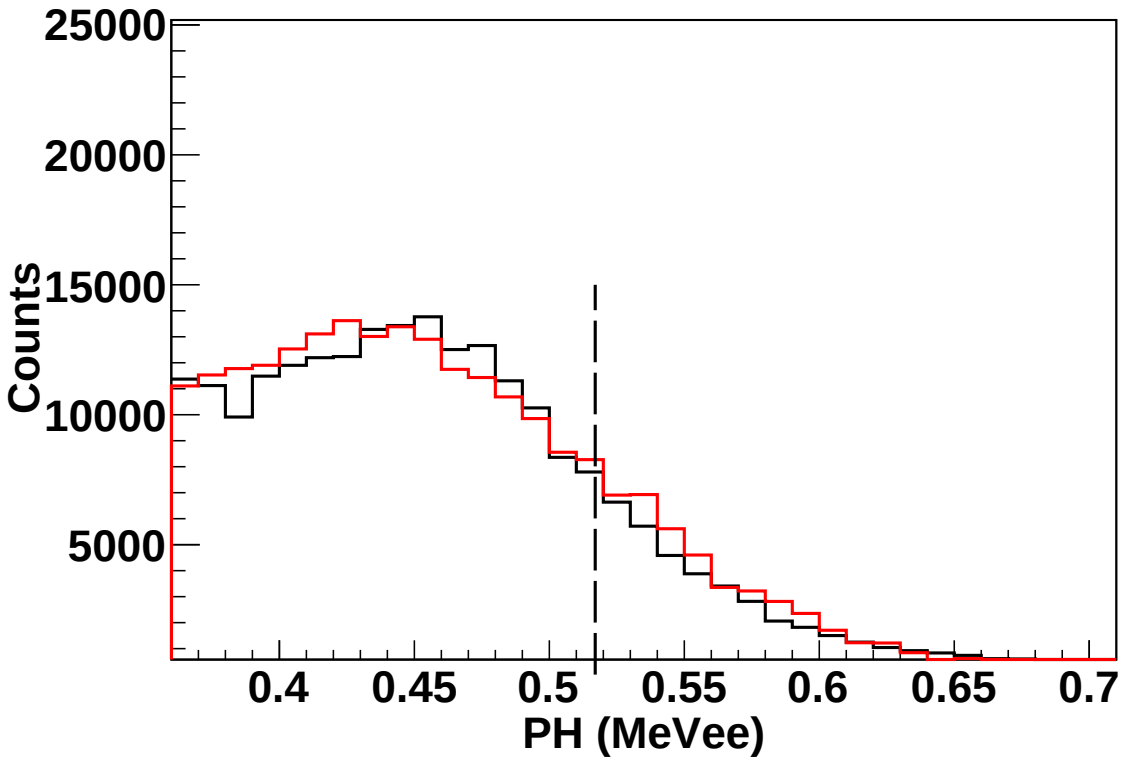

FIGURE 5.4: (Color online) Comparison between the calibrated spectra (black curve) and the simulated response (red curve) of a neutron detector for a point-like ^{137}Cs source. The black-dashed line indicates the cesium edge after calibration.

5.2.2 TDC Calibration

The TDC value recorded for each event is used to determine the TOF of a neutron from the target to the detector. The formula used for the TOF calibration is

$$TOF = TDC_{cal} * (TDC - TDC_{\gamma}) + d/c \tag{5.4}$$

where TDC_{cal} is the conversion factor of the TDC channels to nanoseconds, d is the distance from the center of the target to the detector and c the speed of light. The addition of the d/c factor is necessary in order to account for the fact that it takes d/c ns for a γ ray to travel from the center of the target to the detector.

There are two equivalent ways to find the TDC_{cal} factor. The first way is to

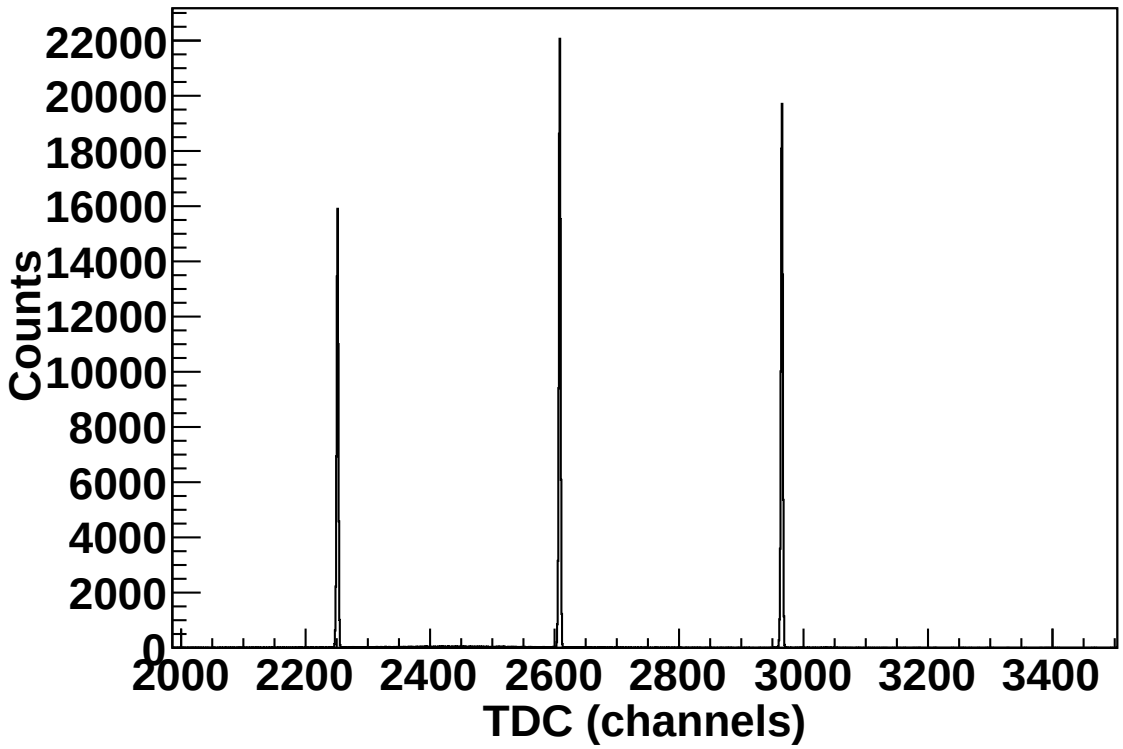

FIGURE 5.5: The self-timing peak of a neutron detector after adding two ∼16 ns delays.

determine the conversion factor with the use of lines with known delays. The delays of these lines are measured using an oscilloscope with a sub-nanosecond precision. A pulser is used to provide the common start for the TDC module. A copy of the same signal is delayed by a fixed amount and is used as the stop of the input channel of the TDC. Additional delay lines are added and the procedure is repeated. Figure 5.5 shows the self-timing peak of a neutron detector moving to lower channels after adding two consecutive delays of ∼16 ns. The ratio of the delays to the channel difference between the peaks is equal to the conversion factor TDC_{cal}.

Another way to find the TDC_{cal} factor for each detector is to use the TDC neutron spectra acquired from a D_2O target together with the results of a d(γ,n)p GEANT4 simulation. The conversion factor is given by

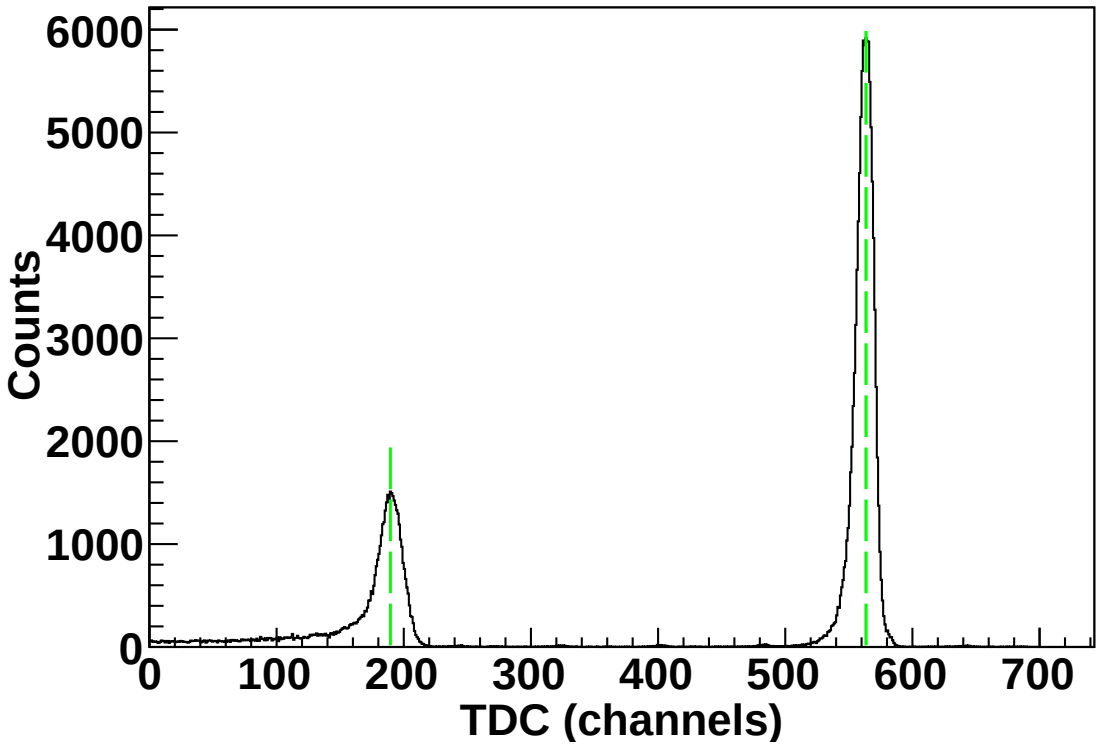

FIGURE 5.6: (Color online) The TDC spectra acquired with a a D_2O target. The dashed-lines point to the centroids of the γ-ray and neutron peaks.

$$TDC_{cal} = \frac{TOF_n - TOF_\gamma}{TDC_n - TDC_\gamma} \tag{5.5}$$

where TDC_n is the centroid value of the neutron peak at the TDC spectra and TOF_n (TOF_γ) is the simulated TOF that it takes for a neutron (γ-ray) to reach the detector. Figure 5.6 shows the TDC spectra acquired with a D_2O target. The γ-ray peak is dominant and can be seen on the right side of the histogram while the neutron peak is on the left. The dashed-lines point to the centroids of the peaks.

A thin aluminum rod placed at the center of the detector array is used to confirm the location of the γ-flash, TDC_γ, initially determined with the D_2O target. The Compton-scattered γ-rays produced a peak in the TDC spectra which can be seen

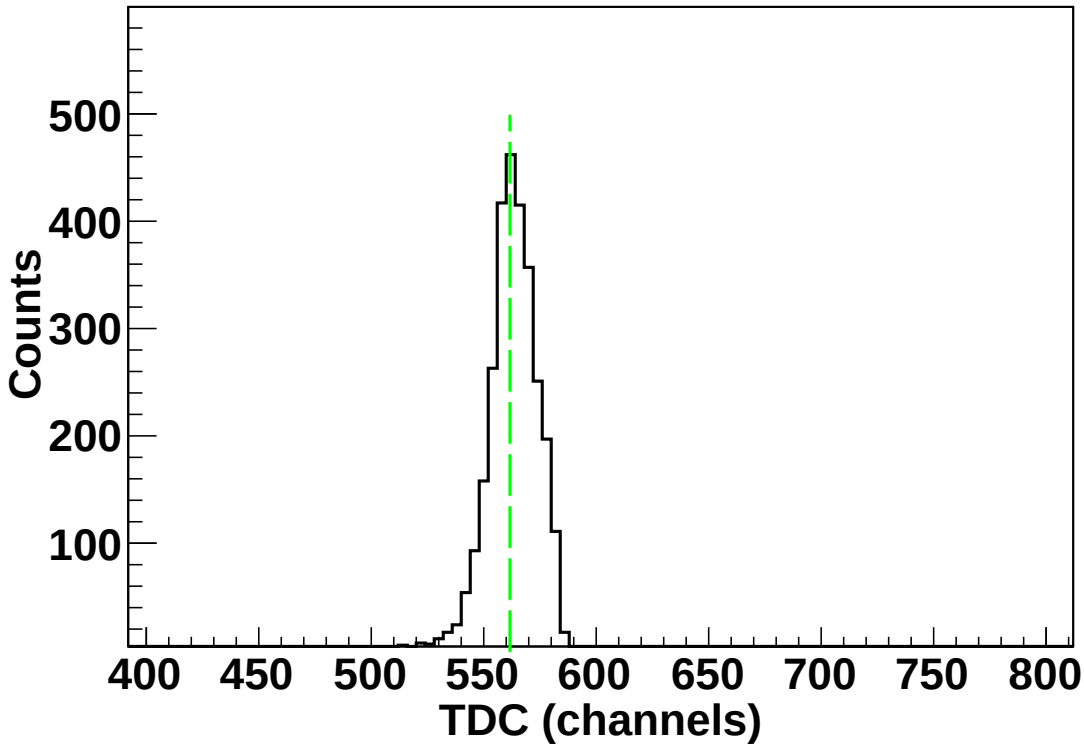

FIGURE 5.7: (Color online) The γ-flash peak resulting from the Compton-scattred γ-rays onto the thin aluminum rod placed at the center of the primary detector array.

in Figure 5.7. The channel location of the centroid of the peak is located at the same position as the γ-ray peak in Figure 5.6 and provides a zero point for the TDC calibration of each individual detector.

The calibrated TOF spectra acquired with the D_2O target are compared with the results of the GEANT4 simulation. This GEANT4 simulation generated neutrons following the expected distribution and kinematics of d(γ,n)p reaction. The simulated distribution is smeared using a Gaussian distribution to match the experimental resolution. Figure 5.8 shows the TOF neutron spectrum in comparison to the results of a GEANT4 simulation with and without smearing.

The extracted TOF for each event is used to reconstruct the outgoing neutron energy based on the Equation 5.6:

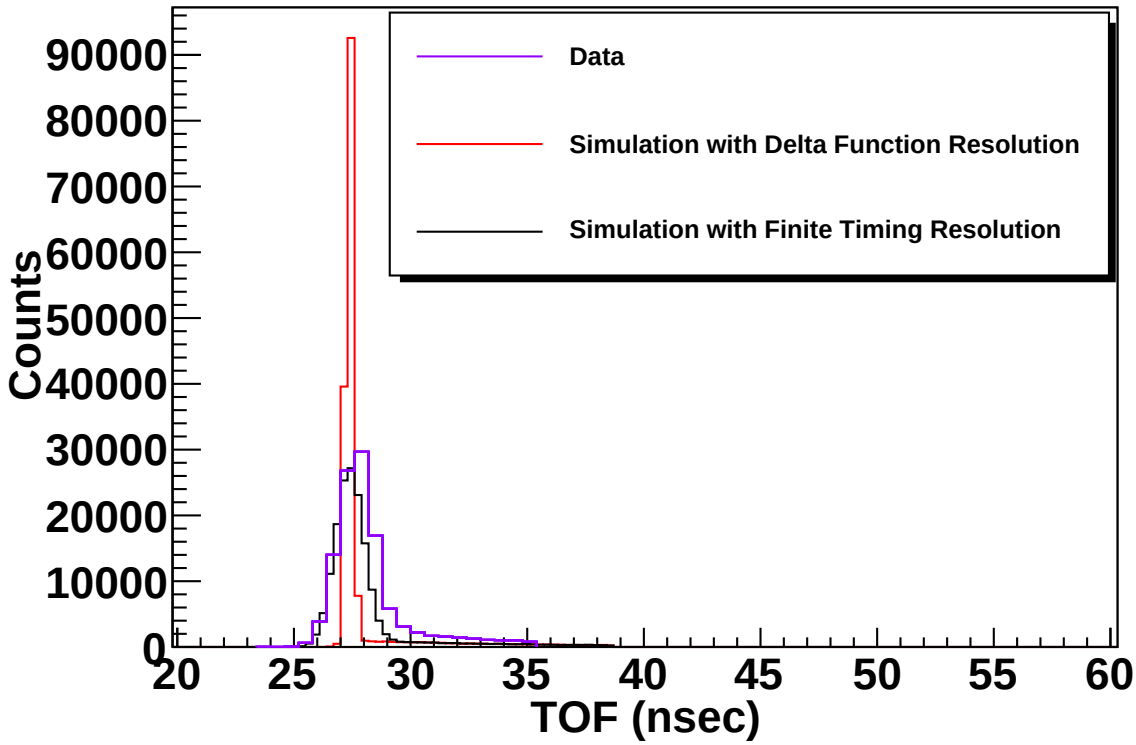

FIGURE 5.8: (Color online) The TOF neutron spectrum (purple curve) in comparison to the results of the GEANT4 simulation. The red line histogram is the result of the simulation using a delta function resolution. The black line histogram is the simulation with experimental timing resolution.

$$E_n(TOF) = \frac{m_n}{\sqrt{1-(\frac{d}{TOF*c})^2}} - m_n \tag{5.6}$$

with m_n being the neutron mass, assuming the neutrons originate from the center of the target. This technique allowed us to extract absolute differential cross sections distributions with respect to the outgoing neutron energy.

5.2.3 Pulse Shape Discrimination (PSD)

As described in chapter 3, the discrimination based on the pulse height of neutrons and γ-rays was accomplished with the use of the commercially available MPD-

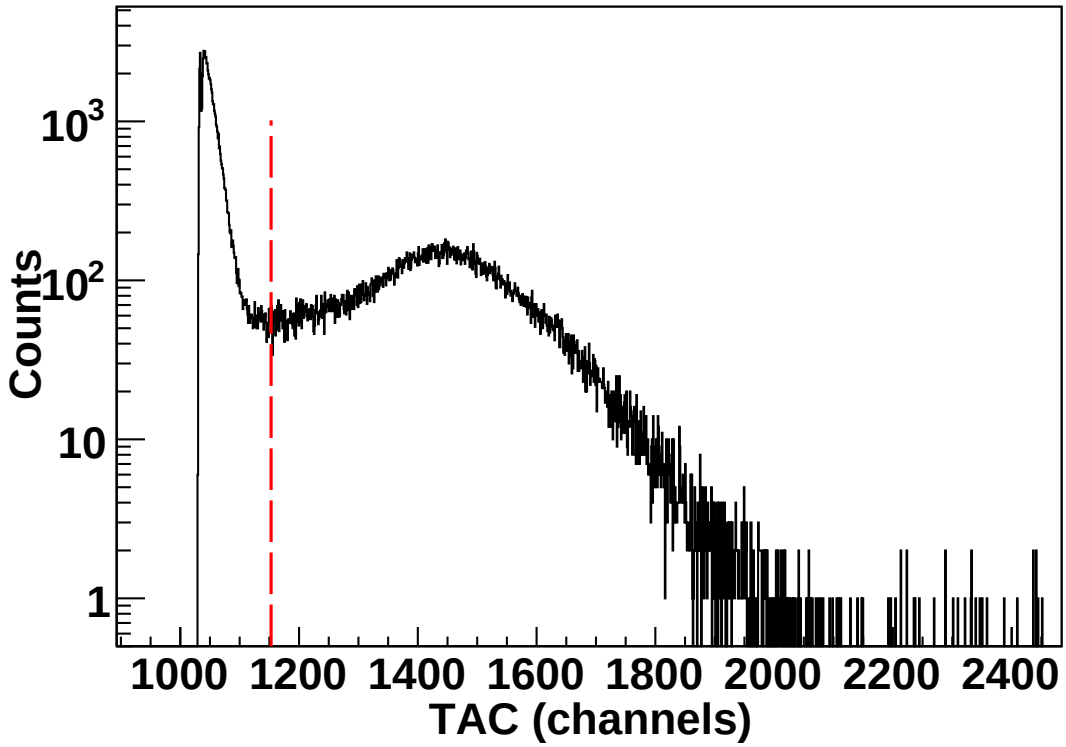

FIGURE 5.9: (Color online) A PSD spectrum in TAC channels. The hardware threshold can be seen around the channel 1000. The software threshold is indicated by the red-dashed line located around channel 1200. The γ-rays lay to the left of the software threshold while the neutron are to the right.

4 [mes08b] units. The amplitude of the TAC output of the unit indicates the PSD value and therefore the type of particle. Larger TAC values indicate neutrons while smaller values indicate γ-rays. The MPD-4 module has a hardware threshold that cut out most of the γ-rays. The gain of the output pulses is adjustable so that some γ-rays are above the threshold. This ensures that no neutrons are omitted due to the applied hardware threshold. The hardware threshold is initially defined by using an ^{241}Am/Be source emitting both neutrons and γ-rays. The TAC software cut applied offline is different for each detector. Figure 5.9 shows a PSD spectrum in TAC channels together with the hardware and software thresholds.

5.3 Calibrations of the Proton Detectors

5.3.1 TDC Calibration

The TDC value recorded for each event was used to determine the TOF of a proton from the target to a SSB detector. The conversion factor was determined with the use of lines with known delays. This method was identical to that which was described in the previous section.

5.3.2 ADC Calibration

The ADC calibration of the SSB detectors to proton energy, E_p, was performed with the use of an ^{241}Am source which emits alpha particles at the energies of 5.486 (85%) and 5.443 MeV (13%). The alpha particles have a short range in air $\sim$5 cm. For this reason, the calibration of the SSB detectors was performed offline after the experiment using the same electronics circuit described in Chapter 3. The formula used for the conversion of ADC to E_p is

$$E_p = E_\alpha \frac{ADC - PED}{ADC_\alpha - PED} \tag{5.7}$$

where E_α=5.486 MeV, ADC_α is the ADC channel number of the centroid of the alpha particles peak and PED is the pedastal value. A spectrum of the alpha source can be seen in Figure 5.10. The resolution of the detectors is found to be from 10-40 keV.

5.4 Analysis Cuts for Three-body Photodisintegration Experiment

The application of analysis cuts is necessary for the identification of the neutrons events and the rejection of the γ-rays. A combination of one dimensional and two dimensional cuts which utilized the correlations between the PH, PSD and TOF parameters is employed for the effective isolation of the neutron signal and the cal-

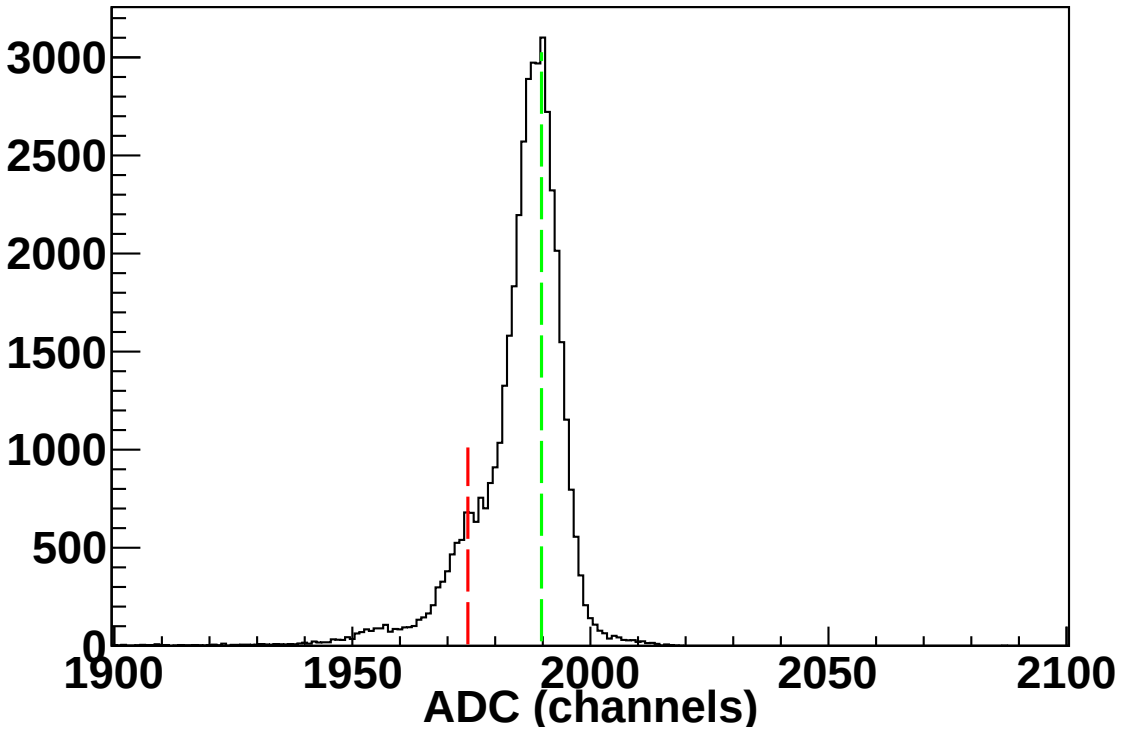

FIGURE 5.10: (Color online) The response of a SSB detector to the alpha source ^{241}Am. The green-dashed line is located at the centroid of the dominant alpha peak. The dashed-red line points to the location of the secondary alpha peak. The centroid value of the dominant peak corresponds to 5.486 MeV while pedastal corresponds to zero energy.

culation of the neutron yields for both ^{3}He and N_2 reference cells. In the next sections, we will describe the cuts used in the three-body photodisintegration analysis.

5.4.1 Self-timing Cut

As described in chapter 3 the common start and individual stop configuration of the TDC produces the so called self-timing peak for each neutron detector. The raw TDC spectrum can be seen in Figure 5.11. The spectrum contains a very narrow peak which represents a constant delay. A cut is placed around the self-timing peak to reject all events where the given neutron detector did not trigger.

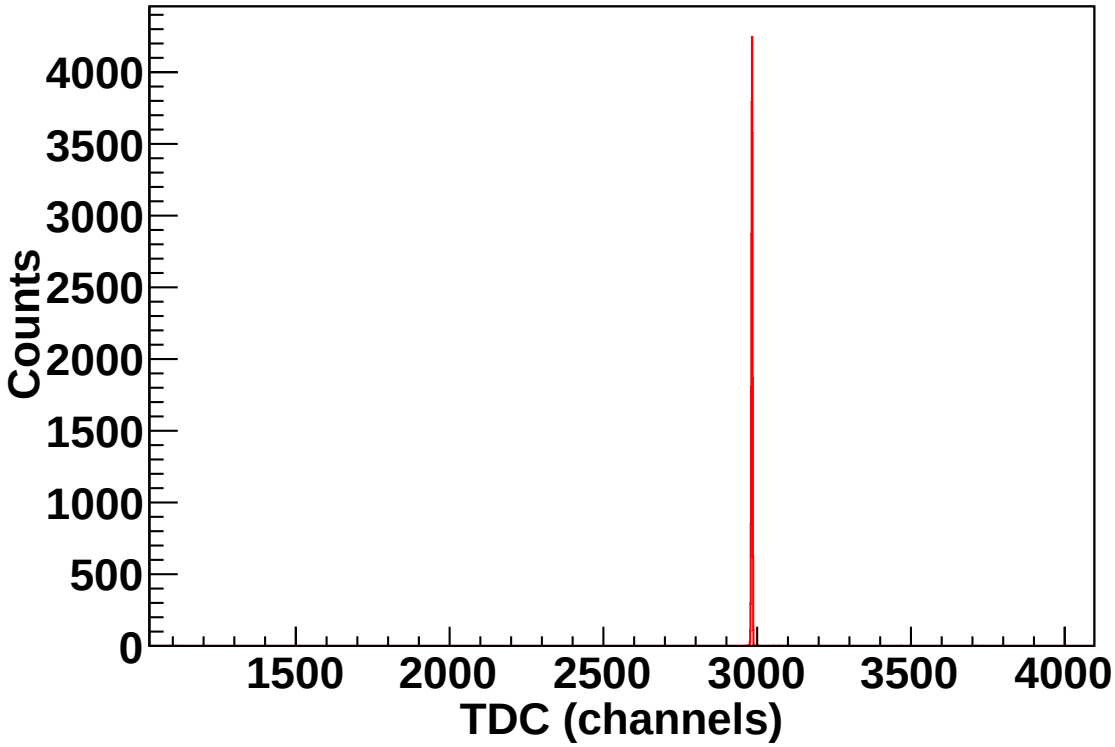

FIGURE 5.11: (Color online) A spectrum of the raw TDC of a neutron detector.

5.4.2 Pulse Height Cut

As described in the previous section hardware thresholds were set at all detectors using the internal CFD of the MPD-4 module. The hardware thresholds are different due to gain differences between the detectors. The acquired ADC spectra were calibrated and a higher software threshold was used in the offline analysis to determine a common intrinsic efficiency for all neutron detectors. The software threshold used in the offline analysis is $\frac{5}{16}\times 0.517$ MeV$_{ee}$ and 1×0.517 MeV$_{ee}$ for the ^{3}He and deuteron data, respectively.

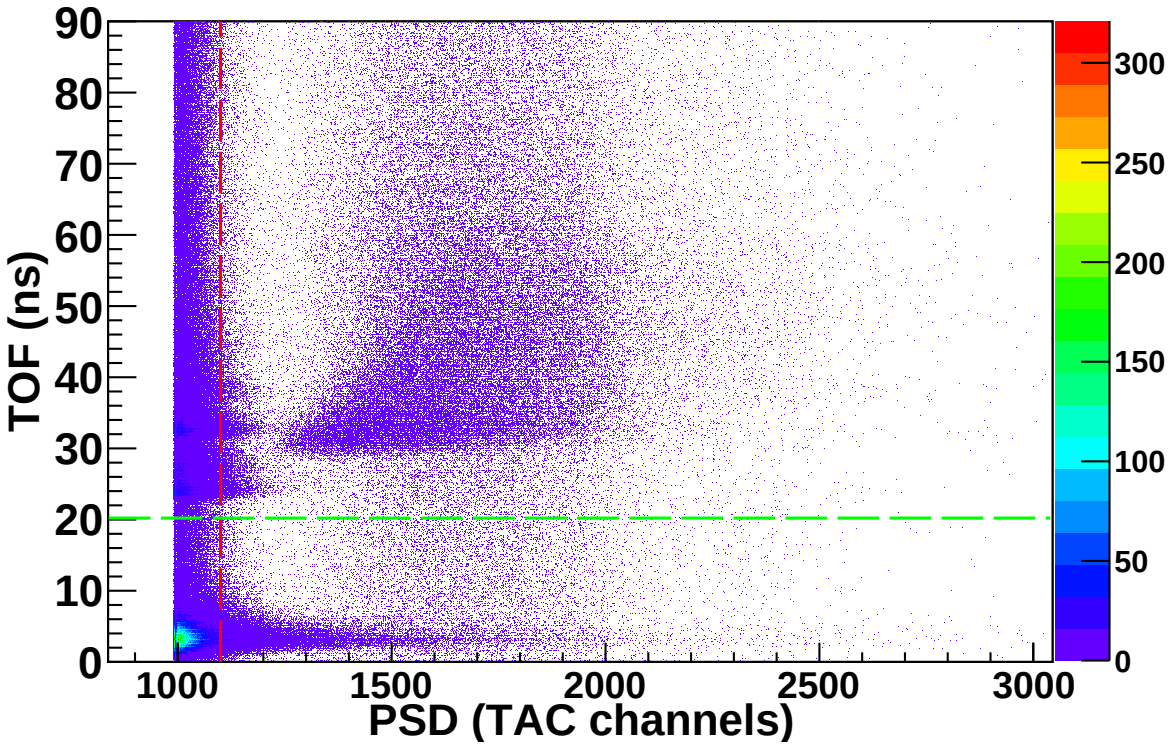

FIGURE 5.12: (Color online) A typical TOF versus PSD spectrum of a neutron detector. The neutron events are located at the right of the red-dashed line and are well separated from the γ-rays located at the left. A TOF cut indicated by the green dashed line is used to remove the γ-flash events. The data are acquired at E_γ=16.5 MeV for $theta_n = 90\,^\circ$.

5.4.3 Cuts using the correlation between PH, PSD and TOF parameters

After the application of the self-timing and PH cuts, we utilized the correlations between the PH, PSD and TOF parameters. The first correlation is the one between PSD and TOF. Figure 5.12 shows the 2-dimensional histogram of the PSD plotted versus TOF.

A hardware threshold was applied at the time of the experiment located at the TAC channel ∼1000 to eliminate some of the incident γ-rays while a small portion of γ-rays were allowed to pass the threshold. A 2-dimensional cut applied at the TOF

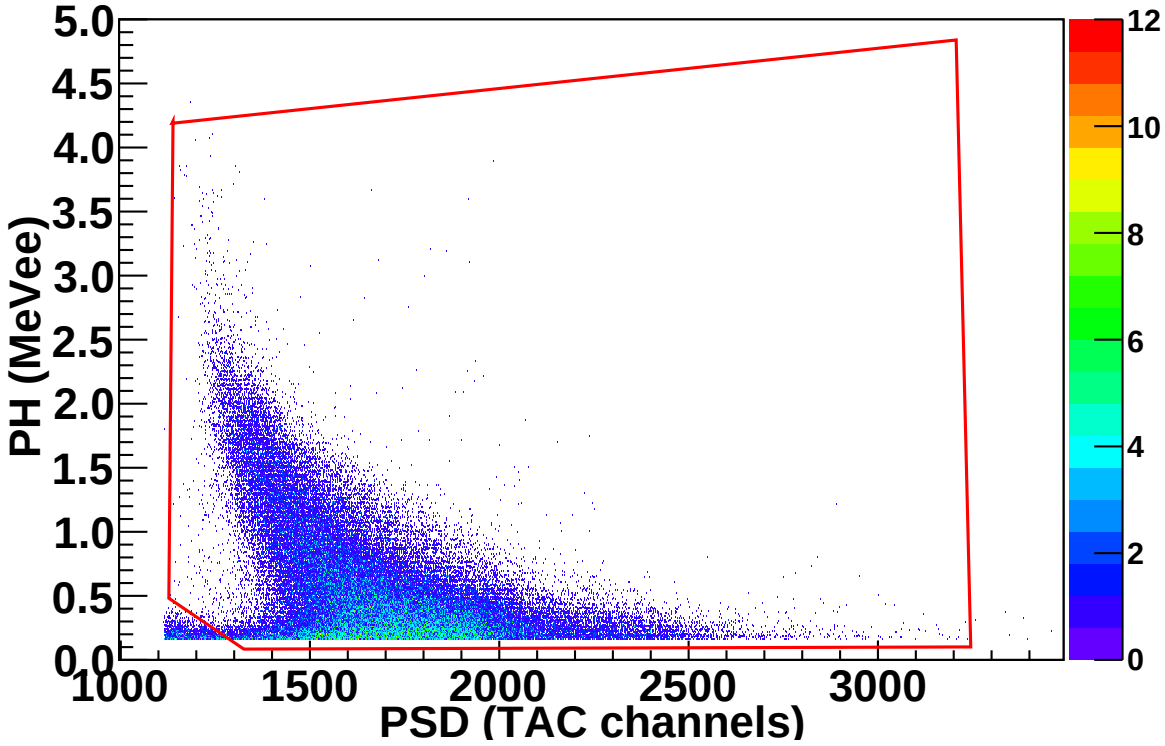

FIGURE 5.13: (Color online) A PSD versus PH spectrum for a neutron detector. The neutrons are chosen by applying a second 2-dimensional cut indicated by a red curve and are well separated from the γ-ray events. The data were acquired at E_γ=16.5 MeV.

versus PSD spectra is used in the offline analysis to reject most of the γ-rays that arrived at the detector almost uniformly in time while a TOF cut was applied at 20 ns in order to reject the γ-flash events that arrived at $\sim$3.3 ns(=d/c).

After that, additional γ-rays were rejected based on cuts in the PSD versus PH spectra. Fig. 5.13 shows the 2-dimensional histogram of PSD plotted versus PH. The neutron events are located at the right of the histogram, very well separated from the γ-rays located at the bottom left of the histogram.

The detected neutron events originate from the $^3\vec{H}e(\vec{\gamma},n)pp$ reaction and from other (γ,n) reactions with various elements contained in the Pyrex glass, the air,

and the N_2 inside the ^{3}He target. The Pyrex glass is composed of (as percentage of weight) oxygen (54%), silicon (37.7%), boron (4.0%), sodium (2.8%) and aluminum (1.1%). Other elements may also be contained with smaller than 1% contributions to the total composition. O and Si, which are the main components of Pyrex glass, do not undergo (γ,n) reaction at the energies of our present experiment. B, Al, Na, and N inside the ^{3}He target cell and in the air undergo (γ,n) reaction with cross sections which are generally lower at 12.8 MeV and higher at 14.7 MeV and 16.5 MeV.

Although Rb and K–vital components of the SEOP as we saw in the previous chapter–can leak into the transfer tube and the target chamber, they immediately condense on the cell walls due to the temperature gradient. The temperature of the target chamber was measured during the experiment and did not exceed ∼300 K. The alkali-metal number densities in the target chamber can be calculated based on the vapor pressure curves given in [Lid04] and are found to be $\sim 10^{10}$ and 10^9 cm^{-3} for Rb and K, respectively. Given the very low alkali-metal number densities, the measured photo-neutron cross sections of Rb [Lep71, Zhe08], and K [Web71, Vey74], and the integrated photon flux during the experiment, the neutron background from the alkali-metals in the target chamber is found to be negligible.

In order to measure and subtract the overall background neutron yield, a N_2-only reference cell is employed. The cuts applied to the N_2 reference cell data are the same as in the ^{3}He target case. Fig. 5.14 shows the neutron counts acquired from the ^{3}He target cell compared to the N_2 only reference cell normalized to the same number of photons.

The clean neutron yields were extracted after the conversion of TOF to neutron energy and the subsequent subtraction of the N_2 background data. The clean yield is essential for the calculation of the cross sections presented in the next chapter.

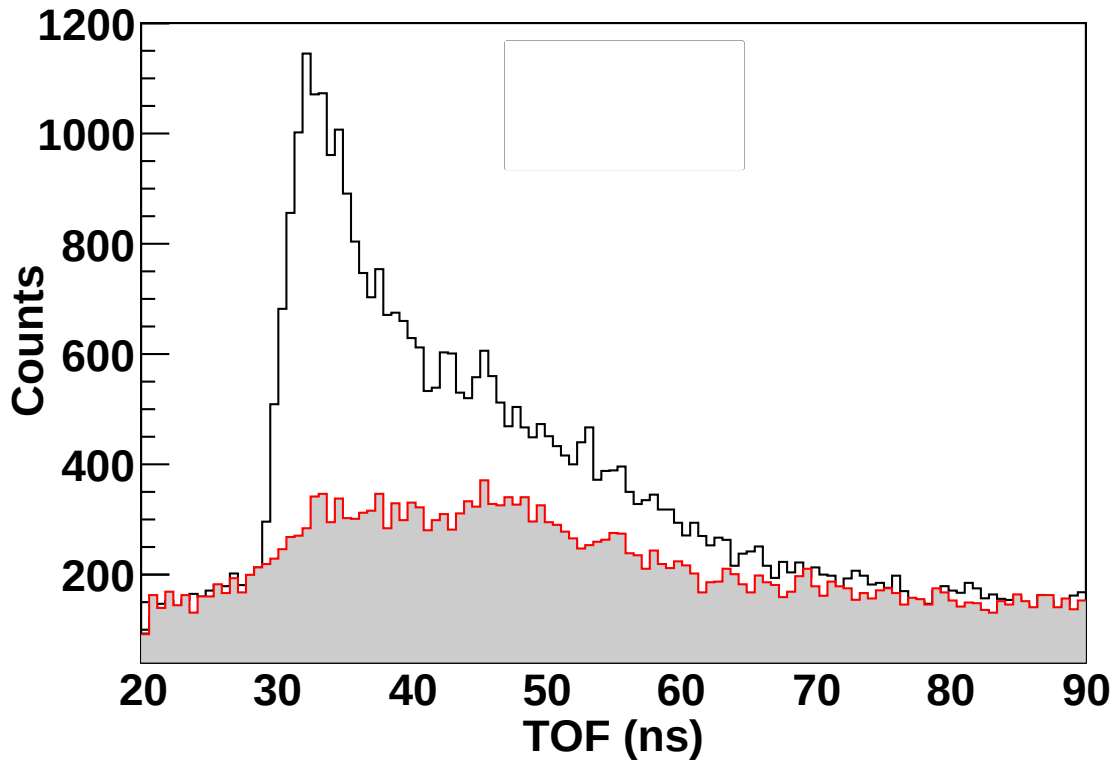

FIGURE 5.14: (Color online) The TOF spectrum of ^{3}He (black-line histogram) in comparison to the N_2 reference cell (filled red-line histogram) normalized to the same flux. The data are acquired at E_γ=16.5 MeV.

5.5 Analysis Cuts for Two-body Photodisintegration Experiment

5.5.1 Self-timing Cut

The self-timing cut is the first of the two cuts used in the analysis of the two-body photodisintegration experiment. The method for the determination and application of this cut is identical to the one used for the three-body experiment shown in the previous section.

5.5.2 Cuts using the correlation between E_p and TOF parameters

After the application of the self-timing cut, cuts were made in the Ep versus TOF spectra. Figure 5.15 shows the 2-dimensional histogram of the TOF plotted versus

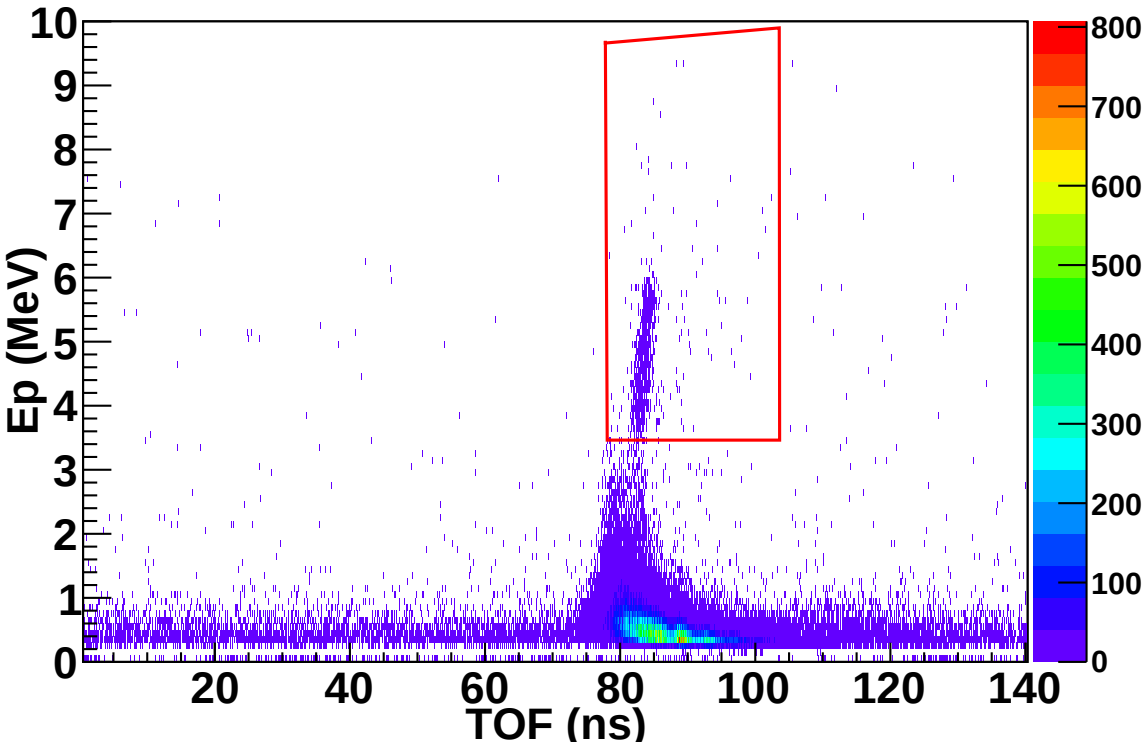

FIGURE 5.15: (Color online) The TOF versus E_p spectrum for a SSB detector at 95°. The protons were chosen by applying a 2-dimensional cut indicated by a red curve and are well separated from the electrons. The data are acquired at E_γ=29.0 MeV.

E_p.

A 2-dimensional cut was applied to select the proton events. Most of the events recorded by the detector are electrons located ∼80 ns. The electron-flash contains electrons which were Compton scattered by the γ-beam. These electrons can have energies up to 29 MeV based on the Compton kinematics and can easily pass through the collimators used to stop protons.

Just as before, in order to measure and subtract the overall background proton yield, a N_2 reference cell was employed and the same cuts were applied. Fig. 5.16 shows the proton counts acquired from the ^{3}He target cell compared to the N_2 only

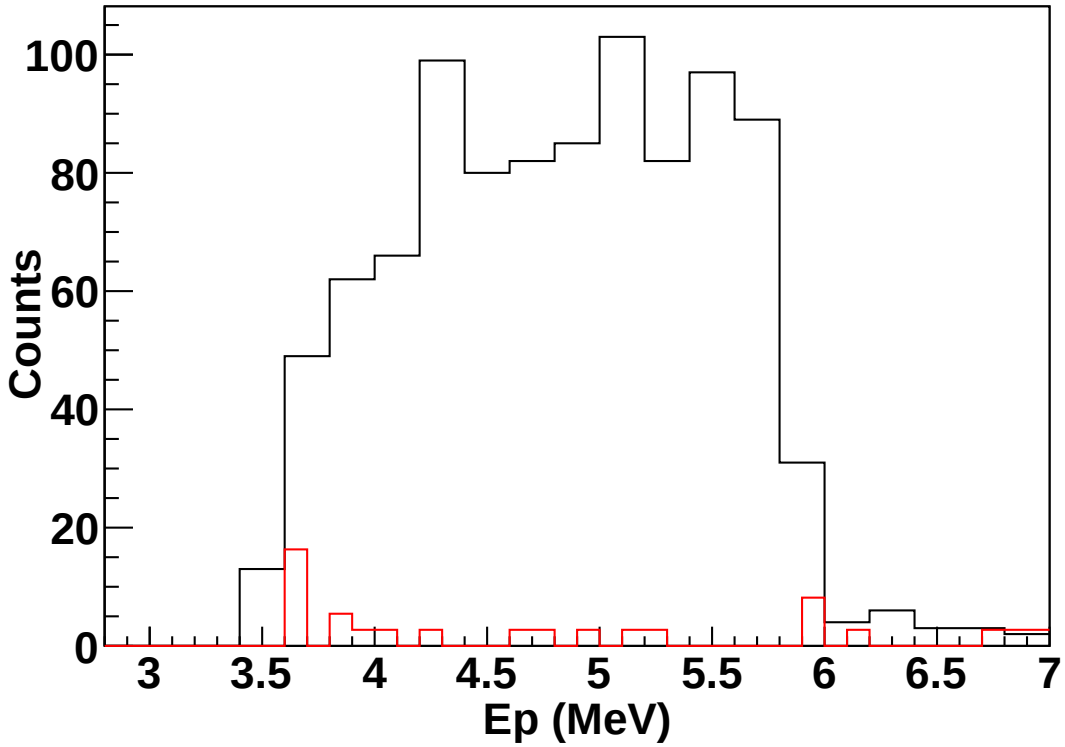

FIGURE 5.16: (Color online) The proton energy spectrum of ^{3}He (black-line histogram) in comparison to the N_2 reference cell (red-line histogram) normalized to the same flux. The data are acquired at E_γ=29.0 MeV.

reference cell normalized to the same photon intensity. The technique to measure and extract the intensity for both two- and three-body photodisintegration experiments will be presented in the next section.

5.6 Beam Intensity Determination

The beam intensity monitor based on the d(γ,n)p reaction was described in chapter 3. The purpose of the monitor is to extract the absolute integrated γ-beam intensity corresponding to each ^{3}He run. A D_2O cell was used for the three-body photodisintegration experiments at 12.8 and 14.7 MeV while a C_6D_6 cell was used for the three-body experiment at 16.5 MeV and two-body experiment at 29.0 MeV.

Two BC-501A neutron detectors placed transverse to the beam direction were employed to detect the neutrons from the deuteron photodisintegration reaction. A low background environment was achieved by placing two lead walls before the neutron detectors to shield them from the Compton-scattered γ-rays passing through the air. Although the lead walls can reduce the γ-rays background in the detectors, γ-rays scattered by the cell can still reach the detectors. In order to remove the majority of the γ-rays, a high hardware PH and PSD thresholds were applied to the acquired data.

The correlation between the TOF and PSD parameters was utilized in order to isolate the neutron signal in the same way as we described before. Figure 5.17 shows the 2-dimensional histogram of the TOF versus PSD acquired at the incident photon energy of 16.5 MeV after the application of self-timing and the software PH cut of 0.517 MeV_{ee}.

Two bands can be seen in the histogram. The γ-flash band is located $\sim$1 ns while the neutrons from the d(γ,n)p reaction lay after $\sim$8 ns. A TOF cut at 7.0 ns was applied to cut away the γ-flash. The amount of neutron events, N_n, integrated above the TOF cut was used to extract the beam intensity.

The formula used for determining the beam intensity, F, is given by

$$F = \frac{N_n D_t}{\Delta\Omega \frac{d\sigma}{d\omega} N_t \epsilon_{sys}}, \tag{5.8}$$

where $\Delta\Omega$ and ϵ_{sys} are the detector acceptance and the system efficiency of the detectors calculated using GEANT4 simulations as we will see in the next section, D_t is the correction factor for the dead time of the DAQ system, N_t is the number density of either $\mathrm{D_2O}$ or $\mathrm{C_6D_6}$ and $\frac{d\sigma}{d\omega}$ is the differential cross section of the deuteron photodisintegration.

The number density of $\mathrm{D_2O}$ is equal to

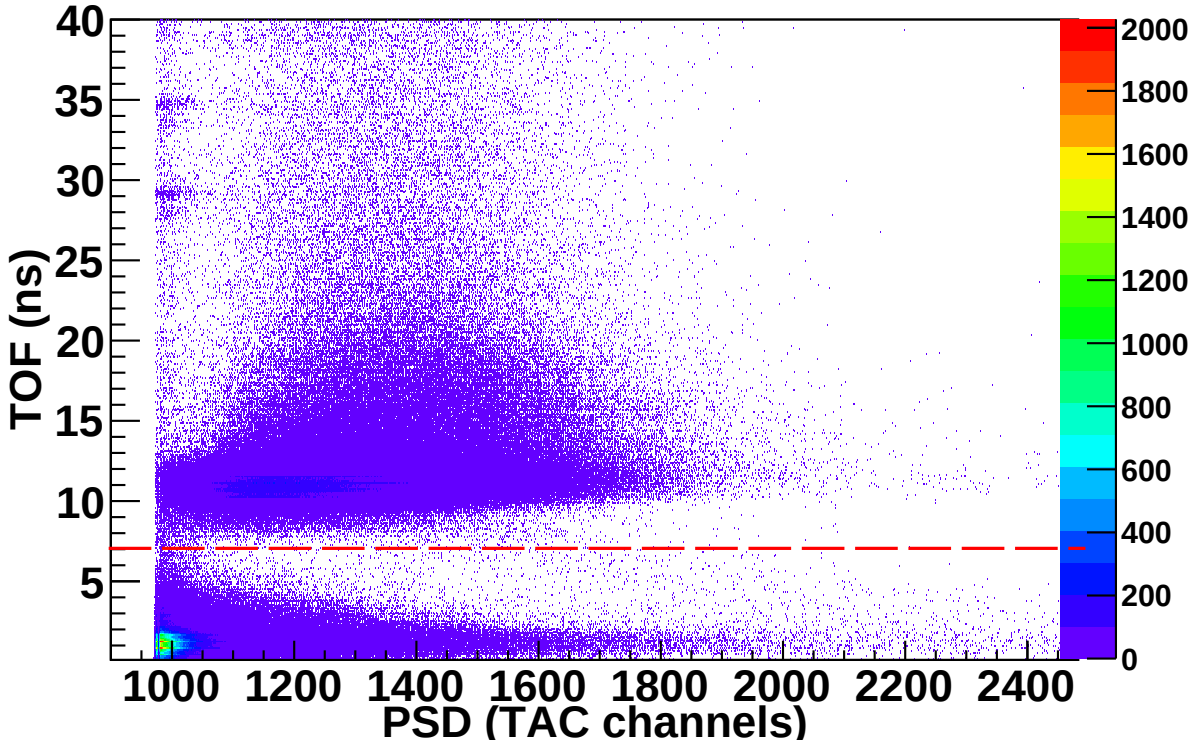

FIGURE 5.17: (Color online) A typical TOF versus PSD spectrum of a neutron detector used at the beam intensity monitor. The neutron events are located above the TOF cut (red dashed line) and are well separated from the γ-rays located at the bottom. The data are acquired at E_γ=16.5 MeV.

$$N_t = 2\frac{\rho_{D_2O} N_a L_t}{2M_d + M_O} \tag{5.9}$$

where N_a is the Avogadro number, ρ_{D_2O}=1.1047 gr/cm^3 is the density of the heavy water, M_d=2.012 amu is the mass of deuteron, M_O=15.995 amu is the mass of oxygen and L_t=4.74 cm is the target length. The number density of C_6D_6 is given by

$$N_t = 6\frac{\rho_{C_6D_6} N_a L_t}{6M_d + 6M_C} \tag{5.10}$$

where $\rho_{C_6D_6}$=0.95 gr/cm^3, M_C=12 and L_t=10.56 cm.

The differential cross section was extracted assuming the angular distribution

$$\frac{d\sigma}{d\Omega} = \sigma[\frac{3}{8\pi}(1-f)sin^2(\theta_n^{cm}) + \frac{f}{4\pi}] \tag{5.11}$$

where σ is the total cross photodisintegration cross section and f is the fraction of M1 contribution to the total cross section. The total cross section values at the energies of the experiments were found by performing a global fit to all available cross section data [DG92, Bir85, Ber86, Sko74] below 100 MeV. Theoretical calculations [Are04, Sch01a, Sch01b] predict that parameter f was $\sim$2 % while the most recent measurement [Bla07] at 14 MeV found M1 contribution equal to 9%. For analysis purposes, the M1 contribution varied between 0-10% which resulted in a change of γ beam intensity on the order of $\sim$0.5%. The value of f=0.05 is used for the determination of the beam intensities at all energies. The beam intensity for the two-body photodisintegration experiment was (1-3)$\times 10^7 \gamma/s$. The intensity for the three-body photodisintegration experiments at 12.8 and 14.7 MeV was found to be 1 - 2$\times 10^8 \gamma/s$ while at 16.5 MeV is (7.3-9.5)$\times 10^7 \gamma/s$.

5.7 Monte Carlo Simulations

5.7.1 Description

The toolkit used for the study of several experimental effects in the two- and three-body photodisintegration experiments is the simulation package GEANT4 [Ago03, All06]. The GEANT4 toolkit was used to model the target systems and detector environments of the two- and three-body photodisintegration experiments and the transportation of particles through these environments.

Only the volumes in the flight path between the ^{3}He cell and the SSB detectors were simulated in the case of two-body photodisintegration due to the limited range of low energy protons in matter. However, the neutrons produced by the three-

body photodisintegration were energetic enough that elastic scattering off of any surrounding volume could result in neutron scattering into the detector sensitive volumes. Figures 5.18 and 5.19 give an overview of the simulated environments of the three- and two-body photodisintegration of ^{3}He, respectively, including all the physical volumes that are considered to be important for the simulation outcome.

At the center of the three-body target system lays the ^{3}He cell made of Pyrex glass and filled with ^{3}He gas and a small amount of N_2. The support structure for the ^{3}He and the N_2 reference cell (green color at the figure) is made of the fiber glass material G7. A set of RF coils (small red coils) made of copper and located above and below the ^{3}He cell are used for the performance of the NMR and EPR polarimetry measurements. A set of large Helmholtz coils (big red coils) also made of copper are used to keep ^{3}He gas polarized. Sixteen Bicron neutron detectors encased in μ-metal tubes surround the ^{3}He cell. Two plastic vacuum tubes with front and end windows made of kapton are used to deliver the beam to and from the target cells. The space between the physical volumes is filled with Air.

Due to the limited range of protons produced by the two-body photodisintegration of ^{3}He, it is not necessary to simulate all the surrounding volumes of the targets. Instead we simulate only the volumes that they may affect the track of protons. In Figure 5.19 the target chamber of the ^{3}He cell (red color at the figure) filled with ^{3}He and N_2 gas lays at the middle of the seventy two SSB detectors array. The glass thicknesses of the ^{3}He and N_2 reference cells are measured at the University of Virginia and the results were implemented in the simulation. The space between the cell and the detectors is filled with Air to properly account for the straggling of protons. Aluminum collimators (green color) with rectangular apertures of 2 cm $\times$ 0.4 cm, and a length of 3 cm, are positioned in front of the detectors. Cups made of aluminum are used at the back of the detectors to shield them from the ambient light.

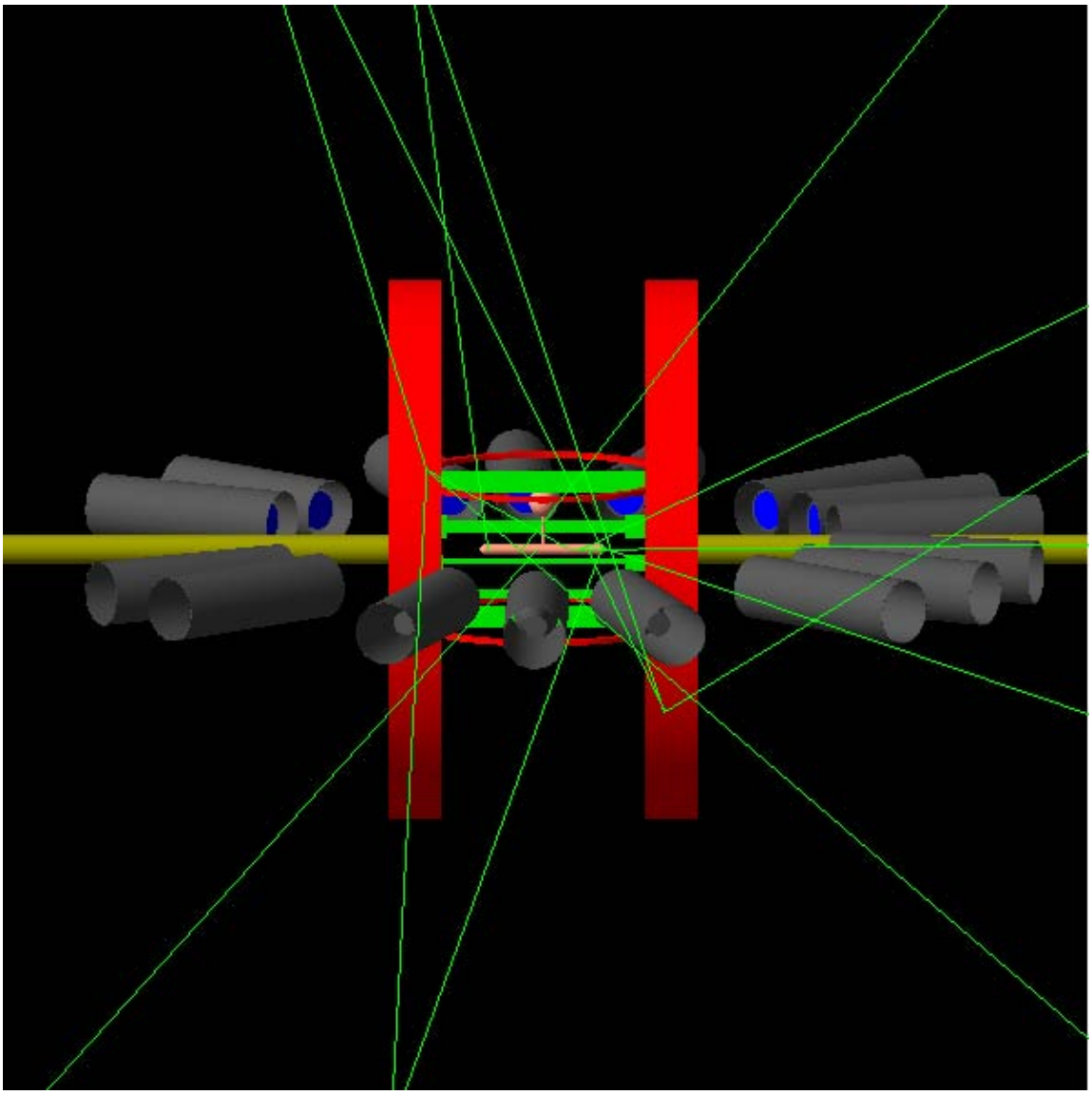

FIGURE 5.18: (Color online) An overview of the simulation environment for the three-body photodisintegration experiment. At the middle of the neutron detector array is the ^{3}He cell. Neutrons (green tracks) are generated uniformly throughout the target chamber of the cell. The detectors are encased in μ-metal cylinders. The front part of the detector (blue) is the active volume containing the liquid scintillator BC-501A. All important volumes such as the target support (green), the vacuum tubes (yellow) and the Helmholtz coils (red) that can contribute to the multiscattering of neutrons are included in the simulation.

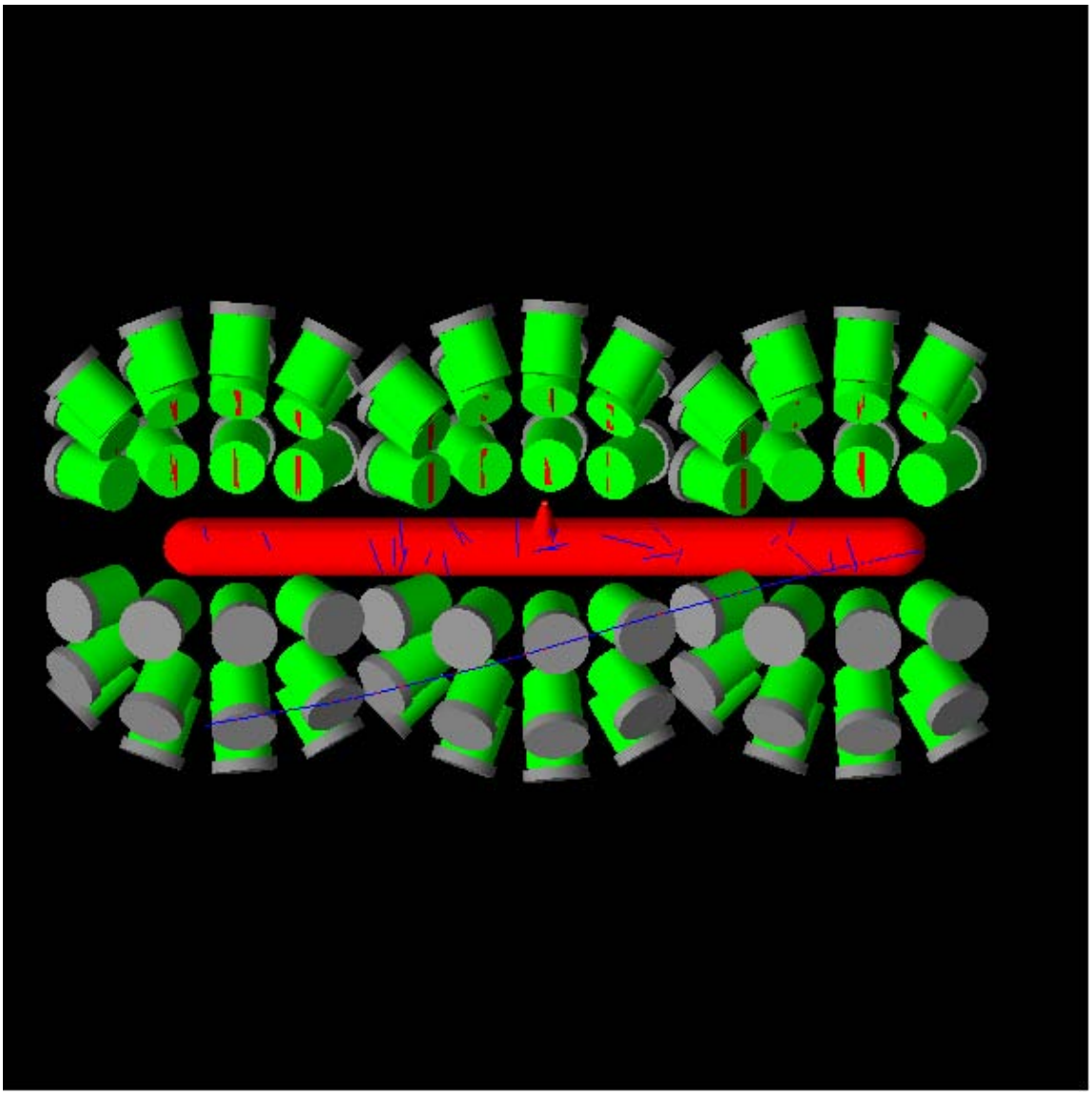

FIGURE 5.19: (Color online) An overview of the simulation environment for the two-body photodisintegration experiment. The target chamber (red) of the ^{3}He cell is located at the middle of the seventy two silicon surface barrier detectors array. Protons (blue tracks) are generated uniformly throughout the target chamber of the cell. The detectors' solid angles are constrained by cylindrical collimators (green) with rectangular apertures.

5.7.2 Physics List

GEANT4 simulation package includes 32 pre-built physics lists. The pre-built list **LHEP_PRECO_HP** was used to simulate both the two- and three-body photodisintegration experiments. This physics list includes the following processes: (i) **LHEP** (Low and High Energy Parametrization) of all hadronic interactions. The standard electromagnetic interactions are also included; (ii) **PRECO** stands for Pre-Compound model for generating final states for hadrons with energies less than 150 MeV; (iii) **HP** means that the library includes a High Precision neutron and proton model for energies less than 20 MeV based on data taken from the evaluated nuclear database ENDF/B-VI.

LHEP_PRECO_HP also includes the following: (a) elastic and inelastic scattering for neutrons and protons; (b) photoelectric effect, Compton scattering, pair production and photonuclear reactions for the γ-rays and (c) Bremsstrahlung, synchroton radiation, ionization, annihilation, electronuclear reactions and multiple scattering for electrons and positrons.

5.7.3 The Goals of the Simulations

Simulations were necessary for the unfolding of the acquired data from several experimental effects. To calculate these effects different types of particles such as neutrons, protons and geantinos were used along with various simulation configurations. Geantino is a boson particle without charge used for ray-tracing applications. Although geantinos do not interact with matter, they can be detected by the volume designated as "sensitive" in GEANT4. In the following section we will give a brief description of the configurations, the particles and the quantities that we extracted.

- The extended nature of the ^{3}He target leads to the need of an accurate simulation for the calculation of the acceptances in the case of the three-body

photodisintegration. The simulation configuration used for the calculation of the acceptances from the extended target to the neutron detectors can be seen in Figure 5.18. Virtual particles named geantinos were generated uniformly throughout the 40 cm cell. The calculated acceptances for the three-body photodisintegration experiments will be given in the next section.

- Although the D_2O and C_6D_6 targets are much shorter than the target chamber of the ^{3}He cell, geantinos were also used for the calculation of the acceptances from the deuteron targets to the detectors for the primary array and the beam intensity monitor. The calculated acceptances for the deuteron photodisintegration measurements will be given in the next section.

- The efficiency of the detectors with respect to neutron energy was calculated for each incident photon energy using two GEANT4 simulations. The first simulation was performed with all the volumes of Figure 5.18 in place while the second one was performed in vacuum with no volumes present. As we will show in the next section, these two simulations are sufficient take into account, the multiscattering of the neutrons into the surrounding volumes. The neutrons were generated uniformly throughout the 40 cm cell according to the angular distributions provided by Deltuva *et al.* and Skibiński *et al.* An iterative procedure was followed as will be shown in chapter 6 and the distributions were adjusted until they match the data. The resulting distribution was used to calculate the efficiencies.

- The results of the aforementioned calculations were used for a direct comparison of the experimental data with the theoretical predictions of both groups convoluted with the extended target effect. The results of these simulations will be presented in chapter 6 and compared with the experimental data.

- Uniformly generated neutrons along the D_2O and C_6D_6 targets were used for the calculation of the efficiency of the neutron detectors. The neutrons follow the distribution of d(γ,n)p reaction which was shown in the previous section. As in the ^{3}He case, two simulations were performed: one with all the volumes present and one in vacuum. The results of the simulations were used for the calculation of the system efficiency of the detectors at the primary array and the beam intensity monitor.

The unfolding of the proton data acquired during the two-body photodisintegration experiment required geometrically precise simulations using protons. Several simulations were performed and presented below:

- The uneven nature of the glass wall of ^{3}He and N_2 cells underlined the need for a precise measurement of their thicknesses. Although the glass thickness of both cells was measured at several points and implemented in the simulation, a need for small adjustments of the thickness in the simulation became apparent. An iterative process was performed where protons are generated uniformly along the cell and the results are compared to the experimental energy spectra. The cell thickness is adjusted, accordingly, within the uncertainty of the wall thickness measurements and the process is repeated until an agreement between the simulated and the acquired energy spectra is reached.

  here you need to state that the adjusted amount is consistent with the uncertainty of the wall thickness as we discussed on Sunday.

- After the adjustment of the glass thickness, protons with uniform distributions following the kinematics of ^{14}N(γ,p)^{13}C were generated in both ^{3}He and N_2 reference cell. The results were employed in order to subtract the N_2 background correctly.

- Protons were generated according to the theoretical distributions provided by Deltuva *et al.* and Skibiński *et al.* The results of these simulations will be presented in chapter 6 and compared with the experimental data.

5.7.4 Extracted Information

The goal of the simulation is to reproduce the quantities experimentally observed in order to unfold the underlying cross sections and angular distributions from the experimental effects. The parameters extracted from the experimental data are the pulse height, the time of flight and the pulse shape discrimination value between neutrons and γ-rays in the case of the three-body photodisintegration experiment while the deposited energy in the SSB detectors and the TOF are recorded for the two-body photodisintegration of ^{3}He. The corresponding quantities of the simulation together with other quantities useful for the analysis of the simulation results are kept for each event incident on the detectors.

In the case of three-body photodisintegration simulations, the following list of the variables was saved:

- The **event number** was recorded in order to keep track of every new particle entered in the detector volume.

- The **TOF** from the generation point inside the target to the point of interaction inside the sensitive volume of the detector is recorded. The TOF was smeared with a Gaussian distribution with standard deviation determined based on the experimental data as shown in Figure 5.8 to match the experimental resolution.

- The **incoming energy** of the neutron at the moment that it crosses the boundary of the sensitive detector.

- The **detector number** in the array that received a particle hit.

- The **deposited energy** is the sum of the total energy deposited inside the neutron detector by the recoiling particles.

- The **light output** was calculated from the deposited energy using the light yield curves generated using the measurements performed at PTB [Tro09]. Tables of the light output response functions were generated for all the particles which can interact with BC-501A including H, ^{2}H, ^{3}H, ^{3}He, ^{4}He, ^{8}Be, ^{9}Be, ^{10}Be, ^{12}C, ^{13}C, ^{16}O, muons and pions. The light output for one interaction in the detector is given by $\Delta L = L(E) - L(E - \Delta E)$ where $L(E)$ is the light yield of the interacting particle and ΔE is the energy deposited during the step. The sum of the light output of all interactions was recorded and stored for each event.

- The **vertex information** of the point where the particle is generated.

- The **name of the particle** which is the simulation counterpart of the experimental parameter PSD used for the particle identification.

All the aforementioned variables apart from the pulse height which is not applicable to SSB detectors were also recorded in the case of two-body photodisintegration. Additional to those, the **initial and final polar angles** were also stored.

5.8 Neutron Detector Acceptances and Efficiency

The geometric acceptances, intrinsic and system efficiencies of the neutron detectors were calculated using GEANT4 simulations. The results were used for the determination of the differential cross sections for the deuteron photodisintegration, the γ beam intensities and the spin-dependent double differential cross sections of $^{3}\vec{H}e(\vec{\gamma}$,n)pp reaction at all incident photon energies.

5.8.1 Acceptances

The acceptances of the neutron detectors were calculated based on GEANT4 simulations which employed geantino particles. The geantinos were generated uniformly throughout the length of the targets and inside an area defined by the collimator diameter following isotropical distributions. The acceptance from the target to the neutron detectors is defined as

$$\Delta\Omega = 4\pi \frac{\text{number of geantinos incident on the detector}}{\text{total number of geantinos generated}} \tag{5.12}$$

6×10^8 geantinos were generated for each calculation. The results for the acceptances can be seen in Table 5.1, 5.2 and 5.3.

5.8.2 Intrinsic and System Efficiency

The two-body photodisintegration of deuteron produces monoenergetic neutrons for a given polar angle. On the other hand the three-body photodisintegration of ^{3}He produces a continuum of neutrons with anywhere from zero to the maximum kinematically allowed energy. Although there is a difference in the kinematics, the same method was used to calculate the efficiencies corresponding to both reactions.

Efficiencies for d(γ,n)p reaction

Two different GEANT4 simulations were used to calculate the system efficiency of the neutron detectors. The first simulation was performed with all the surrounding volumes in place while the second one was performed in vacuum with no volumes present. The neutrons were generated uniformly throughout the deuteron target following the angular distribution of d(γ,n)p reaction. The system efficiency is defined as

Table 5.1: Acceptances calculated using GEANT4 simulations of the D_2O and ^3He targets as well as the neutron detectors at the incident photon energies of 12.8 and 14.7 MeV. The detectors 1-16 are located at the primary array while detectors 17 and 18 correspond to the beam intensity monitor. A D_2O cell is used at the beam intensity flux monitor.

Detector	Target Distance to Detector (cm)	Polar Angle (°)	Acceptance of D_2O Target (msr)	Acceptance of ^3He Target (msr)
1	100.3	30	12.5	12.8
2	99.4	45	12.7	13.0
3	99.1	75	12.8	12.8
4	100.3	90	12.5	12.5
5	99.4	105	12.7	12.7
6	106.7	136	11.1	11.2
7	100.0	150	12.5	12.8
8	99.1	165	12.9	13.3
9	100.3	32	12.5	12.8
10	100.3	48	12.5	12.7
11	100.3	75	12.5	12.5
12	100.3	90	12.5	12.4
13	99.7	105	12.6	12.6
14	100.3	138	12.5	12.7
15	101.3	153	12.3	12.6
16	100.3	165	12.5	13.0
17	37.1	90	89.0	89.0
18	37.1	90	89.0	89.0

$$\epsilon_{syst} = \frac{\text{number of neutrons detected after cuts in volume}}{\text{number of neutrons incident on the detector in vacuum}} \tag{5.13}$$

Based on the aforementioned simulation performed in vacuum, the intrinsic efficiencies can be also calculated as

$$\epsilon_{int} = \frac{\text{number of neutrons detected after cuts in vacuum}}{\text{number of neutrons incident on the detector in vacuum}}, \tag{5.14}$$

The intrinsic and system efficiencies of the neutron detectors for the d(γ,n)p reaction are given in Table 5.4 and 5.5.

Table 5.2: Acceptances calculated based on GEANT4 simulations from the D_2O and ^3He targets to the neutron detectors at the incident photon energy of 16.5 MeV. The detectors 1-16 are located at the primary array while detectors 17 and 18 correspond to the beam intensity monitor. A C_6D_6 cell is used at the beam intensity flux monitor.

Detector	Target Distance to Detector (cm)	Polar Angle (°)	Acceptance of D_2O Target (msr)	Acceptance of ^3He Target (msr)
1	100.0	30	12.6	12.9
2	100.0	43	12.6	12.8
3	100.0	72	12.6	12.6
4	100.0	89	12.6	12.6
5	100.0	105	12.6	12.6
6	100.0	135	12.6	12.8
7	100.0	150	12.6	12.9
8	100.0	165	12.5	13.0
9	100.0	30	12.6	12.9
10	100.0	45	12.6	12.8
11	100.0	73	12.6	12.6
12	100.0	87	12.6	12.5
13	100.0	105	12.6	12.6
14	100.0	135	12.6	12.8
15	100.0	150	12.6	12.9
16	100.0	165	12.5	13.0
17	39.5	90	78.3	78.3
18	37.5	90	87.0	87.0

Table 5.3: Acceptances calculated based on GEANT4 simulations from the C_6D_6 target to the neutron detectors at the incident photon energy of 29.0 MeV.

Detector	Target Distance to Detector (cm)	Polar Angle (°)	Acceptance (msr)
1	120.0	90	8.7
2	119.9	90	8.7

Table 5.4: The intrisic and system efficiencies are listed for d(γ,n)p reaction at all incident photon energies of three-body experiments. The detectors 1-16 were located at the primary array while detectors 17 and 18 correspond to the beam intensity monitor. A D_2O target was used as the beam intensity flux monitor at 12.8 and 14.7 MeV while a C_6D_6 target was used at beam energies of 16.5 MeV.

	12.8 MeV		14.7 MeV		16.5 MeV	
Detector	ϵ_{int}	ϵ_{syst}	ϵ_{int}	ϵ_{syst}	ϵ_{int}	ϵ_{syst}
1	0.21	0.28	0.20	0.27	0.19	0.21
2	0.21	0.23	0.20	0.22	0.19	0.19
3	0.21	0.22	0.20	0.22	0.19	0.19
4	0.21	0.21	0.20	0.21	0.20	0.19
5	0.21	0.22	0.20	0.22	0.20	0.19
6	0.22	0.25	0.21	0.25	0.20	0.21
7	0.21	0.31	0.21	0.32	0.20	0.25
8	0.21	0.65	0.21	0.68	0.21	0.39
9	0.21	0.27	0.20	0.26	0.19	0.22
10	0.21	0.22	0.20	0.22	0.19	0.19
11	0.21	0.22	0.20	0.21	0.19	0.19
12	0.21	0.21	0.20	0.21	0.20	0.19
13	0.21	0.22	0.20	0.22	0.20	0.19
14	0.21	0.26	0.21	0.26	0.20	0.21
15	0.21	0.34	0.21	0.35	0.20	0.25
16	0.21	0.64	0.21	0.69	0.20	0.39
17	0.18	0.19	0.18	0.19	0.17	0.18
18	0.18	0.19	0.18	0.19	0.17	0.18

Table 5.5: The intrisic and system efficiencies of the beam flux monitor using a C_6D_6 target at the incident photon energy of 29.0 MeV.

Detector	ϵ_{int}	ϵ_{syst}
1	0.14	0.15
2	0.13	0.15

Efficiencies for $^3\vec{H}e(\vec{\gamma},n)pp$ reaction

The detector efficiencies for the calculation of the spin dependent differential cross sections of $^3\vec{H}e(\vec{\gamma}$,n)pp reaction were determined by generating neutrons uniformly throughout the ∼40 cm ^{3}He cell. The neutrons were generated following the angular distributions provided by Deltuva *et al.* and Skibiński *et al.* An iterative procedure was followed and intrinsic angular distributions were adjusted until they matched the experimental data. The resulting distribution was used to calculate the efficiencies. The system efficiencies were calculated for each neutron energy bin based on Equation 5.13. The neutron energy was reconstructed based on the TOF following Equation 5.6. Figures 5.20, 5.21 and 5.22 show the intrinsic and system efficiencies calculated for the incident photon energies of 12.8, 14.7 and 16.5 MeV, respectively.

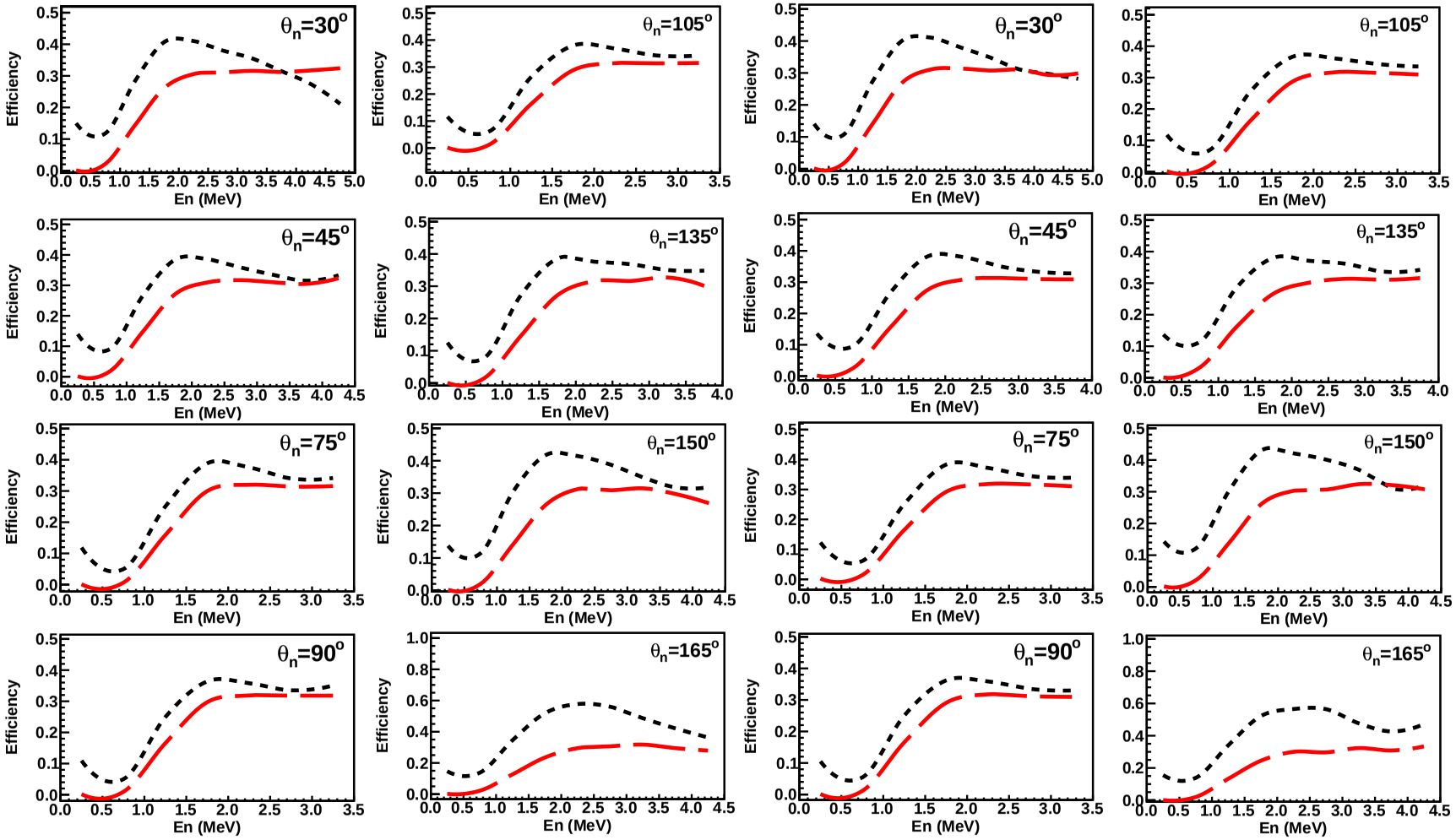

FIGURE 5.20: (Color online) Intrinsic (long-dashed red curve) and system efficiencies (short-dashed black curve) of neutron detector for $^3\vec{H}e(\vec{\gamma},\mathrm{n})\mathrm{pp}$ reaction at 12.8 MeV.

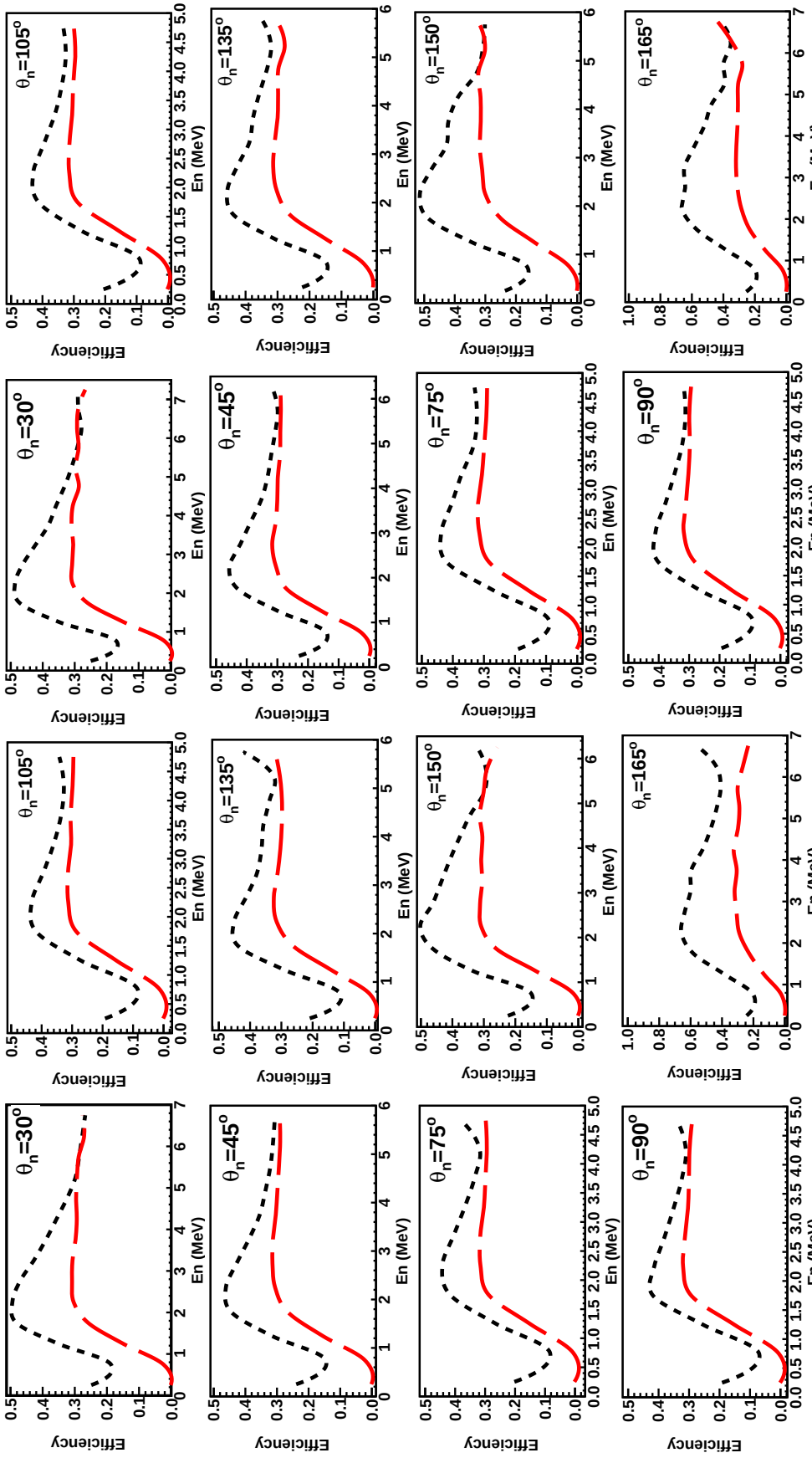

FIGURE 5.21: (Color online) Intrinsic (long-dashed red curve) and system efficiencies (short-dashed black curve) of neutron detector for $^3\vec{H}e(\vec{\gamma},n)pp$ reaction at 14.7 MeV.

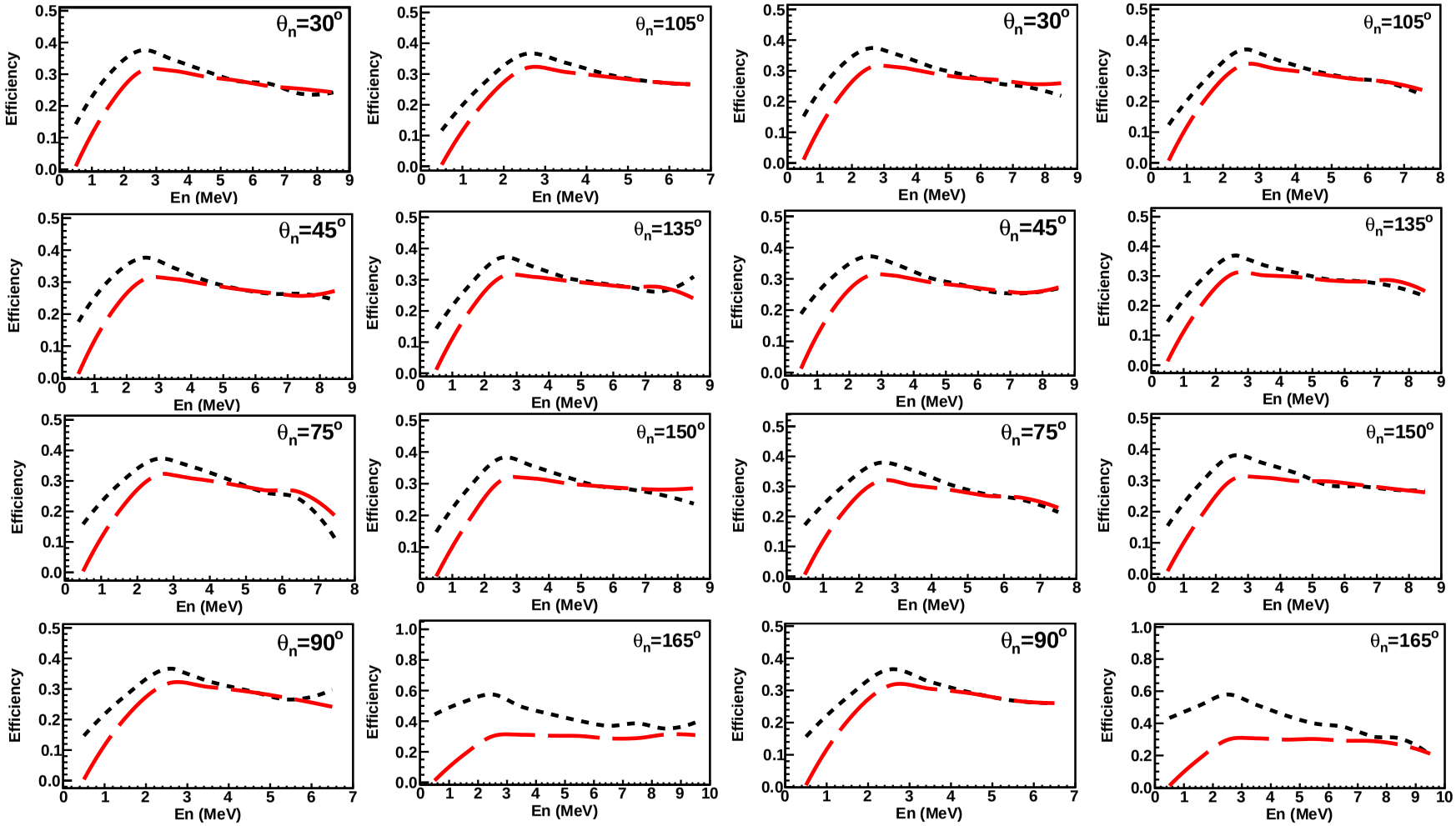

FIGURE 5.22: (Color online) Intrinsic (long-dashed red curve) and system efficiencies (short-dashed black curve) of neutron detector for $^3\vec{H}e(\vec{\gamma}$,n)pp reaction at 16.5 MeV.

6

Results and Discussion

6.1 Introduction

In this Chapter we present the experimental findings and compare them with the theoretical calculations discussed in Chapter 2. The absolute spin-helicity dependent double-, single-differential and total cross sections have been extracted from the measurements of the three-body photodisintegration of ^{3}He. The contribution of the three-body photodisintegration channel to the GDH sum rule is also extracted for all incident energies and it is compared to the predictions of the theoretical calculations. The current status of the two-body photodisintegration analysis is presented in the last section of this Chapter and a detailed plan for the extraction of the spin-helicity dependent single-differential cross sections and the contributions to the GDH are discussed. In the next section we present the extracted single-differential cross sections from the reaction d(γ,n)p. This study serves as an additional quality check of the photodisintegration analysis for ^{3}He.

6.2 Single Differential Cross Sections of the Reaction d(γ,n)p

Apart from the neutron data acquired by the three-body photodisintegration of ^{3}He, neutron data were also acquired from the d(γ,n)p reaction at all incident photon energies (12.8, 14.7 and 16.5 MeV). As described in Chapter 3, these data were acquired using a D_2O target mounted in the center of the primary detector setup. The data were used to verify of the measurements since the extraction of the single-differential cross sections of deuteron validates further the three-body photodisintegration analysis and simulations. This measurement is not an independent measurement since the γ-ray beam intensities were extracted based on a previous measurement of the total cross section as discussed in Chapter 5. However, it was a useful check of the analysis methods and some of the simulation results as the acceptances and efficiencies.

The differential cross sections for each and every scattering angle in the laboratory reference frame can be calculated based on the equation

$$\frac{d\sigma}{d\Omega} = \frac{Y}{N_t \epsilon_{syst} \Delta\Omega} \tag{6.1}$$

where Y is the ratio of the neutron events from d(γ,n)p reaction to the integrated photon flux, F. All other symbols were defined in Chapter 5.

Figures 6.1, 6.2 and 6.3 show the single-differential cross section measurements extracted at the incident photon energies of 12.8, 14.7 and 16.5 MeV. The measurements are compared with the theoretical distributions given by Equation 5.11 assuming an M1 contribution of f=5%. The total d(γ,n)p reaction cross section was taken to be to σ=1083.7$\pm$44.8 μb (12.8 MeV), σ=925$\pm$39.4 μb (14.7 MeV) [Ber86] and σ=787$\pm$23.5 μb (16.5 MeV). The cross section values at 12.8 and 16.5 MeV were found by performing a global fit to all available cross section data [DG92, Bir85, Ber86, Sko74] below 100 MeV.

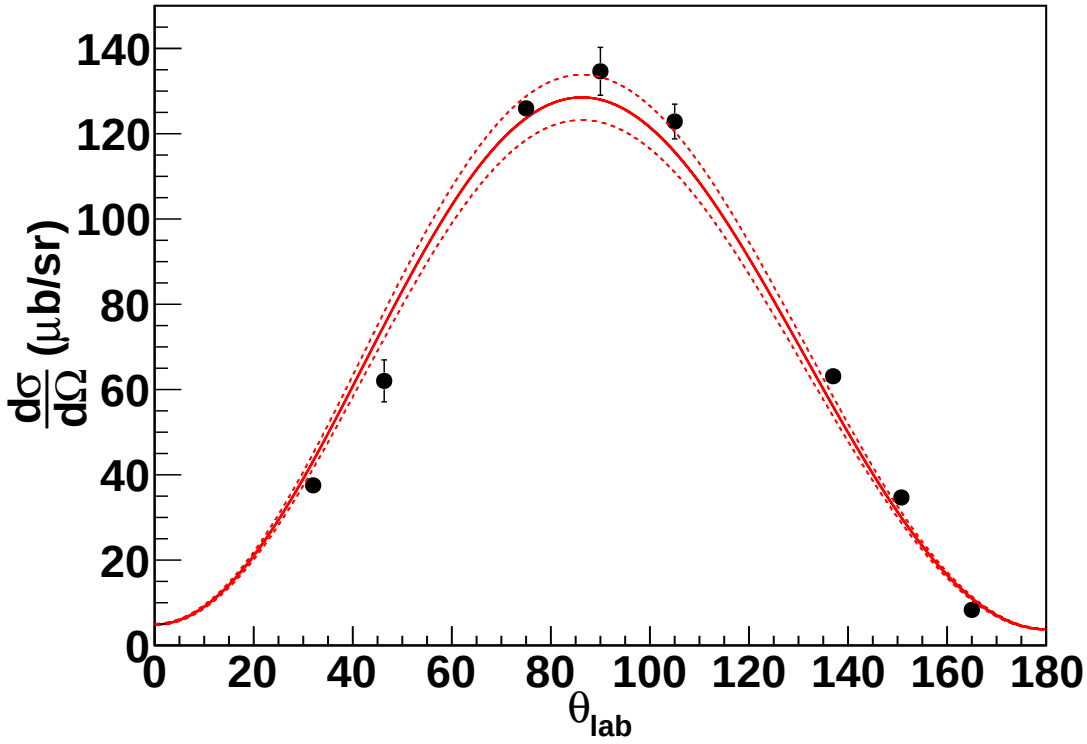

FIGURE 6.1: (Color online) The single-differential cross sections of the reaction d(γ,n)p as a function of the neutron scattering angle at the incident photon energy of E_γ=12.8 MeV. While the statistical uncertainties are smaller than the point markers in all angles, the error bars represent the systematic uncertainties. The solid red curve represents the centroid value based on the theoretical distribution and the total cross section 1083.7 μb [DG92, Bir85, Ber86, Sko74]. The long-dashed curves give the variation in the total cross section corresponding to systematic uncertainty of $\pm$44.8 μb.

The data from one of the detectors at the neutron scattering angle of 30.0°, located at the left of the γ-ray beam was removed from the study of both d(γ,n)p reaction and three-body photodisintegration of ^{3}He at the incident photon energies of 12.8 and 14.7 MeV. The data from the detector was removed due to the fact that the high PH signals went off scale for this particular detector. The data from both 30.0° detectors were not taken into account in the analysis of the d(γ,n)p reaction at 16.5 MeV. These far-forwards neutron detectors were overwhelmed by the Compton scattered γ-rays from the D_2O target. A very high PH threshold was placed at both

Table 6.1: The values of the single-differential cross sections of the reaction d(γ,n)p together with their statistical and systematic uncertainties, respectively, as a function of the neutron scattering angle at the incident photon energies of E_γ=12.8 and 14.7 MeV. The systematic uncertainties for each neutron scattering angle are taken as half the difference between the cross section values calculated for the detector left and right of the beam. Systematic uncertainties due to flux determination and the acceptance are calculated in a later section but are not included here. One of the detectors laying at the left of the beam at 30.0° is removed from this analysis.

θ_{lab}	$d\sigma^{12.8}/d\Omega(\mu b/sr)$	$d\sigma^{14.7}/d\Omega(\mu b/sr)$
32.0°	37.5±0.2±–	31.2±0.2±–
46.5°	62.5±0.2±4.9	55.3±0.2±1.9
75.0°	126.0±0.3±1.1	98.2±0.3±3.8
90.0°	134.6±0.3±5.6	103.5±0.3±7.0
105.0°	122.9±0.3±4.0	98.6±0.3±0.8
137.0°	63.1±0.2±1.7	54.5±0.2±2.9
151.5°	36.6±0.1±0.1	28.3±0.2±1.0
165.0°	8.3±0.1±0.3	6.2±0.1±0.2

detectors during the d(γ,n)p measurement in order to improve the dead time which eventually reduced the neutron events statistics to a not meaningful level. The PH hardware thresholds were reduced during the measurement of the three-body photodisintegration of ^{3}He.

The measured d(γ,n)p differential cross sections are listed in Tables 6.1 and 6.2. The systematic uncertainties are taken as half the difference between the single-differential cross sections calculated for the detectors at the same scattering angle laying at the left and right of the beam. The systematic uncertainties due to the determination of flux and the acceptances are calculated in a later section.

As can be seen in Figures 6.1, 6.2 and 6.3 the extracted single-differential cross sections agree well with the previous measurements used to calculate the γ-beam intensity both in shape and magnitude. The measurements made with the primary detector array are consistent with the measurements performed with the beam intensity monitor. The agreement validates in the analysis for the three-body photo-

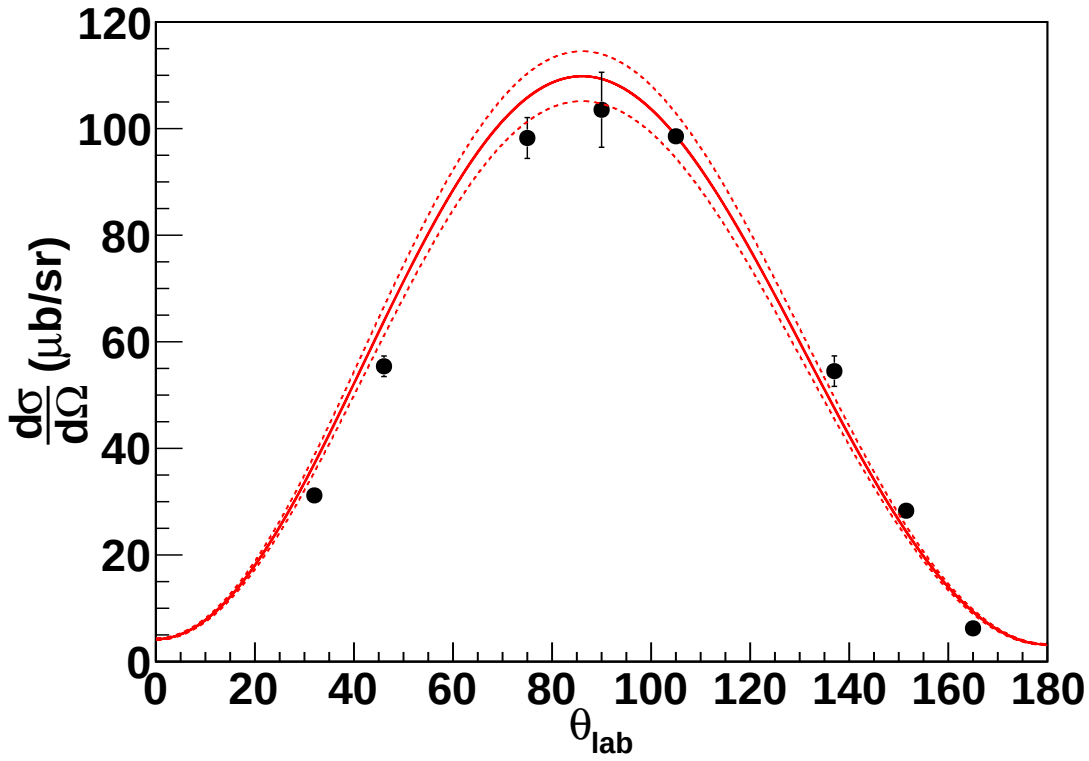

FIGURE 6.2: (Color online) The same as in Figure 6.1 but for E_γ=14.7 MeV. The total cross is 925±39.4 μb [DG92, Bir85, Ber86, Sko74]. One of the detectors left of the beam at 30.0° was removed from this analysis.

disintegration of ^{3}He.

6.3 Spin-Helicity Dependent Double Differential Cross Sections of $^3\vec{H}e(\vec{\gamma}, n)pp$ Reaction

Neutron energy spectra for the ^{3}He and N_2 targets were generated based on the extracted TOF for each incident photon energy and detector angle. The energy spectra of the ^{3}He and N_2 targets were normalized to their corresponding integrated photon flux and the neutron background subtracted yield (^{3}He neutron events/F) of ^{3}He at the i^{th} energy bin is calculated as

$$Y_i^{P/A} = Y_i^{P/A,^3He} - Y_i^{N_2} \tag{6.2}$$

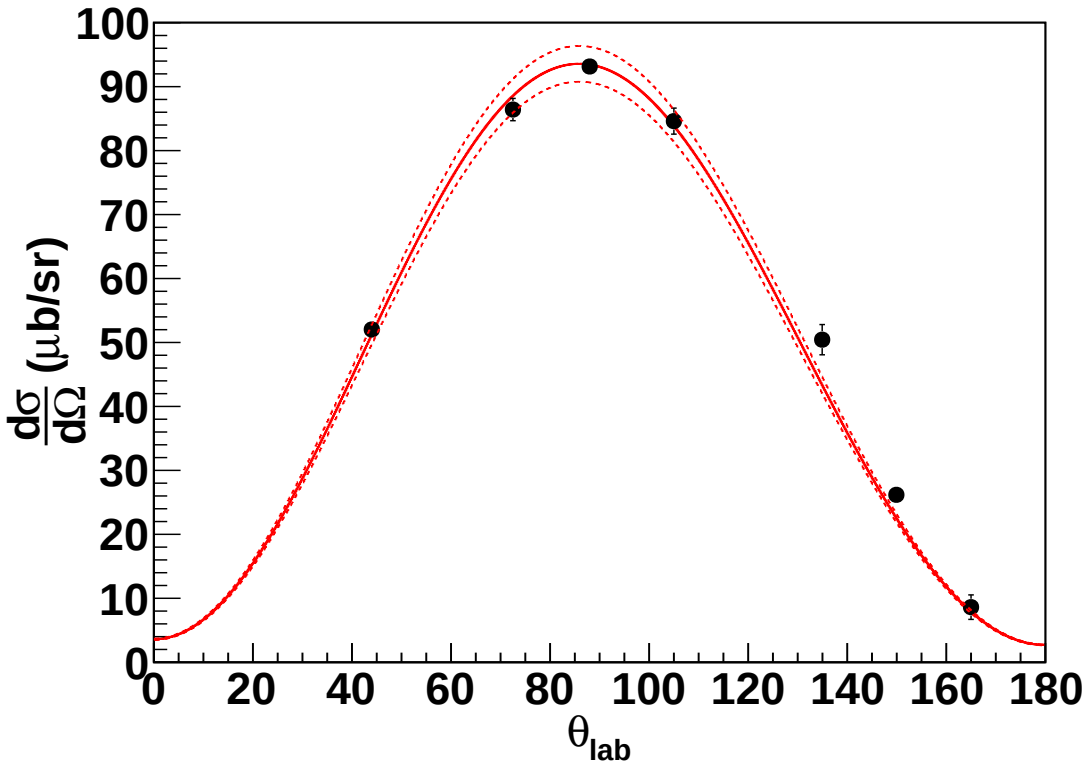

FIGURE 6.3: (Color online) The same as in Figure 6.1 but for E_γ=16.5 MeV. The total cross is equal to 787±23.5 μb [DG92, Bir85, Ber86, Sko74].

Table 6.2: The same as in Table 6.1 but for E_γ=16.5 MeV. Both detectors at 30.0° were removed from this analysis.

θ_{lab}	$d\sigma/d\Omega(\mu b/sr)$
44.0°	52.0±0.4±0.4
72.5°	86.4±0.5±1.7
89.0°	93.2±0.5±0.8
105.0°	84.6±0.5±2.0
135.0°	50.0±0.4±2.4
150.0°	26.3±0.3±0.7
165.0°	8.6±0.2±1.9

where $Y_i^{P/A,^3He}$ and $Y_i^{N_2}$ are the measured yields of ^{3}He and N_2 cells. The background subtracted yields are combined and the yields for parallel and antiparallel spin-helicity states are extracted as

$$Y_{i,ext}^{P/A} = \frac{1}{2}(Y_i^P(1 \pm \frac{1}{P_{tc}P_b}) + Y_i^A(1 \mp \frac{1}{P_{tc}P_b})) \tag{6.3}$$

where P_{tc} and P_b are the target and the beam polarization, respectively. The double-differential cross section is defined as

$$\frac{d^3\sigma^{P/A}}{d\Omega dE_n} = \frac{Y_{i,ext}^{P/A}}{\epsilon_i^{syst}\Delta\Omega\Delta E N_t} \tag{6.4}$$

where ϵ_i^{syst} is the system efficiency accounting for both the intrinsic efficiency of the neutron detector and the neutron multiple scattering effect calculated at the i^{th} energy bin, $\Delta\Omega$ is the acceptance from the 40 cm long target to the neutron detector, ΔE is the width of the neutron energy bin and N_t is the ^{3}He target thickness determined to be $(8.4\pm0.1)\times10^{21}$ atoms/cm^2 (at 12.8 and 14.7 MeV) and $(8.3\pm0.3)\times10^{21}$ atoms/cm^2 (at 16.5 MeV). The system efficiencies ϵ_i^{syst} were calculated as a function of E_n based on TOF using a GEANT4 simulation of the experiment and the light-output response of the neutron detectors that is determined in Ref. [Tro09].

Figures 6.4 and 6.5 show the spin-helicity dependent double-differential cross sections obtained at incident photon energies of 12.8 and 14.7 MeV respectively for both spin-helicity states as a function of the outgoing neutron energy and laboratory angles. The solid and dashed curves are the GEANT4 simulation results using the calculations provided by Deltuva *et al.* and Skibiński *et al.* as cross section inputs. The band in each panel shows the overall systematic uncertainties combined in quadrature.

The experimental results agree better with the calculations of Deltuva *et al.* at

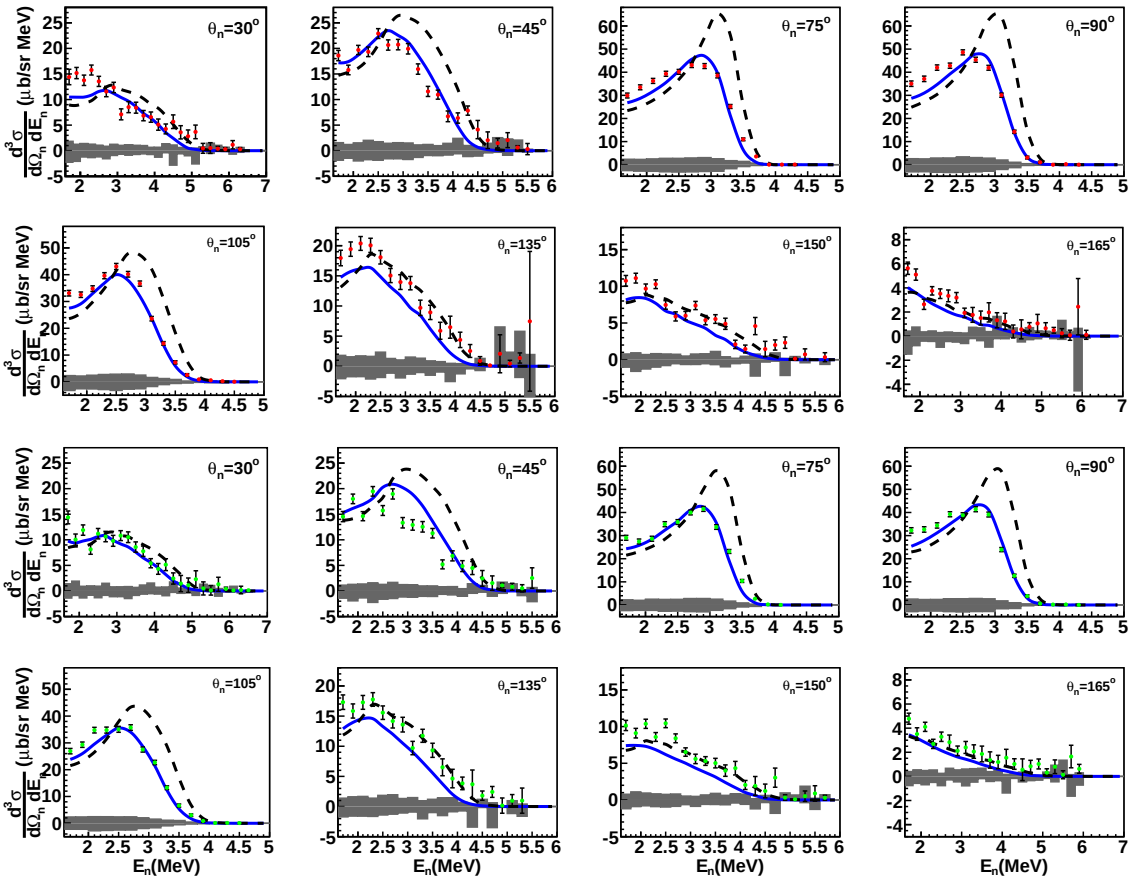

FIGURE 6.4: (Color online) Experimental spin-helicity dependent double-differential cross sections for both parallel (two top rows) and antiparallel (two bottom rows) spin-helicity states as a function of the neutron energy, E_n, E_γ=12.8 MeV. They are compared with the calculations of Deltuva *et al.* (solid curve) and Skibiński *et al.* (dashed curve). The neutron energy bin width is 0.2 MeV. The band at the bottom of each histogram shows the combined systematic uncertainties.

45 °-105 ° neutron angles. More specifically, the data favor the location of the high energy neutron peak predicted by Deltuva's *et al.* as well as the sharp decrease of the energy distributions predicted by both groups. At 30 °, 135 °, 150 ° and 165 °, the results do not appear to have any discriminating power between the calculations, although the magnitudes and the shapes of the distributions are in general agreement with both calculations. This is due to two reasons: first, the calculations do not differ significantly at the far forward and backward angles and thus the limited statistics

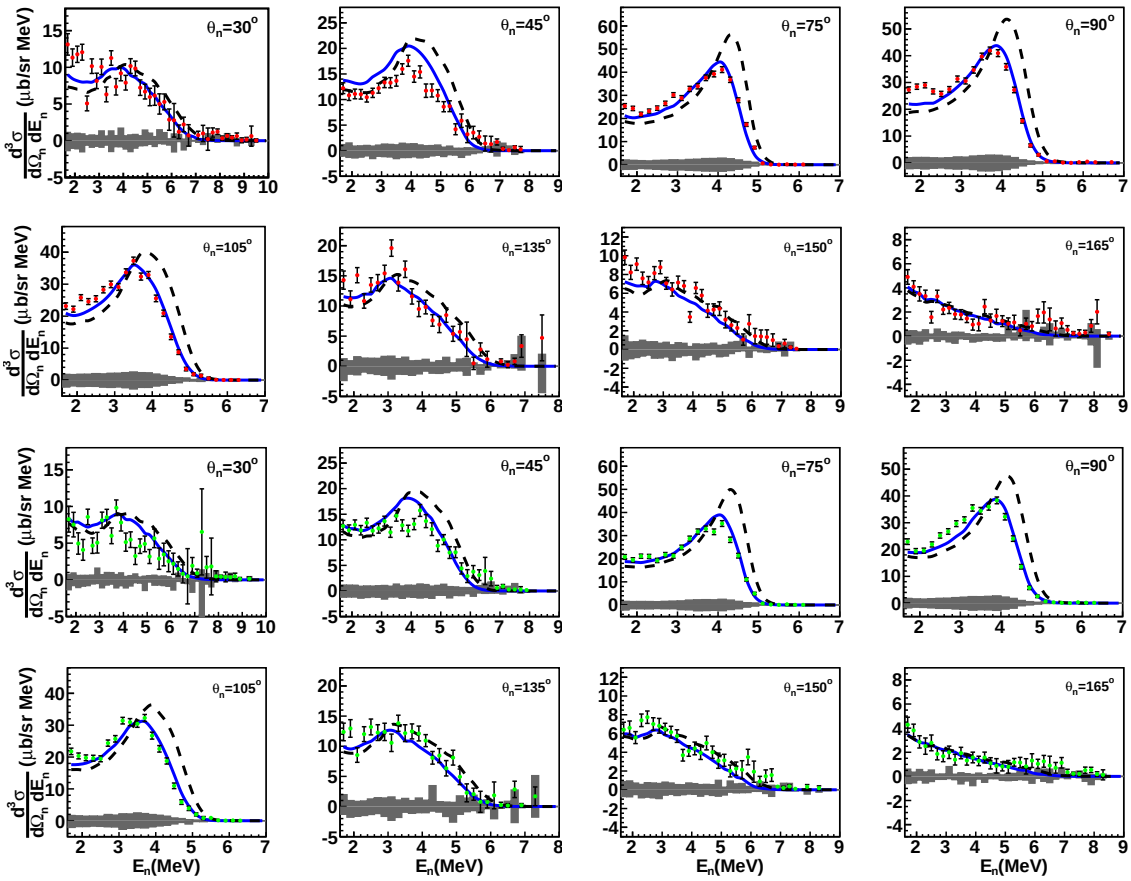

FIGURE 6.5: (Color online) As in Figure 6.4 at E_γ=14.7 MeV.

do not allow to discriminate between the predictions; second, the finite-geometry effect resulting from the long target is significant and so the reconstructed energies based on the TOF appear to be higher compared to the actual energies predicted by the kinematics. This results in the spread of the neutron counts to a wider energy region and the consequent smearing of the distributions. However, the spin-helicity dependent double-differential cross sections are overall larger in the parallel than those in the antiparallel spin-helicity state as predicted by the calculations for both incident photon energies and all neutron scattering angles.

Fig.6.6 show the spin-helicity dependent double differential cross sections for the extended target obtained at incident photon energy of 16.5 MeV for both spin-helicity states as a function of neutron energy, E_n and laboratory angles. Although the cross

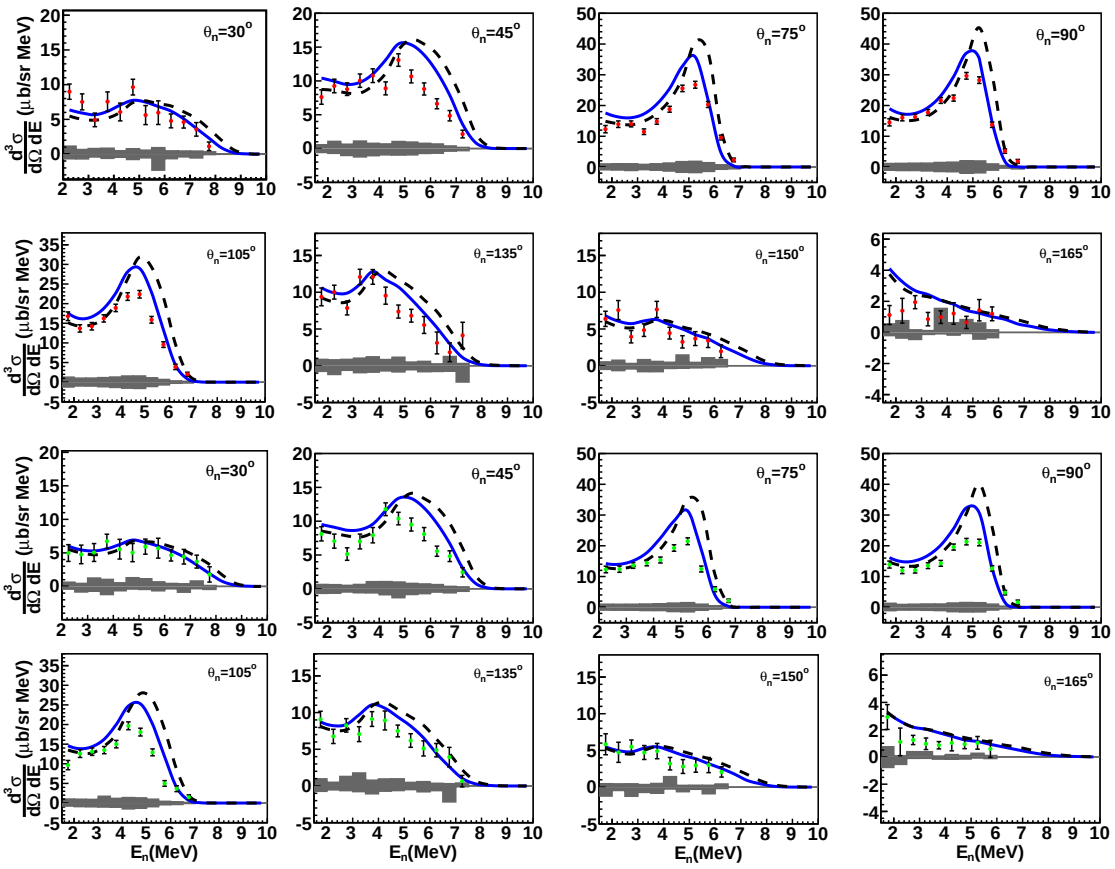

FIGURE 6.6: (Color online) As in Figure 6.4 at E_γ=16.5 MeV. The neutron energy bin width is 0.5 MeV.

sections are overall larger in the parallel than those in the antiparallel spin-state, the distributions can no longer be described by any of the aforementioned calculations in terms of their magnitudes. An abnormal excess of neutron events is observed close to the end-point energies of the distributions for 30 °, 45 °, 150 ° and 165 ° laboratory scattering angles due to large backgrounds. These energy bins are removed and their contribution to the overall strength of the distributions which is found to be $\sim$ 1% for both spin-states and all scattering angles, is added heuristically based on the theory.

6.4 The Correction of Data for Finite Geometry Effects

The extended nature of the target used in this experiment and the dimensions of the detector made necessary finite-geometry corrections in order to extract the differential cross sections. To correct for the finite-geometry effect and extract the experimentally determined spin-helicity dependent cross sections for a point-like target, an iterative analysis was necessary. First, a conversion of E_n(TOF) to actual neutron energies, E_n, was calculated for all measured angles and spin-states using a two dimensional map. The x-axis of the map is the E_n(TOF) while the y-axis is E_n. All vertical bins of the map corresponding to E_n(TOF) are normalized to unity. The map is constructed based on an initially assumed distribution and each map element represented the probability of a neutron event with observed E_n(TOF) having an actual neutron energy E_n. Figure 6.7 shows the two dimensional map for the neutron scattering angle of 165 °.

The double differential cross sections expressed in terms of E_n, $\frac{d^3\sigma^{ext,exp}}{\Delta\Omega dE_n}$, are further multiplied by the ratio of the point-like cross sections, $\frac{d^3\sigma^{point,sim}}{d\Omega dE_n}$, (initially chosen to construct the map) to the extended target GEANT4 simulation results, $\frac{d^3\sigma^{ext,sim}}{\Delta\Omega dE_n}$, in order to cancel out the extended target effect. The operation can be expressed mathematically as

$$\frac{d^3\sigma^{point,exp}}{d\Omega dE_n} = \frac{\frac{d^3\sigma^{ext,exp}}{\Delta\Omega dE_n}}{\frac{d^3\sigma^{ext,sim}}{\Delta\Omega dE_n}} \frac{d^3\sigma^{point,sim}}{d\Omega dE_n}. \tag{6.5}$$

A new simulation was performed using the distributions resulting from Equation 6.5, a new map was constructed and the process was repeated until a full convergence was reached between the converted experimental distributions and the extended target results from the GEANT4 simulation.

Figures 6.8, 6.9 and 6.10 show the spin-helicity dependent double-differential cross

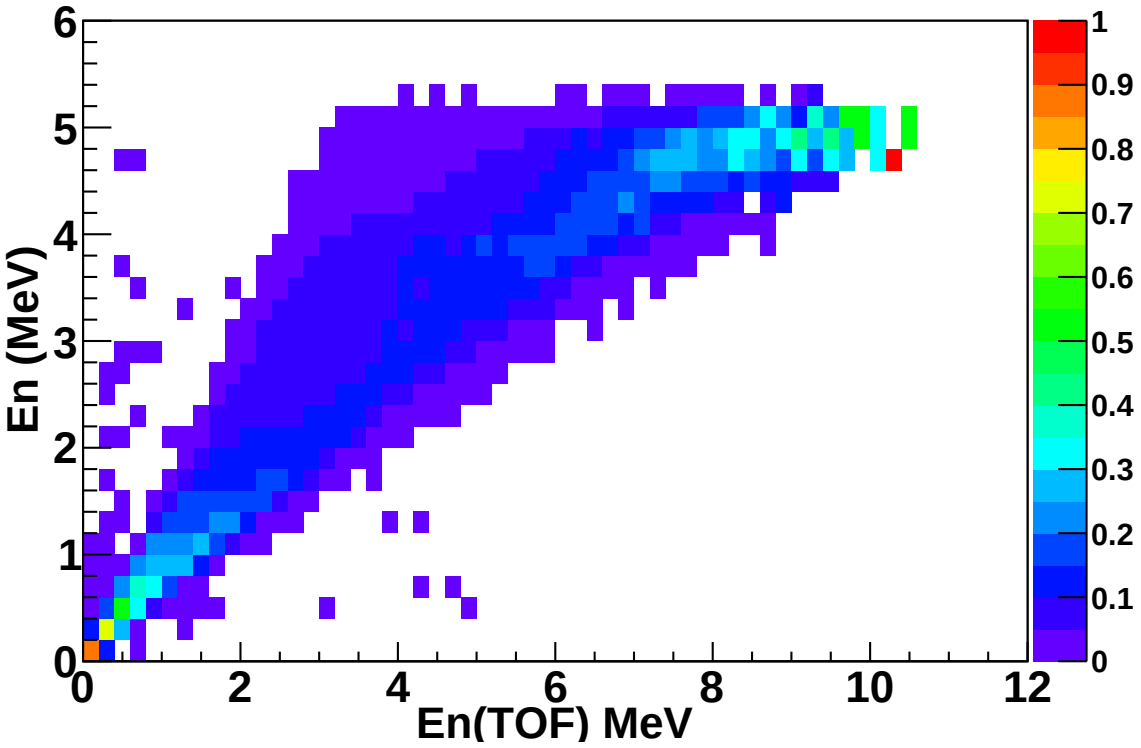

FIGURE 6.7: (Color online) The two dimensional map used for the conversion of the E_n(TOF) to E_n at the neutron scattering angle of 165° and the incident photon of 16.5 MeV. The values of the energy reconstructed based on the time of flight appears to be much larger than the actual neutron energies.

sections corrected for the finite geometry effect at the incident photon energies of 12.8, 14.7 and 16.5 MeV. While the statistical fluctuations of the distributions with respect to E_n(TOF) are mainly in the far forward and backward angles due to the spread of the neutron counts to a wider reconstructed energy region, the fluctuations of the distributions with respect to E_n are smoothed out since the neutrons concentrate in a much smaller actual energy region.

Good agreement between the data and the calculations of Refs. [Del04, Del05b, Del05a, Del09] can be seen for all neutron scattering angles and both target spin and beam helicity states at the incident photon energies of 12.8 and 14.7 MeV. Although at the incident photon energy of 12.8 MeV similar agreement is observed for most of

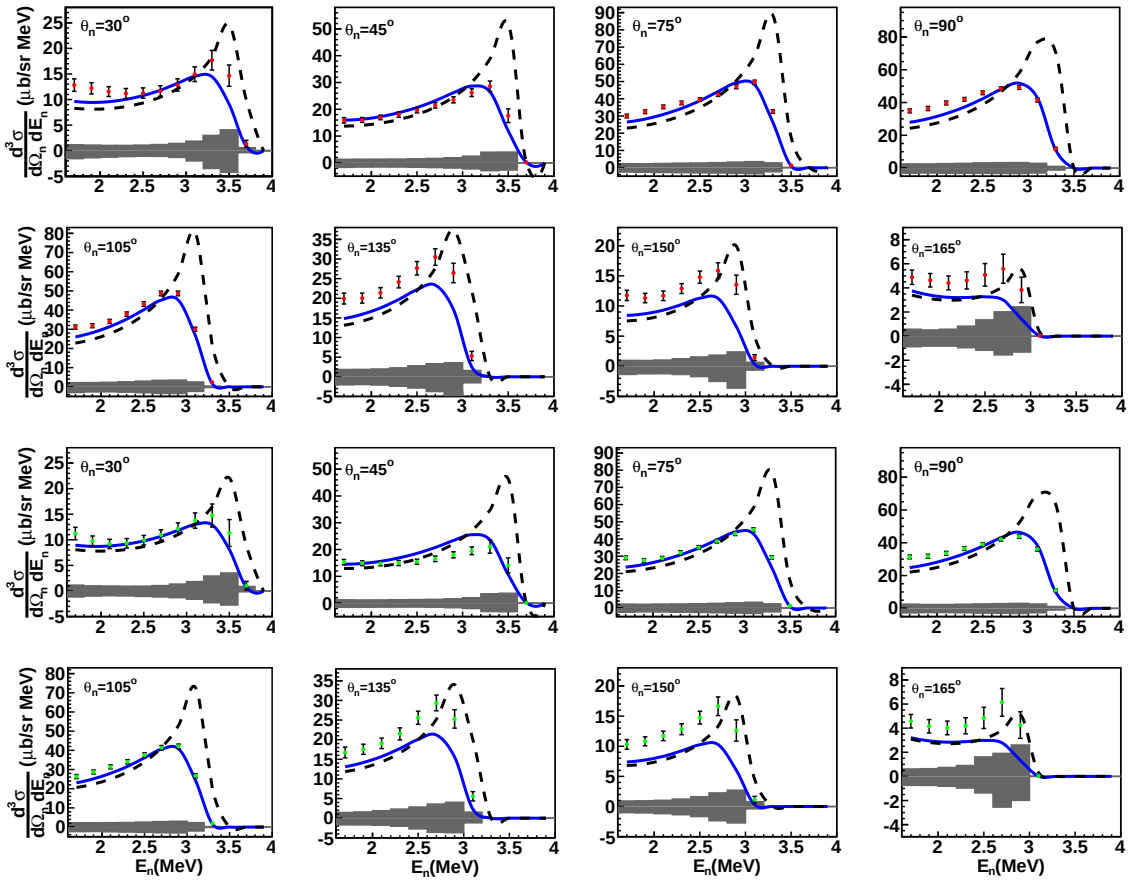

FIGURE 6.8: (Color online) Spin-helicity dependent double-differential cross sections corrected for the acceptance effect, for parallel (two top rows) and antiparallel (two bottom rows) spin-helicity states as a function of the neutron energy, E_n, compared with the calculations based on Refs. [Del04, Del05b, Del05a, Del09] (solid curve) and Refs. [RS03, RS05] (dashed curve) at the incident photon energy of 12.8 MeV. The neutron energy bin width is 0.2 MeV. The band at the bottom of each histogram shows the combined systematic uncertainties.

the angles, the amplitudes of the experimental distributions appear to be systematically higher than the calculations of Refs. [Del04, Del05b, Del05a, Del09] at 135°, 150° and 165° neutron angles. A good agreement between the double-differential cross sections of the unpolarized three-body break up of ^{3}He and the calculations of Refs. [Del04, Del05b, Del05a, Del09] is also reported in Refs. [Per10, Per11]. Apart from the data presented in Refs. [Per10, Per11], only one other measurement [Gor74] provided data on double-differential cross sections and none of the other measure-

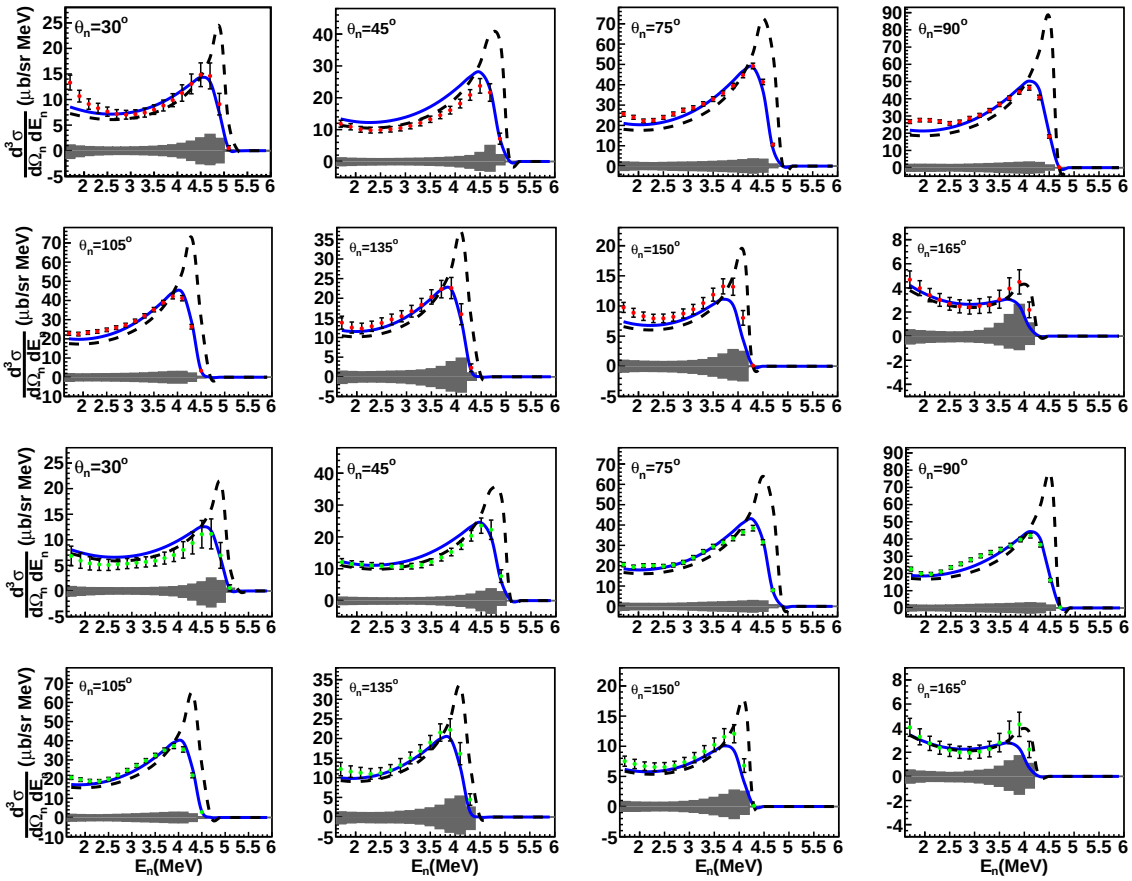

FIGURE 6.9: (Color online) As in Figure 6.8 at 14.7 MeV.

ments prior to our experiment used polarized photon beam and a polarized ^{3}He target. The differences between the two calculations are dominated by the proton-proton Coulomb force that is included only in Refs. [Del04, Del05b, Del05a, Del09].

On the contrary a difference between the data and the calculations can be seen for all neutron scattering angles and both target spin and beam helicity states at the incident photon energy of 16.5 MeV. This difference in magnitude between the measured cross sections and the calculations is smaller at the low neutron energy bins while it gets bigger at the high energy neutron peak region.

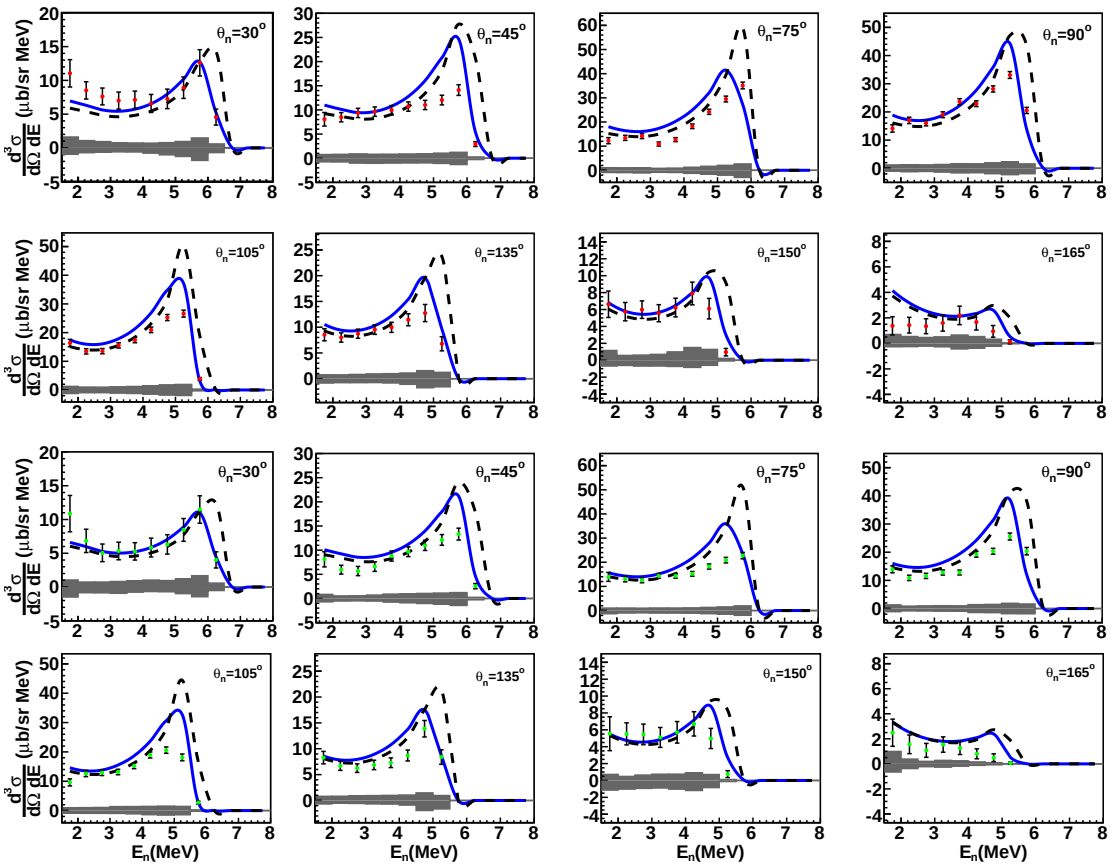

FIGURE 6.10: (Color online) As in Figure 6.8 at 16.5 MeV. The neutron energy bin width is 0.5 MeV.

6.5 Spin-Helicity Dependent Single Differential Cross Sections of ^{3}He($\vec{\gamma}$,n)pp Reaction

The partial single-differential cross sections for E_n>1.5 MeV (at 12.8 and 14.7 MeV) and E_n>2.0 MeV (at 16.5 MeV) are extracted by integrating the corrected double-differential cross section distributions over the outgoing neutron energy. At the incident photon energies of 12.8 and 14.7 MeV, the unmeasured part of the distributions is taken to be equal to the average of the calculated cross sections of Refs. [Del04, Del05b, Del05a, Del09] and [RS03, RS05] for $E_n < 1.5$ MeV. The difference between the calculations is small as can be seen in the Figures of Appendix A and only varied from 1 to 8% depending on the incident photon energy, the spin-

Table 6.3: The spin-helicity dependent single-differential cross sections and their statistical and systematic uncertainties, respectively, as a function of the neutron scattering angle at E_γ=12.8 MeV.

Angle	$d\sigma_P/d\Omega(\mu b/sr)$	$d\sigma_A/d\Omega(\mu b/sr)$
30°	40.2±1.3±5.7	35.8±1.5±4.8
45°	60.4±1.3±6.2	51.2±1.5±5.5
75°	99.0±0.9±7.8	88.8±0.9±6.7
90°	100.8±1.0±7.9	88.7±1.0±6.7
105°	90.6±0.9±7.3	79.9±0.9±6.0
135°	54.0±1.4±6.6	48.8±1.4±5.6
150°	31.9±1.0±4.7	29.8±1.0±3.8
165°	15.7±1.0±3.9	14.5±1.0±4.1

helicity state and the scattering angle. This introduced an additional systematic uncertainty to the single-differential cross sections of no more than 4%. At the incident photon energy of 16.5 MeV, the unmeasured part for E_n <2 MeV was added based on the theoretical distributions which were normalized to the magnitude of the first valid neutron bin (2.0-2.5 MeV) for both states and all angles.

Figures 6.11, 6.12 and 6.13 show the spin-helicity dependent single-differential cross sections for parallel (filled squares) and antiparallel (open squares) spin-helicity states at E_γ of 12.8, 14.7 MeV and 16.5 MeV in comparison with both calculations. The cross section data are in general agreement in all angles with the calculations based on Refs. [Del04, Del05b, Del05a, Del09] for the incident photon energies of 12.8 and 14.7 MeV. The cross sections do not agree with either theoretical calculation at 16.5 MeV. The larger difference between data and the theoretical calculations is observed at the central angles while a smaller difference is observed at the far forward and backward angles. The results of the spin-helicity dependent single-differential cross sections for all incident energies are given in Tables 6.3, 6.4 and 6.5.

Legendre polynomials up to the 4^{th} order were used to fit the differential cross sections acquired for each spin-helicity state at both incident photon energies. The

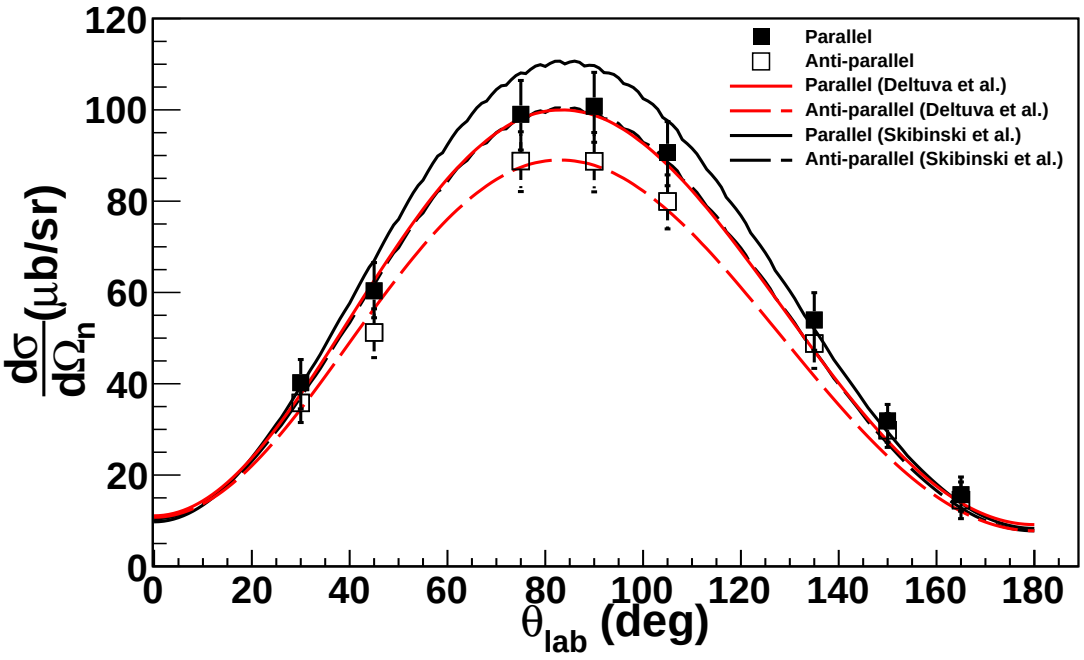

FIGURE 6.11: (Color online) Spin-helicity dependent single-differential cross sections for parallel (filled squares) and antiparallel (open squares) spin-helicity states with statistical and systematic uncertainties as a function of the neutron scattering angle, θ_{lab} at E_γ=12.8 MeV. The data are compared with the calculations based on Refs. [Del04, Del05b, Del05a, Del09] (red curves) and [RS03, RS05] (black curves). The solid and the long-dashed curves are the calculations for the parallel and antiparallel spin-helicity states, respectively. (The statistical uncertainties in most of the angles are small and can not be seen in the figure.)

Table 6.4: As in Table 6.3 at E_γ=14.7 MeV.

Angle	$d\sigma_P/d\Omega(\mu b/sr)$	$d\sigma_A/d\Omega(\mu b/sr)$
30°	43.3±1.5±5.6	32.6±1.9±5.0
45°	60.0±1.5±6.4	59.2±1.5±6.7
75°	118.0±1.0±8.8	99.1±1.1±7.3
90°	118.4±1.1±8.8	105.3±1.1±7.7
105°	105.4±1.0±8.1	92.2±1.0±7.2
135°	57.6±1.8±7.4	52.3±1.8±7.6
150°	36.0±1.0±4.8	30.6±1.0±4.3
165°	16.0±0.9±4.0	13.9±1.0±3.2

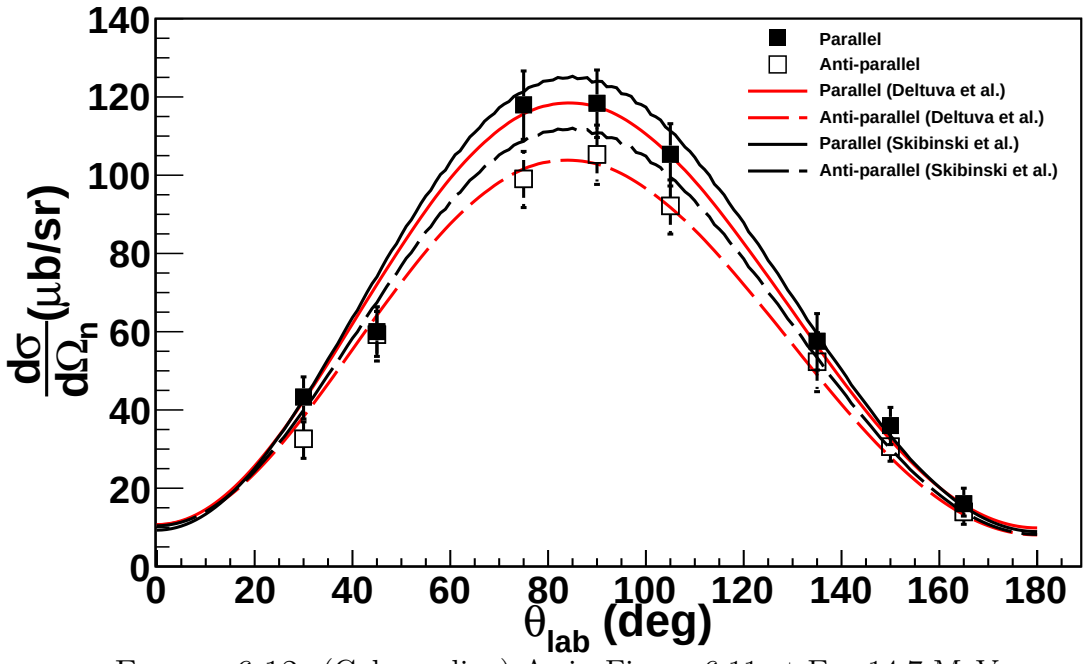

FIGURE 6.12: (Color online) As in Figure 6.11 at E_γ=14.7 MeV.

fitted curves were integrated over the angle and the total cross sections were extracted for both energies and the two spin-helicity states. The systematic uncertainties of the total cross sections were determined by varying the differential cross sections from the central values by plus or minus the overall systematic uncertainties that can be seen in Tables 6.3, 6.4, 6.5 and then performing the fit. The systematic uncertainty of the total cross sections was taken as half of the difference between

Table 6.5: As in Table 6.3 at E_γ=16.5 MeV.

Angle	$d\sigma_P/d\Omega(\mu b/sr)$	$d\sigma_A/d\Omega(\mu b/sr)$
30°	50.6±3.0±7.7	42.9±3.3±7.7
45°	56.4±1.8±6.2	48.7±1.9±5.6
75°	95.1±1.8±7.4	85.0±2.0±6.6
90°	109.3±1.9±8.3	84.8±1.9±6.5
105°	90.6±1.8±6.8	72.3±1.8±6.2
135°	48.6±2.2±6.4	40.7±2.1±6.1
150°	32.2±2.3±5.9	27.7±2.5±4.5
165°	8.6±1.3±3.5	8.9±1.7±2.1

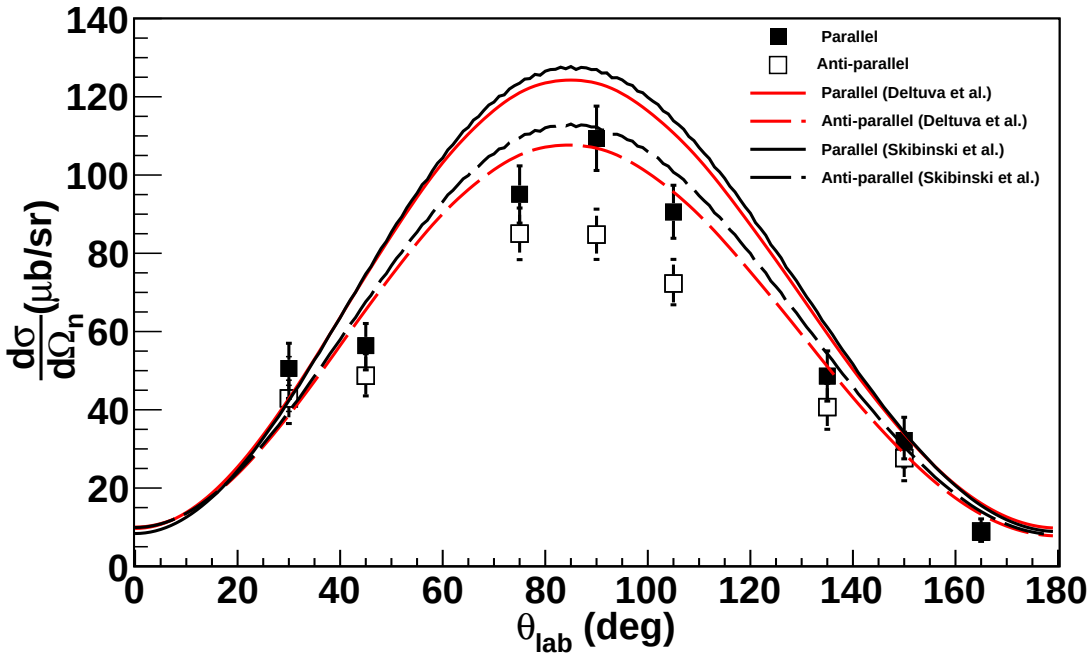

FIGURE 6.13: (Color online) As in Figure 6.11 at E_γ=16.5 MeV.

these two integrals of the new fits. The spin-helicity dependent total cross sections and the contributions from the three-body breakup channel to the GDH integrand are presented in the next section.

6.6 Contributions from the Three-body Photodisintegration of ^{3}He to the GDH Integral

Table 6.6 summarizes the spin-helicity dependent total cross sections and the contributions from the three-body photodisintegration to the ^{3}He GDH integrand for both photon energies and predictions from Deltuva *et al.* and Skibiński *et al.* The difference $\sigma^P - \sigma^A$ is sensitive not only to Coulomb repulsion, but also to relativistic single-nucleon charge corrections [Del04, Del05b, Del05a, Del09].

Fig. 6.14 shows the contributions from three-body photodisintegration to the ^{3}He GDH integrand together with the theoretical calculations [Del04, Del05b, Del05a, Del09, RS03, RS05] as a function of the incident photon energy. Both predictions

Table 6.6: Total cross sections, σ^P and σ^A and the contributions from the three-body photodisintegration to the ^{3}He GDH integrand, $(\sigma^P - \sigma^A)/\nu$, with statistical uncertainties followed by systematics, compared with theoretical predictions.

ν (MeV)	$\sigma^P(\mu b)$	$\sigma^A(\mu b)$	$(\sigma^P - \sigma^A)/\nu$ (fm^3)
This work 12.8	861±5±81	765±5±71	0.147±0.010±0.018
Deltuva *et al.*	872	777	0.146
Skibiński *et al.*	956	872	0.131
This work 14.7	999±5±89	869±5±78	0.174±0.011±0.020
Deltuva *et al.*	1026	900	0.168
Skibiński *et al.*	1079	970	0.146
This work 16.5	898±9±84	743±10±76	0.186±0.017±0.015
Deltuva *et al.*	1076	935	0.169
Skibiński *et al.*	1099	979	0.143

show that the GDH integrand maximizes at 16 MeV and decreases significantly after 40 MeV. A very good agreement is observed between the measurements and the calculations from Deltuva *et al.* at 12.8 and 14.7 MeV while the value of the measurement at 16.5 MeV is consistent with the theoretical prediction of Deltuva *et al.* within the statistical and systematic uncertainties. To further quantify the three-body contribution to the GDH integral, measurements above 16.5 MeV for the three-body photodisintegration channel are necessary. These measurements combined with the recently acquired data from the two-body photodisintegration channel will help to constrain further the dominant contribution to the GDH integral for ^{3}He below the pion-threshold.

6.7 Unpolarized Total Cross Sections of the Three-body Photodisintegration of ^{3}He

The extracted spin-helicity dependent cross sections were averaged and the total unpolarized cross sections were calculated for each incident photon energy. Figure 6.15 shows all unpolarized total cross sections data up to 30 MeV together with the total cross section calculations from Refs. [Del04, Del05b, Del05a, Del09] (solid curve) and

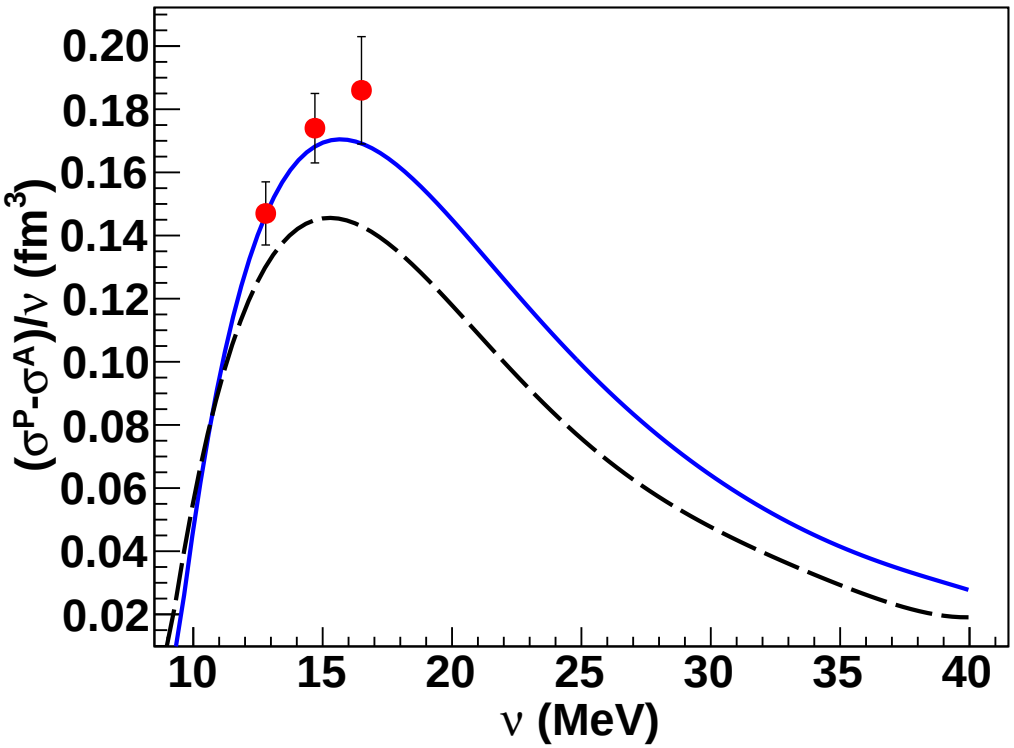

FIGURE 6.14: (Color online) GDH integrand results with statistical uncertainties only compared with the theoretical predictions from Deltuva *al.* (dashed curve) and Skibiński *et al.* (solid curve).

Refs. [RS03, RS05] (dash-dotted curve). The results at 12.8 and 14.7 MeV are in very good agreement with the most recently published data (filled stars) using an unpolarized ^{3}He target at the same incident photon energies [Per10, Per11]. The averaged cross section at 16.5 MeV agrees with the measurements of Refs. [Ber74, Ger66b] and the recent measurement of Refs. [Nai06].

Although a general agreement between the two models and most of the experimental data can be seen in Figure 6.15 for incident photon energy below 15 MeV, a serious discrepancy can be observed above 15 MeV between the data of Refs. [Ger66b] (open circles) and [Ber74] (open squares) and the theoretical predictions. This discrepancy leads to the need of more precise data at the energy region above 16.5 MeV using preferably monochromatic photon energy beams as the one used at the HIγS

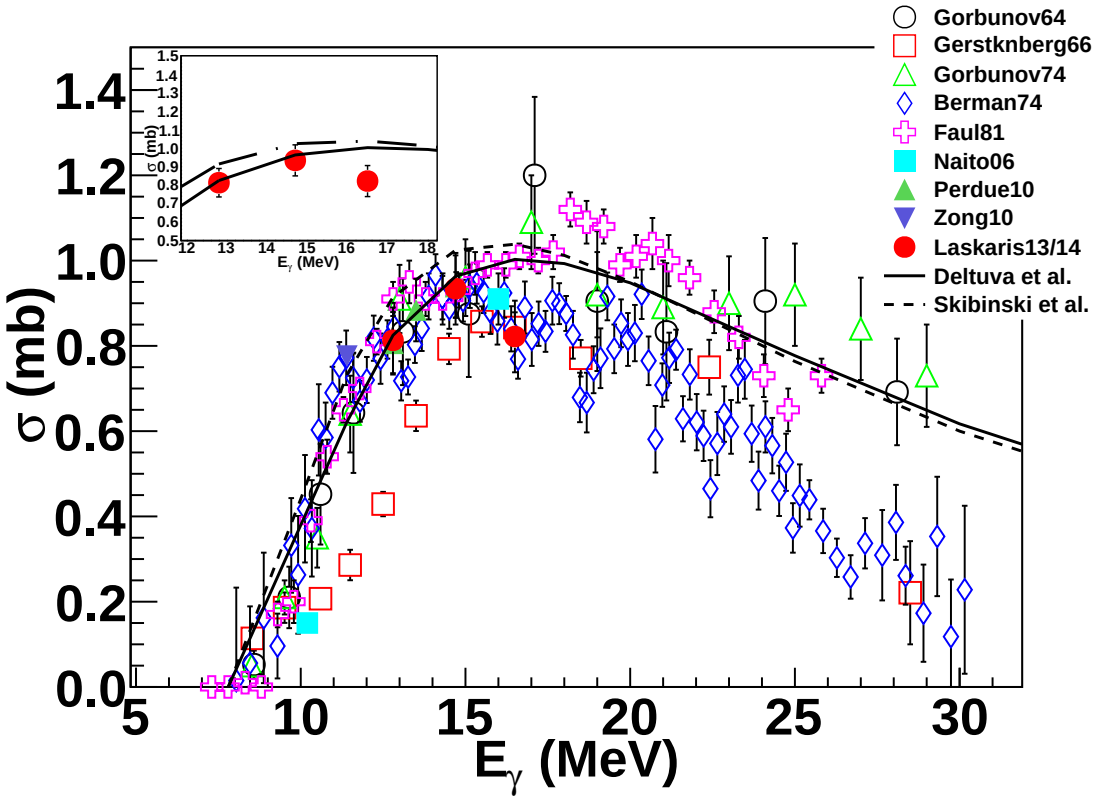

FIGURE 6.15: (Color online) All currently available total cross section data for the $^3He(\gamma, n)pp$ reaction up to 30 MeV: Refs. [Las13, Las14] and data presented for first time in this thesis (filled circles), Ref. [Gor64] (open circles), Ref. [Ger66b] (open squares), Ref. [Gor74] (open upward triangles), Ref. [Ber74] (diamonds), Ref. [Fau81] (open crosses), Ref. [Nai06] (filled squares), Ref. [Per10] (filled upward triangles), Ref. [Zon10] (filled donward triangle) in comparison to the calculations by Deltuva *et al.* (solid curve) and Skibiński *et al.* (dashed-curve). We used filled and open markers for the recent and old data, respectively. In the insert, the data presented in this thesis are shown and compared with the theories.

facility. However, the performance of similar experiments on $^3\vec{H}e(\vec{\gamma}, n)pp$ reaction at higher energies has to deal with the problem of neutron backgrounds. All glass target cells of polarized ^{3}He consist of elements that undergo (γ, n) reactions with cross sections higher or much higher than the cross sections of the reaction of interest. A detailed study of the backgrounds has shown that the same experimental technique described in this paper can not be applied to the detection of neutrons

above 16.5 MeV since beyond this energy the contribution of oxygen in the air and in the glass to the neutron background becomes important. A possible solution to this background problem would require the detection of one of the protons and the neutron from the $^3He(\gamma, n)pp$ reaction in coincidence. The two-body experiment can be considered as a first step towards the three-body coincidence measurement.

6.8 Systematic Uncertainties

Two types of systematic uncertainties were identified in this experiment: the bin dependent uncertainties and the overall normalization uncertainties. The bin dependent systematic uncertainties are in principle asymmetric and arose from the uncertainty associated with the PH cut location. In order to study the PH cut contribution to the overall systematic uncertainty, the PH cut location was varied and the corresponding double-differential cross sections have been extracted. The PH cut location was changed by 0.01 to 0.02 MeV_{ee} determined by the uncertainty at the cesium edge for each detector. The systematic uncertainty due to the PH cut was calculated as the difference between the nominal double-differential cross sections and the cross sections obtained after the change of the PH cut location. The contribution of the systematic uncertainty from the PH cut to the overall systematic uncertainty varied from ∼2% to ∼10% for each detector angle with a maximum of ∼30% at 165 °.

The normalization systematic uncertainties are symmetric and affected only the magnitude of the double-differential cross sections but not the shape of the distributions. The major sources of the normalization uncertainties are:

- The uncertainty on the intrinsic efficiency of the detectors which is inherited by the $\delta\epsilon_i^{syst}$ and it is found to be 2.8% [Tro09, Set96].

- The uncertainty on the ^{3}He cell thickness, δN_t, in which the main contributor

is the uncertainty in the temperature of the ^{3}He cell and it is found to be 1.3% (at 12.8 and 14.7 MeV) and 4.2% (at 16.5 MeV).

- The uncertainty on the acceptance, $\delta\Delta\Omega$, 2% which is determined by the uncertainty of distance from the center of the target to the face of the detectors.

- The uncertainty of the integrated photon flux is 5.7% (at 12.8 and 14.7 MeV) and 4.2% (16.5 MeV), it is dominated by the uncertainties of D_2O photodisintegration cross sections 4.0% (12.8 MeV), 4.6% (14.7 MeV) and 3.0% (16.5 MeV). Other contributors are the intrinsic efficiency of neutron detectors 2.8%, the solid angle 1% and the thickness of the D_2O or C_6D_6 target 0.6%.

- The uncertainty of the polarization of ^{3}He in the target chamber, δP_{tc}, which is 2.2% (12.8 and 14.7 MeV) and 4.2% (16.5 MeV). The main contributors to this uncertainty are the uncertainty of the constant κ, 1.5%, the number density n_{pc}, 1.1% (12.8 and 14.7 MeV) and 3.2% (16.5 MeV) and the derivative $\frac{d\nu_{EPR}}{dB}$, 0.16%.

- The photon beam polarization, P_b and its systematic uncertainty were determined by G. Rusev [Rus] based on data taken right before our experiment. The beam polarization was found to be consistent with 100% with a systematic uncertainty of 3% for both normal and reversed beam helicity states. Since the beam polarization was not measured during our experiment, we assigned a 5% systematic uncertainty for δP_b.

Table 6.7 gives a summary of all the normalization uncertainties at the incident photon energies of 12.8, 14.7 and 16.5 MeV.

Table 6.7: Summary of the sources of systematic uncertainty.

Source	Value at 12.8/14.7 MeV (%)	Value at 16.5 MeV (%)
δP_{tc}	2.2	4.2
δP_b	5.0	5.0
δP_γ	5.7	4.2
δN_t	1.3	4.2
$\delta \epsilon_i^{syst}$	2.8	2.8
$\delta \Delta\Omega$	2.0	2.0

6.9 Current Status of the Two-body Photodisintegration Analysis

The analysis for the two-body photodisintegration of ^{3}He in not concluded. In this section, we will present the current status of the analysis for the two-body photodisintegration of ^{3}He with double polarizations and the future plan for the conclusion of the analysis.

A description of data analysis for calibrating the SSB and extracting the proton events for each detector was given in Chapter 5. The extracted proton spectra divided by the integrated photon flux are compared with the simulated spectra using as input the calculations of Deltuva *et al.* The glass thickness implemented in the simulation is modified accordingly and always within the range dictated by the measurements taken throughout the ^{3}He and N_2 reference cells at the University of Virginia. An example of the current status of the comparison for all SSB detectors laying at the proton scattering angle of 95° is given in Figure 6.16. The same procedure needs to be repeated for both ^{3}He and N_2 reference cells until all simulated spectra at all proton scattering angles match the shape of the observed experimental proton yield spectra.

After that the background subtraction will occur in a similar way to the one described by Equation 6.2 in order to extract the clean proton yield. The yields for each spin-helicity state will be combined linearly according to Equation 6.3. The

integrated clean yields will be divided by the yield extracted from the simulation for each and every detector and will be multiplied by the point differential cross section in the same way as described by the Equation 6.5. The resulting differential cross section distribution will be used as the input for the next iteration until the observed experimental yield distributions match perfectly with the simulated ones. A fit using Legendre polynomials will be performed as described above in order to extract the spin-helicity dependent total cross sections and calculate the resulting contribution from the two-body photodisintegration channel to the GDH integrand of ^{3}He. This analysis is currently in progress and meaningful results will be presented soon.

6.10 Summary and Conclusions

We have carried out the first measurement of the two- and three-body breakup of polarized ^{3}He with circularly polarized photons at the incident photon energies of 29.0 MeV (two-body) and 12.8, 14.7, 16.5 MeV (three-body). The spin-helicity dependent double- and single-differential cross sections are extracted for the three-body photodisintegration experiments and compared with the state-of-the-art three-body calculations provided by Deltuva *et al.* and Skibiński *et al.*. The results agree significantly better with the calculations of Refs. [Del04, Del05b, Del05a, Del09] for the incident photon energies of 12.8 and 14.7 MeV. This leads to the conclusion that the inclusion of the proton-proton Coulomb repulsion in the calculations is important for the correct prediction of the magnitude and shape of the cross sections from the $^3\vec{H}e(\vec{\gamma}, n)pp$ reaction. The relativistic single-nucleon charge corrections together with the Δ-isobar excitation play also an important role in the correct estimation of the difference between the spin-helicity dependent cross sections.

None of the theoretical calculations can describe the results for the spin-helicity dependent double differential cross sections for the three-body photodisintegration of ^{3}He at 16.5 MeV. The spin-helicity dependent total cross sections and consequently

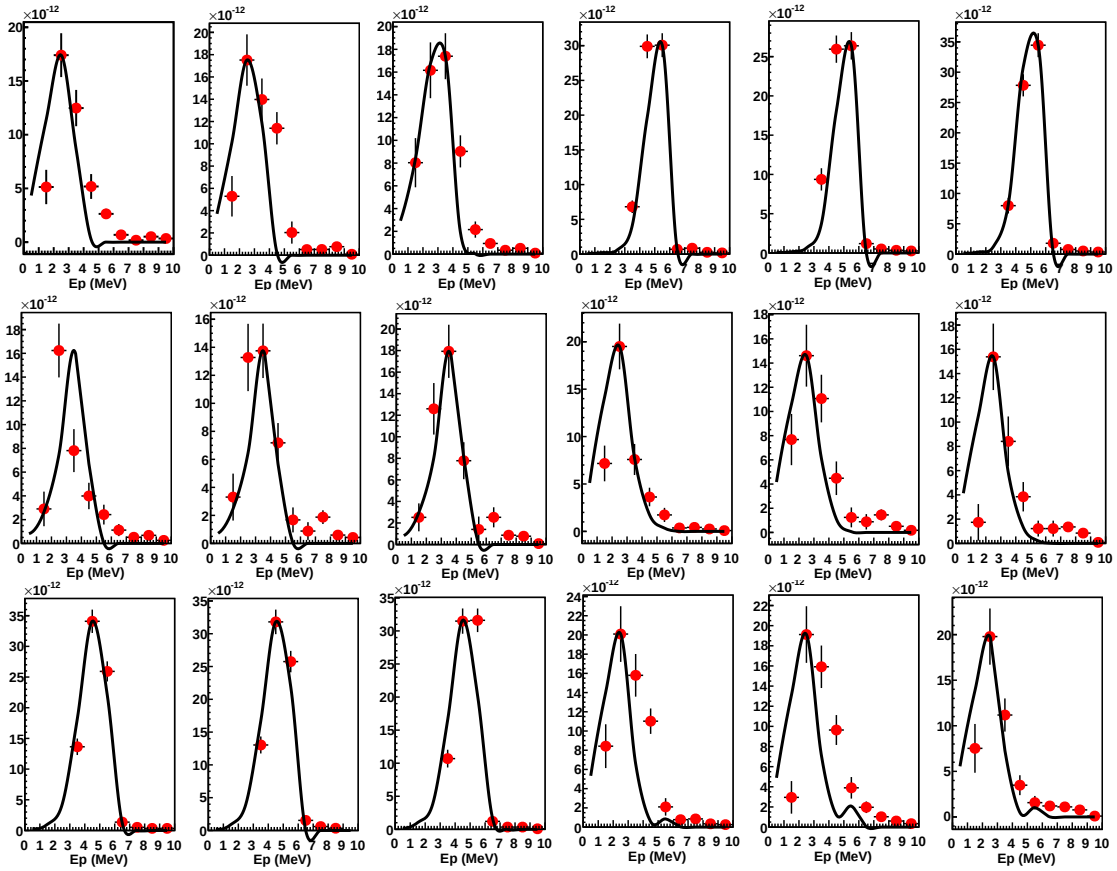

FIGURE 6.16: (Color online) The experimental proton yield spectra (red markers) in comparison to the spectra simulated using as input the calculations (black curves) provided by Deltuva *et al.* for all detectors at the proton scattering angle of 95°. The thickness of the glass in the simulation is adjusted in order to match the location of the proton energy peaks and an almost perfect agreement is observed at all angles. The proton energy bin width is 1.0 MeV.

the absolute magnitude of the unpolarized cross section are found to be smaller than the values predicted by the theories while the contribution from the three-body photodisintegration of ^{3}He to the GDH integrand at 16.5 MeV is found to be consistent within uncertainties with the calculations of Deltuva *et al.* Precise measurements of the three-body photodisintegration channel below and above the incident photon energy of 16.5 MeV will allow for further testing of the theoretical calculations and shed light on the GDH integrand of ^{3}He below pion production threshold.

Additional simulations are required for the extraction of the spin-helicity dependent single differential and total cross sections from the two-body photodisintegration of ^{3}He with double polarizations at 29.0 MeV. This is the first measurement of $^3\vec{H}e(\vec{\gamma}, p)d$ reaction and its contribution to the GDH integrand. The extracted result will be compared with theoretical predictions.

Appendix A

Appendix A

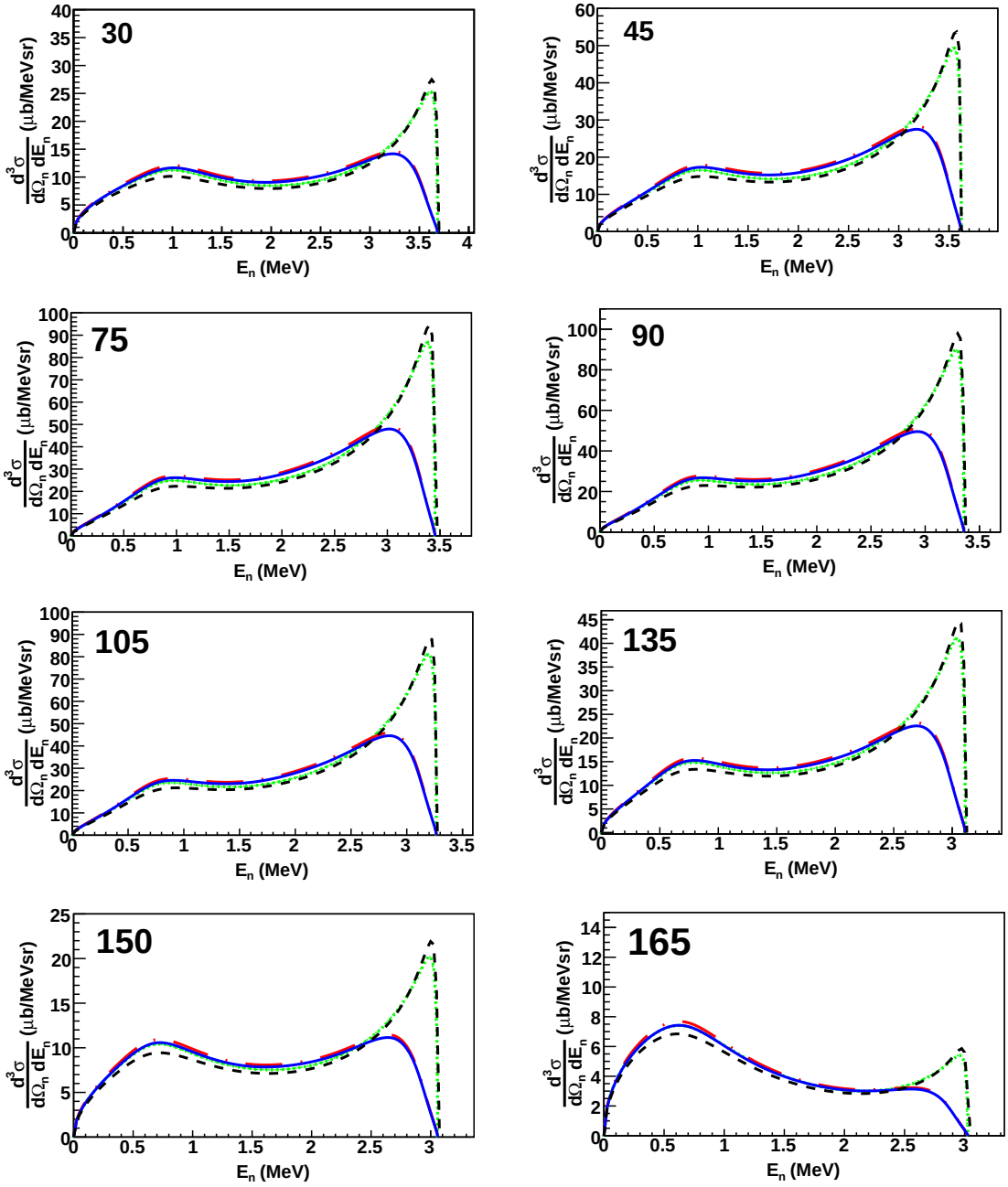

FIGURE A.1: (Color online) The double-differential cross section as a function of the outgoing neutron energy for the unpolarized three-body photodisintegration of ^{3}He at E_γ=12.8 MeV and all neutron scattering angles measured during the experiment. The short-dashed (black) curve is the calculation from Ref. [RS03, RS05] including AV18 + UIX + seagull + pion-in-flight-terms. The second group of calculations from Ref. [Del04, Del05b, Del05a, Del09] are (from top to bottom): dotted (green) curve: CD Bonn + RC; long-dashed dotted (red) curve (nearly invisible behind the solid curve): CD Bonn + RC + Coulomb force; solid (blue) curve: CD Bonn + Δ-isobar + RC + Coulomb force.

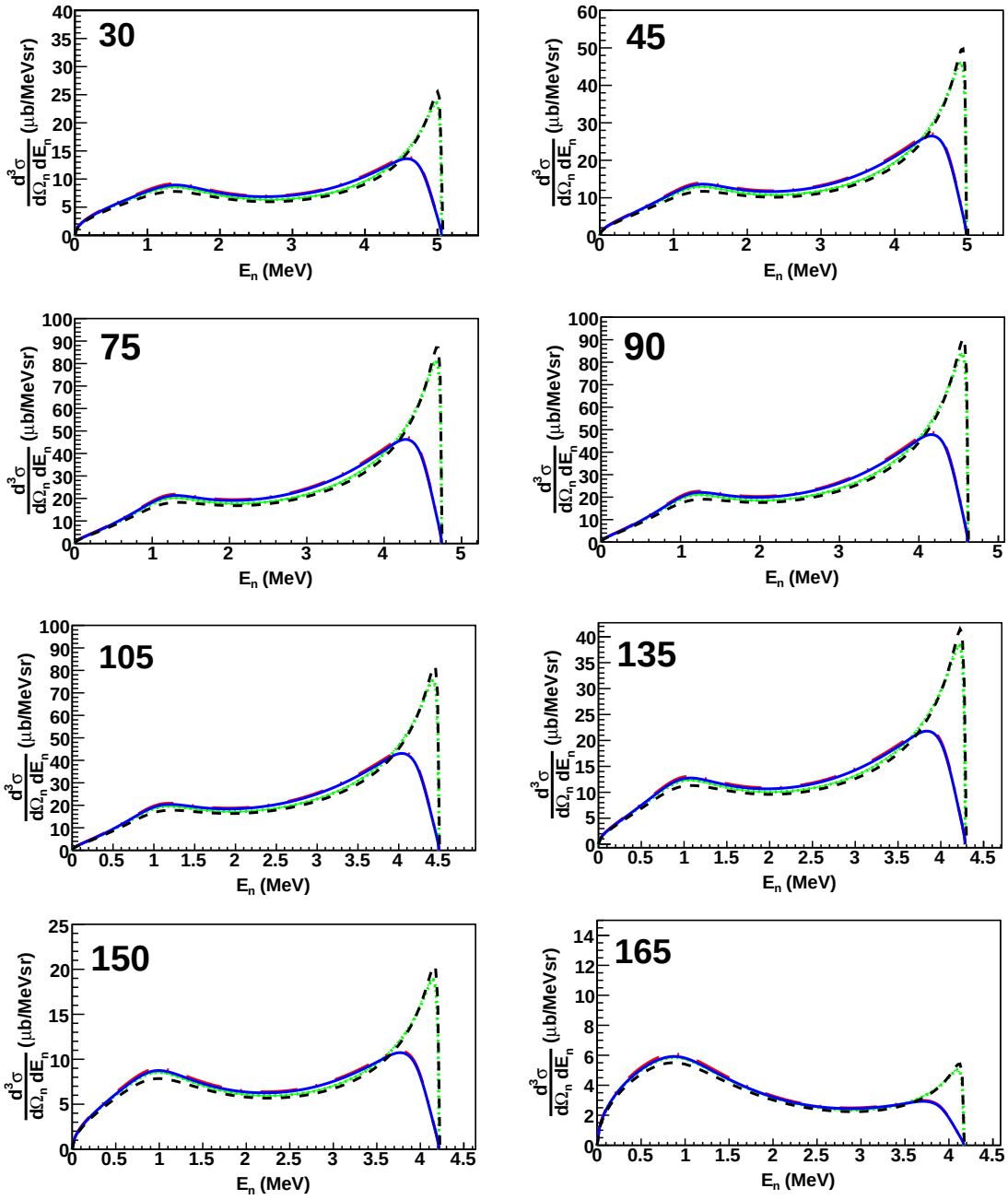

FIGURE A.2: (Color online) The same as Figure A.1 but for E_γ=14.7 MeV

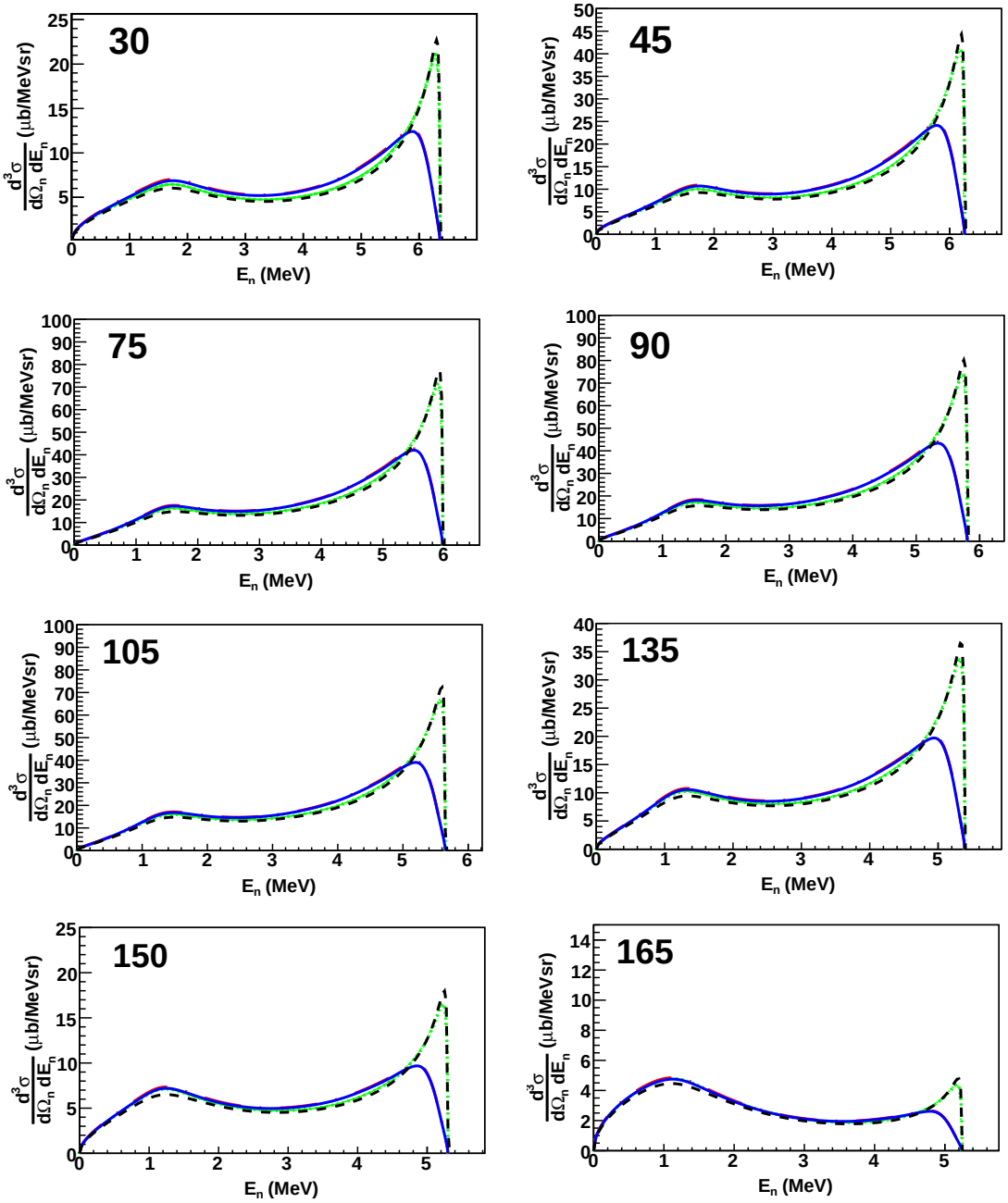

FIGURE A.3: (Color online) The same as Figures A.1 and A.2 but for E_γ=16.5 MeV

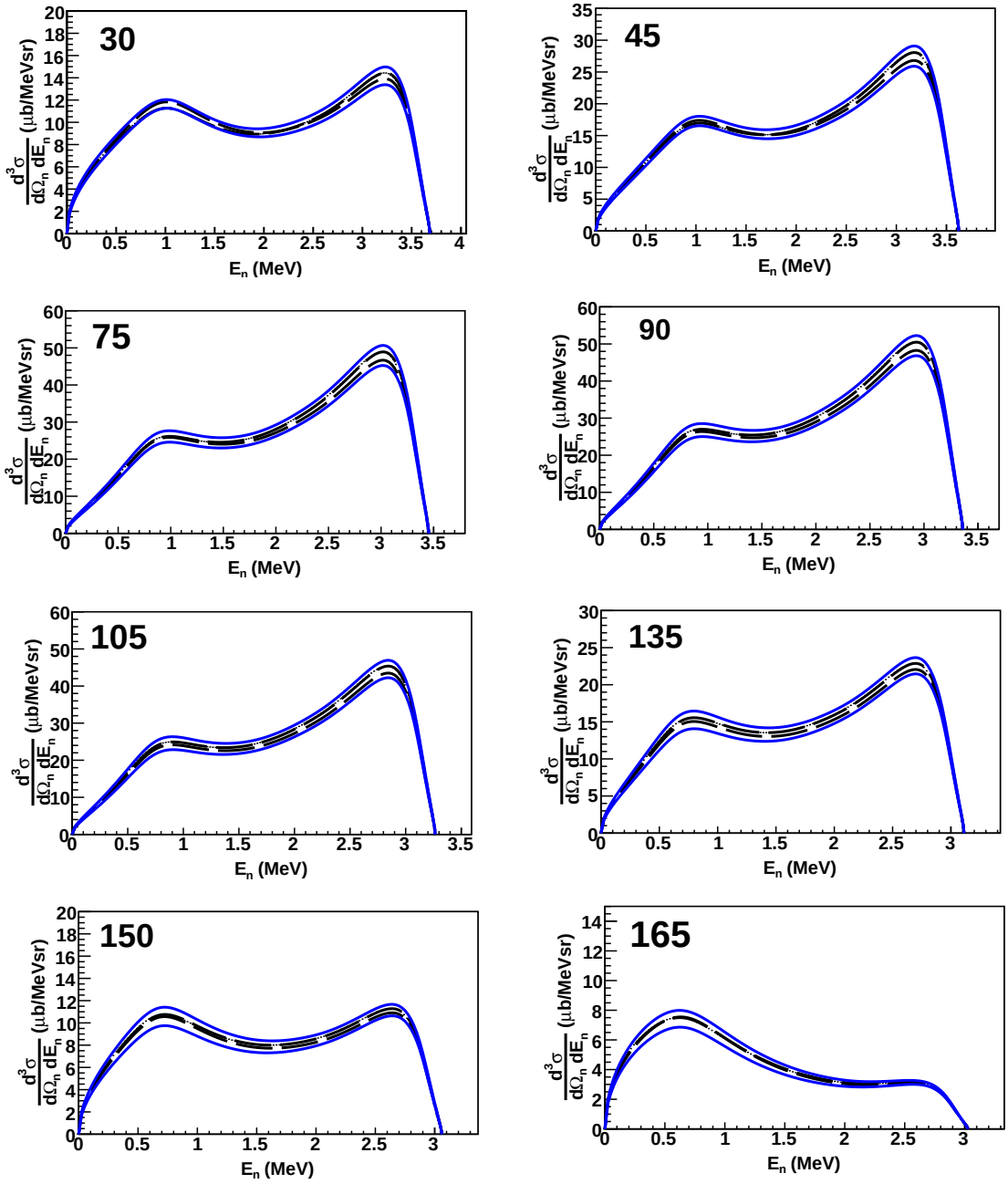

FIGURE A.4: (Color online) Various predictions of the double-differential cross sections of the three-body photodisintegration of ^{3}He as a function of the outgoing neutron energy for both parallel (two top curves) and antiparallel (two bottom curves) spin-helicity states at E_γ=12.8 MeV and all neutron scattering angles measured during the experiment. The calculations from Ref. [Del04, Del05b, Del05a, Del09] are: solid (blue) curves: CD Bonn + Δ-isobar + RC + Coulomb; long-dashed (black) curves: CD Bonn + Δ-isobar + Coulomb force. The CD Bonn + Coulomb force alone do not have any significant contribution to the difference of the cross sections between the spin-helicity states and the corresponding curves—if plotted—would be in the middle of the long-dashed curves.

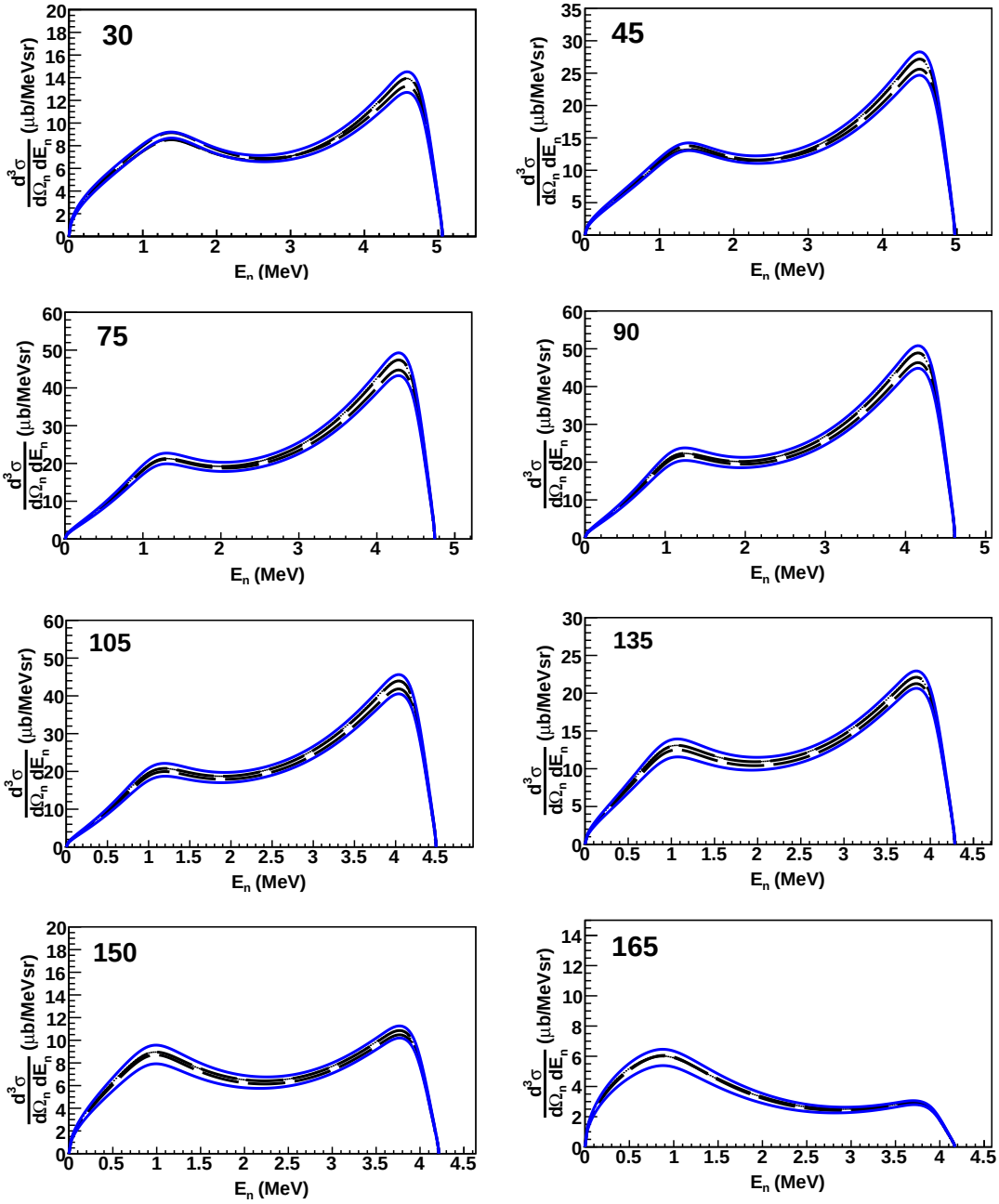

FIGURE A.5: (Color online) The same as Figure A.4 but for E_γ=14.7 MeV

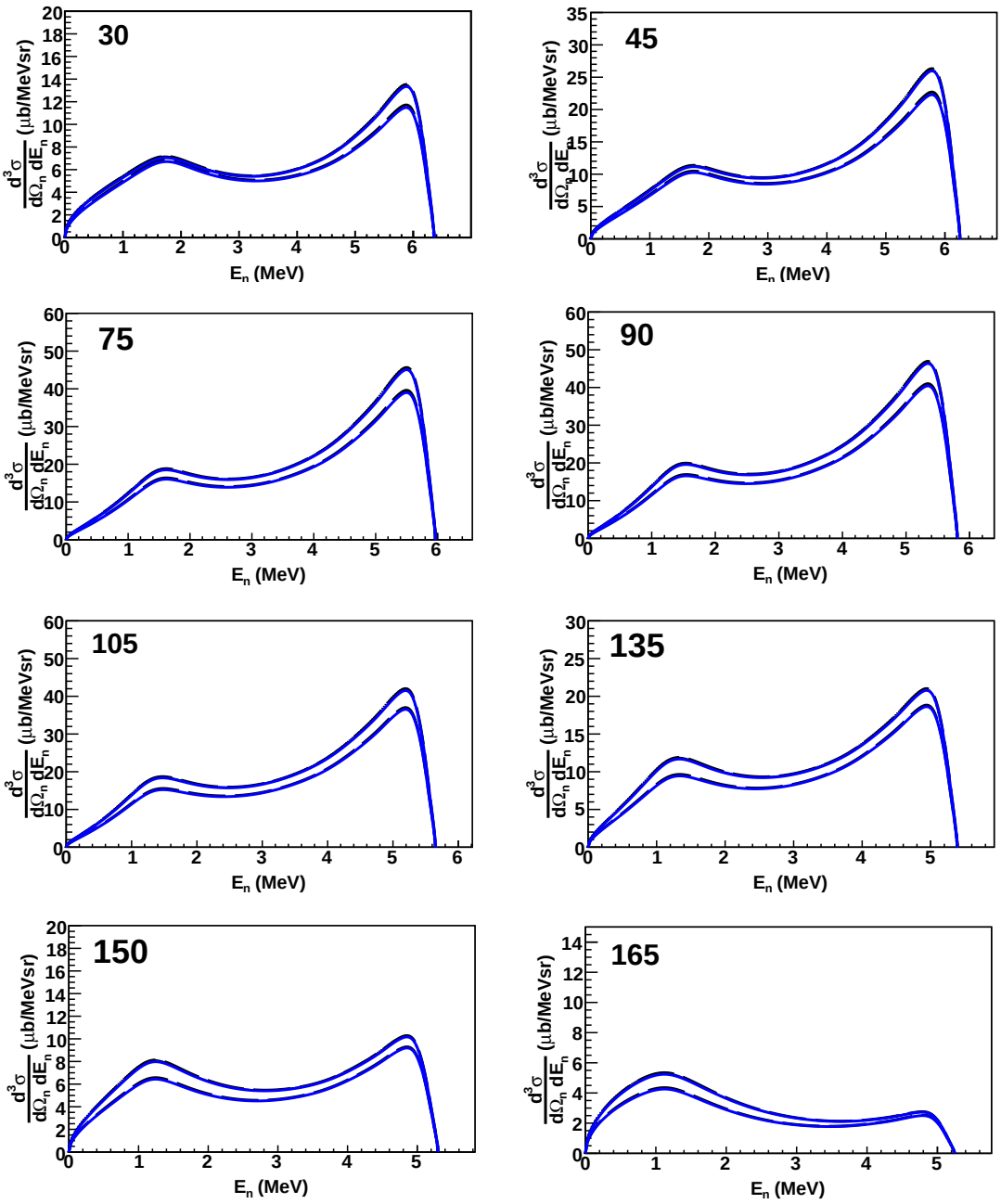

FIGURE A.6: (Color online) Various predictions of the double-differential cross sections of the three-body photodisintegration of ^{3}He as a function of the outgoing neutron energy for both parallel (two top curves) and antiparallel (two bottom curves) spin-helicity states at E_γ=16.5 MeV and all neutron scattering angles measured during the experiment. The calculations from Ref. [Del04, Del05b, Del05a, Del09] are: solid (blue) curves: CD Bonn + Δ-isobar + RC + Coulomb; long-dashed (black) curves: CD Bonn + RC + Coulomb force. The CD Bonn + Coulomb force alone do not have any significant contribution to the difference of the cross sections between the spin-helicity states and the corresponding curves—if plotted—would be in the middle of the long-dashed curves.

Appendix B

Appendix B

B.1 Laser Intensity per Unit Area and Time

The calculation of $\phi(z, \nu, P)$ (Equation (4.2)) assumes that the spectrum of the laser has a Gaussian form and the power P is concentrated in the FWHM $\delta\lambda$. This is an approximation because some of the laser power lies in the tails of the Gaussian.

In order to find the optical pumping rate $R(z, P)$ (Equation (4.3)), a second approximation is needed. Since

$$\begin{aligned} R(z,P) &= \int_0^\infty \phi(z,\nu,P)\sigma_{Rb}(\nu)d\nu \\ &= \frac{P}{Ah\nu_0 d\nu}\int_0^\infty e^{-\xi\sigma_{Rb}(\nu)}\sigma_{Rb}(\nu)d\nu \end{aligned} \tag{B.1}$$

where $\xi = [Rb](1 - P_\infty P_{Rb}(z, P))z$. If the substitution $x = \frac{2\Delta}{\gamma_{Rb}}$ is made, the equation becomes

$$R(z,P) = \frac{\sigma_{Rb0}\gamma_{Rb}P}{2Ah\nu_0 d\nu}\int_{-\frac{2\nu_0}{\gamma_{Rb}}}^\infty e^{-\frac{\xi}{1+x^2}}\frac{1}{1+x^2}dx \tag{B.2}$$

This integral is approximately equal to

$$R(z,P) \cong \frac{\sigma_{Rb0}\gamma_{Rb}P}{2Ah\nu_0 d\nu}\int_{-\infty}^{\infty} e^{-\frac{\xi}{1+x^2}}\frac{1}{1+x^2}dx \tag{B.3}$$

for any numerical value of ξ. Since the integration function is symmetric with respect to 0, equation (B.3) equals

$$R(z,P) \cong \frac{\sigma_{Rb0}\gamma_{Rb}P}{Ah\nu_0 d\nu}\int_{0}^{\infty} e^{-\frac{\xi}{1+x^2}}\frac{1}{1+x^2}dx \tag{B.4}$$

After a change of variable $y = \frac{1}{1+x^2}$ is made

$$R(z,P) \cong \frac{\sigma_{Rb0}\gamma_{Rb}P}{2Ah\nu_0 d\nu}\int_{0}^{1} \frac{1}{\sqrt{(1-y)y}}e^{-\xi y}dy \tag{B.5}$$

Solving it gives equation (4.3).

B.2 The Rate Equations for a Double-chamber System

The rate equations for a double-chamber system are given by (rate equations in [Chu92] with the X parameter included)

$$\frac{dP_p}{dt} = -G_p(P_p - P_t) - ((1+X)f_{opc}\gamma_{se}^{Rb/K} + \Gamma_p)P_p + P_{Rb}f_{opc}\gamma_{se}^{Rb/K} \tag{B.6}$$

$$\frac{dP_t}{dt} = G_t(P_p - P_t) - \Gamma_t P_t \tag{B.7}$$

$$P_p(0) = P_t(0) = 0;\ P_p'(\infty) = P_t'(\infty) = 0 \tag{B.8}$$

The assumptions are that the alkali metals are confined in the pumping chamber and the sources of ^{3}He polarization in the pumping chamber are spin exchange between alkali metals and ^{3}He and diffusion of polarized ^{3}He atoms from the target cell. Relaxation in the pumping (target) chamber is due to the combined relaxation

mechanisms (dipole-dipole effect, magnetic field gradient effect and wall effect) and ^{3}He diffusion to the target (pumping) chamber. The G_p is the polarized ^{3}He transfer rate from the pumping cell to the target cell and G_t is the transfer rate in the other direction (Appendix in [Chu92]). They are defined as

$$G_p = \frac{D_p S}{L V_p} \tag{B.9}$$

$$G_t = \frac{D_t S}{L V_t} \tag{B.10}$$

where S, L are the cross-sectional area and length of the connecting tube between the pumping chamber and target chamber. $D_{p(t)}$ and $V_{p(t)}$ are the ^{3}He diffusion coefficient and volume of each chamber, respectively. The diffusion coefficient is given by $D = \frac{\overline{v}\lambda}{3}$ where $\overline{v}$ is the ^{3}He mean thermal velocity and λ is the mean free path. The total theoretical transfer rate is equal to $G = G_p + G_t$.

The relaxation rates are defined as (Equation (6) in [Chu92])

$$\Gamma_p = \Gamma'_p \frac{n_p V_p}{n_p V_p + n_t V_t} \tag{B.11}$$

$$\Gamma_t = \Gamma'_t \frac{n_t V_t}{n_p V_p + n_t V_t} \tag{B.12}$$

where Γ'_p and Γ'_t are the averaged relaxation rates in the pumping and target chambers. Theoretically, the spin exchange rate is given by $\gamma_{se}^{Rb/K} = k_{se}^{Rb}[Rb] + k_{se}^{K}[K]$ [Bab06].

The general time-dependent solution of this coupled equations system is given by

$$P_p(t) = \frac{(G_t+\Gamma_t)P_{Rb}f_{opc}\gamma_{se}^{Rb/K}}{(G_p+f_{opc}\gamma_{se}^{Rb/K}(1+X)+\Gamma_p)(G_t+\Gamma_t)-G_pG_t}$$

$$+\frac{P_{Rb}f_{opc}\gamma_{se}^{Rb/K}}{\sqrt{(G_p+f_{opc}\gamma_{se}^{Rb/K}(1+X)+\Gamma_p-G_t-\Gamma_t)^2+4G_pG_t}}$$

$$\cdot\Bigg[-\frac{G_p+f_{opc}\gamma_{se}^{Rb/K}(1+X)+\Gamma_p-G_t-\Gamma_t+\sqrt{(G_p+f_{opc}\gamma_{se}^{Rb/K}(1+X)+\Gamma_p-G_t-\Gamma_t)^2+4G_pG_t}}{G_p+f_{opc}\gamma_{se}^{Rb/K}(1+X)+\Gamma_p+G_t+\Gamma_t+\sqrt{(G_p+f_{opc}\gamma_{se}^{Rb/K}(1+X)+\Gamma_p-G_t-\Gamma_t)^2+4G_pG_t}}$$

$$\cdot e^{-\frac{1}{2}(G_p+f_{opc}\gamma_{se}^{Rb/K}(1+X)+\Gamma_p+G_t+\Gamma_t+\sqrt{(G_p+f_{opc}\gamma_{se}^{Rb/K}(1+X)+\Gamma_p-G_t-\Gamma_t)^2+4G_pG_t})t}$$

$$+\frac{G_p+f_{opc}\gamma_{se}^{Rb/K}(1+X)+\Gamma_p-G_t-\Gamma_t-\sqrt{(G_p+f_{opc}\gamma_{se}^{Rb/K}(1+X)+\Gamma_p-G_t-\Gamma_t)^2+4G_pG_t}}{G_p+f_{opc}\gamma_{se}^{Rb/K}(1+X)+\Gamma_p+G_t+\Gamma_t-\sqrt{(G_p+f_{opc}\gamma_{se}^{Rb/K}(1+X)+\Gamma_p-G_t-\Gamma_t)^2+4G_pG_t}}$$

$$\cdot e^{-\frac{1}{2}(G_p+f_{opc}\gamma_{se}^{Rb/K}(1+X)+\Gamma_p+G_t+\Gamma_t-\sqrt{(G_p+f_{opc}\gamma_{se}^{Rb/K}(1+X)+\Gamma_p-G_t-\Gamma_t)^2+4G_pG_t})t}\Bigg] \tag{B.13}$$

$$P_t(t) = \frac{G_tP_{Rb}f_{opc}\gamma_{se}^{Rb/K}}{(G_p+f_{opc}\gamma_{se}^{Rb/K}(1+X)+\Gamma_p)(G_t+\Gamma_t)-G_pG_t}$$

$$+\frac{2G_tP_{Rb}f_{opc}\gamma_{se}^{Rb/K}}{\sqrt{(G_p+f_{opc}\gamma_{se}^{Rb/K}(1+X)+\Gamma_p-G_t-\Gamma_t)^2+4G_pG_t}}$$

$$\cdot\Bigg[\frac{1}{G_p+f_{opc}\gamma_{se}^{Rb/K}(1+X)+\Gamma_p+G_t+\Gamma_t+\sqrt{(G_p+f_{opc}\gamma_{se}^{Rb/K}(1+X)+\Gamma_p-G_t-\Gamma_t)^2+4G_pG_t}}$$

$$\cdot e^{-\frac{1}{2}(G_p+f_{opc}\gamma_{se}^{Rb/K}(1+X)+\Gamma_p+G_t+\Gamma_t+\sqrt{(G_p+f_{opc}\gamma_{se}^{Rb/K}(1+X)+\Gamma_p-G_t-\Gamma_t)^2+4G_pG_t})t}$$

$$-\frac{1}{G_p+f_{opc}\gamma_{se}^{Rb/K}(1+X)+\Gamma_p+G_t+\Gamma_t-\sqrt{(G_p+f_{opc}\gamma_{se}^{Rb/K}(1+X)+\Gamma_p-G_t-\Gamma_t)^2+4G_pG_t}}$$

$$\cdot e^{-\frac{1}{2}(G_p+f_{opc}\gamma_{se}^{Rb/K}(1+X)+\Gamma_p+G_t+\Gamma_t-\sqrt{(G_p+f_{opc}\gamma_{se}^{Rb/K}(1+X)+\Gamma_p-G_t-\Gamma_t)^2+4G_pG_t})t}\Bigg] \tag{B.14}$$

Using condition $P_p'(\infty) = P_t'(\infty) = 0$, the equilibrium ^{3}He polarization in each chamber is

$$P_p(t \to \infty) = \frac{(G_t + \Gamma_t) P_{Rb} f_{opc} \gamma_{se}^{Rb/K}}{(G_p + f_{opc}\gamma_{se}^{Rb/K}(1+X) + \Gamma_p)(G_t + \Gamma_t) - G_p G_t} \quad \text{(B.15)}$$

$$P_t(t \to \infty) = \frac{G_t \cdot P_{Rb} f_{opc} \gamma_{se}^{Rb/K}}{(G_p + f_{opc}\gamma_{se}^{Rb/K}(1+X) + \Gamma_p)(G_t + \Gamma_t) - G_p G_t} \quad \text{(B.16)}$$

The transfer rate is also measured experimentally by destroying the polarization in the target chamber using a rectangular RF coil, and measuring the recovery of the NMR free induction decay signal as polarized ^{3}He atoms diffuse into the target chamber from the pumping chamber. The diffusion rate is much larger than the relaxation rate, $G_t \gg \Gamma_t$, and consequently $G_t + \Gamma_t \simeq G_t$. We have

$$P_p(t \to \infty) = P_t(t \to \infty) = \frac{G_t P_{Rb} f_{opc} \gamma_{se}^{Rb/K}}{(G_p + f_{opc}\gamma_{se}^{Rb/K}(1+X) + \Gamma_p)(G_t + \Gamma_t) - G_p G_t} \quad \text{(B.17)}$$

Assuming that $G_p \simeq G_t$, the equation becomes

$$P_{^3He} = P_{Rb}(z=0, P) \frac{f_{opc}\gamma_{se}^{Rb/K}}{f_{opc}\gamma_{se}^{Rb/K}(1+X) + 1/T_1} \quad \text{(B.18)}$$

where $\Gamma = \frac{1}{T_1} = \Gamma_p + \Gamma_t$ is the total relaxation rate.

Bibliography

[Abb99] D.J. Abbott, W.G. Heyes, E. Jastrzembski, R.W. MacLeod, C. Timmer, and E. Wolin. *CODA performance in the real world.* In *Real Time Conference, 1999. Santa Fe 1999. 11th IEEE NPSS*, pages 119–122, 1999.

[Abe97] K. Abe et al. *Precision Determination of the Neutron Spin Structure Function* g_1^n. Phys. Rev. Lett., **79**(1997) 26–30.

[Abr61] A. Abragam. *Principles of Nuclear Magnetism.* Oxford University Press, Oxford, UK, 1961.

[Ack97] K. Ackerstaff et al. *Measurement of the neutron spin structure function* g_1^n *with a polarized* ^{3}He *internal target.* Physics Letters B, **404**(1997) 383 – 389.

[Ago03] S. Agostinelli et al. *Geant4-a simulation toolkit.* Nuclear Instruments and Methods in Physics Research Section A: Accelerators, Spectrometers, Detectors and Associated Equipment, **506**(2003) 250 – 303.

[Ahm08] M. Ahmed, M. Blackston, B. Perdue, W. Tornow, H. Weller, B. Norum, B. Sawatzky, R. Prior, and M. Spraker. *Near-threshold deuteron photodisintegration: An indirect determination of the* G*erasimov-*D*rell-*H*earn sum rule and forward spin polarizability* (γ_0) *for the deuteron at low energies.* Phys. Rev. C, **77**(2008) 044005.

[Ahr00] J. Ahrens et al. *Helicity Dependence of* $\gamma p \rightarrow N\pi$ *below 450 MeV and Contribution to the Gerasimov-Drell-Hearn Sum Rule.* Phys. Rev. Lett., **84**(2000) 5950–5954.

[Ahr01] J. Ahrens et al. *First Measurement of the Gerasimov-Drell-Hearn Integral for* ^1H *from 200 to 800 MeV.* Phys. Rev. Lett., **87**(2001) 022003.

[Ahr09] J. Ahrens et al. *Helicity dependence of the total inclusive cross section on the deuteron.* Physics Letters B, **672**(2009) 328 – 332.

[All06] J. Allison et al. *Geant4 developments and applications.* Nuclear Science, IEEE Transactions on, **53**(2006) 270–278.

[Alt67] E.O. Alt, P. Grassberger, and W. Sandhas. *Reduction of the three-particle collision problem to multi-channel two-particle Lippmann-Schwinger equations.* Nuclear Physics B, **2**(1967) 167 – 180.

[Ama02] M. Amarian et al. *Q^2 Evolution of the Generalized* G*erasimov-*D*rell-*H*earn Integral for the Neutron using a* ^{3}He *Target.* Phys. Rev. Lett., **89**(2002) 242301.

[Ant96] P. Anthony et al. *Deep inelastic scattering of polarized electrons by polarized* ^{3}He *and the study of the neutron spin structure.* Phys. Rev. D, **54**(1996) 6620–6650.

[App98] S. Appelt, A. Ben-Amar Baranga, C. J. Erickson, M. V. Romalis, A. R. Young, and W. Happer. *Theory of spin-exchange optical pumping of* ^{3}He *and* ^{129}Xe. Phys. Rev. A, **58**(1998) 1412–1439.

[Are04] Hartmuth Arenhövel, Alexander Fix, and Michael Schwamb. *Spin Asymmetry and Gerasimov-Drell-Hearn Sum Rule for the Deuteron.* Phys. Rev. Lett., **93**(2004) 202301.

[Arn02] R. A. Arndt, W. J. Briscoe, I. I. Strakovsky, and R. L. Workman. *Analysis of pion photoproduction data.* Phys. Rev. C, **66**(2002) 055213.

[Aru63] F.R. Arutyunian and V.A. Tumanian. *The Compton effect on relativistic electrons and the possibility of obtaining high energy beams.* Physics Letters, **4**(1963) 176 – 178.

[Aud91] G. Audit et al. *DAPHNE: a large-acceptance tracking detector for the study of photoreactions at intermediate energies.* Nuclear Instruments and Methods in Physics Research Section A: Accelerators, Spectrometers, Detectors and Associated Equipment, **301**(1991) 473 – 481.

[Bab90] D. Babusci, L. Casano, A. DÁngelo, P. Picozza, C. Schaerf, and B. Girolami. *Project GRAAL: the scientific case.* Il Nuovo Cimento A, **103**(1990) 1555–1576.

[BAB98] A. Ben-Amar Baranga, S. Appelt, M. V. Romalis, C. J. Erickson, A. R. Young, G. D. Cates, and W. Happer. *Polarization of* ^{3}He *by Spin Exchange with Optically Pumped Rb and K Vapors.* Phys. Rev. Lett., **80**(1998) 2801–2804.

[Bab05] E. Babcock. *Spin-Exchange Optical Pumping with Alkali Metal Vapors.* Ph.D. Thesis, University of Wisconsin, Madison, 2005.

[Bab06] E. Babcock, B. Chann, T. G. Walker, W. C. Chen, and T. R. Gentile. *Limits to the Polarization for Spin-Exchange Optical Pumping of* ^{3}He. Phys. Rev. Lett., **96**(2006) 083003.

[Bal69] J. Ballam et al. *Total and Partial Photoproduction Cross Sections at 1.44, 2.8, and 4.7 GeV.* Phys. Rev. Lett., **23**(1969) 498–501.

[Bar98] A. Ben-Amar Baranga, S. Appelt, C. J. Erickson, A. R. Young, and W. Happer. *Alkali-metal-atom polarization imaging in high-pressure optical-pumping cells.* Phys. Rev. A, **58**(1998) 2282–2294.

[Bar13] P. Aguar Bartolomé et al. *First measurement of the helicity dependence of* ^{3}He *photoreactions in the resonance region.* Physics Letters B, **723**(2013) 71 – 77.

[Bec99] J. Becker et al. *Determination of the neutron electric form factor from the reaction* $^3\mathrm{He}(e, e'n)$ *at medium momentum transfer.* The European Physical Journal A - Hadrons and Nuclei, **6**(1999) 329–344.

[Bel70] B. D. Belt, C. R. Bingham, M. L. Halbert, and A. van der Woude. *Radiative Capture of Deuterons by Protons.* Phys. Rev. Lett., **24**(1970) 1120–1123.

[Bem65] Carlo Bemporad, Richard H. Milburn, Nobuyuki Tanaka, and Mircea Fotino. *High-Energy Photons from Compton Scattering of Light on 6.0 GeV Electrons.* Phys. Rev., **138**(1965) B1546–B1549.

[Ben65] Reuben Benumof. *Optical Pumping Theory and Experiments.* American Journal of Physics, **33**(1965) 151–160.

[Ber74] B. L. Berman, S. C. Fultz, and P. F. Yergin. *Three-body photodisintegration of* ^{3}He. Phys. Rev. C, **10**(1974) 2221–2236.

[Ber86] R. Bernabei et al. *Total Cross Section for Deuteron Photodisintegration between 15 and 75* MeV. Phys. Rev. Lett., **57**(1986) 1542–1545.

[Ber03] J. Bermuth et al. *The neutron charge form factor and target analyzing powers from* $^3\vec{H}e(\vec{e}, e'n)pp$ *scattering.* Physics Letters B, **564**(2003) 199 – 204.

[Bia99] N Bianchi and E Thomas. *Parameterisation of $[\sigma_{1/2} - \sigma_{3/2}]$ for $Q^2 \geqslant 0$ and non-resonance contribution to the* GDH *sum rule.* Physics Letters B, **450**(1999) 439 – 447.

[Bir64] J.B. Birks. *The Theory and Practice of Scintillation Counting.* Pergamon Press, Ltd., Oxford, 1964.

[Bir85] Y. Birenbaum, S. Kahane, and R. Moreh. *Absolute cross section for the photodisintegration of deuterium.* Phys. Rev. C, **32**(1985) 1825–1829.

[Bla07] M.A. Blackston. *Precision Measurements of Deuteron Photodisintegration Using Linearly Polarized Photons of 14 and 16 MeV.* Ph.D. Thesis, Duke University, 2007.

[Bru97] Rene Brun and Fons Rademakers. *{ROOT}-An object oriented data analysis framework.* Nuclear Instruments and Methods in Physics Research Section A: Accelerators, Spectrometers, Detectors and Associated Equipment, **389**(1997) 81 – 86. New Computing Techniques in Physics Research V.

[Car83] J. Carlson, V.R. Pandharipande, and R.B. Wiringa. *Three-nucleon interaction in 3-, 4- and ∞-body systems.* Nuclear Physics A, **401**(1983) 59 – 85.

[Cat88] G. D. Cates, S. R. Schaefer, and W. Happer. *Relaxation of spins due to field inhomogeneities in gaseous samples at low magnetic fields and low pressures.* Phys. Rev. A, **37**(1988) 2877–2885.

[Cha02] B. Chann, E. Babcock, L. W. Anderson, and T. G. Walker. *Measurements of* ^{3}He *spin-exchange rates.* Phys. Rev. A, **66**(2002) 032703.

[Cha03] B. Chann, E. Babcock, L. W. Anderson, T. G. Walker, W. C. Chen, T. B. Smith, A. K. Thompson, and T. R. Gentile. *Production of highly polarized* ^{3}He *using spectrally narrowed diode laser array bars.* Journal of Applied Physics, **94**(2003) 6908–6914.

[Che07] W. C. Chen, T. R. Gentile, T. G. Walker, and E. Babcock. *Spin-exchange optical pumping of* ^{3}He *with Rb-K mixtures and pure K.* Phys. Rev. A, **75**(2007) 013416.

[Chi02] Wen-Tai Chiang, Shin Nan Yang, Lothar Tiator, and Dieter Drechsel. *An isobar model for photo- and electroproduction on the nucleon.* Nuclear Physics A, **700**(2002) 429 – 453.

[Chu92] T. E. Chupp, R. A. Loveman, A. K. Thompson, A. M. Bernstein, and D. R. Tieger. *Tests of a high density polarized* ^{3}He *target for electron scattering.* Phys. Rev. C, **45**(1992) 915–930.

[Chu13] P.-H. Chu, A. Dennis, C. Fu, H. Gao, R. Khatiwada, G. Laskaris, K. Li, E. Smith, W. Snow, H. Yan, and W. Zheng. *Laboratory search for spin-dependent short-range force from axionlike particles using optically polarized* ^{3}He *gas.* Phys. Rev. D, **87**(2013) 011105.

[Col63] F. D. Colegrove, L. D. Schearer, and G. K. Walters. *Polarization of* He^3 *Gas by Optical Pumping.* Phys. Rev., **132**(1963) 2561–2572.

[Com23] Arthur H. Compton. *A Quantum Theory of the Scattering of X-rays by Light Elements.* Phys. Rev., **21**(1923) 483–502.

[Cos14] S. Costanza et al. *Helicity dependence of the* γ^3He$\rightarrow\pi X$ *reactions in the* Δ*(1232) resonance region.* The European Physical Journal A, **50**(2014).

[Cra70] R.L. Craun and D.L. Smith. *Analysis of response data for several organic scintillators.* Nuclear Instruments and Methods, **80**(1970) 239 – 244.

[Del03] A. Deltuva, R. Machleidt, and P. Sauer. *Realistic two-baryon potential coupling two-nucleon and nucleon-*Δ*-isobar states: Fit and applications to three-nucleon system.* Phys. Rev. C, **68**(2003) 024005.

[Del04] A. Deltuva, L. Yuan, J. Adam, A. Fonseca, and P. Sauer. *Trinucleon photonuclear reactions with* Δ*-isobar excitation: Processes below pion-production threshold.* Phys. Rev. C, **69**(2004) 034004.

[Del05a] A. Deltuva, A. Fonseca, and P. Sauer. *Momentum-space description of three-nucleon breakup reactions including the Coulomb interaction.* Phys. Rev. C, **72**(2005) 054004.

[Del05b] A. Deltuva, A. Fonseca, and P. Sauer. *Momentum-space treatment of the Coulomb interaction in three-nucleon reactions with two protons.* Phys. Rev. C, **71**(2005) 054005.

[Del08] A. Deltuva, A.C. Fonseca, and P.U. Sauer. *Nuclear Many-Body Scattering Calculations with the Coulomb Interaction.* Annual Review of Nuclear and Particle Science, **58**(2008) 27–49.

[Del09] A. Deltuva, A. Fonseca, and P. Sauer. *Relativistic corrections of one-nucleon current in low-energy three-nucleon photonuclear reactions.* Phys. Rev. C, **80**(2009) 064004.

[DG92] A. De Graeve et al. *Absolute total cross sections for deuteron photodisintegration between 7 and 19 MeV.* Phys. Rev. C, **45**(1992) 860–862.

[Dre66] S. D. Drell and A. C. Hearn. *Exact Sum Rule for Nucleon Magnetic Moments.* Phys. Rev. Lett., **16**(1966) 908–911.

[Dri96] B. Driehuys, G. D. Cates, E. Miron, K. Sauer, D. K. Walter, and W. Happer. *High-volume production of laser-polarized ^{129}Xe.* Applied Physics Letters, **69**(1996) 1668–1670.

[Dum83] O. Dumbrajs, R. Koch, H. Pilkuhn, G.C. Oades, H. Behrens, J.J. de Swart, and P. Kroll. *Compilation of coupling constants and low-energy parameters.* Nuclear Physics B, **216**(1983) 277 – 335.

[Dut03] H. Dutz et al. *First Measurement of the Gerasimov-Drell-Hearn Sum Rule for* ^{1}H *from 0.7 to 1.8 GeV at ELSA.* Phys. Rev. Lett., **91**(2003) 192001.

[Dut04] H. Dutz et al. *Experimental Check of the* G*erasimov-*D*rell-*H*earn Sum Rule for* ^{1}H. Phys. Rev. Lett., **93**(2004) 032003.

[Dut05] H. Dutz et al. *Measurement of Helicity-Dependent Photoabsorption Cross Sections on the Neutron from 815 to 1825* M*eV.* Phys. Rev. Lett., **94**(2005) 162001.

[D.W05] D.Watts. In *Calorimetry in Particle Physics:Proceedings of the 11th International Conference*, page 560, 2005.

[dZ60] Robert L. de Zafra. *Optical Pumping.* American Journal of Physics, **28**(1960) 646–654.

[Fad61] L.D. Faddeev. *Scattering theory for a three particle system.* Sov. Phys. JETP, **12**(1961) 1041.

[Fau81] D. D. Faul, B. L. Berman, P. Meyer, and D. L. Olson. *Photodisintegration of* ^{3}H *and* ^{3}He. Phys. Rev. C, **24**(1981) 849–873.

[Fet65] V.N. Fetisov, A.N. Gorbunov, and A.T. Varfolomeev. *Nuclear photoeffect on three-particle nuclei.* Nuclear Physics, **71**(1965) 305 – 342.

[Fri90] J. L. Friar, B. F. Gibson, G. L. Payne, A. M. Bernstein, and T. E. Chupp. *Neutron polarization in polarized* ^{3}He *targets.* Phys. Rev. C, **42**(1990) 2310–2314.

[Gam65] Rodger L. Gamblin and Thomas R. Carver. *Polarization and Relaxation Processes in* He^3 *Gas.* Phys. Rev., **138**(1965) A946–A960.

[Gao94] H. Gao et al. *Measurement of the neutron magnetic form factor from inclusive quasielastic scattering of polarized electrons from polarized* ^{3}He. Phys. Rev. C, **50**(1994) R546–R549.

[Gao09] H. Gao, W. Chen, and X. Zong. *Study of the* GDH *sum rule of* ^{3}He *at* HIγS. In 6^{th} *International Worshop on Chiral Dynamics*, page 101, 2009.

[Ger66a] S.B. Gerasimov. *A Sum Rule for Magnetic Moments and the Damping of the Nucleon Magnetic Moment in Nuclei.* Sov. J. Nucl. Phys., **2**(1966) 430.

[Ger66b] H. M. Gerstenberg and J. S. O'Connell. *Three-Body Photodisintegration of* ^{3}He. Phys. Rev., **144**(1966) 834–838.

[Gib88] B.F. Gibson and B.H.J. McKellar. *The three-body force in the trinucleons.* Few-Body Systems, **3**(1988) 143–170.

[Glo83] Walter Glockle. In *The Quantum Mechanical Few-Body Problem*, Texts and Monographs in Physics, pages 83–164. Springer Berlin Heidelberg, 1983.

[Gol05] J. Golak, R. Skibiński, H. Witała, W. Glockle, A. Nogga, and H. Kamada. *Electron and photon scattering on three-nucleon bound states.* Physics Reports, **415**(2005) 89 – 205.

[Gor64] A.N. Gorbunov and A.T. Varfolomeev. *Cross sections of the reactions* $^3\mathrm{He}(\gamma, p)^2\mathrm{D}$ *and* $^3\mathrm{He}(\gamma, \mathrm{n})2\mathrm{p}$. Physics Letters, **11**(1964) 137 – 139.

[Gor74] A.N. Gorbunov. *Nuclear Photoeffects at Helium Isotopes.* In *Photonuclear and Photomesic Processes*, pages 1–117, 1974.

[Gri62] G. M. Griffiths, E. A. Larson, and L. P. Robertson. *THE CAPTURE OF PROTONS BY DEUTERONS.* Canadian Journal of Physics, **40**(1962) 402–411.

[Hap72] William Happer. *Optical Pumping.* Rev. Mod. Phys., **44**(1972) 169–249.

[Hel02] K Helbing, G Anton, M Fausten, D Menze, T Michel, A Nagel, D Ryckbosch, T Speckner, R Van de Vyver, and G Zeitler. *The GDH-Detector.* Nuclear Instruments and Methods in Physics Research Section A: Accelerators, Spectrometers, Detectors and Associated Equipment, **484**(2002) 129 – 139.

[Hel06] Klaus Helbing. *The Gerasimov-Drell-Hearn sum rule.* Progress in Particle and Nuclear Physics, **57**(2006) 405 – 469.

[Hol01] H. Holvoet. Ph.D. Thesis, University of Gent, Belgium, 2001.

[Hou71] Theodore L. Houk. *Neutron-Proton Scattering Cross Section at a Few Electron Volts and Charge Independence.* Phys. Rev. C, **3**(1971) 1886–1903.

[How98] C.R Howell, Q Chen, T.S Carman, A Hussein, W.R Gibbs, B.F Gibson, G Mertens, C.F Moore, C Morris, A Obst, E Pasyuk, C.D Roper, F Salinas, I Slaus, S Sterbenz, W Tornow, R.L Walter, C.R Whiteley, and M Whitton. *Toward a resolution of the neutron-neutron scattering-length issue.* Physics Letters B, **444**(1998) 252 – 259.

[KÖ9] S. Kölling, E. Epelbaum, H. Krebs, and U. Meißner. *Two-pion exchange electromagnetic current in chiral effective field theory using the method of unitary transformation.* Phys. Rev. C, **80**(2009) 045502.

[Kaz84] A.A. Kazakov et al. *FISSION OF U-238 AND NP-237 BY INTERMEDIATE-ENERGY GAMMA RAYS.* JETP Lett., **40**(1984) 1271–1274.

[Kel40] J. M. B. Kellogg, I. I. Rabi, N. F. Ramsey, and J. R. Zacharias. *An Electrical Quadrupole Moment of the Deuteron The Radiofrequency Spectra of HD and* D_2 *Molecules in a Magnetic Field.* Phys. Rev., **57**(1940) 677–695.

[Kez93] G.Ya. Kezerashvili, A.M. Milov, and B.B. Wojtsekhowski. *The gamma ray energy tagging spectrometer of the ROKK-2 facility at the VEPP-3 storage ring.* Nuclear Instruments and Methods in Physics Research Section A: Accelerators, Spectrometers, Detectors and Associated Equipment, **328**(1993) 506 – 511.

[Kez95] G. Ya. Kezerashvili et al. *ROKK1M is the Compton source of the high intensity polarized and tagged gamma beam at the VEPP-4M collider.* AIP Conference Proceedings, **343**(1995) 260–263.

[Kez98] G.Ya. Kezerashvili, A.M. Milov, N.Yu. Muchnoi, and A.P. Usov. *A Compton source of high energy polarized tagged -ray beams. The ROKK-1M facility.* Nuclear Instruments and Methods in Physics Research Section B: Beam Interactions with Materials and Atoms, **145**(1998) 40 – 48.

[Kla84] S Klarsfeld, J Martorell, and D W L Sprung. *Deuteron properties and the nucleon-nucleon interaction.* Journal of Physics G: Nuclear Physics, **10**(1984) 165.

[Klu12] K.A. Kluttz. *Studies of Polarized and Unpolarized ^{3}He in the Presence of Alkali Vapor.* Ph.D. Thesis, The College of William and Mary, 2012.

[Klu13] Kelly A. Kluttz, Todd D. Averett, and Brian A. Wolin. *Pressure broadening and frequency shift of the D_1 and D_2 lines of Rb and K in the presence of ^{3}He and N_2.* Phys. Rev. A, **87**(2013) 032516.

[Kno10] G.F. Knoll. *Radiation Detection and Measurement.* John Wiley & Sons, Inc., 2010.

[Koe75] L. Koester and W. Nistler. *New determination of the neutron-proton scattering amplitude and precise measurements of the scattering amplitudes on carbon, chlorine, fluorine and bromine.* Zeitschrift fur Physik A Atoms and Nuclei, **272**(1975) 189–196.

[Kor98] W. Korsch. *Technical note on EPR.* Jefferson National Accelerator Facility, 11 1998.

[Kra03] K.M. Kramer. *A search for Higher Twist Effects In the The neutron Spin Structure Function $g_2^n(x, Q^2)$.* Ph.D. Thesis, The College of William and Mary, 2003.

[Kra07] Kevin Kramer, Xing Zong, Rongchun Lu, Dipangkar Dutta, Haiyan Gao, Xin Qian, Qiang Ye, Xiaofeng Zhu, Todd Averett, and Sabine Fuchs. *A high-pressure polarized* ^{3}He *gas target for the High Intensity Gamma Source (*HIγS*) facility at Duke Free Electron Laser Laboratory.* Nuclear Instruments and Methods in Physics Research Section A: Accelerators, Spectrometers, Detectors and Associated Equipment, **582**(2007) 318 – 325.

[Kul64] O.F Kulikov, Y.Y Telnov, E.I Filippov, and M.N Yakimenko. *Compton effect on moving electrons.* Physics Letters, **13**(1964) 344 – 346.

[Kun71] S.K. Kundu, Y.M. Shin, and G.D. Wait. *Photodisintegration of ^{3}He.* Nuclear Physics A, **171**(1971) 384 – 400.

[Las13] G. Laskaris et al. *First Measurements of Spin-Dependent Double-Differential Cross Sections and the* G*erasimov*-D*rell*-H*earn Integrand from* $^3\vec{H}e(\vec{\gamma}, n)pp$ *at Incident Photon Energies of 12.8 and 14.7* M*eV*. Phys. Rev. Lett., **110**(2013) 202501.

[Las14] G. Laskaris et al. *Spin-dependent cross sections from the three-body photodisintegration of* ^{3}He *at incident energies of 12.8 and 14.7 MeV*. Phys. Rev. C, **89**(2014) 024002.

[Leo87] W. R. Leo. *IEEE Standard for a Versatile Backplane Bus: VMEbus*. ANSI/IEEE Std, 1987.

[Leo94] W. R. Leo. *Techniques for Nuclear and Particle Physics Experiments*. Springer-Verlag, Germany, 1994.

[Lep71] A. Lepretre, H. Beil, R. Bergere, P. Carlos, A. Veyssiere, and M. Sugawara. *The giant dipole states in the* $A = 90$ *mass region*. Nuclear Physics A, **175**(1971) 609 – 628.

[Lid04] D. Lide. *Handbook of Chemistry and Physics*. CRC Press, 2004.

[Lit96] V.N. Litvinenko, B. Burnham, J.M.J. Madey, S.H. Park, and Y. Wu. *Duke storage ring UV/VUV FEL: status and prospects*. Nuclear Instruments and Methods in Physics Research Section A: Accelerators, Spectrometers, Detectors and Associated Equipment, **375**(1996) 46 – 52. Proceedings of the 17th International Free Electron Laser Conference.

[Lit97] V. N. Litvinenko et al. *Gamma-Ray Production in a Storage Ring Free-Electron Laser*. Phys. Rev. Lett., **78**(1997) 4569–4572.

[Lit01a] V.N. Litvinenko, S.F. Mikhailov, O.A. Shevchenko, N.A. Vinokurov, N.G. Gavrilov, G.N. Kulipanov, T.V. Shaftan, P.D. Vobly, and Y. Wu. *The OK-5/Duke storage ring* {*VUV*} {*FEL*} *with variable polarization*. Nuclear Instruments and Methods in Physics Research Section A: Accelerators, Spectrometers, Detectors and Associated Equipment, **475**(2001) 407 – 416. FEL2000: Proc. 22nd Int. Free Electron Laser Conference and 7th F {EL} Users Workshop.

[Lit01b] V.N. Litvinenko, S.F. Mikhailov, N.A. Vinokurov, N.G. Gavrilov, G.N. Kulipanov, O.A. Shevchenko, and P.D. Vobly. *Helical wigglers for the OK-5 storage ring* {*VUV*} {*FEL*} *at Duke*. Nuclear Instruments and Methods in Physics Research Section A: Accelerators, Spectrometers, Detectors and

Associated Equipment, **475**(2001) 247 – 252. FEL2000: Proc. 22nd Int. Free Electron Laser Conference and 7^{th} {FEL} Users Workshop.

[Lor93] W. Lorenzon, T. Gentile, H. Gao, and R. McKeown. *NMR calibration of optical measurement of nuclear polarization in* ^{3}He. Phys. Rev. A, **47**(1993) 468–479.

[Lus88] C.P. Lusher, M.F. Secca, and M.G. Richards. *Nuclear magnetic relaxation of* ^{3}*He gas. I. Pure* ^{3}*He.* Journal of Low Temperature Physics, **72**(1988) 25–69.

[Mac87] R. Machleidt, K. Holinde, and Ch. Elster. *The bonn meson-exchange model for the nucleon-nucleon interaction.* Physics Reports, **149**(1987) 1 – 89.

[Mac89] R. Machleidt. In J.W. Negele and Erich Vogt, editors, *Advances in Nuclear Physics*, volume 19 of *Advances in Nuclear Physics*, pages 189–376. Springer US, 1989.

[Mac96] R. Machleidt, F. Sammarruca, and Y. Song. *Nonlocal nature of the nuclear force and its impact on nuclear structure.* Phys. Rev. C, **53**(1996) R1483–R1487.

[Mac01] R. Machleidt. *High-precision, charge-dependent Bonn nucleon-nucleon potential.* Phys. Rev. C, **63**(2001) 024001.

[MAI03] MAID. www.kph.uni-mainz.de/MAID/, 2003.

[Mar85] T. C. Marshall. *Free Electron Lasers.* Macmillan Inc., 1985.

[Mat74] J.L. Matthews, T. Kruse, M.E. Williams, R.O. Owens, and W. Savin. *Radiative capture of protons by deuterons at Ep = 16 MeV.* Nuclear Physics A, **223**(1974) 221 – 233.

[mes08a] mesytec GmbH & Co. KG. *Eight channel preamplifier and shaper and timing filter amplifier*, 2008.

[mes08b] mesytec GmbH & Co. KG. *Four channel particle discriminator module for liquid scintillators*, 2008.

[Mey94] M. Meyerhoff et al. *First measurement of the electric formfactor of the neutron in the exclusive quasielastic scattering of polarized electrons from polarized* ^{3}He. Physics Letters B, **327**(1994) 201 – 207.

[Mil63] Richard H. Milburn. *Electron Scattering by an Intense Polarized Photon Field*. Phys. Rev. Lett., **10**(1963) 75–77.

[Mil90] G.A. Miller, B.M.K. Nefkens, and I. laus. *Charge symmetry, quarks and mesons*. Physics Reports, **194**(1990) 1 – 116.

[Mul90] W.J. Mullin, F. Laloë, and M.G. Richards. *Longitudinal relaxation time for dilute quantum gases*. Journal of Low Temperature Physics, **80**(1990) 1–13.

[Nai06] S. Naito et al. *New data for total* ^{3}He*(γ,p)D and* ^{3}He*(γ,pp)n cross sections compared to current theory*. Phys. Rev. C, **73**(2006) 034003.

[Nak98] T. Nakano et al. *New projects at SPring-8 with multi-GeV polarized photons*. Nuclear Physics A, **629**(1998) 559 – 566. Quark Lepton Nuclear Physics.

[Nak01] T. Nakano et al. *Multi-GeV laser-electron photon project at SPring-8*. Nuclear Physics A, **684**(2001) 71 – 79. Few-Body Problems in Physics.

[New93] N. R. Newbury, A. S. Barton, G. D. Cates, W. Happer, and H. Middleton. *Gaseous* ^{3}*–*^{3}*He magnetic dipolar spin relaxation*. Phys. Rev. A, **48**(1993) 4411–4420.

[Per10] B.A. Perdue. *Measurements of the Absolute Cross Section of the Three-body Photodisintegration of* ^{3}He *between* E_γ*=11.4* MeV *and 14.7* MeV *at HIγS*. Ph.D. Thesis, Duke University, 2010.

[Per11] B. Perdue, M. Ahmed, S. Henshaw, P.-N. Seo, S. Stave, H. Weller, P. Martel, and A. Teymurazyan. *Cross sections for the three-body photodisintegration of* ^{3}He *at* E_γ*=12.8, 13.5, and 14.7* MeV. Phys. Rev. C, **83**(2011) 034003.

[Pud97] B. S. Pudliner, V. R. Pandharipande, J. Carlson, Steven C. Pieper, and R. B. Wiringa. *Quantum Monte Carlo calculations of nuclei with A<7*. Phys. Rev. C, **56**(1997) 1720–1750.

[Qia11] X. Qian et al. *Single Spin Asymmetries in Charged Pion Production from Semi-Inclusive Deep Inelastic Scattering on a Transversely Polarized* ^{3}He *Target at* $Q^2 = 1.4 - 2.7$ GeV^2. Phys. Rev. Lett., **107**(2011) 072003.

[Rio10] S. Riordan et al. *Measurements of the Electric Form Factor of the Neutron up to $Q^2 = 3.4$ GeV^2 Using the Reaction $^3\vec{H}e(\vec{e}, e'n)pp$.* Phys. Rev. Lett., **105**(2010) 262302.

[Roh99] D. Rohe et al. *Measurement of the Neutron Electric Form Factor $G_{\rm en}$ at 0.67 (GeV/c)^2 via $^3\vec{H}e(\vec{e}, e'n)$.* Phys. Rev. Lett., **83**(1999) 4257–4260.

[Rom97] M. V. Romalis, E. Miron, and G. D. Cates. *Pressure broadening of Rb D_1 and D_2 lines by ^{3}He, ^{4}He, N_2, and Xe: Line cores and near wings.* Phys. Rev. A, **56**(1997) 4569–4578.

[Rom98] M. Romalis and G. Cates. *Accurate* ^{3}He *polarimetry using the Rb Zeeman frequency shift due to the* Rb$-^3$He *spin-exchange collisions.* Phys. Rev. A, **58**(1998) 3004–3011.

[Roz11] D. Rozpedzik, J. Golak, S. Kölling, E. Epelbaum, R. R. Skibiński, H. Witała, and H. Krebs. *Signatures of the chiral two-pion exchange electromagnetic currents in the* ^{2}H *and* ^{3}He *photodisintegration reactions.* Phys. Rev. C, **83**(2011) 064004.

[RS03] R. R. Skibiński, J. Golak, H. Kamada, H. Witała, W. Glöckle, and A. Nogga. *Search for three-nucleon force effects in two-body photodisintegration of* ^{3}He(^{3}H) *and in the time reversed proton-deuteron radiative capture process.* Phys. Rev. C, **67**(2003) 054001.

[RS05] R. R. Skibiński, J. Golak, H. Witała, W. Glöckle, A. Nogga, and H. Kamada. *Polarization observables in the semiexclusive photoinduced three-body breakup of* ^{3}He. Phys. Rev. C, **72**(2005) 044002.

[Rub07] A. Ruben, T.E. Hoagland, R. Fox, P.L. Kerr, G. Montermann, and R. Schneider. *A new four channel pulse shape discriminator.* In *Nuclear Science Symposium Conference Record, 2007. NSS '07. IEEE*, volume 1, pages 681–684, Oct 2007.

[Rus] G. Rusev et al. private communication.

[San83] A.M. Sandorfi, M.J. LeVine, C.E. Thorn, G. Giordano, G. Matone, and C. Schaerf. *High Energy Gamma Ray Beams from Compton Backscattered Laser Light.* Nuclear Science, IEEE Transactions on, **30**(1983) 3083–3087.

[San03] R. Skibiński, J. Golak, H. Witała, W. Glöckle, H. Kamada, and A. Nogga. *Three-nucleon photodisintegration of* ^{3}He. Phys. Rev. C, **67**(2003) 054002.

[Sau96] M. Sauer, A. Fuchs, P. Grabmayr, and J. Leypoldt. *The ring shaped plastic scintillator detector STAR for forward angle reconstruction.* Nuclear Instruments and Methods in Physics Research Section A: Accelerators, Spectrometers, Detectors and Associated Equipment, **378**(1996) 143 – 148.

[Sch01a] Michael Schwamb and Hartmuth Arenhövel. *Off-shell effects in electromagnetic reactions on the deuteron.* Nuclear Physics A, **696**(2001) 556 – 580.

[Sch01b] Michael Schwamb and Hartmuth Arenhövel. *The role of meson retardation in deuteron photodisintegration above pion threshold.* Nuclear Physics A, **690**(2001) 682 – 710.

[Set96] H.R. Setze et al. *Verification of the space-star anomaly in nd breakup.* Physics Letters B, **388**(1996) 229 – 234.

[Sie37] A. J. F. Siegert. *Note on the Interaction Between Nuclei and Electromagnetic Radiation.* Phys. Rev., **52**(1937) 787–789.

[Sim02] S. Simula, M. Osipenko, G. Ricco, and M. Taiuti. *Leading and higher twists in the proton polarized structure function g_1^p at large Bjorken x.* Phys. Rev. D, **65**(2002) 034017.

[Sin10] J. Singh. *Alkali-Hybrid Spin-Exchange Optically-Pumped Polarized ^{3}He Targets Used for Studying Neutron Structure.* Ph.D. Thesis, University of Virginia, 2010.

[Sko74] D. M. Skopik, Y. M. Shin, M. C. Phenneger, and J. J. Murphy. *Photodisintegration of deuterium determined from the electrodisintegration process.* Phys. Rev. C, **9**(1974) 531–536.

[Sko79] D. M. Skopik, H. R. Weller, N. R. Roberson, and S. A. Wender. ^{2}H(p, γ)^{3}He *reaction using polarized and unpolarized protons.* Phys. Rev. C, **19**(1979) 601–609.

[Sta57] H. P. Stapp, T. J. Ypsilantis, and N. Metropolis. *Phase-Shift Analysis of 310 MeV Proton-Proton Scattering Experiments.* Phys. Rev., **105**(1957) 302–310.

[Sta01] A. Starostin et al. *Measurement of* $K^- \overrightarrow{p} \eta\Lambda$ *near threshold.* Phys. Rev. C, **64**(2001) 055205.

[Sto94] V. Stoks, R. Klomp, C. Terheggen, and J. de Swart. *Construction of high-quality NN potential models*. Phys. Rev. C, **49**(1994) 2950–2962.

[Sun09] C. Sun. *Characterizations and Diagnostics of Compton Light Source*. Ph.D. Thesis, Duke University, 2009.

[Tak56] Mituo Taketani, Seitaro Nakamura, and Muneo Sasaki. *Part V. On the Method of the Theory of Nuclear Forces*. Progress of Theoretical Physics Supplement, **3**(1956) 169–174.

[Tia02] L. Tiator. *MAID and the GDH Sum Rule in the Resonance Region*. In *Symposium on the Gerasimov-Drell-Hearn Sum Rule and the Nucleon Spin Structure in the Resonance Region*, page 2736, 2002.

[Tic73] G. Ticcioni, S.N. Gardiner, J.L. Matthews, and R.O. Owens. *The two-body photodisintegration of ^{3}He*. Physics Letters B, **46**(1973) 369 – 371.

[Tor11] W. Tornow et al. *Two-body photodisintegration of ^{3}He between 7 and 16 MeV*. Physics Letters B, **702**(2011) 121 – 126.

[Tro99] González Trotter et al. *New Measurement of the $^1S_0$ Neutron-Neutron Scattering Length Using the Neutron-Proton Scattering Length as a Standard*. Phys. Rev. Lett., **83**(1999) 3788–3791.

[Tro09] D.E. González Trotter, F. Salinas Meneses, W. Tornow, A.S. Crowell, C.R. Howell, D. Schmidt, and R.L. Walter. *Neutron detection efficiency determinations for the TUNL neutron-neutron and neutron-proton scattering-length measurements*. Nuclear Instruments and Methods in Physics Research Section A: Accelerators, Spectrometers, Detectors and Associated Equipment, **599**(2009) 234 – 242.

[Tso11] N. Tsoulfanidis and S. Landsberger. *Measurement and Detection of Radiation*. CRC Press, 2011.

[vdW71] A. van der Woude, M. L. Halbert, C. R. Bingham, and B. D. Belt. *Evidence for a $T = \frac{1}{2}$ Resonance in the ^{3}He System*. Phys. Rev. Lett., **26**(1971) 909–912.

[Vey74] A. Veyssire, H. Beil, R. Bergre, P. Carlos, A. Leprtre, and A. De Miniac. *A study of the photoneutron contribution to the giant dipole resonance of s-d shell nuclei*. Nuclear Physics A, **227**(1974) 513 – 540.

[War63] J. B. Warren, K. L. Erdman, L. P. Robertson, D. A. Axen, and J. R. Macdonald. *Photodisintegration of* He^3 *near the Threshold.* Phys. Rev., **132**(1963) 1691–1692.

[Web71] D.V. Webb, E.G. Muirhead, and B.M. Spicer. *The* ^{39}K *photoneutron cross-section to the* ^{38}K *isomeric state.* Nuclear Physics A, **171**(1971) 324 – 336.

[Wei92] Steven Weinberg. *Three-body interactions among nucleons and pions.* Physics Letters B, **295**(1992) 114 – 121.

[Wel09] Henry R. Weller, Mohammad W. Ahmed, Haiyan Gao, Werner Tornow, Ying K. Wu, Moshe Gai, and Rory Miskimen. *Research opportunities at the upgraded* HIγS *facility.* Progress in Particle and Nuclear Physics, **62**(2009) 257 – 303.

[Wir95] R. Wiringa, V. Stoks, and R. Schiavilla. *Accurate nucleon-nucleon potential with charge-independence breaking.* Phys. Rev. C, **51**(1995) 38–51.

[Wöl66] W. Wölfli, R. Bösch, J. Lang, R. Müller, and P. Marmier. *Proton capture by deuterons.* Physics Letters, **22**(1966) 75 – 76.

[Wu96] Ying Wu, Vladimir N. Litvinenko, Bentley Burnham, John M.J. Madey, and Seong Hee Park. *The performance of the Duke {FEL} storage ring.* Nuclear Instruments and Methods in Physics Research Section A: Accelerators, Spectrometers, Detectors and Associated Equipment, **375**(1996) 74 – 77. Proceedings of the 17th International Free Electron Laser Conference.

[Wu06] Y. K. Wu, N. A. Vinokurov, S. Mikhailov, J. Li, and V. Popov. *High-Gain Lasing and Polarization Switch with a Distributed Optical-Klystron Free-Electron Laser.* Phys. Rev. Lett., **96**(2006) 224801.

[Xu00] W. Xu et al. *Transverse Asymmetry* $A_{T'}$ *from the Quasielastic* $^3\vec{H}e(\vec{e},e')pp$ *Process and the Neutron Magnetic Form Factor.* Phys. Rev. Lett., **85**(2000) 2900–2904.

[Ye10] Q. Ye, G. Laskaris, W. Chen, H. Gao, W. Zheng, X. Zong, T. Averett, G.D. Cates, and W.A. Tobias. *A high-pressure polarized* ^{3}He *gas target for nuclear-physics experiments using a polarized photon beam.* The European Physical Journal A, **44**(2010) 55–61.

[Zhe08] V.A. Zheltonozhsky, V.M. Mazur, Z.M. Bigan, and D.M. Symochko. Yad. Fiz. Energ., **2**(2008) 13.

[Zim13] W. R. Zimmerman. *Direct Observation of the Second $J^\pi = 2^+$ State in ^{12}C.* Ph.D. Thesis, University of Connecticut, 2013.

[Zon10] X. Zong. *First Study of Three-body Photodisintegration of* ^{3}He *with Double Polarizations at* HIγS. Ph.D. Thesis, Duke University, 2010.

Biography

Personal Data

Georgios Laskaris was born the 12^{th} of November 1984, in Athens, Hellenic Republic by a Spartan father and a Lesvian mother. He has one brother. He attended the primary Catholic school Écolle Jeanne D'Arc and the 8^{th} Gymnasium and Lyceum of Piraeus from where he graduated with honors in May, 2002. He got admitted in the School of Applied Mathematical and Physical Sciences of the National Technical University of Athens where he joined the high energy physics group and graduated with honors in May, 2007 (5 years degree). One year later, he was accepted for graduate studies by the physics department of Duke University where he joined the medium energy physics group of professor Haiyan Gao. He received his Master of Arts in May of 2011 and his Doctor of Philosophy in May of 2015.

Awards and Honors

1. 2014, Global Young Scientist Summit @ one-north, Republic of Singapore.
2. 2013-2014, Walter Gordy Fellowship, Physics Department, Duke University, USA.
3. 2011-2014, Henry W. Newson Fellowship, Duke University, TUNL, USA.
4. 2003, Fellowship for Academic Excellence, Hellenic Republic.

Referred Journal Publications

1. **G. Laskaris** *et al.*, *Measurement of the Doubly-Polarized* $^3\vec{H}e(\vec{\gamma}, n)pp$ *Reaction at 16.5 MeV and Implications for the GDH Sum Rule*, in preparation (2015).
2. **G. Laskaris** *et al.*, *Two-body Photodisintegration of* ^3He *with Double-Polarizations at 29.0 MeV*, in preparation (2015).
3. **G. Laskaris** *et al.*, *Spin-dependent cross sections from the three-body photodisintegration of* ^3He *at incident energies of 12.8 and 14.7 MeV*, Phys. Rev. C **89**, 024002 (2014).
4. **G. Laskaris** *et al.*, *First Measurement of Spin-Dependent Double Differential Cross Sections from* $^3\vec{H}e(\vec{\gamma}, n)pp$ *at Incident Photon Energies of 12.8 and 14.7 MeV*, Phys. Rev. Lett. **110**, 202501 (2013).
5. A. Kafkarkou, M.W. Ahmed, P.-H. Chu, R.H. France, H.J. Karwowski, D.P. Kendellen, **G. Laskaris** *et al.*, *Study of the* $^{10}B(p,\alpha)$ *reaction between 2.1 and 6.0 MeV*, Nucl. Instrum. Methods B **316**, 48 (2013).
6. P.-H. Chu, A. Dennis, C. Fu, H. Gao, R. Khatiwada, **G. Laskaris** *et al.*, *Laboratory search for spin-dependent short-range force from axionlike particles using optically polarized* ^3He *gas*, Phys. Rev. D (R) **87**, 011105 (2013).
7. W. Zheng, H. Gao, B. Lalremruata, Y. Zhang, **G. Laskaris** *et al.*, *Search for spin-dependent short-range force using optically polarized* ^3He *gas*, Phys. Rev. D (R) **85**, 031505 (2012).
8. M. Anselmino *et al.*, *Transverse-momentum-dependent parton distribution/ fragmentation functions at an electron-ion collider*, Eur. Phys. J. A. **47**, 3 (2011).
9. Q. Ye, **G. Laskaris** *et al.*, *A High Pressure Polarized* ^3He *Gas Target for the High Intensity Gamma Source Facility at the Duke Free Electron Laser Labora-*

tory, Eur. Phys. J. A. **44**, 55 (2010).

10. A. Floratou, F. Bertsch, J.M. Patel, **G. Laskaris**, *Towards Building Wind Tunnels for Data Center Design*, Very Large Data Bases (2014).

Proceedings

P. H. Chu, A. Dennis, C. B. Fu, H. Gao, R. Khatiwada, **G. Laskaris** *et al.*, *Searches for possible T-odd and P-odd short range interactions using polarized nuclei*, EPJ Web Conf. **66**, 05003 (2014).